INVESTIGATING MESOSTRUCTURED SUPERCONDUCTORS ENGINEERED USING BLOCK COPOLYMER SELF-ASSEMBLY

A Dissertation

Presented to the Faculty of the Graduate School

of Cornell University

In Partial Fulfillment of the Requirements for the Degree of

Doctor of Philosophy

by

Randal Paxton Thedford Jr.

May 2022

INVESTIGATING MESOSTRUCTURED SUPERCONDUCTORS ENGINEERED USING BLOCK COPOLYMER SELF-ASSEMBLY

Randal Paxton Thedford Jr., Ph. D.

Cornell University, 2022

The synthesis and study of quantum materials, e.g., materials showing strong electronic correlations such as superconductors, is of increasing importance to areas including information and energy technology. The vast majority of investigations in quantum materials science are focused at the level of atomic order, but a growing body of work demonstrates that mesoscale (10s-100s of nm) structure can modulate quantum level derived properties. In particular, the field of superconductivity is rich in mesoscale phenomena, such as periodic mesostructure dependent magnetic vortex lattices, thermomagnetic flux avalanche behavior, or effects associated with the Cooper pair coherence length. In this thesis, routes to quantum metamaterials are described, which make use of a particular type of self-assembling soft matter components, i.e., block copolymers (BCPs), to engineer the mesoscopic architecture and associated macroscopic properties of superconductors in a highly tunable fashion.

After an introduction chapter, in which the particular challenges addressed in this thesis are summarized, the second chapter of this thesis provides a broad overview over soft matter enabled quantum materials, both in terms of what has already been accomplished as well as a discussion of particular opportunity spaces for future work. This overview presents the wide spectrum of novel structures and physical phenomena

made assessible through the use of soft matter self-assembly for the study of different classes of quantum materials, i.e., superconductors, topologically protected quantum materials, and magnetic quantum materials. The remaining chapters of this thesis describe experimental studies assessing multiple pathways to BCP self-assembly derived superconductors in an effort to bring new capabilities and insights to the field. Throughout all these chapters, confinement and mesostructure in BCP derived superconductors is reported to affect fundamental, quantum level properties. Further, solution processible routes to superconductors are shown to enable new methods for defining macroscopic shape and form. This thesis investigates BCP templated superconductors though these two lenses: understanding the fundamental role of mesostructure in defining quantum materials properties, and exploring the technological benefits of solution processibility. To these ends, several synthetic routes are developed which provide new scientific insights and/or demonstrate improved compatibility with fabrication by a larger community.

In the third chapter, superconducting mesoporous niobium carbonitride (NbCN) thin films are prepared using a triblock terpolymer as a structure directing agent for niobia sol precursors. The final material structure after thermal processing is consistent with a mesoscale distorted alternating gyroid composed of highly granular, crystalline NbCN. Transport measurements determine the critical magnetic field in these mesoporous thin film superconductors, which is equal to or higher than in bulk material or non-porous films. It is conjectured that the porosity of the BCP templated NbCN is responsible for improved properties due to better penetration of reactive gases during processing. The work also successfully demonstrates transitioning BCP self-assembly

derived superconductors from the bulk to thin films allowing integration of photolithographic top-down methods with bottom-up self-assembly to direct superconducting mesostructures on silicon substrates. This promises the generation of solution accessible device structures from a combination of ideas from the soft and hard condensed matter sciences.

In the fourth chapter, hexagonally mesoporous, crystalline NbCN superconductors are prepared using Pluronics-family BCPs. This achievement overcomes a long-standing hurdle in the mesoporous materials field, creating phase-pure transition metal nitride-type materials without loss of mesostructural order. It is further demonstrated, that small molecule and polymeric pore-expanding agents as well as choice of BCP molar mass and composition lends the ability to finely tune mesostructural parameters like pore size and wall thickness. The wide availability of Pluronics BCPs is expected to accelerate the investigation of this superconducting class of mesoporous non-oxides, which should further enable a wealth of studies, e.g., into host-guest interactions and mesostructure-property correlations.

In the fifth chapter, an alternative route to BCP self-assembly derived superconductors is pursued, which involves backfilling of a BCP templated mesoporous ceramic material with a superconducting metal, i.e., indium, under high pressure to generate thick macroscopic bulk materials. To that end, triblock terpolymers together with oligomeric polysilazanes are first self-assembled and processed to create double gyroid structured silicon oxynitride (SiON) ceramic monoliths of order 60 μm in thickness. After infiltration of these mechanically robust porous ceramic templates with molten indium under high pressure, high-fidelity replication of the double gyroid

structure is observed throughout the thickness of the resulting nanocomposites. Analysis determines that the superconducting coherence length of nanoconfined indium is reduced to the length scale of the gyroid strut thickness, causing a switch from type I to type II superconductor behavior and a large enhancement of the critical magnetic field.

Finally, in a conclusion chapter the results of this thesis are summarized in terms of key insights obtained from the study of BCP self-assembly derived superconductors. Furthermore, an outlook is presented of possible future work that is enabled by the findings described herein for the next generation of Ph.D. students continuing with this line of research at the intersection of the soft and hard condensed matter sciences.

BIOGRAPHICAL SKETCH

R. Paxton Thedford Jr. was born in Victoria, Texas on May 12th, 1994. His general introduction to science and engineering came through his parents, Randal and Lara Thedford, who also seemed to buy him any book he ever asked for (at the time Paxton really thought he was getting away with something). From 2008–2012 he attended Tivy High School in Kerville, Texas, which he will forever hold as his hometown and the location of the inarguably best breakfast tacos in the world. At Tivy, Paxton was lucky to have teachers and friends who encouraged him towards creative writing, mock trial, long-distance running, and advanced chemistry classes (effectively all the basic components of his later graduate work).

Paxton enrolled in the Chemical Engineering program at The University of Texas at Austin, in 2012. It was here that he first became involved in scientific research in the lab of Dr. Dionicio Siegel, synthesizing phthaloyl peroxide for the selective hydroxylation of arenes and eating more burritos than he should have. He later joined the group of Dr. C. Grant Willson, where he had enormous fun making and breaking open square molecules with the excuse of developing new materials for microelectronics packaging. During this time Paxton also spent a summer interning at 3M in St. Paul, Minnesota, where he designed reactor systems for emulsion polymerization during the week and went camping or ate cheese curds (most often cheese curds) on the weekends. During his time at UT – Austin, Paxton's experience was incredibly enriched by his involvement with the local chapter of Camp Kesem, where he found a wonderful community united in the service of others.

Beginning in the fall of 2016, Paxton has been pursuing his Ph.D. in the groups of Profs. Uli Wiesner and Sol Gruner at Cornell University. During this time he worked on using block copolymer self-assembly to control structure and engineer materials properties for several applications, most commonly in superconducting materials.

for those who come into harbors seen for the first time

may you have joy, pleasure, and many summer mornings

ACKNOWLEDGMENTS

Throughout my Ph.D. I have been incredibly fortunate to have the support of many wonderful mentors, collaborators, family, and friends. I would first like to thank my advisors, Uli and Sol, for their inspiration and guidance, and for providing me with interesting questions and a great amount of freedom to pursue them. I cannot imagine having more fun during these past years doing any thesis other than this one, uniquely possible under your supervision. Further, without your constant curiosity, enthusiasm, encouragement, and insight I would have been lost many times over.

I am grateful for the support of many other faculty. Thank you to Prof. Lara Estroff for many excellent and helpful discussions, timely and detailed manuscript edits, and your infectious good spirit. Thanks also to Prof. Katja Nowack and Prof. Bruce van Dover for guidance on superconductivity, without which I would have been grasping in the dark. Thank you also to the members of my special committee, Profs. Yong Lak Joo and Héctor Abruña for your time, input, and quick signatures. Finally, thanks to Prof. Susan Daniel and Paulette Clancy for their critical role on my NSF application, and for their efforts cultivating a positive culture in the CBE department.

I must also acknowledge my fantastic colleagues who taught me how to do science, helped make my time at Cornell enjoyable as well as productive, and contributed to my thesis work. Most especially to Dr. Peter Beaucage, I am deeply grateful for your mentorship and friendship. Thank you to my collaborators, co-authors, and friends Fei Yu, William Tait, Corson Chao, for making the lab an order of magnitude more fun. Particular thanks also to Dr. Ethan Susca, Dr. Sarah Hesse, Konrad Hedderick, Dana Chapman, Gavin Batsimm, Lilly Tsaur, Dr. Yusuke Hibi, Dr. Kate Barteau, Prof. Joerg Werner, Dr. Tom Gardinier, Dr. Melik Turker, Dr. Josh Hinckley, Jacob Erstling, and Rachel Lee for guidance and camaraderie.

Thank you as well to all those who played a role supporting my work.

Particularly to Dr. Guillaume Freychet and Dr. Mikhail Zhernenkov of the NSLS, and Dr. Arthur Woll and Dr. Louisa Smieska of CHESS for aid in synchrotron measurements. Thank you to the staff of CNF and CCMR, especially Malcolm Thomas, Steve Kriske, and Anthony Condo. Thank you to Marty Novak for help with fabrication and repair. And lastly a huge thanks to Dr. Mark Tate for all of his time spent teaching me to use and maintain the lab SAXS apparatus.

My time at Cornell was made vastly more enjoyable by my friends. To Dr. Andrew Ruttinger, Andy Sanchez, Cody Freitag, Urmilla Banerjee, Dr. Tom Gardinier, Will Tait, Dr. Alex Warren, Dr. Peter Beaucage, Konrad Hedderick, Dana Chapman, Dr. Arna Pálsdóttir, Dr. Colleen Lawlor, Meghan O'Leary, Fei Yu, Dr. Abhishek Sharma, Dr. Jon Ludwicki, Dr. Morgan Ludwicki, Dr. Joey Brown, Dr. Andrew Shah, Dr. Carolyn Shurer, Dr. Melik Turker, and so many others: thank you all for every laugh, every beer, every meal, every minute. And special thanks to Greg Chancellor and Thomas Hall for trekking up to Ithaca in the cold and rain solely for my sake.

An enormous thanks to my family, to my parents Lara and Randal, who have been a constant source of encouragement sent up from Texas keeping me warm even in the middle of Ithaca winters. And thanks to my brother, Chris, who has been good company in the final stretch.

Lastly, deepest thanks to Alexandra Gibner, who has supported me by innumerable and myriad methods throughout my time at Cornell. Thank you for all the ways, big and small, in which you helped to keep my spirits high and my days joyful. Every day of this journey I have been grateful for your companionship.

TABLE OF CONTENTS

CHAPTER 1

INTRODUCTION

Soft Matter Self-Assembly for Mesostructured Superconductors

The term soft matter represents a variety of systems which are physically defined or altered by forces of the same magnitude in energy as room temperature thermal fluctuations, and includes liquid crystals, colloids, polymers, and biological materials.[1] Self-assembly refers to the tendency found in many of these systems for matter to spontaneously self-organize into periodic structures. This happens at characteristic lengths just above the atomic or molecular scales i.e., 10's to 100's of nanometers, known as the mesoscale.[2] One important class of self-assembling soft matter systems is known as block copolymers (BCPs), defined as macromolecules obtained from two or more covalently linked, chemically dissimilar polymer blocks. Determined by the interplay of enthalpic and entropic effects, BCPs undergo microphase segregation into distinct mesophases with characteristic lattice dimensions on the mesoscale. For the past several decades, a wealth of studies have shown that sophisticated synthetic techniques can be used to tune the morphology and characteristic periodicity of self-assembled BCP mesostructures with an exquisite degree of control.[3] Much work has been done as well on the use of BCPs as structure directing agents in the co-assembly with organic or inorganic additives, producing a broad range of mesostructured composites and, after removal of the combustible components, ordered mesoporous materials. These materials have found application in

a range of different fields, including separations, energy materials, and quantum materials, where it is found that the mesoscale architecture defined by BCP self-assembly can result in novel phenomena and/or improved properties.[4–7]

In the area of quantum materials, the first case of a BCP self-assembly derived superconductor was reported in 2016.[6] In this work, the authors synthesized niobium nitride superconductors with co-continuous cubic gyroidal morphology using a triblock terpolymer as structure directing agent for a niobium oxide based sol. They found evidence of flux-pinning defined by the BCP induced periodic lattice. While largely limited to the two-dimensional regime in previous studies, there has been much effort made to understand the effects of mesoscale structure on superconductivity. Two important characteristic lengths scales which define superconductor behavior are the London penetration depth and the coherence length, and typically fall in the mesoscopic range of 10-1000 nm.[8] Confinement or periodic structuring of superconductors at this scale can dramatically alter macroscopic properties such as the critical transition temperature or critical magnetic field.[9] Furthermore, in the technologically relevant type II class of superconductors there exist magnetic vortices which allow the penetration of quantized magnetic flux into a superconductor.[8] These vortices can order into periodically pinned arrays and undergo motion and phase transitions, with such structures and dynamics also occurring on the mesoscale. Changing the mesoscopic structure of a superconductor can thus have a large impact over vortex phenomena and relevant properties such as the critical current density.[10]

This thesis expands upon the use of BCPs for the synthesis of superconductors, developing routes which lead to novel form factors, increased materials accessibility,

or entirely new materials systems. The goals of the works described in the following chapters can be ascribed to two general categories: a scientific goal to gain insights into the fundamental ways in which BCP derived mesostructures alter quantum level characteristics and resulting macroscopic superconductor behavior, and a technological goal to discover how BCP solution based self-assembly can give rise to entirely new routes to superconductor formation with novel form factors not accessible via traditional high-vacuum approaches.

Outline

Chapter two reviews the current status and future perspective of soft matter enabled quantum materials i.e., materials made using self-assembling soft matter components. This provides broader context into which the experimental studies described in subsequent chapters fit. In the three categories of quantum materials i.e., superconductors, topological materials, and magnetic materials, current published work is described which lies at the interface of soft matter and quantum materials, and a summary is provided of the key findings and new phenomena or features which come out of these studies. This chapter also includes a discussion of particular opportunity spaces for future work in this area.

Chapter three presents a route to mesoporous NbCN superconductors in a thin film form factor through the use of spin-coating and subsequent thermal processing of a BCP/sol-gel system atop a silicon substrate. Through spin-coating and subsequent patterning of these mesoporous NbCN thin films using conventional photolithographic means, it is shown that polymer solution based superconductor synthesis enables

integration with nanofabrication. This amenability with planar processing is an example of the desirable technological capabilities that soft matter can bring to quantum materials synthesis.[11] It is also expected that the adaptation of BCP templated superconductors to the thin film regime will be a key enabler for device fabrication and more in-depth characterization of electronic transport properties.

Chapter four demonstrates a route to a hexagonally mesoporous, superconducting NbCN making use of Pluronics family polymers as structure directing agents. Previously it was thought that the small wall thickness in mesoporous materials derived from low molar mass Pluronics precluded their use in the templating of non-oxides.[12] This longstanding challenge is overcome through carefully tuned thermal processing protocols. The commercial availability of Pluronics family polymers is expected to greatly increase the accessibility of BCP derived superconductors, as compared to the methods described in other chapters which rely on custom-synthesized triblock terpolymers. Furthermore, this materials route may allow for exploitation of the large body of literature and technology using Pluronics to achieve new capabilities, e.g tunable pore sizes via swelling, host-guest interactions, and novel mesostructure-property correlations.

Chapter five describes the use of high-pressure backfilling of molten indium into BCP derived mesoporous templates to showcase an alternative route to a BCP based mesostructured superconductor. This work addresses the challenge of high quality BCP templating of metals in the bulk regime, which has in the past proven challenging outside of thin films.[13–15]. Furthermore, while the nitride based materials studied in the earlier chapters constitute type-II superconductors, indium is a type-I

superconductor, which poses additional interesting scientific questions addressed in this chapter about how such quantum materials evolve in their macroscopic properties when confined to BCP mesophase derived nanostructures.

Finally, in a conclusion chapter the results of this thesis are summarized and an outlook is presented of work that is enabled by the findings described herein for the next generation of Ph.D. students continuing with this line of research at the intersection of soft and hard condensed matter science.

REFERENCES

1. Israelachvili, J. N. *Intermolecular and surface forces*. (Academic press, 2011).
2. Whitesides, G. M. Self-Assembly at All Scales. *Science* **295,** 2418–2421 (2002).
3. Bates, F. S., Hillmyer, M. A., Lodge, T. P., Bates, C. M., Delaney, K. T. & Fredrickson, G. H. Multiblock Polymers: Panacea or Pandora's Box? *Science* **336,** 434–440 (2012).
4. Templin, M., Franck, A., Du Chesne, A., Leist, H., Zhang, Y., Ulrich, R., Schädler, V. & Wiesner, U. Organically Modified Aluminosilicate Mesostructures from Block Copolymer Phases. *Science* **278,** 1795–1798 (1997).
5. Orilall, M. C. & Wiesner, U. Block copolymer based composition and morphology control in nanostructured hybrid materials for energy conversion and storage: solar cells, batteries, and fuel cells. *Chem Soc Rev* **40,** 520–535 (2011).
6. Robbins, S. W., Beaucage, P. A., Sai, H., Tan, K. W., Werner, J. G., Sethna, J. P., DiSalvo, F. J., Gruner, S. M., Van Dover, R. B. & Wiesner, U. Block copolymer self-assembly–directed synthesis of mesoporous gyroidal superconductors. *Sci. Adv.* **2,** e1501119 (2016).
7. Dorin, R. M., Phillip, W. A., Sai, H., Werner, J., Elimelech, M. & Wiesner, U. Designing block copolymer architectures for targeted membrane performance. *Polymer* **55,** 347–353 (2014).
8. Tinkham, M. *Introduction to superconductivity*. (Dover Publ, 2015).
9. Bose, S. & Ayyub, P. A review of finite size effects in quasi-zero dimensional superconductors. *Rep. Prog. Phys.* **77,** 116503 (2014).

10. Vélez, M., Martín, J. I., Villegas, J. E., Hoffmann, A., González, E. M., Vicent, J. L. & Schuller, I. K. Superconducting vortex pinning with artificial magnetic nanostructures. *J. Magn. Magn. Mater.* **320,** 2547–2562 (2008).
11. Diao, Y., Shaw, L., Bao, Z. & Mannsfeld, S. C. B. Morphology control strategies for solution-processed organic semiconductor thin films. *Energy Env. Sci* **7,** 2145–2159 (2014).
12. Wei, J., Sun, Z., Luo, W., Li, Y., Elzatahry, A. A., Al-Enizi, A. M., Deng, Y. & Zhao, D. New Insight into the Synthesis of Large-Pore Ordered Mesoporous Materials. *J. Am. Chem. Soc.* **139,** 1706–1713 (2017).
13. Cowman, C. D., Padgett, E., Tan, K. W., Hovden, R., Gu, Y., Andrejevic, N., Muller, D., Coates, G. W. & Wiesner, U. Multicomponent Nanomaterials with Complex Networked Architectures from Orthogonal Degradation and Binary Metal Backfilling in ABC Triblock Terpolymers. *J. Am. Chem. Soc.* **137,** 6026–6033 (2015).
14. Hsueh, H.-Y., Huang, Y.-C., Ho, R.-M., Lai, C.-H., Makida, T. & Hasegawa, H. Nanoporous Gyroid Nickel from Block Copolymer Templates via Electroless Plating. *Adv. Mater.* **23,** 3041–3046 (2011).
15. Vignolini, S., Yufa, N. A., Cunha, P. S., Guldin, S., Rushkin, I., Stefik, M., Hur, K., Wiesner, U., Baumberg, J. J. & Steiner, U. A 3D Optical Metamaterial Made by Self-Assembly. *Adv. Mater.* **24,** OP23–OP27 (2012).

CHAPTER 2

THE PROMISE OF SOFT MATTER ENABLED QUANTUM MATERIALS[†]

Abstract

The field of quantum materials has experienced rapid growth over the past decade, driven by exciting new discoveries with immense transformative potential. Traditional synthetic methods to quantum materials have, however, limited the exploration of architectural control beyond the atomic scale. In contrast, soft matter self-assembly can be used to tailor materials structure over a large range of length scales, with a vast array of possible form factors, promising emerging quantum materials properties at the mesoscale. This review explores opportunities for soft matter science to impact the synthesis of quantum materials with advanced properties. We highlight existing work at the interface of these two fields and then provide a perspective on possible future directions by discussing the potential benefits and challenges which could arise from their bridging.

[†]R. Paxton Thedford[*], Fei Yu[*], William Tait[*], Kunal Krishnaraj, Francesco Monticone, and Ulrich Wiesner. *in preparation* (2022)

Introduction

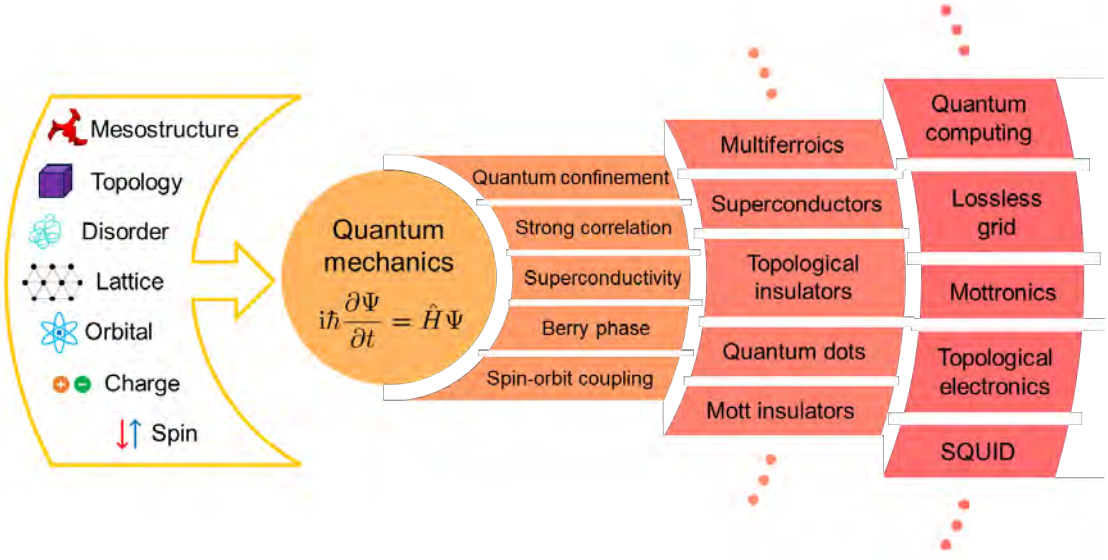

Figure 2.1: *Quantum materials from fundamental system parameters (left) all the way to applications (right). System parameters are the different degrees of freedom that, upon treatment by quantum mechanics, give rise to quantum phenomena underpinning classes of quantum materials. With soft matter, we can identify additional degrees of freedom (e.g., disorder and mesostructure) expected to enable further altering and tuning of quantum materials behavior.*

Driven in large part by the current excitement about quantum information science in general, and quantum computing in particular, the area of quantum materials has seen substantial growth in recent years.[1–3] Similar to the early days of nanotechnology, currently everything "quantum" captures the imagination even of the

public, as evidenced by product labels ranging from "quantum detergents" all the way to "quantum cars". The term 'quantum materials' was originally used more specifically to refer to strongly correlated electron systems, but has since been broadened to encompass a huge landscape of materials with the common thread of having properties which emerge from non-trivial, quantum level effects: spin-orbit interaction, topological order, and quantum coherence among others (Figure 2.1).[1,4–6] This resultingly diverse field has seen an explosion in productivity over the past decade, fueled by such advances as the experimental realization of long sought-after particles/quasiparticles,[7–11] the achievement of room-temperature superconductivity at high pressures,[12] the development of material pathways to realizing qubits for quantum computing,[13] and the discovery of emergent behavior in novel material systems.[14–16] Most importantly, the emergent properties of quantum materials show potential for transformative applications in a number of technological sectors that will impact our daily life. Examples include quantum computers with processing abilities many times more powerful than those available today, cybersecurity and encryption that would be unbreachable by today's standards, a national grid with almost no loss, or new personal and commercial electronics with dynamic on-demand properties.[2]

Coined by Feynman in a speech advocating the further development of science at small scales, the phrase "there's plenty of room at the bottom" describes well the vast majority of approaches to quantum materials. Progress in quantum materials discovery and development has so far primarily relied on atomic scale synthetic methods, often with stringent conditions.[17] Increasingly sophisticated techniques in crystal growth and nanofabrication have given rise to the 'age of silicon', and directly enabled the

systematic study of quantum materials.[17] Conventional synthetic methods for quantum materials like molecular beam epitaxy (MBE), pulsed laser deposition (PLD), or single-crystal growth techniques often require ultra-high vacuum or expensive equipment, however, which can impede widespread adoption and limit throughput. Furthermore, these traditional methods typically lack the ability to control structure beyond the crystal lattice, and are often limited in their range of available form factors.

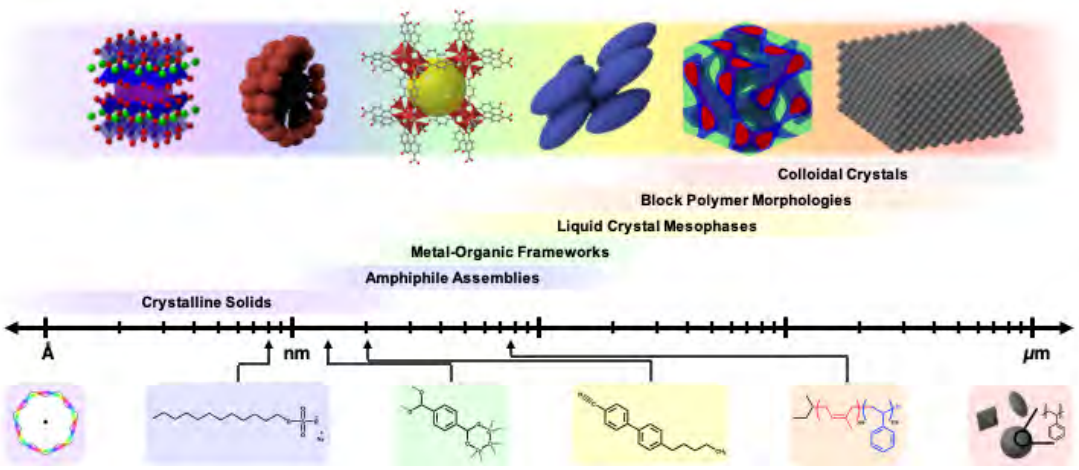

Figure 2.2*: Comparison of the size of various synthetic elements, called synthons (bottom row), the length scales which can be reached by their respective periodic structures (middle row), and representative images of self-organized materials (top row). False coloring is used to connect synthons with their assembled structures, and represents the decrease in free energy of associated assemblies from left (small length scale, high energy) to right (large length scale, low energy). Bottom row from left to right: de Broglie representation of an atom, sodium dodecyl sulfate small molecule amphiphile, representative unit of MOF synthons benzenedicarboxylate and tetrahedrally coordinated Zn^{2+}, liquid crystal synthon (mesogen) 4-*

cyano-4'-pentylbiphenyl (5CB), poly(isoprene-b-styrene) block copolymer, and representation of colloidal polystyrene sphere, octahedron, or ellipsoid. Top row from left to right: $YBa_2Cu_3O_7$ crystal structure, amphiphile based spherical micelle, MOF-5 unit cell, representation of a nematic liquid crystal phase, single unit cell of a block copolymer derived core-shell double gyroid, and close packed colloidal crystal.

Much untapped scientific potential lies in the expansion of quantum materials beyond the confines of these traditional synthetic techniques. In this context, the convergence of hard and soft condensed matter science opens up a particularly large opportunity space. Soft matter provides a wealth of systems with additional degrees of freedom for controlling structure over a wide range of length scales (Figure 2.2).[18] Basic soft matter synthetic elements, or 'synthons' to borrow a term from organic chemistry, encompass a literally infinite set of building blocks with sizes well above the atomic scale that dominates the crystalline state of traditional quantum materials (Figure 2.2, bottom row). A salient feature of soft matter is the ability for these synthons to spontaneously self-organize into a plethora of mesoscopic periodic structures, a process generally referred to as self-assembly. The lattice parameters of these structures typically span a wide range from a few nanometers to several microns, well above those of atomic lattices (Figure 2.2, middle and top).[18] Most interestingly, and in stark contrast to conventional crystalline inorganic materials, in some of these self-assembled soft materials lattice parameters of specific periodic structures can be tailored over a wide range on the mesoscale, *e.g.,* by varying polymer molar mass via living polymerization techniques.[19–22] Synthetic routes to self-assembled materials are often referred to as

"bottom-up" approaches, which stands in contrast to so-called "top-down" strategies including lithography, where materials are structured from the macroscopic scale downwards.

The word 'meso' originates from the Greek language and means 'middle'. The mesoscale, therefore, sits in-between the atomic and macroscopic scales. The mesoscale is a fertile ground for the exploration of emergent quantum effects. For example, take the change in properties due to confinement. In the most basic sense, many quantum materials arise from interfacial phenomena, proximity, or reduced dimensionality.[4,7,23] Thus, the ability to tune interfaces or confinement on the mesoscale of nanometers to microns can have direct consequences on quantum materials properties.[24] Superconducting nanoparticles experience an enhancement in critical parameters as compared to their bulk counterparts.[25,26] In HgTe/(Hg,Cd)Te quantum wells, there exists a threshold thickness of 6.3 nm across which the topologically trivial insulating well starts to harbor edge states, signaling topological phase transformations.[27] Attaining room temperature thermal stability at the 10 nm length scale has been identified as a key challenge for magnetoelectrically coupled multiferroics.[28] An attractive feature of soft matter-derived network structures in particular is the ability to tune confinement in such materials while maintaining three dimensionally continuous connectivity. This could offer opportunities to exploit effects, such as blueshifting of semiconductor band gaps or enhancement in density of states, which arise from 1D-like confinement, while maintaining desirable, more 3D-like transport or other properties.[29] Furthermore, in some quantum materials it is mesoscale characteristic lengths or structures which directly determine behavior. A prime example of this is in superconductors, where

characteristic lengths which govern collective behavior of Cooper pairs and magnetic vortex behavior can range from a few nanometers to microns.[30] Common to other soft materials is the presence of photonic length scale structures for the study of light-electron or light-matter interactions.[31] Another effect which should be considered when shifting focus to larger periodic length scales is the resultant decrease in the frequency domain. This is exemplified very well in the exciting recent detection of topologically protected Weyl points in a macroscopic gyroid photonic crystal sample using microwave transmission experiments.[10] The construction, testing, and analysis of this material was made much more feasible by its increased periodic building block size. Similarly, other topological materials such as photonic topological insulators show much promise in addition to their quantum level, electronic analogues.[32,33]

Moreover, soft matter self-assembly can be used to structure direct other, *e.g.,* inorganic materials lacking this ability for spontaneous self-organization. This enables efficient transfer of diverse and often complex sets of mesostructures, *e.g.,* to more traditional quantum materials thereby enabling emergent behavior. Such bottom-up self-assembly approaches have successfully been demonstrated across very different inorganic materials classes, from amorphous glasses to crystalline transition metal oxides, and from semiconductors across metals all the way to superconductors.[34–39] The enormous amount of structural diversity obtained via self-assembly processes, and the ability to transfer this diversity into relevant 'hard' materials, thus makes possible a plethora of novel synthetic routes towards quantum materials otherwise entirely inaccessible by traditional means.

Finally, as an additional benefit, soft matter processing regularly entails facile and cost-effective solution-based approaches, which typically can be scaled up in straight-forward ways. Techniques like spin-coating or doctor blading, roll-to-roll (R2R) processing, and additive manufacturing or three-dimensional (3D) printing are commonly used in soft matter design and manufacturing, but until today are largely absent in the study and use of quantum materials. Such approaches make soft matter enabled quantum materials particularly appealing for translation into the commercial sector. It is the combination of the enormous scientific as well as technological promise that motivates this rapidly expanding and highly interdisciplinary research area.

The self-assembly of soft matter systems has been employed in ever more sophisticated methods for the creation of periodically ordered materials on the mesoscale, but as yet this toolkit remains vastly underutilized in the synthesis and study of quantum materials.[24] While this will inevitably present new challenges for both the soft and hard condensed matter community, there is much potential for both fundamental scientific discovery and innovation by bridging the artificial separation, which has long divided these two fields. In this review we hope to showcase this immense potential and demonstrate that, through soft matter enabled quantum materials, "there is plenty of room *in the middle"*.

Progress in Soft Matter Enabled Quantum Materials

The twin forces of variety and volume make the prospect of efficiently categorizing the extensive work on quantum materials in conjunction with the even bigger field of soft matter into a comprehensive review a daunting task. As such, in this review we shall follow the example outlined in the *2016 Department of Energy Basic Energy Sciences Workshop Report* on *Quantum Materials for Energy Relevant Technology* of grouping materials based on the nature of their most apparent emergent behavior into three primary categories: superconductors, topological materials, and magnetic materials[2]. While it is inevitable that findings covered in this review will strain the bounds of any single category, we feel this to be a useful framework.

Superconductors

Superconductors have long loomed large in the public imagination. First discovered in mercury at low temperatures in 1911 by Heike Kamerlingh Onnes, one of the most salient features of superconductors is their ability to conduct electricity with zero resistance below a critical transition temperature, T_c.[40] The achievement of this resistance-free electrical transport at ambient conditions would obviously have enormous and far reaching technological impact, and therefore the realization of a 'room temperature superconductor' has long been considered a holy grail of modern condensed matter physics. Central to the development of ever-increasing T_c is a firm understanding of the fundamental underpinnings of superconductivity. This understanding advanced first through phenomenological or macroscopic treatments, capped off by the holistic Ginzburg-Landau theory describing macroscopic

superconductor behavior as a function of two characteristic lengths, the coherence length and the penetration depth.[40] The seminal work of Bardeen, Cooper, and Schrieffer (BCS)[41] later elucidated the microscopic mechanism of superconductivity, identifying supercurrent charge carriers to be electrons coupled by an attractive force into bosonic 'Cooper pairs' which condense to form a macroscopic coherent state. In conventional superconductors, this attractive force is attributed to electron-phonon interactions.

Due to the limiting value of the Debye temperature, this phonon mechanism was predicted at the time to limit the T_c of strongly coupled superconductors of metals and metal alloys to a maximum of around 28 K.[42] This limit was far exceeded, however, with the surprising breakthrough discovery of superconductivity in mixed copper oxides;[43] excitement around this work led to the so called "Woodstock of physics" at the 1987 meeting of the American Physical Society. Cuprates, including the popular YBCO and BSCCO, opened the door to an entirely new category of technologically relevant high-temperature superconductors with T_c's above the boiling point of liquid nitrogen. Importantly, superconducting cuprates also joined organic Bechgaard salts[44] and heavy fermion superconductors[45,46] in the classification of unconventional superconductors, materials which could not be explained through electron-phonon coupling alone. Unconventional and high-temperature superconductors have since remained an extremely active field of study, with much work performed in the service of understanding these exotic materials[47] and achieving superconductivity in novel material classes.[15,48] The drive to achieve ever higher T_c's, however, stalled in 1993 at 133 K.[49] This record has only recently been exceeded, notably in conventional BCS

type, hydrogen rich superconductors with high phonon frequencies and strong electron-phonon coupling under extreme pressures.[12,50,51] Exploration of this class of superconductors has recently achieved long sought-after room-temperature superconductivity; the record now stands at 287 K in carbonaceous sulfur hydride, albeit at a pressure of 267 gigapascals.[12]

A well-studied phenomenon in superconductivity is the effect of material confinement or structure on length scales commensurate with characteristic superconductor length scales.[25,40,52–54] Common considerations in granular superconductors include proximity effects,[55] Josephson coupling between individual grains,[52] quantum phase slips,[56,57] changes in phonon frequency,[58,59] size dependent quantum oscillations[60], vortex pinning forces at interfaces or mesoscopic structures,[61–63] and discretization of electronic energy levels.[64,65] The nano or mesoscale shape, structure, or distribution in a granular superconductor can thus have profound effects on critical parameters and behavior. The elucidation of these effects is important for industrially relevant applications of superconductors, *e.g.,* in composite materials, Josephson arrays, high T_c materials, and engineering magnetic behavior. Most explorations of low dimensional or confined superconductors have utilized traditional solid state synthesis methods.[25,66,67] A few efforts, however, have made use of more facile solution-based techniques, relying on organic moieties in order to control size and shape: small molecule ligands, surfactants, biomolecules, or polymers (Figure 2.3). This work spans quasi 0-dimensional (0-D) nanoparticles, 1-D nanowires or nanorods, 2-D thin films, to bulk 3-D mesoscopic architectures. In all these areas, mesoscale shape and structure has been revealed to intimately affect superconductor properties.

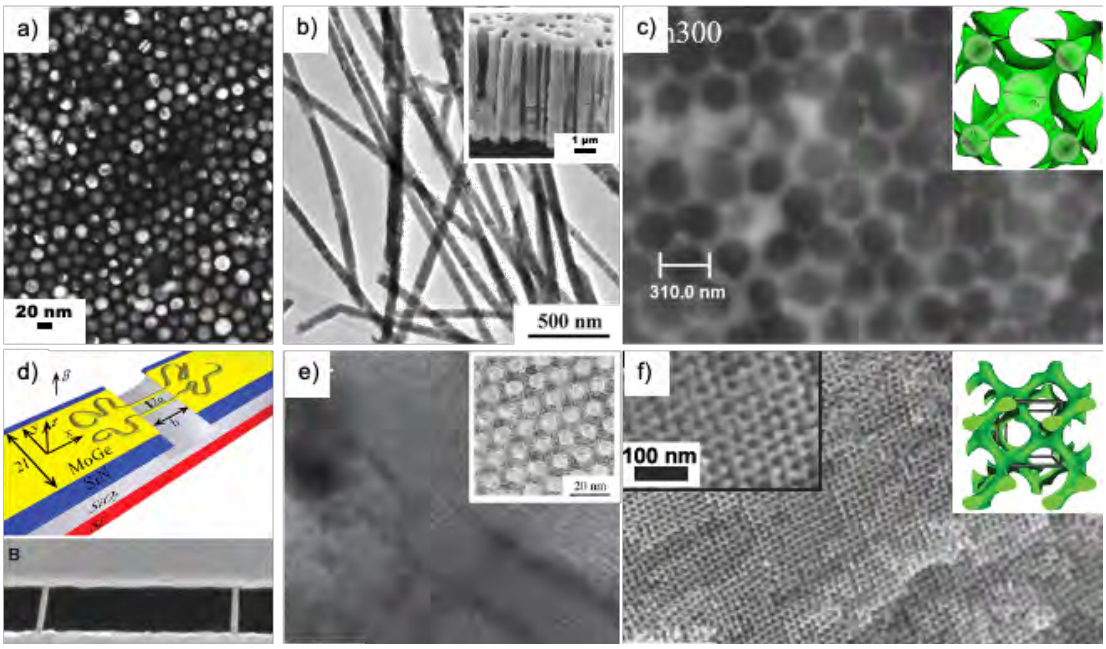

***Figure 2.3**: Superconductors of various geometries via soft matter self-assembly. (a) Lead quantum dot superlattice. Adapted from[68]. (b) Zinc nanowires grown via electrodeposition into a track etched membrane[69]; inset: parent track etched membrane. Adapted from[70]. c) Tin inverse opal via melt injection of opal lattice; inset: depiction of the lattice geometry. Adapted from[63]. (d) MoGe nanowires from DNA templates. Adapted from[57]. (e) Lead nanowires templated with SBA-15 silica adapted from[71]; inset: parent mesoporous SBA-15 silica. Adapted from[72]. (f) Block copolymer directed NbN with alternating gyroid structure; inset depiction of the alternating gyroid lattice. Adapted from[39].*

In the quasi-0-D regime, much work has been performed to create nanoscale superconducting objects. In many studies quantum dot synthetic techniques have been used to create isolated nano-objects or weakly Josephson coupled arrays of superconducting lead nanocrystals,[68,73–76] Pb/PbSe core shell particles,[77] gallium

nanoclusters,[78] or palladium bismuth chalcogenide nanoparticles.[79] In much of this work it has been found that critical field strength and critical temperature typically increase with decreasing material size until a certain material dependent point, at which critical field, H_c, and T_c decrease until superconductivity is lost. This is consistent with seminal Anderson criteria,[80] and can often be understood at least partially in terms of increased phonon coupling strength via surface modes competing with an increasing average energy gap between successive electronic energy levels as material dimension is decreased, the so-called 'kubo gap'. With the claim as the first to demonstrate solution phase synthesis of monodisperse and stable lead nanoparticles, Weitz *et al.* were able to tune both particle size and proximity in the condensed colloidal solid (Figure 2.3a).[68] By decreasing ligand length from eighteen to six carbon chains, this work showed that superconductivity in the lead quantum dots was first suppressed, then localized to a few nanoparticles, then delocalized to the entire particle lattice.[68]

Proximity and shape can also be tuned in superconducting wires or wire networks in the quasi 1-D regime through the use of strategies involving soft matter. Zhang *et al*. made use of sodium dodecyl sulfate for the soft templating of single crystal tin nanowires, and found that both the transition temperature and critical field strength were enhanced[81]. By tuning the ligand composition during growth, Moayed *et al.* synthesized superconducting 'zigzag' PbS nanowires.[77] Bezryadin and co-workers used DNA molecules as templates for superconducting wires (Figure 2.3d).[82–84] Electrodeposition into track etched polycarbonate membranes has also very often been used to create nanowires[85] (Figure 2.3b) of ruthenium,[86] gold,[87] bismuth,[88–91] zinc,[69,92–95] tin,[96–104] lead,[96,98,104–106,106–108] or composites and alloys thereof.[109–111] Wire networks

made in this way have often shown similar behavior as discussed previously in Josephson arrays of nanoparticles, and have been used as a platform to study the Little-Parks effect, phase slip centers, proximity effects, and other effects of nanostructuring on superconductors. A less common templating route to ultra-thin nanowires is through the use of mesoporous SBA-15 silica, reported by Lortz and co-workers for both lead and niobium nitride.[71,112] He *et al.* found that the nanostructured lead confined to 6 nm porous silica (Figure 2.3e) switches to type II superconductor behavior with evidence of long range order in three dimensions via Josephson coupling between parallel nanowires.[71] Wong *et al.*, however, found that 5 nm NbN/silica nanocomposites behaved as a quasi-one-dimensional material, with no percolating bulk superconducting state observed at low temperatures.[112] This is attributed to a suppression of Josephson interactions between neighboring NbN nanowires due to the much smaller coherence length as compared to Pb.

Through bottom-up synthesis methods using self-assembled structures, a number of interesting phenomena have been observed in mesoscale ordered 2-D superconductors. In the work of Vanacken *et al.* for instance, Nb thin films were grown atop polystyrene colloidal crystals in order to create artificial flux pinning lattices.[113] Valdepenas *et al.* utilized a diblock copolymer to alter the domain texture in a thin film Nd-Co/Nb magnetic/superconducting multilayer structure.[114] Jang *et al.* created colloidal suspensions of superconducting nanosheets, which upon electrophoretic deposition formed an asymmetric membrane.[115]

The expansion of the field of mesoscale ordered superconductors into three dimensions has been somewhat limited by a scarcity of appropriate synthetic methods. Several routes to 3D mesostuctured superconductors have begun to be explored, however, which showcase the potential for many classes of soft matter to create novel superconducting materials. For example, in recent work DNA origami was used to create nanowires[116] or a cubic superlattice of octahedral frames coated with niobium.[117] Through targeted design, DNA octahedrons were formed around gold nanoparticles, which then assembled into simple cubic superlattices. By first replicating the DNA struts of this structure in silica, then niobium, Shani *et al.* demonstrated the fabrication of a 3D array of Josephson junctions.[117] Through the use of the highly tailorable platform of computer aided DNA origami, this method shows much promise for achieving a wide array of possible structures and symmetries in mesostructured superconductors.

An alternative route, the most common so far to 3-D mesoscale periodic architectures in superconductors, is via infiltration into self-assembled bulk colloidal crystals. This strategy has been employed to create inverse opal structured lead[118–120], tin,[120–122] indium,[120,123] gallium,[120,124] bismuth,[125] lead/bismuth alloys,[120] and tungsten bronzes.[126] In the cases of classical type-I metals the inverse opal or opal composite materials behave similarly to granular superconductors, with size dependent changes in magnetization behavior and typically increased critical fields and temperatures. Aliev *et al.* observed magnetization behavior in lead inverse opals, which suggested the presence of novel fluxoid states and phase transitions in the nanostructured metal, including multi-vortex and giant vortex states.[118] Additionally, Little-Parks oscillations

were seen with periodicities commensurate with the opal unit cell size. Bykov *et al.* observed similar lattice size dependent superconductivity in inverse opal structured tin (Figure 2.3c), and from the magnetization behavior constructed a vortex phase diagram.[121] Aliev later prepared opal structured LixWO3-y and NaxWO3-y tungsten bronzes, and found evidence for localized non-percolating superconductivity with a high transition temperature of 125-132 K.[126] Previous observations in these opal-type superconductors may suggest the presence of an artificially ordered flux lattice, but this was notably disproved by a study in 2021 by Lee at al. using small-angle neutron scattering (SANS) which found only evidence for disordered flux arrays.[127]

An emerging method for the creation of 3-D mesoscale architectures in superconducting materials is through the use of block copolymer (BCP) self-assembly to structure direct other materials in the bulk or in thin films. This has been demonstrated for both equilibrium and non-equilibrium structures. In the work of Robbins, Beaucage *et al.*, triblock terpolymer polyisoprene-*b*-polystyrene-*b*-polyethylene oxide (PI-*b*-PS-*b*-PEO, or ISO in short) was used to create mesoporous niobium nitride superconductors with cubic co-continuous single gyroid network structure (Figure 2.3f, inset) via evaporation induced self-assembly with sol-gel derived niobium oxide sol-nanoparticles and subsequent heat treatment under ammonia.[39] The mesoporous NbN was found to have incomplete flux exclusion at low field strength, and magnetization behavior suggested flux penetration commensurate with the gyroidal lattice constant. Thedford and Beaucage et al. also found that indium metal switched from type-I to type-II behavior when confined in a gyroidal ceramic template, which similarly suggested that the BCP defined architecture could be responsible for the creation of magnetic vortices

and hard pinning centers.[128] Notably, the use of bulk block copolymer co-assembly has been demonstrated as a versatile method for independently tuning morphology and characteristic lattice parameters across a large mesoscale range (from typically tens to hundreds of nanometers). In 2021 Beaucage et al. applied this tunability in the synthesis of niobium carbonitride (NbCN) superconductors.[129] In addition to creating materials of a quality parallel to traditionally synthesized NbCN (T_c of 16 K), this work found that mesoscale morphology induced by BCP self-assembly had an effect on the transition temperature of NbCN materials which appeared chemically identical via X-ray diffraction analysis.[129] Furthermore, BCPs give access to many morphologies otherwise difficult to obtain, including chiral cubic and networked structures, and enable a wealth of possible processing degrees of freedom. Yu and Thedford et al. showcased this in the use of spin-coating and lithography to create area defined thin film NbCN superconductors.[130] In this work it was further shown that BCP templated mesoporous NbCN materials possessed enhanced critical fields in comparison to dense analogs.[130] Moving to non-equilibrium derived BCP directed structures, in the work of Hesse & Fritz *et al*., co-assembly of a titania sol with the triblock terpolymer polyisoprene-*b*-polystyrene-*b*-poly(4-vinylpyridine) (PI-*b*-PS-*b*-P4VP, or ISV in short) was used in tandem with non-solvent induced phase separation to create hierarchically porous, asymmetrically structured titania membranes. After careful thermal processing under ammonia, these titania membranes were converted into superconducting TiN. At room temperature, such materials displayed record level capacity retention and power density as electrochemical double-layer capacitors, and at low temperature could find application as superconducting membranes for gas separation.[131]

Topological Materials

The exploration of topological phases of matter started when Thouless et. al. identified a completely novel scheme of classifying electronic phases[132] based on the topology of the electronic band structure.[133–135] They showed that the Hall conductivity in the quantum Hall effect for a 2D electron gas in a strong magnetic field is proportional to a topologically invariant number, now called the Chern number.[133,136,137] This topological invariant distinguishes the quantum Hall phase from a trivial insulating phase, and experimentally manifests in the form of Hall conductivity that is protected against disorder, and one-way transport of charges on the edge of the sample[138,139] – features that are not found in conventional insulators. Microscopically, the topologically non-trivial behavior of the quantum Hall state is a consequence of the quantum mechanical behavior of electrons in a magnetic field, in particular, the non-zero phase acquired by the electron wavefunction as it travels a closed loop in momentum space[136] (this is an example of a "geometric phase", which does not originate from wave propagation, but is instead a result of the curved geometry of momentum space). Because of this unconventional origin, topological phases of matter cannot be classified based on Landau's theory of broken symmetry[140] that is used to identify conventional phases of matter.

A few years after this discovery, it was then theorized that an external magnetic field is not necessary to realize a topological material.[141,142] The strong coupling between the spin and orbital angular momenta of electrons in certain materials is sufficient to create a topological state, called the quantum spin Hall state, that can be

described using a spin-Chern number. These topological materials exhibiting quantum spin-Hall effects have conducting edges and an insulating bulk, earning them the name "topological insulators" (whereas the name "quantum Hall insulators" is more common for topologically non-trivial insulators based on the quantum Hall effects). Following these theoretical predictions,[143] the first spin-orbit-coupling induced topological insulator was realized in thin films of HgTe sandwiched between CdTe.[144] In contrast to the quantum Hall phase, topological insulators are not limited to 2D structures.[145,146] 3D topological insulators that exhibit spin-polarized surface states have also been recently studied.[147] It is noteworthy that, in stark contrast to superconductivity, which was first accidently discovered and then explained using theoretical models based on the quantum nature of interactions, topological insulators were first described theoretically before candidate materials were identified and tested.

One of the hallmarks of topological materials described above is the existence of unidirectional edge states that do not backscatter in the presence of defects. These edge states are guaranteed by the so-called "bulk-edge correspondence principle," which states that the net number of unidirectional edge states in a topological material is related to a topological invariant number that is evaluated from the eigenmodes of the bulk material.[148] In the quantum Hall phase, the external magnetic field breaks time reversal symmetry and generates unidirectional conducting channels on the edges of the sample that are unaffected by sample defects.[139] On the other hand, in the quantum spin Hall phase, two counterpropagating channels exist on the sample edges with opposite electron spin polarizations in the absence of an external magnetic field.[143] Since Kramers theorem for electrons prevents any interaction between the two opposite spins

in a time-reversal symmetric system, these edge modes are not backscattered by non-magnetic defects in the sample. Thus, it is time-reversal symmetry itself that guarantees the robustness of edge modes in topological electronic insulators based on the quantum spin-Hall effect.

Since the origin of the non-trivial topology in electronic band structures is due to the geometrical phase acquired by the electron wavefunction, which is a general phenomenon of wave physics, any wave-based platform can, in principle, be engineered to exhibit topological phases. This was first recognized by Haldane and Raghu,[149,150] who showed that an analog of the quantum Hall phase can be constructed for light in a hexagonal array of magnetized ferrites with a periodicity commensurate with the wavelength of light, called a photonic crystal. This unleashed a deluge of research work dedicated to realizing topological phases in various photonic,[151,152] acoustic[153] and mechanical[154] wave-based systems. It must be mentioned, however, that these classical wave-based systems do not have the same properties as their electronic topological counterparts. This is because electrons are fermions whereas photons and phonons are bosons which do not obey Kramers theorem and allow mixing of opposite spins.[155] As a result, while electromagnetic and photonic structures with broken time-reversal symmetry (e.g., magnetized plasmas and ferrites) can realize the equivalent of quantum Hall insulators, additional symmetries are needed to realize the analogs of quantum spin-Hall topological insulators.[155] Furthermore, these light based topological insulators remain fundamentally more fragile to generic perturbations than their electronic counterparts.

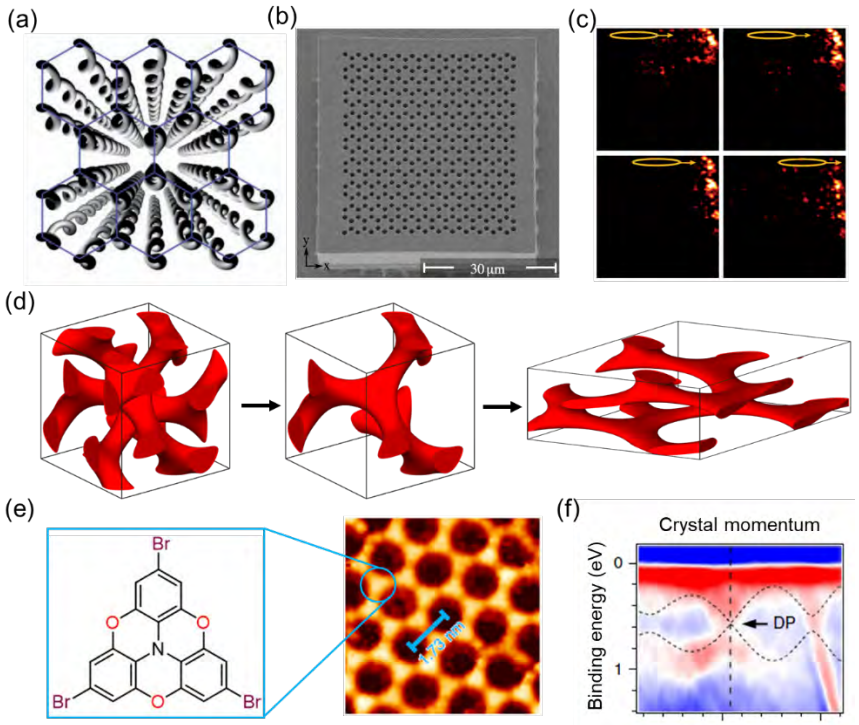

Figure 2.4. *Topological materials from soft matter. (a)-(c) Topological photonics. (a) Schematic arrangement of an optical waveguide array composed of hexagonally organized helices, which implements a Floquet topological photonic insulator (adapted from Ref [156]); (b) image of the waveguide array structure made from an organic photoresist using direct laser writing (adapted from Ref [157]); (c) experimental demonstration of a topological edge mode propagating around the corner of the lattice with minimal backscattering (orange ovals indicate the irradiated regions). (d) Symmetry breaking from double gyroid (left, space group Ia3d) via single gyroid (middle, space group $I4_132$) to orthorhombic networks (right, space group F222) to satisfy the symmetry requirements for the emergence of Weyl points (topological degeneracies in 3D momentum space) from self-assembled block copolymers. (e)-(f) Dirac point (DP) in COFs. Adapted from [158]. (e) Molecular building block and corresponding scanning tunneling microscopy image of honeycomb 2-D structure; (f) Second derivative angle-resolved photoemission spectroscopy (ARPES) data for observed DP with calculated bands (dashed lines).*

Apart from spin-orbit coupling and external magnetizations, time varying periodic potentials can also result in a topological state. Dubbed a Floquet topological insulator, such phenomena were first shown by irradiating a quantum well with microwaves.[159] In photonics, this state was first emulated in a mesoscale structure consisting of honeycomb lattices of helical waveguides in fused silica.[156] This structure is time-invariant, but propagation along the helical waveguides acts as an effective 'time' axis. The signatures of topological protection, such as backscattering-free edge state propagation, ware indeed observed experimentally in this structure (Figure 2.4a-c).[157] The hexagonal (honeycomb) arrangement of chiral helices utilized in this material is especially relevant to soft matter[160] since it can be self-assembled, *e.g.,* using BCPs.[161,162] Soft matter in the form of organic photoresists can similarly be used to construct non-trivial topological structures based on helical waveguides using direct laser writing.

Another topological phase of matter that was recently identified is the Weyl semi-metal state.[163,164] Unlike topological insulators, Weyl semi-metals are 3D materials and are not insulating in the bulk since the valence and conduction band intersect at a point in 3D momentum space. The topological invariant characterizing Weyl semi-metals can be determined from the gauge field corresponding to the phase acquired by the electron wavefunction, called the Berry curvature.[134] The points where the valence and conduction band intersect, known as Weyl points, behave as sources or sinks of Berry curvature.[165] The topological charge of the Weyl point can be calculated by integrating the Berry curvature on a closed surface around the corresponding Weyl

point in momentum space. Since the charge carried by the Weyl points is conserved, disorder or impurities in the material cannot create or destroy Weyl points, making the Weyl semi-metal state exceptionally stable. Based on the symmetries of the Berry curvature it can be shown that Weyl points can only be found in materials that have either broken inversion or time-reversal symmetry.[164]

In photonics, Weyl semi-metals were first experimentally observed in a photonic crystal consisting of a double gyroid structure[166] that is also found in a wide range of assembled soft matter mesostructures. Recently, this structure has inspired a bottom-up approach of self-assembly of BCPs to prepare mesostructures that can host photonic and phononic Weyl points.[167] This is achieved by breaking the inversion symmetry of double gyroids by moving to single gyroids (also referred to as asymmetric double gyroids or alternating gyroids), which is another mesophase accessible from ABC-type triblock terpolymer self-assembly.[168] A further deformation of the single gyroid network lattice to achieve point group D2 symmetry is then required for the Weyl point to emerge. This symmetry reduction has recently been experimentally evidenced in hybrid thin films of heat-treated PI-b-PS-b-PEO (ISO) structure-directing resorcinol resols that are subsequently used in transient laser heating experiments to transfer the structure control into semiconductors like silicon (Figure 2.4d). The appearance of (002) peaks in grazing-incidence small-angle X-ray scattering (GISAXS) of final nanostructured and mesoporous silicon suggested sample deformation-based symmetry breaking from space group $I4_132$ of a single gyroid upon solvent evaporation based self-assembly and subsequent thermal and laser treatments.[169] The facile and scalable processing via spin-coating, solvent vapor annealing (SVA), general furnace heating, and transient laser

annealing paves the way toward photonic/phononic Weyl materials fabrication from BCPs and other soft matter self-assembly. Furthermore, since all of these steps are consistent with semiconductor processing, direct integration into chip fabrication is also possible.

Compared to hard matter-based topological electronic insulators, soft matter mesostructures that implement photonic/acoustic topological materials typically have a less-than-perfect structure and often dissipate the energy of the propagating photonic or acoustic wave in the form of scattering or absorption losses. This dissipation induces non-Hermitian perturbations to the Hamiltonian describing the system.[170] While this is often seen as a nuisance, as it prevents longer propagation distances, recent studies have shown that non-Hermiticity can introduce rich topological features not found in Hermitian systems such as exceptional points:[171,172] degeneracies where both eigenvalues and eigenvectors perfectly coalesce. In addition, exceptional points are associated with a local band dispersion that follows a square-root function around its branch point (in contrast to the linear dispersion of other degeneracies like Dirac points or Weyl points), which has been recently found to be potentially useful for enhanced sensing[173–175] and modal transformations.[176–178] Interestingly, the non-Hermitian nature of these systems does not necessarily alter the topological invariants of the system, which are preserved in the presence of moderate values of dissipation, but rather the specific impact of dissipation depends on the mechanism that makes the system topological i.e., broken time-reversal symmetry or inversion symmetry.[179] Furthermore, at atomic length scales, self-assembled soft matter is typically amorphous; however, this also does not necessarily destroy the topological robustness of the system since

topological edge states have been known to persist in the amorphous liquid regime.[180–182]

While photonic and phononic topological materials have been demonstrated using soft matter, topology has also increasingly begun to permeate soft-matter derived materials based on electronic waves. 2-D metal-organic frameworks (MOFs) have been predicted to possess nontrivial band topology.[183] MOFs are highly porous coordination polymers made from organic ligands stably coordinated to a metal center. MOFs can have 1-,2-,or 3-D structures, and their hybrid organic-inorganic nature can give rise to many exotic electronic and magnetic properties.[184] This transcends the notion that topological phases are restricted to purely inorganic materials.[185–187] The versatility of reticular chemistry in the synthesis of MOFs offers the freedom to perform chemical substitution at the molecular level, to modify the connectivity, and hence the lattice type, of the MOF network, and to tune quantum effects such as spin-orbit coupling by changing the metal ion. We expect the organic molecular linker, as with other soft matter, to be adaptive in that it can be engineered over a wide range of length scales and physically strained to the extent not allowed for atomic lattices. Indeed, linear degeneracies, called Dirac cones, have been revealed by angle-resolved photoelectron spectroscopy (ARPES) in 2-D π-conjugated polymers (or covalent organic frameworks, COFs), whose lattice is an order of magnitude greater than that of graphene (Figure 2.4e and f).[158] In this scenario, certain perturbations that break inversion or time-reversal symmetry could then open a non-trivial topological gap in the spectrum resulting in a transition to a topological phase.

In summary, we foresee that soft matter will play an important role in fabricating topological materials for photons, phonons, and electrons, for applications spanning different domains of physics and engineering. In addition, further explorations into the combined structure formation of both high-quality crystalline atomic lattices of topological electronic materials and the periodically ordered mesophases of topological photonic/phononic soft matter may open new opportunities at the intersection of different disciplines.

Magnetic Materials

Magnetism has been studied for centuries, with arguably the first published approach of scientific inquiry to magnetism being William Gerbert's *De Magnete* from the year 1600.[188] While inquiries into magnetism have ranged from its impact on nanoparticles all the way to planet earth, much recent work in this area has probed into quantum mechanics, elucidating exotic magnetic quantum materials.[188] In the broadest sense, magnetism as a quantum phenomenon is associated with the electronic spin degrees of freedom.[2] Magnetism has been used to produce a variety of interesting physical phenomena that hold great promise for and increasing fundamental understanding of exotic systems,[2] as well as applications in areas including computing and energy.

Multiferroics are materials that simultaneously display more than one type of "ferroic ordering" *i.e.,* ferromagnetism, ferroelectricity, and ferroelasticity.[28] Of particular interest for future applications in energy and "smart" technologies are magnetoelectric multiferroics, in which the materials are both ferroelectric and

ferromagnetic, or some associated weaker version of those orderings, and the magnetic field affects the electronic properties and vice versa. There are multiple routes to multiferroics.[28,189] A common route is making heterogenous structures combining independently ferromagnetic and ferroelectric materials. Typically, this strategy involves making magnetic islands in a ferroelectric matrix; traditional "top-down" methods include nucleating and growing magnetic islands randomly on a substrate with methods such as nucleation and growth, and then backfilling or growing the ferroelectric matrix around the islands.[190] Lithography and epitaxy have been employed to overcome this random nucleation and try to impose a periodic order on the nanoislands.[190] However, these methods are still expensive and not friendly to high through-put processing. Soft matter has offered some promising alternatives in heterogenous multiferroics.

While lithography and epitaxy can provide periodic order and shape control, soft matter offers similar advantages, with the added benefit of solution processability. Ren *et al.* made a common heterogenous multiferroic of magnetic $CoFe_2O_4$ (CFO) and lead zirconate titanate (PZT) using sol-gel methods and the diblock copolymer poly(styrene-*block*- ethylene oxide) (PS-*b*-PEO) as a structure directing agent.[191] Multiferroic nanocomposites made from block copolymers have also been fabricated by using one of the blocks as the ferroelectric component.[192] Terzić *et al.* made a lamellar multiferroic heterostructured nanocomposite using an ABA-type poly(2-vinylpyridine)-*block*-poly(vinylidene fluoride-trifluoroethylene)-block-poly(2-vinylpyridine) tri-block copolymer (P2VP-*b*-P(VDF-TrFE)-*b*-P2VP), where the P(VDF-TrFE) block itself was ferroelectric and gallic acid-modified CFO nanoparticles were segregated into the P2VP

blocks[192] (Figure 2.5a-c). Exciton photovoltaic polymers have also been used to progress towards all polymeric multiferroics; Lohrman *et al.* developed a diblock copolymer of poly(3-hexylthiophene)-*block*-(3-hexylcarboxylate thiophene) (P3HT-*b*-P3HCT), which had an all conjugated backbone connecting two blocks with distinct electronic properties and crystallinities.[193] This allowed for high charge separation and excitonic ferromagnetism in a thin film made of the micro-phase segregated block copolymer, creating a material with a strong magnetoelectric effect and paving the way for organic excitonic multiferroics.[193] The promise of polymers as the future of heterostructured multiferroics has not gone unnoticed; a recent prospective published by Xu *et al.* highlighted polymer templating methods as a low-cost alternative for fabricating large-area, nanostructured thin films of complex metal oxides, particularly focusing on multiferroic nanocomposites.[194]

Another soft matter enabled heterostructured multiferroic was a core-shell multiferroic nanocomposite made from DNA-functionalized $NiFe_2O_4$ (NFO) and $BaTiO_3$ (BTO) that were tethered together by complimentary DNA oligomers (Figure 2.5d-f).[195] These particular nanocomposites were able to be directed into superstructures by a magnetic field, due to the reversibility of DNA hybridization. The core-shell nanocomposites showed magnetoelectric coupling, and the bulk composites produced upon sintering were shown to have stronger magnetoelectric coupling than a bulk composite made from randomly mixing NFO and BTO nanoparticles.[195]

Furthermore, magnetoelectric multiferroics can be realized with a hybrid single-phase material. Soft matter has offered a route to these materials in the form of MOFs. One family of MOFs, the dimethylamino manganese formates (DMAMnF) form into

perovskite-like structures; these MOFs display multiferroic behavior that occurs through temperature-dependent order-disorder transitions (Figure 2.5 g-i). [196,197] This induces MOF transitions from antiferroelectric to ferroelectric, and paramagnetic to antiferromagnetic states, respectively. Other types of MOFs can also exhibit multiferroicity.[198] One example is a 3-D porous MOF structure with ethanol included in it as a guest molecule.[199] Due to order-disorder transitions affecting the orientation of the polar ethanol molecules, the $[Mn_3(HCOO)_6](C_2H_5OH)$ MOF underwent paraelectric to ferroelectric and paramagnetic to ferromagnetic transitions at 165 K and 8.5 K, respectively.[199] The diverse and dynamic structures of MOFs, as well as the large variability of their chemical make up for each potential structure, renders them strong candidates for soft matter that will have intrinsic emergent quantum properties in magnetics and other fields.

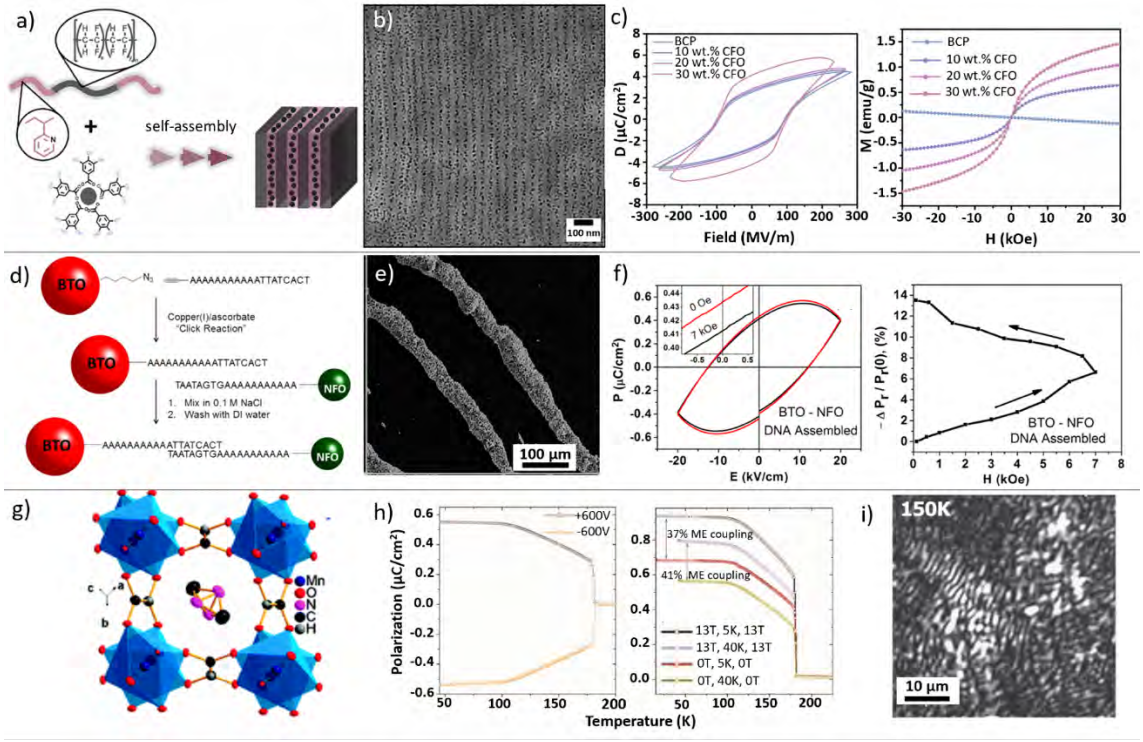

Figure 2.5: *Examples of soft matter-enabled multiferroics prepared from a variety of material classes: BCPs in the first row adapted from Terzić et al.[192], DNA in the second row adapted from Sreenivasulu et al.[195], and MOFs in the third row adapted from Jain et al.[197] a) Schematic of BCP with CFO NPs co-assembly to make lamellar multiferroics. b) SEM of lamellar multiferroic made from co-assembly of BCP and CFO NPs. c) Polarization and magnetic behavior of the BCP-CFO nanocomposite. d) Schematic showing the DNA-DNA self-assembled BTO-NFO nanocomposites. e) SEM depicting core-shell nanoparticles arranged into colloids by external magnetic field. f) Characterization of polarization and magnetic behavior of BTO-NFO DNA-assisted nanocomposites. g) Cartoon of the structure of DMAMnF MOF. h) Temperature-dependent polarization behavior of MOF, along with demonstration of the effect of external magnetic field on polarization behavior, demonstrating magnetoelectric coupling. i) Optical image showing second-harmonic generation (SHG) in domains (bright areas) of the DMAMnF MOF, exhibiting areas that are non-centrosymmetric due to phase transition.*

Spin ices are another class of magnetic quantum materials that display interesting properties. Spin ices are geometrically frustrated spins that with their magnetic moments follow the "ice rule", first described for the atomic placement of hydrogen atoms in water ice lattices:[200] similar to the "two-near" and "two-far" positions of hydrogen around an oxygen atom in crystalline water (from two hydrogens of the H_2O molecule and two hydrogens from two neighboring H_2O molecules, respectively), they consist of corner-linked tetrahedra of magnetic ions with non-zero magnetic moment each ("spin"). In the low energy state, two of these moments point outwards ("two-out") and two point inwards ("two-in") for each of the tetrahedra. Due to these magnetic frustrations, spin ices realize exotic properties such as magnetic monopoles

and residual entropy, the latter just like in water ice, where the number of configurations conforming to the ice rule grows exponentially with system size, leading to a substantial zero-temperature entropy. Typically, a spin ice is realized as nanomagnets at vertex points of periodic structures; this periodic nature leaves open a runway for soft materials to play a part in fabricating spin ices.[201] The spin ice was first discovered in rare earth titanate pyrochlores, which has a crystal structure that has magnetic moments at the vertices of tetrahedra.[201] Attempting to replicate and control this phenomenon with synthesized materials led to the expansive field of artificial spin ices (ASIs). ASIs started as 2-D square and kagome lattices with nanomagnets placed at vertices, but as the field developed, 3-D ASIs were synthesized as well. One section of soft matter that has found much use in the field of ASI is colloidal crystals. Using magnetic particles and clever processing methods, colloidal scientists have generated a number of ASI and ASI analogs with colloidal crystals.[202–205] In 2013, Mistonov *et al.* fabricated an inverse opal like structure of cobalt by backfilling a colloidal array of polystyrene microspheres; the resulting structure was able to follow the ice rule, making it a 3-D ASI.[202] Further investigation of the micromagnetic structure in cobalt inverse opals via simulation and small-angle neutron scattering followed in 2019.[206] Ortiz-Ambriz and Tierno combined lithography with soft matter, using the colloidal self-assembly of paramagnetic particles in double-well traps to realize another colloidal spin ice.[203] In 2016, Shishkin *et al.* generated another inverse opal like structure from a colloid, this time made from nickel;[207] their structure was considered a spin-ice analog since it was larger than considering lattice sites on an inorganic crystalline material.[204] Block copolymer templated architectures have also been investigated for controlled micromagnetic

structure, first in 2011 by Hsueh et al. in nickel and more recently in an in-depth study by Llandro et al. investigating Ni-Fe gyroidal networks.[208]

Spintronics is a vast field that does include materials that are multiferroic and spin ices; however, there are other types of materials that can be used for spintronics that are enabled by soft matter. Spintronics, or spin electronics, is a field of growing interest that uses electron spin, rather than charge, to carry information; the associated extra degree of freedom with spin offers potential benefits including reduced power consumption and increased processing speeds.[209,210] While there is crossover in the fields of multiferroics and spintronics, the field is employing a variety of materials. One type of commercially available spintronic is the spin valve used in magnetic hard drives, which works due to the giant magnetoresistive effect, independently discovered by Fert and Grunberg in 1988, earning them the 2007 Nobel Prize in Physics.[210] It should be noted that biological soft matter has also shown intrinsic properties than could allow them to play a part in molecular spintronics.[205] While lead sulfide (PbS) colloidal crystals have been known for their electronic properties, Moayed *et al.* demonstrated the potential value of colloids in spintronics.[211] The group was able to break the centrosymmetric O_h symmetry of PbS by confining the material to a 2D nanosheet and then subjecting the nanosheet to external asymmetric boundaries. The 2D nanosheet was sandwiched between the interface of SiO_2 and vacuum, and a gate electric field was applied; this resulted in the nanosheet of PbS belonging to the point group C_{4v} with no inversion symmetry. The resulting PbS colloid demonstrated spin-orbit coupling and the ability for solution-processible, industry-compatible colloidal crystals to be integrated into the growing field of spintronics.[211] Due to their highly tunable

dimensionality, geometry, and chemistry, MOFs have also been investigated for applications in spintronics. For example, Chakravarity *et al.* used theoretical arguments and calculations to predict that bis(dithioline)(BHT)-based MOFs have potential uses in spintronics and in realizing geometrically frustrated systems.[212] Beyond the first principal studies, Song *et al.* realized a semi-conducting MOF thin film that was able to perform as a spin valve, using the MOF Cu_3(2,3,6,7,10,11-hexahydroxytriphenylene)$_2$.[213] The thin films were fabricated using layer-by-layer deposition, and had a magnetoresistance of up to 25% at 10 K.[213] Self-assembly of block copolymers has also begun to be used for the manipulation of spin waves, as shown by Manuguri et al. in the use of BCP micelles to direct a magnonic assembly (i.e., a material with magnetic properties periodically varied in space).[214]

The convergence of soft and hard condensed matter

Over the past 30 years the progression of soft matter science towards advanced functional materials provides illustrative examples of the opportunities and challenges for soft matter enabled quantum materials. Observing the convergence of soft and hard condensed matter physics over this timeline showcases several runways towards novel quantum materials in multiple soft materials classes (Figure 2.6). In soft matter, the characteristic length scale and morphology of mesoscale architectures is widely tunable via synthetic or processing means. Mesostructure is also adjustable via choice in soft matter agent, though notably a number of morphologies appear commonly throughout multiple materials classes due to some shared thermodynamic features.[215,216]

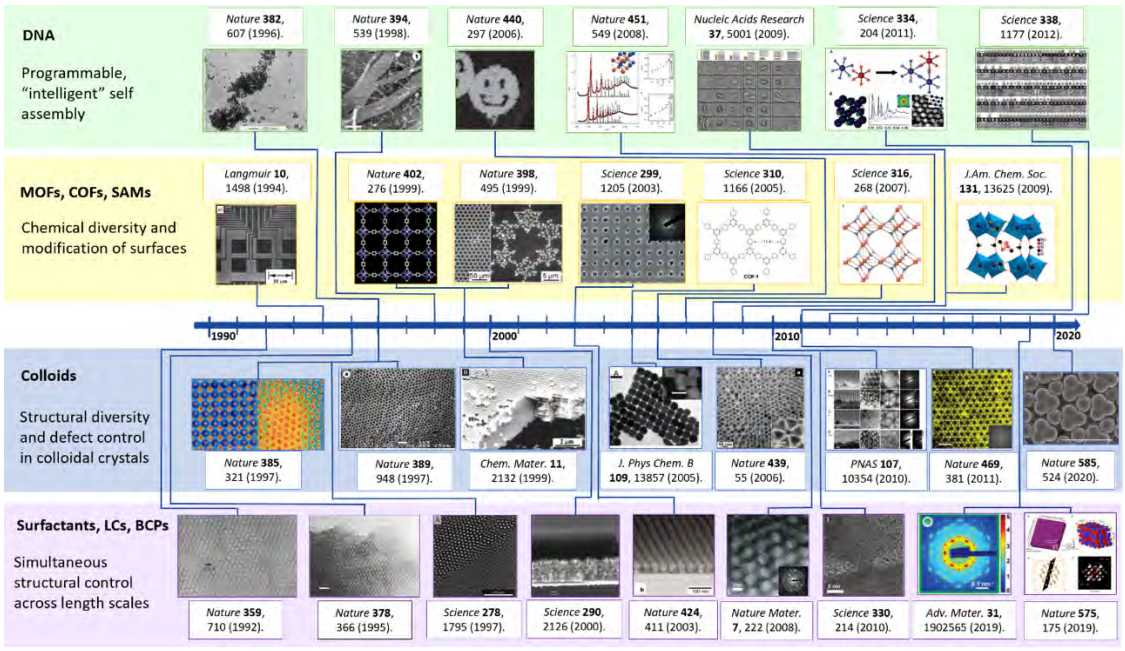

Figure 2.6: *A timeline detailing seminal progress of the convergence of soft and hard matter across different material classes. The timeline shows a general trend of increasing sophistication of control over self-assembly, variety of materials being structure-directed, and quality of functional materials being structure-directed. DNA (top row) has shown progress from directing colloidal crystals of gold nanoparticles to intelligent, computer assisted design of DNA "origami." MOFs, COFs, and SAMs (second row) have introduced high levels of controllable crystallinity and intrinsic functionality into the field of soft matter. Colloids (third row) have offered routes to the hard and soft templating of functional materials, with geometric variety ranging from packed spheres, to complex binary superlattices to kagome lattices. Surfactants, liquid crystals (LCs), and block copolymers (BCPs, bottom row) have progressed from serving as a mere template for a few nanostructured silica and metal oxide mesostructures to sophisticated structure directing agents whose combined self-assembly with a variety of organic and inorganic precursors provides access to a plethora of mesostructured inorganic*

materials with varying symmetries and topologies as well as mesoporous materials with large surface areas.

Molecular and Macromolecular Self-Assembly for Structure Direction and Templating

Self-assembling soft matter "synthons" can be used to induce nanostructure in other organic and inorganic materials that lack mesostructural ordering by themselves. This can be done through either structure direction, or soft or hard templating. Structure direction involves the cooperative assembly of a self-assembling 'synthon' and other organic or inorganic precursor species. In particular, structure direction entails that the soft matter component and additive closely associate and assemble in tandem into intimately mixed hybrid phases. Precursor species can then be crosslinked or condensed in the resulting hybrid material, and the soft matter component removed via selective etching or heat treatment.[217] In 1992, Kresge *et al.* published a seminal paper using ionic amphiphilic surfactants to direct the structure of silica in solution into a periodically ordered mesoporous molecular sieve known as MCM-41 (Figure 2.6).[34] This paper can be considered as an important focal point for the use of soft matter self-assembly to structure direct inorganic materials.

Templating strategies also involve the use of a self-assembling soft matter component to impose a designer nanostructure on an inorganic or organic additive, but via routes which do not involve cooperative assembly as in structure direction. Templating strategies can be broadly classified into either 'soft' or 'hard' templating. Soft templating entails the use of "soft" materials, such as small molecule surfactants or polymeric species, which natively assemble into an ordered structure; organic or

inorganic precursors then assemble around these soft templates and are transformed through various processing means.[217] The soft template structure is typically mechanically weak and prone to deformation, but can easily be removed via dissolution or heat treatment. An example of a soft templating approach can be found in the work of Thurn-Albrecht *et al.*, where a self-assembled BCP thin film was used to template cobalt nanowires in a high density hexagonally packed array. After the neat diblock polymer film was assembled in a hexagonal array, one polymer phase was selectively etched out with UV light to create a porous polymer template in which cobalt was electrodeposited.[218]

In contrast, hard templating involves a rigid nanostructure made out of a material such as silica or carbon which already possesses an ordered mesostructure designed through earlier processes.[219] If such nanostructures are porous, the void space can be backfilled with various precursors which are then transformed into the final material. In such a way the final inorganic or organic material adopts an inverse nanostructure to the template. The hard templates can endure harsher conditions such as high temperature and pressure, or corrosive and reactive environments during the templating and the following processing steps, which are not tolerated by soft templates under normal circumstances. However, selective removal of the template is often more difficult and requires harsh etchants. While one's intuition might not make the immediate connection between soft self-assembled materials and hard templates, using self-assembling materials to structure-direct or soft template inorganic materials leads to a large variety of nanostructures and materials which can subsequently be used as hard templates. For example, Ryoo *et al*. used the small molecule surfactant soft templated silica molecular

sieve MCM-48 as a hard template for the synthesis of ordered mesoporous carbon: the silica template was first created, filled with a carbon precursor solution of sucrose and sulfuric acid, heat treated in inert atmosphere, and then selectively etched away to yield a mesoporous carbon framework.[220]

At the smallest length scale, small molecules are known to form a variety of supramolecular architectures both in solution and the bulk, including spherical micelles, tubular micelles, lamellar sheets, and co-continuous mesophases.[221–223] Liquid crystal (LC) mesophases appear in many systems of anisotropic organic molecules, termed mesogens.[224] While lacking the full 3D positional and orientational order typically defining a crystalline solid, liquid crystals possess limited degrees of orientational and positional order, which also distinguishes them from an isotropic liquid state. Lyotropic liquid crystals contain a mixture of an amphiphilic mesogen and solvent, and their phase behavior is governed by concentration. Thermotropic liquid crystals consist of neat mesogens, and their phase behavior is largely governed by temperature. The molecular structure of the mesogen, its size, rigidity, and asymmetry, plays a large role in determining the collective condensed phase assembly.[215,216,224] Understanding of the thermodynamic and structural constraints in this assembly allows for a fairly rigorous ability to describe mesomorphism via structural phase diagrams.[225,226] Characteristic lengths in small molecule self-assembly can range from nanometer diameter micelles to hundreds of nanometers in liquid crystal blue phases[227,228] or cholesteric chiral field periodicities.[229] Typically, the upper size limit can be substantially increased by the transition from small molecule to macromolecular building blocks.

Another class of soft materials that plays a significant role in opportunities for soft matter enabled quantum materials is the class of BCPs. BCPs consist of two or more chemically dissimilar, covalently linked polymer blocks. The wealth of existing techniques in polymer synthesis allow for an exquisite degree of control over many characteristics in these macromolecular synthons; tailoring of synthetic parameters leads to tunability in chemical composition, individual block length, and chain architecture.[230] Linear, cyclic, bottlebrush, dendrimer, and miktoarm star copolymers are all known to self-assemble into various periodically mesoscale ordered structures in which the morphology and mesoscopic unit cell are tunable over a wide range of length scales (Figure 2.2).[19] For example, in bulk linear AB diblock copolymers consisting of two immiscible blocks A and B,[231] mesoscopic morphologies ranging from close packed spherical micelles to the bicontinuous double gyroid[232] (Figure 2.2) can form depending on the relative volume fraction of the two blocks and the segregating strength between them. This phase behavior, sometimes referred to as a hallmark of soft condensed matter science, is understood to be due to the interplay of enthalpic contributions from interfacial energy and entropic effects from chain stretching, and can often be estimated from the molecular characteristics of a given polymer.[233] In more complex polymers such as linear ABC triblock terpolymers consisting of three chemically distinct blocks A, B, and C, the phase space can be quite rich;[234–236] additional blocks or other block architectures make this space even richer.[237] The ability to systematically design and produce a vast variety of BCP morphologies by synthetic control combined with the ability to tune the mesoscopic unit cell size via polymer chain length yields a powerful toolbox for the control of materials structure on the mesoscale.

Like small molecule surfactants, BCPs offer pathways to mesostructured organic and inorganic materials through structure direction and templating strategies.[219] While low molar mass nonionic BCP surfactants have shown to structure direct silica in solution,[72] the thermodynamics of bulk BCP self-assembly has been used to structure direct inorganic materials in the condensed phase at larger length scales from higher molar mass copolymers, originally in the form of sol-gel derived (alumino-)silicate nanoparticles.[35,72] While phase behavior typically becomes more complex with inorganic precursors involved, when the correct design rules are being followed the sequence of morphologies observed in the bulk adding more and more inorganic material can be very similar to that of the parent BCP.[219,238,239] This provides facile access to hybrid and mesoporous materials via evaporation induced self-assembly (EISA) of bulk block copolymer mesophases, thereby coupling inorganic materials structure formation with block copolymer bulk phase thermodynamics.[240,241] In addition to acting as structure-directing agents, BCPs have been used as bulk soft templates to fabricate nanomaterials, as described earlier in the work of Thurn-Albrecht *et al.* among other examples.[217,218,242] BCP self-assembly-derived ceramic molds have been used as hard templates to fabricate gyroidal networks of superconducting indium.[128] Furthermore, hard templates derived from BCPs have played a part in non-equilibrium transient processes; single crystal homo- and hetero-epitaxial semiconductor and metal nanostructures, respectively, have been prepared using transient laser heating on the nanosecond time scale of materials that conformally backfill mesoporous BCP-directed templates.[243]

A strength of the chemical diversity of BCPs is that careful selection of blocks can allow for the combination of strategies to overcome obstacles. In 2008, Lee *et al.* used the combined assembly of soft and hard (CASH) chemistries method in order to successfully generate highly crystalline mesostructured metal oxides directed by bulk block copolymer self-assembly. Previously, mesostructured metal oxide crystals would outgrow the mesopores and collapse the structure during heat treatments to improve the degree of crystallinity. CASH chemistries involved the structure direction of metal oxides with a poly(isoprene)-containing BCP. The self-assembled hybrid material was first heat treated in argon, partially converting the sp^2 hybridized carbon containing poly(isoprene) into a hard carbon template that confined the metal oxide crystal growth and prevented mesostructure collapse; the resulting materials were then subsequently calcined in air, burning away the carbon and leaving behind the highly crystalline mesostructured metal oxides.[36] This example illustrates the versatility of soft-matter enabled structure formation, here combining structure direction and hard templating in a so-called "one-pot" process, to make high-quality inorganic materials.

Colloidal Assemblies

Similar to the considerations describing macromolecules, colloidal self-assembly is rooted in intermolecular and microscopic forces, but scaled to particles comprised of many discrete atoms or macromolecules.[244] The combined effect of steric, dispersive, or coulombic interactions of many constituent species creates attractive and repulsive inter-particle forces. When these forces are properly balanced, colloidal particles self-assemble into close packed structures. In the simplest case, spherical

nanoparticles will often organize into hexagonally closed packed (hcp) structures much like artificial atoms.[245] More complex colloidal crystals can be obtained by co-assembling particles of different size or surface charge.[246,247] While typically the interactions involved in such assembly are non-specific, the introduction of complementary binding, *e.g.*, via particle tethered DNA hybridization, can introduce a further level of rational design.[248–250] Beyond simple spherical particles, exotic structures can be created through the use of more complex colloidal building blocks and shapes: tetrahedra, ellipsoids, platelets, and so forth.[251–256] In all colloidal systems, the periodicity of close packed structures is dictated primarily by the size of the basic particle synthon(s). Synthetic advances have allowed for the creation of narrowly size-dispersed colloidal particles ranging from a few nanometers in size to multiple microns. Colloidal crystals thus cover a very broad range of length scales (Figure 2.2).

In the 1990s, colloids began to be used in templating methods to produce nanostructured inorganic materials from filling the interstitial space in emulsions or self-assembled polymer spheres (Figure 2.6).[257] Colloidal techniques were further refined by the innovation of colloidal epitaxy.[258] Colloids also saw a variety of creative approaches to new products in the 2000s. Colloidal crystals of a variety of exotic structures were produced by methods such as lost-wax approaches, using charged particles, or using binary particles of different shapes or sizes.[247,259,260] "Patchy" particles were also employed to self-assemble a colloidal kagome lattice from intermolecular forces in 2011 by Chen *et al.*.[261] Recently, a similar strategy using deformed tetrahedral particles with tailored DNA patches accomplished the long sought after goal of a diamond structured colloidal crystal.[262] The progression in the field of

colloid science once again highlights the potential of soft matter enabled quantum materials, *e.g.,* via the templating of inorganic materials into deliberate, well-controlled, and increasingly sophisticated periodically ordered nano- and meso-structures.

Soft Interfaces and Coordination Polymers

Self-assembled monolayers (SAMs) were first generated from alkane-thiols self-assembled into crystalline monolayer structures on gold.[263] Sometimes referred to as the "poor man's version of single crystal surfaces", they provide a large and versatile toolbox for the tuning and patterning of interfaces. For example, SAM surfaces can be chemically modified in myriad ways by controlling the chemistry of the alkane-thiol headgroup.[264] In 1999, Aizenberg *et al.* employed this ability to control the nucleation of calcite crystals (Figure 2.6).[265] This control was subsequently extended by fabricating patterned SAMs used to generate large micropatterned single crystals of calcite,[266] thereby generating a large runway for the controlled formation of quantum materials at SAM directed organic-inorganic interfaces.

As described in the previous section, MOFs and covalent organic frameworks (COFs) also have a place in identifying routes from soft matter to quantum materials. MOFs are a type of soft matter that falls under the category of coordination polymers.[267] Generally, MOFs consist of one or more metal ions at the center, which coordinate to several polytopic organic linkers; this make up leads to a variety of geometries, depending on the metal centers and ligands used, as well as a variety of pore sizes of the final structure.[268] MOFs have been heavily studied for applications such as catalysis and gas storage since their inception due to their favorable properties such as high

porosity, high crystallinity, and large chemical variety.[267,268] MOFs have such a variety of tailor-made properties because they exist as an exotic single-phase mixture of inorganic and organic matter.[267,268] In addition to the make-up of MOFs giving them a large spectrum of utensils from the toolbox of the period table, the variability in metal center and organic linker also leads to a vast array of possibilities for exotic structural topologies.[267] MOFs and COFs have well-controlled pores and crystallinity, as well as the ability to take on complex structural topologies in 2-D and 3-D.[267,269] The organic-inorganic hybrid characteristic of MOFs gives them exotic properties that make them more functional than many other classes of periodically organized soft matter. For example, as described in the previous section (Figure 2.5), MOFs in the dimethylammonium manganese formate (DMMnF) family mimic perovskite-like structures and show multiferroic properties through phase transitions.[196]

Rational design via biomolecules

Another significant class of soft matter is associated with biological materials. Rational structural design employing DNA is a field of soft matter that began in 1982 thanks to the work of Seeman et al., which suggested that DNA could be used to make stable junction structures, and that those individual structures could be brought together through DNA base pairing to generate arbitrary nanoarchitectures.[270] DNA base pairs were subsequently used as tools for the assembly of nanoscale structures and materials, rather than just viewed as the basis for the genetic code, paving the way for the eventual rise of the field of DNA origami.[271] The use of these DNA base pairings to enable and control the assembly of matter at the nanoscale has since expanded from simple DNA-

DNA interactions (Figure 2.6). In 1996, Mirkin *et al.* published seminal work on DNA oligomers being used to direct nanoparticles into colloidal crystals.[249] Biological soft materials based on DNA took another quantum step via the extremely impactful paper by Rothemund *et al.* in 2006, directly combining the powerful structure-directing capabilities of DNA origami with the use of computer algorithms for their structural design.[272] This paved the way to "hands-off" materials formation all the way from computer algorithm-based design to robotic synthesis and purification. Progressing further into the 2000s, the ability of DNA-assisted self-assembly to make increasingly crystalline and complex colloidal crystals has been investigated.[273,274] The progress in DNA self-assembly led to the advent of computer-aided design in self-assembly.[275] This powerful tool has made it possible to use CAD software to explore self-assembly building bricks from DNA, opening up a world of possibilities in terms of structure control and its automated synthesis (as opposed to more conventional synthesis often guided by trial and error).

The past few decades has seen the field of soft matter develop such that a variety of organic and inorganic chemistries can be tuned across the nano- and mesoscopic scales in a multitude of geometries and periodic lattices. Progression in soft matter techniques have given rise to increasingly well-controlled and well-ordered materials, slowly beginning to move in the direction of the quality achieved in electronic materials. Crucially, high quality samples enable sophisticated measurements, *e.g.,* of electronic and magnetic behavior necessary for identification, characterization and understanding of novel quantum phenomena. While there are many opportunities afforded by considering soft matter routes to quantum materials, there are therefore also challenges

which will need to be addressed. The foremost challenge is to achieve, in soft matter systems, the same level of structural control available in traditional solid state or atomistic synthetic methods. Defects, grain boundaries, and disorder all can greatly impact measurements and obscure intrinsic properties. For example, grain boundaries have been shown to limit supercurrents in high-temperature superconductors.[276] The challenge posed is significant, but much work has already begun tackling the characterization and elimination of mesoscale defects. Coming back to the example of the fascinating cubic co-continuous gyroidal network structures, in 2019 Feng *et al.* utilized "slice and view" SEM to quantitatively characterize topological defects in the gyroidal morphology of block copolymers.[277] In the same year, Susca *et al.* produced the first macroscopic single crystals of gyroidal block copolymers with grains on the scale of millimeters.[278] Should the challenge of long-range periodic mesoscale order, as well as associated challenges in orthogonal device fabrication and measurement be met for a broad range of materials, soft matter is poised to open up a vast realm of new scientific and technological pursuits. Impactful contributions of soft matter are already being made, but there is plenty more room in the middle.

Comparing traditional and soft matter enabled quantum materials fabrication techniques

A unifying concept in all soft matter systems is that assembly and behavior is governed by interactions of a similar magnitude as room temperature thermal energy. Individually weak hydrogen bonding, hydrophobic, screened electrostatic, or entropic forces collectively dictate mesoscopic structure and macroscopic properties. As a result,

intermolecular or interparticle interactions are easily disrupted by low energy perturbations, but can just as easily recover. This leads to a substantial pathway complexity from synthons to the final self-assembled structure, with many possible metastable intermediate order states that may get trapped on the way to the lowest energy structure. At the same time, as energy minima are shallow, intrinsic structural variability can be substantial, and orientation distribution functions used to characterize molecular order in soft matter may be rather broad. Moreover, ordered states can be strongly influenced, *e.g.,* by external mechanical, electrical, or magnetic fields, making the final structure exquisitely sensitive to material processing history, *e.g.,* in injection molding or 3D printing. Most importantly, soft materials like polymers, colloids, and liquid crystals all are solution processible and therefore typically enable large scale fabrication methods including, *e.g.,* roll-to-roll (R2R) processing and 3D printing from solution-based precursors. In turn, this flexibility in material processing leads to a wealth of possible form factors unavailable to traditional quantum materials synthesis. This can readily be inferred from a comparison of some typical form factors derived from both traditional 'hard' and "soft" materials synthesis methods (Figure 2.7).

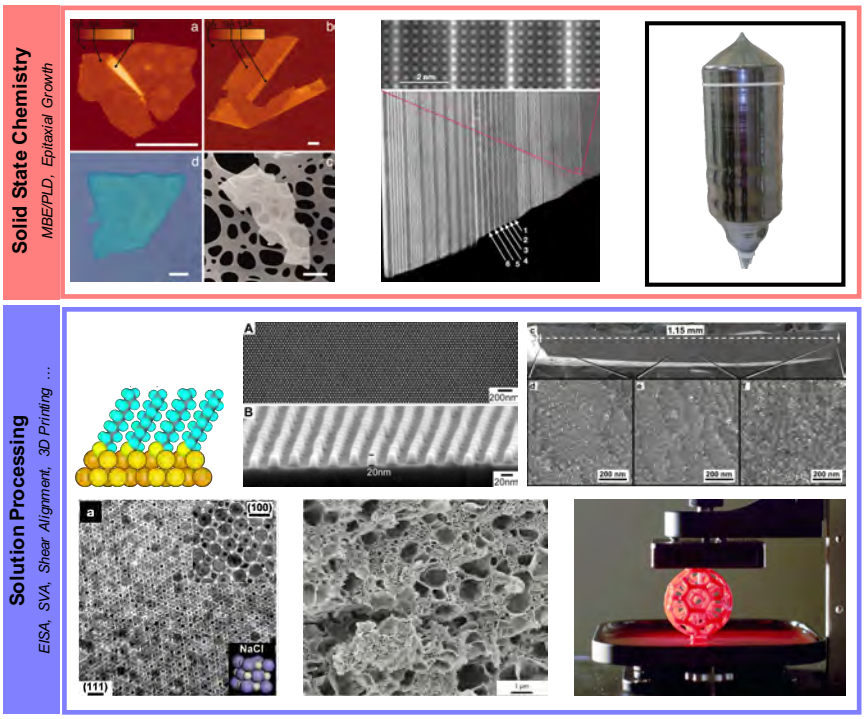

Figure 2.7: *Comparison of typically available form factors in traditional solid-state synthesis (top, red box) and soft matter based materials synthesis (bottom, blue box) methods. Top row from left to right: 2D single layer atomic crystallites of NbSe2, graphite, BSCCO, and MoS_2 adapted from*[279]*, superlattice of single $LaTiO_3$ layers separated by $SrTiO_3$ of controlled thickness via PLD adapted from*[280]*, and Czochralski (CZ) grown single crystal silicon ingot (image retrieved from Wikimedia Commons). Middle row from left to right: depiction of a self-assembled monolayer (SAM) on a gold surface, adapted from*[263]*, Cr and Si dot/pillar thin film arrays made via lithography relying on the directed self-assembly of a diblock copolymer, adapted from*[281]*, triblock terpolymer derived gyroidal structured SiON ceramic consisting of a single macroscopic domain with coherent ordering from one side to the other, adapted from*[278]*. Bottom row from left to right: NaCl type binary colloidal superlattice, adapted from*[247]*, hierarchically porous polymer scaffold derived from the combination of spinodal decomposition and macromolecular assembly in a block copolymer containing system, adapted from*[282]*, 3D*

printing of a dodecahedron via Continuous Liquid Interface Printing (CLIP), retrieved from Carbon3D[283].

2D Materials

Starting with graphene,[284] the family of 2-D materials has grown rapidly to include a wide array of materials such as transition metal dichalcogenides (TMDs), hexagonal boron-nitride, and layered oxides.[279,285,286] These single layers can also be stacked together to form diverse and intimately controllable heterostructures with interlayer van der Waals bonding.[287] 2-D materials and van der Waals solids have shown a plethora of exciting and exotic quantum materials properties such as 2D superconductivity, proximity derived effects, and novel states in Moiré patterned multilayers.[288,289] Mechanical exfoliation provides a relatively facile and cost-effective means for obtaining many 2-D materials, but lacks capability for high throughput. While much progress has been made on solution based methods, 2-D and van der Waals materials often rely on chemical vapor deposition under ultra-high vacuum or versatile yet difficult layer-by-layer directed mechanical assembly.[290,291]

In soft matter, an equivalent to 2-D materials in hard condensed matter physics lies in 2-D polymers. 2-D polymers are a scaled-up analogue of atomic 2D materials such as graphene and transition metal dichalcogenides. While solid state chemical reaction from evaporated constituents is reported, 2-D covalent-organic frameworks or metal-organic frameworks have been successfully synthesized via low-cost, high-throughput solution reactions.[292] The soft matter constituent, small organic molecules in this case, is amenable to modification of chemical composition, linker size, and

coordination geometry, all of which are severely restricted for atomic 2-D materials. By perfecting the 2-D structures, 2-D polymers are a tunable form of soft matter awaiting interrogation of their quantum behavior and properties.

Also on the 2-D level, self-assembled monolayers (SAMs) organize on substrates into a highly crystalline form in a self-limiting way.[293] Such single molecular layers can tune the surface energy, useful for controlling crystal nucleation.[265] In a similar fashion, polymer brushes are another type of surface-tethering soft matter, though they usually functionalize the substrate with an amorphous layer. In addition to changing molecular identity as in SAMs, polymer brushes can be designed with different chain composition to match the target surface energy, *e.g.,* to prepare a neutral surface to avoid preferential wetting.[294] Surface-functionalizing soft matter thus offers opportunities for both the study of quantum phenomena in confined dimensions and the fabrication of novel quantum materials.

Thin films

Above two-dimensional materials is the very well-developed and well-studied form factor of thin film materials. Through the refinement of methods such as atomic layer deposition (ALD), MBE, and PLD, experimentalists have obtained precise control over parameters such as composition[295] and strain[296] in crystalline thin films.[297] This has contributed greatly to the study of 2-D electron gases,[298] magnetic heterostructures,[299] and many other hybrid materials and emergent phenomena at interfaces.[280,300] The variety of techniques available for growing epitaxial heterostructures provides useful

breadth in synthetic capabilities, but all suffer from limitations imposed by the stringent synthesis conditions required.

From a soft matter perspective, thin films are rich both in available mesostructures and materials composition. It is worth noting that the thickness of thin films prepared from soft matter can range from the nanometer up to the micrometer scale *i.e.,* significantly thicker than the typical thin films in the physics or electronic device community. To fabricate thin films, using polymers as an example, homogeneous solutions of polymers in appropriate solvents are first prepared before casting onto a substrate. This requires the solvents to be able to dissolve the polymer and to have favorable wettability on the substrate. Dip coating involves immersing the substrate into the solution before gradually pulling out.[301] The more commonly practiced way is spin-coating, where solutions are spun off the substrate at a defined rotational speed, and a smooth thin film is derived after rapid solvent evaporation of the small amount of polymer solution that adheres to the substrate. Film thickness can be precisely controlled through varying the rotational speed and solution concentration (as well as secondary parameters such as acceleration).

Since the thin film is supported on a substrate, the energetics between the substrate surface and the thin-film materials can dictate their structures.[302] It is possible to engineer the surface energy to preferentially align the thin-film substructure, thereby growing mesoscale periodic structures epitaxially from the substrate.[281,303] Another route to prepare epitaxial thin films capitalizes on the guiding of topographical elements to direct the structures, termed graphoepitaxy.[304,305] On top of such 2-D patterns, multilayers of mesostructures with well-defined orientations can be prepared,[306–308]

allowing for use in nanofabrication and investigation of emergent properties related to quantum behavior.

The rapid evaporation of solvents during spin-coating often does not leave enough time for the thin-film structure to fully order. Post-spin-coating treatments can be employed to improve the periodic ordering through annealing, a concept borrowed from conventional hard inorganic materials processing. Apart from thermal annealing, the solution-processable soft matter can be subjected to solvent vapor annealing,[309] which dramatically mobilizes the constituent species and shortens the annealing time to achieve high order. As is commonly applied in inorganic materials processing, post-deposition annealing is one more knob to turn for structural manipulation without changing the materials composition. By changing the solvent ratio, flow rate, annealing time, among other parameters, different morphologies can be obtained, *e.g.,* form a single block copolymer[310] or other self-assembly enabling synthons and intrinsically 3-D mesostructures can be fabricated without resorting to tedious multilayer deposition.[311]

Bulk single crystals

Beyond the thin film regime, advances in the synthesis of bulk single crystals have played an invaluable and enabling role for the discovery, study and understanding of quantum materials. Whether guided by theoretical predictions or breaking new ground, the creativity and ability of crystal growers has led to many of the seminal discoveries in quantum materials.[17] Evaluation of the properties in any crystalline system is directly dependent on forging routes towards highly perfect bulk materials; defects, grain boundaries, and disorder in general obscure transport behavior and are

often considered obstacles to be surmounted via synthetic optimization. In this pursuit, experimentalists can exercise an exquisite degree of control over atomic ordering via the wealth of techniques pioneered by semiconductor manufacturing: Czochralski (CZ) growth, float-zone methods, or Bridgman techniques among others.[312] This enables rational design of new quantum materials though such means as careful tuning of stoichiometry, precise doping, or introduction of lattice strain, *e.g.,* via appropriate substrate choice.

Because of the inherently large defect density often present, obtaining bulk *mesoscale* single crystals through soft matter self-assembly is often a challenge. In anisotropic systems such as colloidal nanorods[313] or lamellar and hexagonal block-copolymer morphologies,[314,315] external fields such as shear have been used to great effect to produce macroscale alignment of mesoscopic domains. Much progress has also been made with isotropic particles in cubic colloidal crystals, where single crystals of multiple millimeters in size are now regularly reported.[245,316–318] Achieving the same level of long-range order has remained more elusive in networked block copolymer morphologies, but recent work has achieved gyroidal single crystals up to a centimeter in size. The preparation of single-domain periodic mesostructures on a macroscopic scale is tantamount to atomic single crystals (*e.g.,* using float zone or Czochralski method), and such samples are expected to enable sophisticated property measurements in a similar way.[278,319]

Additional Form Factors

Whether in the 2-D, thin film, or bulk regime, from the foregoing discussion it is apparent that soft matter methods have to progress towards the same level of order and structure control as already available in traditional solid-state techniques. While there is still much work to be done towards this end, soft matter enabled synthetic methods offer further benefits. Solution processing is not limited to thin film or monolithic bulk single crystals in the same way that traditional methods are, and thus soft matter enables a wealth of possible form factors. Colloidal superlattices for instance offer the opportunity to control symmetry/structure and composition across multiple length scales simultaneously.[246,247] Likewise, hierarchical materials can be made through such means as block copolymer self-assembly in tandem with spinodal decomposition[282] or phase inversion.[320] Furthermore, through additive manufacturing / 3-D printing methods such as continuous liquid interface printing (CLIP)[321] and high area rapid pringing (HARP)[322] (Figure 2.7), polymeric resins and polymer composites can be defined in arbitrary macroscopic shapes. Exploration has already begun on this front, with Li *et al.* demonstrating printable superconductor composites by dispersing exfoliated monolayers of the 2D superconductor $NbSe_2$ in organic solvents and commercial 3D-printing resins.[323] This expansion in accessible form factors for quantum materials synthesis is but one of the contributions, which soft matter science could make to the field. In the next section, we explore a few more of these possibilities as examples of the promise of soft matter enabled quantum materials.

Future Perspectives

While previous sections have shown that there is a growing body of work bridging soft and hard condensed matter physics, there remains much to be explored in the use of soft matter for the synthesis and study of quantum materials. In this next section we will explore a few paradigms for future work at this interface, organized under the following general thrusts: expanding structural control, mesoscale lattice engineering, tuning disorder and composition, considering increased interfaces, convergence in the thin film regime, and harnessing extreme conditions. A few vignettes will be used in each case as a way to showcase the opportunities for soft matter enabled quantum materials, but the general concepts underpinning each thrust can and should be extended beyond any single soft matter system or quantum materials class.

Expanding structural control

As described, access to novel and often unique molecular and nano- to mesoscale architectures is one of the most salient strengths of soft matter enabled quantum materials; one of the biggest challenges facing their widespread impact is the inherent difficulty in creating well-ordered single-crystal type materials with low defect densities. To fully realize the potential of soft matter in quantum materials synthesis, structural control must be expanded and refined across the atomic, nanoscopic and mesoscopic levels. The myriad of possible structures available through soft matter self-assembly is exemplified by the diversity in colloidal assembly. Thus far only simple close packed assemblies of colloidal spheres have been translated into quantum materials. Synthetic advances in controlling shape and functionality of nanoparticles

have led to a wide diversity in colloidal crystals, however, with many different packing geometries and lattice symmetries.[247,255,262,324] Translation of these architectures into quantum materials, *e.g.,* via soft or hard templating would yield a vast array of novel materials to explore.

Future work should also address the challenge of achieving high degrees of ordering over macroscopic distances. Much work has been performed in order to align and perfect soft self-assembled structures, in thin film or bulk regimes as well as across different soft matter materials classes.[278,303,325,326] At the same time, many studies have explored structure control via confined crystallization.[327–329] At the convergence of these two efforts is a long sought-after goal in the field of soft templating *i.e.,* the simultaneous control over soft and hard materials ordering. As an example, it has been shown that single crystalline nanowires of various quantum materials can be grown via nanoporous templates.[330] As we described earlier, recent work has made available mesoporous gyroidal ceramic templates consisting of single, macroscopically coherent gyroid domains.[278] The combination of these techniques could yield a gyroidally structured superconductor, topological insulator, or artificial spin ice in which an atomic single crystalline material possesses a single orientation conserved throughout the bulk of a single crystal mesoscale structure. Accomplishment of such a *hard* single crystal in tandem with a *soft* single crystal *i.e.,* a "*single crystal in a single crystal*", would unlock the full investigation of emergent transport properties, angle dependent behavior, or other unique effects of mesoscale ordering on quantum materials, but in general remains rather challenging to obtain.

Mesoscale lattice engineering

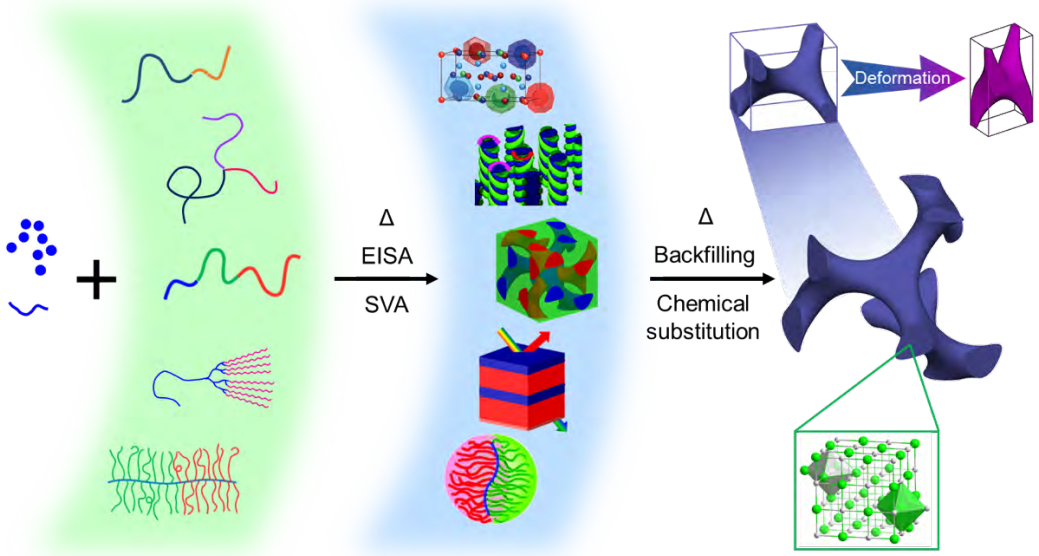

Figure 2.8: *Schematic pathway from soft matter (using blocked polymer architectures as an example) to quantum materials. Block copolymers with tailor-made chain architectures and compositions (left, green background) can direct the mesostructure formation of additives that may be precursors of inorganic quantum materials (left, blue spheres) through solution-compatible processing steps, including evaporation induced self-assembly (EISA) and solvent vapor annealing (SVA). Via a host of possible physical and chemical transformations, the resulting mesoscale lattices (middle, blue background. Adapted from*[331–334]*) can be transformed into structures that confer mesoscale ordering on top of local crystalline atomic lattices of traditional quantum materials (right, using a gyroidal minority network in blue and a perovskite atomic lattice in the green inset as examples). Due to the soft nature of polymers, as well as their periodic lattice parameter dependence on the number of monomers along the chain,*

polymer-based mesoscale lattices are amenable to substantial variations of their lattice constants as well as deformations leading to symmetry breaking (upper right), both largely unavailable in atomic lattice engineering.

Soft matter, after all, is pliable and deformable, a characteristic that earned it its name. Soft matter also enables large scale roll-to-roll manufacturing. In stark contrast with atomically crystalline hard materials, which typically render lattice engineering across substantial length scales challenging as a result of well-defined bond lengths and bond angles, soft matter offers substantive flexibility for lattice engineering of mesostructures. Therefore, we can identify a pathway where a palette of soft-matter templating materials can be adopted to direct the mesostructure formation of additives, which upon various chemical and physical transformation processes result in the desired relevant quantum materials (Figure 2.8). An exceptional feature here is that, through careful choice of materials and processing parameters, the mesostructure can undergo enormous deformations (*e.g.,* as large as 75 % changes in lattice constants) and symmetry breaking[333] unimaginable in hard matter, while still achieving highly crystalline atomic lattices at the local scale enabling desired electronic, magnetic, optical, and phononic properties. Engineered soft matter structures or templates are also often transferrable to other arbitrary surfaces[311,335] providing more materials design choices, *e.g.,* via backfilling and integration into devices, all thanks to their deformable nature.

Tuning disorder and composition

The myriad of achievable molecular and nano- to mesoscale structures and form factors offered by soft matter brings the notion of controlled disorder into the study of quantum materials. Long considered undesirable compared to crystalline order, structural disorder is often an intrinsic signature of materials derived from soft matter, from amorphous and semicrystalline polymers to nematic/smectic phases of liquid crystals. However, there has been growing evidence of the significance of disorder in the study of quantum materials.[2] Controlled disorder has manifested itself as an indispensable ingredient in unleashing intriguing quantum phenomena in Anderson topological insulators.[336] Dubbed amorphous quantum nanomaterials, glassy dye-encapsulating nanoparticles hold tremendous promise in photo-dynamic therapy (PDT), thanks to spin-orbit coupling.[337] In such glassy solids, atomic average distances of heavy atoms to the delocalized π-electron system of the encapsulated dye can be fine-tuned via substantial variations in composition, typically not achievable in crystalline solids without changing the crystal structure/nature, in turn providing new handles on tuning the strength of spin-orbit coupling.[338] Though the physical origins warrant further deeper understanding both theoretically and experimentally, these results clearly point in the direction of embracing the control of disorder as part of our toolbox for the design and application of soft-matter enabled quantum materials.

Composition is a strong tuning knob for the design of quantum materials provided by soft matter. What is helpful in achieving compositional variability is that details of molecular structure, such as the organic ligands in metal-organic frameworks, the block chemistry of block copolymers or the details of surfactant molecular structure,

can often be neglected in understanding the observed mesoscale structure formation. Earlier examples, albeit from simulation work, demonstrated the possibility of designing various organic ligands that link metal centers to engineer the spin-orbit coupling effect for the creation of topological insulators.[339–341] Given a metal center's coordination chemistry and geometry, there is a wealth of molecular structures, and consequently compositions, that can be ingeniously fine-tuned by organic/materials chemists to achieve practical real-life examples of topological materials. Such compositional variability does not come at the expense of structural integrity, since the self-assembly is a highly modular process where the interactions between soft matter building blocks are more forgiving than the exact bonding between atoms in typical inorganic quantum materials.

Considering increased interfaces

Nobel laureate Herbert Kroemer famously said "the interface is the device," in reference to devices realized with thin film semiconductors.[342] Twenty years after he received his Nobel Prize in Physics, this statement still rings true. The importance of interfaces is a common thread in both mesoscale science and quantum materials.[24] In quantum materials, interfaces are often a key component in emergent quantum properties, whether they be used to realize a quantum behavior or have a direct effect on an already-emergent property.[211,343] Using self-assembly directed molecular and nano to meso-scale structures and, in particular, micro- to mesoporous materials, means working with extremely high surface area materials. In the case of the BCP directed gyroidal superconductors mentioned earlier, this high-surface area mesoporous material

already is a quantum material. The substantial pore volume in 3-D of such gyroidal superconductors can subsequently be backfilled with a host of other materials, e.g., in the form of insulators, semiconductors, metals, or another superconductor. This provides a route to 3-D interpenetrating composite materials with large interfaces, and with exotic interface geometries, well beyond the common planar interfaces observed, *e.g.,* in MBE or PLD derived materials. Considering the large field of self-assembly directed porous solids,[219,344,345] this is a vast and to date largely unexplored playground for the study of emergent quantum materials properties.

As another example, it is known that $SrTiO_3$ and $LaAlO_3$, two insulators, exhibit superconductivity at their interface.[280] It has also been shown that a $SrTiO_3$ substrate with a FeSe film, already a superconductor with T_c of 9.4 K in the bulk, shows an extremely elevated T_c of above 100 K at monolayer thickness.[343] These unintuitive results of superconductivity at insulator interfaces, or drastically increased T_c over the bulk of a thin film at monolayer thickness, have led to interfacial superconductivity to be considered as a new frontier for the field.[346] Now regarding soft matter, it has been demonstrated that metal oxides can be structure directed into high surface area, mesoporous materials with varying 2-D and 3-D geometries.[36,39] Combining these two concepts could give rise to superconductors with large area superconducting interfaces and with potentially more interesting geometries and properties than the traditionally planar interfacial superconductors. However, as previously mentioned, such a step forward would perhaps require a more precise level of control in structure direction than is typically achieved today.

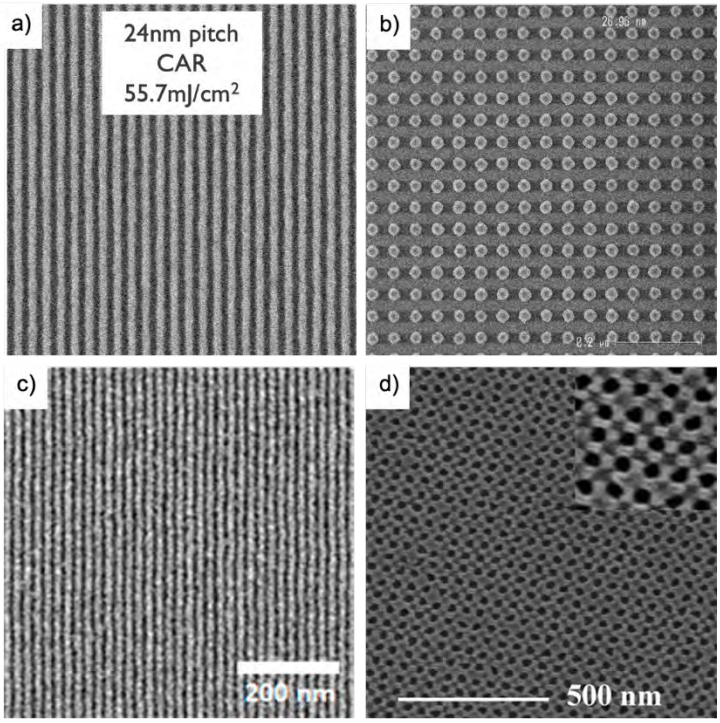

Figure 2.9: *Comparison of conventional lithographically patterned structures (top) with those obtained via soft matter self-assembly (bottom). (a) Demonstration of 24 nm pitch lines via single exposure EUV lithography, image retrieved from* [347]*. (b) 50 nm pitch pillars fabricated via EUV lithography, image retrieved from* [348] *.(c) 20 nm pitch lines fabricated via directed self-assembly of a silicon containing block-copolymer, adapted from* [349]*. (d) 50 nm pitch pores fabricated in silicon via self assembly and selective etching of a block-copolymer, adapted from* [350].

Perhaps the most natural area for overlap between the soft matter and quantum materials communities, and the area in which there is the richest potential for initial collaboration, the thin film regime is intimately familiar to those in both disciplines. Moreover, in both communities there have been decades worth of inquiry and

development of thin film fabrication and processing techniques. In traditional quantum materials synthesis, many epitaxial growth and deposition methods exist which have been highly refined for the creation of thin film materials[2,17]. As shown by the examples in figure 2.9, directed self-assembly (DSA) of soft matter has often been demonstrated as a promising alternative method for bottom-up synthesis of nanoscopic features in thin films.[281,325,351–353] Cutting across both disciplines, providing routes to devices and motivation for research, are all the techniques associated with microlithography, nanofabrication, and semiconductor manufacturing.[354]

The application of soft matter for the synthesis of quantum materials in the thin film regime has already begun paying dividends, shown in earlier sections on superconductors,[113,114] topological materials,[355,356] multiferroics,[191,194] or spintronics.[77,202–204,213] However, future work in this area may seek to take full advantage of the established techniques and capabilities present in soft matter thin film formation for the creation of new quantum metamaterials or devices. To begin, soft matter is already ubiquitous in nanofabrication in the form of photoresists, lift off layers, packaging materials, and many other forms. This ubiquity is born of utility; spin coating, direct patterning, thermal or solvent annealing, and etching all allow for an extremely high degree of control over thickness, areal coverage, material composition, and final film properties through relatively facile processing means. Through means such as co-assembly and soft or hard templating, this processing ease may be transferred into the area of quantum materials which do not natively possess such desirable characteristics. This will enable more accessible and scalable routes toward quantum materials, a crucial step towards further research and widespread adoption. Further, the use of soft-matter

self-assembly to define thin film quantum materials structure likely will enable the observation of emergent metamaterials behavior. For example, interesting interfaces between superconducting oxides or topological insulators could be defined in three dimensions in interpenetrating networks, and fabricated into planar devices to make use of the plethora of available synthesis and measurement techniques. Multiferroic domains of crystalline materials could be defined on length scales from the atomic to the mesoscopic for the engineering of spin and charge properties, and then easily integrated into sensing platforms. Nanofabrication is an area in which both quantum materials and soft matter investigators have a large presence, and that is backed by a long history of device integration resulting in tremendous scientific and technological promise. In the area of thin films, a bridge from soft matter to quantum materials has already been created, and invites heavier traffic.

Harnessing extreme conditions

Extreme conditions are common in quantum materials synthesis, from high temperatures in laser annealing[48] to ultrahigh pressures.[50,51] Such methods may at first glance seem to preclude the use of soft materials. As it turns out, however, through careful choice of processing parameters the instability of soft matter under these conditions can often be overcome. For instance, by setting the time scale of transient laser annealing processes below that of the chemical reactions governing soft materials decomposition, one can 'outrun' their oxidative degradation kinetics.[37,357,358] Even though at first sight this sounds impossible, using transient laser annealing this concept has already enabled thin film porous polymeric templates to structure direct liquid

silicon, with a melting temperature well above 1000 °C, into 3D porous silicon nanostructures.[34] Moreover, extreme processing conditions have uncovered previously unknown materials phases or may stabilize previously inaccessible metastable phases.[359] These early and encouraging experimental results open up a whole new range of non-equilibrium and extreme processing conditions that may become available to generate soft matter enabled quantum materials. This research direction also poses a number of interesting questions. For example, what is the ultimate tolerance of soft matter under these harsh conditions and how can that tolerance be extended? How can we identify additional extreme conditions appropriate for streamlining materials discovery and application? Given more questions asked than answered, this new paradigm encourages creative thinking out of the box.

Conclusions

While the fields of soft matter and quantum materials in the minds of many have so far remained largely separate, we have presented here a review of work which begins to bridge this divide. This body of research is growing at an accelerating pace, and hints at the great potential of the emerging field of soft matter enabled quantum materials. By describing the landscapes of both of these original fields, and areas where they start to overlap, we have elucidated some of the potential for scientific discovery and innovation. But clearly much remains untapped. The field of soft matter and its self-assembly is already highly developed, and advances in our understanding of associated phenomena have already paid enormous dividends, from paint dispersions to cosmetic products, to functional devices, such as organic light emitting diodes and lithium-ion

polymer batteries,[360,361] to increased stability of novel vaccines via self-assembly processes.[362,363] Advances in the field of quantum materials science could revolutionize, *e.g.,* the information science sector, changing how we communicate and compute,[2,3] how we move people and goods from point A to B, or how we interpret imaging data in health care. If the acquired knowledge in the field of soft matter is fully brought to bear on the preparation and study of novel quantum materials, the resulting expansion of scope beyond the more traditional pathways to this exciting materials class would open up an enormous space for exploration and innovation.

As previously stated, the importance of interfaces is common to both soft matter and quantum materials. Interfaces modulate the thermodynamics of self-assembly, the appearance of topological insulators, and the transition temperature of superconductors. The convergence of the two fields of 'soft' and 'hard' condensed matter science provides tremendous opportunities and substantial challenges. With much work to be done in order to address such challenges and realize the full potential of soft matter in quantum materials design, synthesis, science and engineering, we hope that this review will inspire researchers to take interest in working 'across the aisle.' It is only by reaching through *this* interface that we may fully realize the promise of soft matter enabled quantum materials.

REFERENCES

1. The rise of quantum materials. *Nat. Phys.* **12,** 105–105 (2016).
2. Broholm, C., Fisher, I., Moore, J., Murnane, M., Moreo, A., Tranquada, J., Basov, D., Freericks, J., Aronson, M., MacDonald, A., Fradkin, E., Yacoby, A., Samarth, N., Stemmer, S., Horton, L., Horwitz, J., Davenport, J., Graf, M., Krause, J., Pechan, M., Perry, K., Rhyne, J., Schwartz, A., Thiyagarajan, T., Yarris, L. & Runkles, K. *Basic Research Needs Workshop on Quantum Materials for Energy Relevant Technology*. 1616509 (2016). doi:10.2172/1616509
3. Andrew, S. Quantum Computing. *Rep. Prog. Phys.* **61,** 117–173 (1998).
4. Keimer, B. & Moore, J. E. The physics of quantum materials. *Nat. Phys.* **13,** 1045–1055 (2017).
5. Basov, D. N., Averitt, R. D. & Hsieh, D. Towards properties on demand in quantum materials. *Nat. Mater.* **16,** 1077–1088 (2017).
6. Tokura, Y., Kawasaki, M. & Nagaosa, N. Emergent functions of quantum materials. *Nat. Phys.* **13,** 1056–1068 (2017).
7. Beenakker, C. W. J. Search for Majorana Fermions in Superconductors. *Annu. Rev. Condens. Matter Phys.* **4,** 113–136 (2013).
8. Manna, S., Wei, P., Xie, Y., Law, K. T., Lee, P. A. & Moodera, J. S. Signature of a pair of Majorana zero modes in superconducting gold surface states. *Proc. Natl. Acad. Sci.* **117,** 8775–8782 (2020).

9. Hsieh, D., Qian, D., Wray, L., Xia, Y., Hor, Y. S., Cava, R. J. & Hasan, M. Z. A topological Dirac insulator in a quantum spin Hall phase. *Nature* **452,** 970–974 (2008).

10. Lu, L., Wang, Z., Ye, D., Ran, L., Fu, L., Joannopoulos, J. D. & Solja i, M. Experimental observation of Weyl points. *Science* **349,** 622–624 (2015).

11. Xu, S.-Y., Belopolski, I., Alidoust, N., Neupane, M., Bian, G., Zhang, C., Sankar, R., Chang, G., Yuan, Z., Lee, C.-C., Huang, S.-M., Zheng, H., Ma, J., Sanchez, D. S., Wang, B., Bansil, A., Chou, F., Shibayev, P. P., Lin, H., Jia, S. & Hasan, M. Z. Discovery of a Weyl fermion semimetal and topological Fermi arcs. *Science* **349,** 613–617 (2015).

12. Snider, E., Dasenbrock-Gammon, N., McBride, R., Debessai, M., Vindana, H., Vencatasamy, K., Lawler, K. V., Salamat, A. & Dias, R. P. Room-temperature superconductivity in a carbonaceous sulfur hydride. *Nature* **586,** 373–377 (2020).

13. Ladd, T. D., Jelezko, F., Laflamme, R., Nakamura, Y., Monroe, C. & O'Brien, J. L. Quantum computers. *Nature* **464,** 45–53 (2010).

14. Kamihara, Y., Watanabe, T., Hirano, M. & Hosono, H. Iron-Based Layered Superconductor La[$O_{1-x}F_x$]FeAs (x = 0.05−0.12) with T_c = 26 K. *J. Am. Chem. Soc.* **130,** 3296–3297 (2008).

15. Cao, Y., Fatemi, V., Fang, S., Watanabe, K., Taniguchi, T., Kaxiras, E. & Jarillo-Herrero, P. Unconventional superconductivity in magic-angle graphene superlattices. *Nature* **556,** 43–50 (2018).

16. Cao, Y., Fatemi, V., Demir, A., Fang, S., Tomarken, S. L., Luo, J. Y., Sanchez-Yamagishi, J. D., Watanabe, K., Taniguchi, T., Kaxiras, E., Ashoori, R. C. &

Jarillo-Herrero, P. Correlated insulator behaviour at half-filling in magic-angle graphene superlattices. *Nature* **556,** 80–84 (2018).

17. Samarth, N. Quantum materials discovery from a synthesis perspective. *Nat. Mater.* **16,** 1068–1076 (2017).
18. Whitesides, G. M. Self-Assembly at All Scales. *Science* **295,** 2418–2421 (2002).
19. Mai, Y. & Eisenberg, A. Self-assembly of block copolymers. *Chem. Soc. Rev.* **41,** 5969 (2012).
20. Kamigaito, M. & Sawamoto, M. Synergistic Advances in Living Cationic and Radical Polymerizations. *Macromolecules* **53,** 6749–6753 (2020).
21. *Anionic polymerization: principles, practice, strength, consequences and applications*. (Springer, 2015).
22. Matyjaszewski, K. Advanced Materials by Atom Transfer Radical Polymerization. *Adv. Mater.* **30,** 1706441 (2018).
23. Hwang, H. Y., Iwasa, Y., Kawasaki, M., Keimer, B., Nagaosa, N. & Tokura, Y. Emergent phenomena at oxide interfaces. *Nat. Mater.* **11,** 103–113 (2012).
24. Crabtree, G., Sarrao, J., Alivisatos, P., Barletta, W., Bates, F., Brown, G., French, R., Greene, L., Hemminger, J., Kastner, M., Kay, B., Lewis, J., Ratner, M., Anthony, R., Rubloff, G., Spence, J., Tobias, D., Tranquada, J., & Basic Energy Sciences Advisory Committee (BESAC). *From Quanta to the Continuum: Opportunities for Mesoscale Science*. 1183982 (2012). doi:10.2172/1183982
25. Bose, S. & Ayyub, P. A review of finite size effects in quasi-zero dimensional superconductors. *Rep. Prog. Phys.* **77,** 116503 (2014).

26. Leavens, C. R. & Fenton, E. W. Superconductivity of small particles. *Phys. Rev. B* **24,** 5086–5092 (1981).

27. Bernevig, B. A., Hughes, T. L. & Zhang, S.-C. Quantum Spin Hall Effect and Topological Phase Transition in HgTe Quantum Wells. *Science* **314,** 1757–1761 (2006).

28. Spaldin, N. A. & Ramesh, R. Advances in magnetoelectric multiferroics. *Nat. Mater.* **18,** 203–212 (2019).

29. Khlebnikov, S. & Hillhouse, H. W. Electronic structure of double-gyroid nanostructured semiconductors: Perspectives for carrier multiplication solar cells. *Phys. Rev. B* **80,** 115316 (2009).

30. Donnelly, R. J. in *Phys. Vade Mecum* (American Institute of Physics).

31. Wang, K., Dahan, R., Shentcis, M., Kauffmann, Y., Ben Hayun, A., Reinhardt, O., Tsesses, S. & Kaminer, I. Coherent interaction between free electrons and a photonic cavity. *Nature* **582,** 50–54 (2020).

32. Khanikaev, A. B., Hossein Mousavi, S., Tse, W.-K., Kargarian, M., MacDonald, A. H. & Shvets, G. Photonic topological insulators. *Nat. Mater.* **12,** 233–239 (2013).

33. Rechtsman, M. C., Zeuner, J. M., Plotnik, Y., Lumer, Y., Podolsky, D., Dreisow, F., Nolte, S., Segev, M. & Szameit, A. Photonic Floquet topological insulators. *Nature* **496,** 196–200 (2013).

34. Kresge, C. T., Leonowicz, M. E., Roth, W. J., Vartuli, J. C. & Beck, J. S. Ordered mesoporous molecular sieves synthesized by a liquid-crystal template mechanism. *Nature* **359,** 710–712 (1992).

35. Templin, M., Franck, A., Du Chesne, A., Leist, H., Zhang, Y., Ulrich, R., Schädler, V. & Wiesner, U. Organically Modified Aluminosilicate Mesostructures from Block Copolymer Phases. *Science* **278,** 1795–1798 (1997).

36. Lee, J., Christopher Orilall, M., Warren, S. C., Kamperman, M., DiSalvo, F. J. & Wiesner, U. Direct access to thermally stable and highly crystalline mesoporous transition-metal oxides with uniform pores. *Nat. Mater.* **7,** 222–228 (2008).

37. Tan, K. W., Jung, B., Werner, J. G., Rhoades, E. R., Thompson, M. O. & Wiesner, U. Transient laser heating induced hierarchical porous structures from block copolymer–directed self-assembly. *Science* **349,** 54–58 (2015).

38. Warren, S. C., Messina, L. C., Slaughter, L. S., Kamperman, M., Zhou, Q., Gruner, S. M., DiSalvo, F. J. & Wiesner, U. Ordered Mesoporous Materials from Metal Nanoparticle-Block Copolymer Self-Assembly. *Science* **320,** 1748–1752 (2008).

39. Robbins, S. W., Beaucage, P. A., Sai, H., Tan, K. W., Werner, J. G., Sethna, J. P., DiSalvo, F. J., Gruner, S. M., Van Dover, R. B. & Wiesner, U. Block copolymer self-assembly–directed synthesis of mesoporous gyroidal superconductors. *Sci. Adv.* **2,** e1501119 (2016).

40. Tinkham, M. *Introduction to superconductivity*. (Dover Publ, 2015).

41. Bardeen, J., Cooper, L. N. & Schrieffer, J. R. Theory of Superconductivity. *Phys. Rev.* **108,** 1175–1204 (1957).

42. McMillan, W. L. Transition Temperature of Strong-Coupled Superconductors. *Phys. Rev.* **167,** 331–344 (1968).

43. Bednorz, J. G. & Müller, K. A. Possible highT c superconductivity in the Ba?La?Cu?O system. *Z. Für Phys. B Condens. Matter* **64,** 189–193 (1986).

44. *Ten Years of Superconductivity: 1980–1990*. **7,** (Springer Netherlands, 1993).

45. Ott, H. R., Rudigier, H., Fisk, Z. & Smith, J. L. U Be 13 : An Unconventional Actinide Superconductor. *Phys. Rev. Lett.* **50,** 1595–1598 (1983).

46. Steglich, F., Aarts, J., Bredl, C. D., Lieke, W., Meschede, D., Franz, W. & Schäfer, H. Superconductivity in the Presence of Strong Pauli Paramagnetism: Ce Cu 2 Si 2. *Phys. Rev. Lett.* **43,** 1892–1896 (1979).

47. Scalapino, D. J. A common thread: The pairing interaction for unconventional superconductors. *Rev. Mod. Phys.* **84,** 1383–1417 (2012).

48. Bhaumik, A., Sachan, R., Gupta, S. & Narayan, J. Discovery of High-Temperature Superconductivity (T_c = 55 K) in B-Doped Q-Carbon. *ACS Nano* **11,** 11915–11922 (2017).

49. Schilling, A., Cantoni, M., Guo, J. D. & Ott, H. R. Superconductivity above 130 K in the Hg–Ba–Ca–Cu–O system. *Nature* **363,** 56–58 (1993).

50. Drozdov, A. P., Eremets, M. I., Troyan, I. A., Ksenofontov, V. & Shylin, S. I. Conventional superconductivity at 203 kelvin at high pressures in the sulfur hydride system. *Nature* **525,** 73–76 (2015).

51. Drozdov, A. P., Kong, P. P., Minkov, V. S., Besedin, S. P., Kuzovnikov, M. A., Mozaffari, S., Balicas, L., Balakirev, F. F., Graf, D. E., Prakapenka, V. B., Greenberg, E., Knyazev, D. A., Tkacz, M. & Eremets, M. I. Superconductivity at 250 K in lanthanum hydride under high pressures. *Nature* **569,** 528–531 (2019).

52. Beloborodov, I. S., Lopatin, A. V., Vinokur, V. M. & Efetov, K. B. Granular electronic systems. *Rev. Mod. Phys.* **79,** 469–518 (2007).

53. Perenboom, J. A. A. J., Wyder, P. & Meier, F. Electronic properties of small metallic particles. *Phys. Rep.* **78,** 173–292 (1981).

54. Qin, S., Kim, J., Niu, Q. & Shih, C.-K. Superconductivity at the Two-Dimensional Limit. **324,** 5 (2009).

55. Guéron, S., Pothier, H., Birge, N. O., Esteve, D. & Devoret, M. H. Superconducting Proximity Effect Probed on a Mesoscopic Length Scale. *Phys. Rev. Lett.* **77,** 3025–3028 (1996).

56. Astafiev, O. V., Ioffe, L. B., Kafanov, S., Pashkin, Yu. A., Arutyunov, K. Yu., Shahar, D., Cohen, O. & Tsai, J. S. Coherent quantum phase slip. *Nature* **484,** 355–358 (2012).

57. Bezryadin, A., Lau, C. N. & Tinkham, M. Quantum suppression of superconductivity in ultrathin nanowires. *Nature* **404,** 971–974 (2000).

58. Bose, S., Galande, C., Chockalingam, S. P., Banerjee, R., Raychaudhuri, P. & Ayyub, P. Competing effects of surface phonon softening and quantum size effects on the superconducting properties of nanostructured Pb. *J. Phys. Condens. Matter* **21,** 205702 (2009).

59. Dickey, J. M. & Paskin, A. Phonon Spectrum Changes in Small Particles and Their Implications for Superconductivity. *Phys. Rev. Lett.* **21,** 1441–1443 (1968).

60. Bose, S., García-García, A. M., Ugeda, M. M., Urbina, J. D., Michaelis, C. H., Brihuega, I. & Kern, K. Observation of shell effects in superconducting nanoparticles of Sn. *Nat. Mater.* **9,** 550–554 (2010).

61. Berdiyorov, G. R., Milošević, M. V. & Peeters, F. M. Vortex lattice in effective type-I superconducting films with periodic arrays of submicron holes. *Phys. C Supercond. Its Appl.* **437–438,** 25–28 (2006).

62. Geim, A. K., Grigorieva, I. V., Dubonos, S. V., Lok, J. G. S., Maan, J. C., Filippov, A. E. & Peeters, F. M. Phase transitions in individual sub-micrometre superconductors. *Nature* **390,** 259–262 (1997).

63. Grigorieva, I. V., Escoffier, W., Misko, V. R., Baelus, B. J., Peeters, F. M., Vinnikov, L. Y. & Dubonos, S. V. Pinning-Induced Formation of Vortex Clusters and Giant Vortices in Mesoscopic Superconducting Disks. *Phys. Rev. Lett.* **99,** 147003 (2007).

64. Guo, Y. Superconductivity Modulated by Quantum Size Effects. *Science* **306,** 1915–1917 (2004).

65. von Delft, J. & Ralph, D. C. Spectroscopy of discrete energy levels in ultrasmall metallic grains. *Phys. Rep.* **345,** 61–173 (2001).

66. Chibotaru, L. F., Ceulemans, A., Bruyndoncx, V. & Moshchalkov, V. V. Symmetry-induced formation of antivortices in mesoscopic superconductors. *Nature* **408,** 833–835 (2000).

67. Eley, S., Gopalakrishnan, S., Goldbart, P. M. & Mason, N. Approaching zero-temperature metallic states in mesoscopic superconductor–normal–superconductor arrays. *Nat. Phys.* **8,** 59–62 (2012).

68. Weitz, I. S., Sample, J. L., Ries, R., Spain, E. M. & Heath, J. R. Josephson Coupled Quantum Dot Artificial Solids. *J Phys Chem B* **104,** 44288–4291 (2000).

69. Wang, J.-G., Tian, M.-L., Kumar, N. & Mallouk, T. E. Controllable Template Synthesis of Superconducting Zn Nanowires with Different Microstructures by Electrochemical Deposition. *Nano Lett.* **5,** 1247–1253 (2005).

70. Apel, P. Track etching technique in membrane technology. *Radiat. Meas.* **34,** 559–566 (2001).

71. He, M., Wong, C. H., Tse, P. L., Zheng, Y., Zhang, H., Lam, F. L. Y., Sheng, P., Hu, X. & Lortz, R. "Giant" Enhancement of the Upper Critical Field and Fluctuations above the Bulk T_c in Superconducting Ultrathin Lead Nanowire Arrays. *ACS Nano* **7,** 4187–4193 (2013).

72. Zhao, D. Triblock Copolymer Syntheses of Mesoporous Silica with Periodic 50 to 300 Angstrom Pores. *Science* **279,** 548–552 (1998).

73. Zolotavin, P. & Guyot-Sionnest, P. Meissner Effect in Colloidal Pb Nanoparticles. *ACS Nano* **4,** 5599–5608 (2010).

74. Lin, X.-M., Claus, H., Welp, U., Beloborodov, I. S., Kwok, W.-K., Crabtree, G. W. & Jaeger, H. M. Growth and Properties of Superconducting Anisotropic Lead Nanoprisms. *J. Phys. Chem. C* **111,** 3548–3550 (2007).

75. Nabais, C., Schneider, R., Bellouard, C., Lambert, J., Willmann, P. & Billaud, D. A new method for the size- and shape-controlled synthesis of lead nanostructures. *Mater. Chem. Phys.* **117,** 268–275 (2009).

76. Lu, X. L., Wang, W., Zhang, G. Q. & Li, X. G. Dual-Activity Controlled Asymmetric Synthesis of Superconducting Lead Hemispheres. *Adv. Funct. Mater.* **17,** 2198–2202 (2007).

77. Ramin Moayed, M. M., Kull, S., Rieckmann, A., Beck, P., Wagstaffe, M., Noei, H., Kornowski, A., Hungria, A. B., Lesyuk, R., Stierle, A. & Klinke, C. Function Follows Form: From Semiconducting to Metallic toward Superconducting PbS Nanowires by Faceting the Crystal. *Adv. Funct. Mater.* **30,** 1910503 (2020).

78. Hagel, J., Kelemen, M. T., Fischer, G., Pilawa, B., Wosnitza, J., Dormann, E., v. Löhneysen, H., Schnepf, A., Schnöckel, H., Neisel, U. & Beck, J. Superconductivity of a Crystalline Ga 84 Cluster Compound. *J. Low Temp. Phys.* **129,** 133–142 (2002).

79. Roslova, M., Opherden, L., Veremchuk, I., Spillecke, L., Kirmse, H., Herrmannsdörfer, T., Wosnitza, J., Doert, T. & Ruck, M. Downscaling Effect on the Superconductivity of $Pd_3Bi_2X_2$ (X = S or Se) Nanoparticles Prepared by Microwave-Assisted Polyol Synthesis. *Inorg. Chem.* **55,** 8808–8815 (2016).

80. Anderson, P. W. Theory of dirty superconductors. *J. Phys. Chem. Solids* **11,** 26–30 (1959).

81. Zhang, Y., Wong, C. H., Shen, J., Sze, S. T., Zhang, B., Zhang, H., Dong, Y., Xu, H., Yan, Z., Li, Y., Hu, X. & Lortz, R. Dramatic enhancement of superconductivity in single-crystalline nanowire arrays of Sn. *Sci. Rep.* **6,** 32963 (2016).

82. Bezryadin, A. & Goldbart, P. M. Superconducting Nanowires Fabricated Using Molecular Templates. *Adv. Mater.* **22,** 1111–1121 (2010).

83. Hopkins, D. S., Pekker, D., Wei, T.-C., Goldbart, P. M. & Bezryadin, A. Local superfluid densities probed via current-induced superconducting phase gradients. *Phys. Rev. B* **76,** 220506 (2007).

84. Hopkins, D. S. Quantum Interference Device Made by DNA Templating of Superconducting Nanowires. *Science* **308,** 1762–1765 (2005).

85. Martin, C. R. Nanomaterials: A Membrane-Based Synthetic Approach. *Science* **266,** 1961–1966 (1994).

86. Wang, H., Wang, J., Tian, M., Bell, L., Hutchinson, E., Rosario, M. M., Liu, Y., Amma, A. & Mallouk, T. Metallic contacts with individual Ru nanowires prepared by electrochemical deposition and the suppression of superconductivity in ultrasmall Ru grains. *Appl. Phys. Lett.* **84,** 5171–5173 (2004).

87. Wang, J., Shi, C., Tian, M., Zhang, Q., Kumar, N., Jain, J. K., Mallouk, T. E. & Chan, M. H. W. Proximity-Induced Superconductivity in Nanowires: Minigap State and Differential Magnetoresistance Oscillations. *Phys. Rev. Lett.* **102,** 247003 (2009).

88. Tian, M., Wang, J., Kumar, N., Han, T., Kobayashi, Y., Liu, Y., Mallouk, T. E. & Chan, M. H. W. Observation of Superconductivity in Granular Bi Nanowires Fabricated by Electrodeposition. *Nano Lett.* **6,** 2773–2780 (2006).

89. Tian, M., Kumar, N., Chan, M. H. W. & Mallouk, T. E. Evidence of local superconductivity in granular Bi nanowires fabricated by electrodeposition. *Phys. Rev. B* **78,** 045417 (2008).

90. Ye, Z., Zhang, H., Liu, H., Wu, W. & Luo, Z. Observation of superconductivity in single crystalline Bi nanowires. *Nanotechnology* **19,** 085709 (2008).

91. Ye, Z., Zhang, H., Liu, H., Wu, W. & Luo, Z. Evidence for superconductivity in single crystalline Bi nanowires. *Phys. B Condens. Matter* **403,** 1529–1530 (2008).

92. Tian, M., Kumar, N., Xu, S., Wang, J., Kurtz, J. S. & Chan, M. H. W. Suppression of Superconductivity in Zinc Nanowires by Bulk Superconductors. *Phys. Rev. Lett.* **95,** 076802 (2005).

93. Tian, M., Kumar, N., Wang, J., Xu, S. & Chan, M. H. W. Influence of a bulk superconducting environment on the superconductivity of one-dimensional zinc nanowires. *Phys. Rev. B* **74,** 014515 (2006).

94. Liu, H., Ye, Z., Luo, Z., Rathnayaka, K. D. D. & Wu, W. Long-range superconducting proximity effect in template-fabricated single-crystal nanowires. *J. Phys. Conf. Ser.* **400,** 022136 (2012).

95. Liu, H., Ye, Z., Luo, Z., Rathnayaka, K. D. D. & Wu, W. Boundary effect on superconductivity in long single-crystal superconducting nanowires. *Phys. C Supercond.* **468,** 304–309 (2008).

96. Michotte, S., Mátéfi-Tempfli, S. & Piraux, L. Current–voltage characteristics of Pb and Sn granular superconducting nanowires. *Appl. Phys. Lett.* **82,** 4119–4121 (2003).

97. Michotte, S., Piraux, L., Boyer, F., Ladan, F. R. & Maneval, J. P. Development of phase-slip centers in superconducting Sn nanowires. *Appl. Phys. Lett.* **85,** 3175–3177 (2004).

98. de Menten de Horne, F., Piraux, L. & Michotte, S. Electroless template grown superconducting lead and tin nanotubes. *Nanotechnology* **20,** 385603 (2009).

99. de Menten de Horne, F., Piraux, L. & Michotte, S. Proximity effect in superconducting nanowires. *Phys. C Supercond.* **460–462,** 1441–1442 (2007).

100. Lucot, D., Pierre, F., Mailly, D., Yu-Zhang, K., Michotte, S., de Menten de Horne, F. & Piraux, L. Multicontact measurements of a superconducting Sn nanowire. *Appl. Phys. Lett.* **91,** 042502 (2007).

101. Vodolazov, D. Y., Peeters, F. M., Piraux, L., Mátéfi-Tempfli, S. & Michotte, S. Current-Voltage Characteristics of Quasi-One-Dimensional Superconductors: An S -Shaped Curve in the Constant Voltage Regime. *Phys. Rev. Lett.* **91,** 157001 (2003).

102. Tian, M., Wang, J., Snyder, J., Kurtz, J., Liu, Y., Schiffer, P., Mallouk, T. E. & Chan, M. H. W. Synthesis and characterization of superconducting single-crystal Sn nanowires. *Appl. Phys. Lett.* **83,** 1620–1622 (2003).

103. Liu, H., Ye, Z., Zhang, H., Wu, W., Luo, Z., Rathnayaka, K. D. D. & Naugle, D. G. Superconducting proximity effect in single-crystal Sn nanowires. *Phys. B Condens. Matter* **403,** 1542–1543 (2008).

104. Dubois, S., Michel, A., Eymery, J. P., Duvail, J. L. & Piraux, L. Fabrication and properties of arrays of superconducting nanowires. *J. Mater. Res.* **14,** 665–671 (1999).

105. Michotte, S., Piraux, L., Dubois, S., Pailloux, F., Stenuit, G. & Govaerts, J. Superconducting properties of lead nanowires arrays. *Phys. C Supercond.* **377,** 267–276 (2002).

106. Michotte, S., Mátéfi-Tempfli, S. & Piraux, L. 1D-transport properties of single superconducting lead nanowires. *Phys. C Supercond.* **391,** 369–375 (2003).

107. Yi, G. & Schwarzacher, W. Single crystal superconductor nanowires by electrodeposition. *Appl. Phys. Lett.* **74,** 1746–1748 (1999).

108. Wang, J., Sun, Y., Tian, M., Liu, B., Singh, M. & Chan, M. H. W. Superconductivity in single crystalline Pb nanowires contacted by normal metal electrodes. *Phys. Rev. B* **86,** 035439 (2012).

109. Riminucci, A. & Schwarzacher, W. Coexistence of superconductivity and superparamagnetism in Pb–Co electrodeposited nanowires. *Appl. Phys. A* **123,** 161 (2017).

110. Kumar, N., Tian, M. L., Wang, J. G., Watts, W., Kindt, J., Mallouk, T. E. & Chan, M. H. W. Investigation of superconductivity in electrochemically fabricated AuSn nanowires. *Nanotechnology* **19,** 365704 (2008).

111. de Menten de Horne, F., Piraux, L. & Michotte, S. Fabrication and physical properties of Pb⁄Cu multilayered superconducting nanowires. *Appl. Phys. Lett.* **86,** 152510 (2005).

112. Wong, C. H., Lam, F. L. Y., Shen, J., He, M., Hu, X. & Lortz, R. The role of the coherence length for the establishment of global phase coherence in arrays of ultra-thin superconducting nanowires. *Supercond. Sci. Technol.* **30,** 105004 (2017).

113. Vanacken, J., Vinckx, W., Moshchalkov, V. V., Mátéfi-Tempfli, S., Mátéfi-Tempfli, M., Michotte, S., Piraux, L. & Ye, X. Vortex pinning in superconductors laterally modulated by nanoscale self-assembled arrays. *Phys. C Supercond. Its Appl.* **468,** 585–588 (2008).

114. Ruiz-Valdepeñas, L., Velez, M., Valdés-Bango, F., Alvarez-Prado, L. M., Garcia-Alonso, F. J., Martin, J. I., Navarro, E., Alameda, J. M. & Vicent, J. L.

Imprinted labyrinths and percolation in Nd-Co/Nb magnetic/superconducting hybrids. *J. Appl. Phys.* **115,** 213901 (2014).

115. Jang, E.-S., Chang, J.-J., Gwak, J., Ayral, A., Rouessac, V., Cot, L., Hwang, S.-J. & Choy, J.-H. Asymmetric High- T_c Superconducting Gas Separation Membrane. *Chem. Mater.* **19,** 3840–3844 (2007).
116. Shani, L., Tinnefeld, P., Fleger, Y., Sharoni, A., Shapiro, B. Ya., Shaulov, A., Gang, O. & Yeshurun, Y. DNA origami based superconducting nanowires. *AIP Adv.* **11,** 015130 (2021).
117. Shani, L., Michelson, A. N., Minevich, B., Fleger, Y., Stern, M., Shaulov, A., Yeshurun, Y. & Gang, O. DNA-assembled superconducting 3D nanoscale architectures. *Nat. Commun.* **11,** 5697 (2020).
118. Aliev, A. E., Lee, S. B., Zakhidov, A. A. & Baughman, R. H. Superconductivity in Pb inverse opal. *Phys. C Supercond.* **453,** 15–23 (2007).
119. Lungu, A., Bleiweiss, M., Amirzadeh, J., Saygi, S., Dimofte, A., Yin, M., Iqbal, Z. & Datta, T. Superconductivity in nanostructured lead. *Phys. C Supercond.* **349,** 1–7 (2001).
120. Bogomolov, V. N., Kumzerov, Y. A., Romanov, S. G. & Zhuravlev, V. V. Josephson properties of the three-dimensional regular lattice of the weakly coupled nanoparticles. *Phys. C Supercond.* **208,** 371–384 (1993).
121. Bykov, A. A., Gokhfeld, D. M., Savitskaya, N. E., Terentjev, K. Y., Popkov, S. I., Mistonov, A. A., Grigoryeva, N. A., Zakhidov, A. & Grigoriev, S. V. Flux pinning mechanisms and a vortex phase diagram of tin-based inverse opals. *Supercond. Sci. Technol.* **32,** 115004 (2019).

122. Ciou, Y. S., Lee, M. K., Charnaya, E. V., Tien, C., Chang, L. J., Kumzerov, Y. A. & Samoylovich, M. I. Superconductivity in Sn nanocomposites. *Supercond. Sci. Technol.* **26,** 055009 (2013).

123. Shamshur, D. V. Electrical Conductivity and Superconductivity of Ordered Indium–Opal Nanocomposites. *Phys. Solid State* **47,** 2005 (2005).

124. Charnaya, E. V., Tien, C., Lin, K. J., Wur, C. S. & Kumzerov, Yu. A. Superconductivity of gallium in various confined geometries. *Phys. Rev. B* **58,** 467–472 (1998).

125. Johnson, R. C., Nieskoski, M. D., Disseler, S. M., Huber, T. E. & Graf, M. J. Superconductivity of Bi Confined in an Opal Host. *J. Low Temp. Phys.* **170,** 205–215 (2013).

126. Aliev, A. E. High- T_c superconductivity in nanostructured $Na_x WO_{3-y}$: sol–gel route. *Supercond. Sci. Technol.* **21,** 115022 (2008).

127. Lee, M. K., Charnaya, E. V., Mühlbauer, S., Jeng, U., Chang, L. J. & Kumzerov, Yu. A. The morphologic correlation between vortex transformation and upper critical field line in opal-based nanocomposites. *Sci. Rep.* **11,** 4807 (2021).

128. Thedford, R. P., Beaucage, P. A., Susca, E. M., Chao, C. A., Nowack, K. C., Van Dover, R. B., Gruner, S. M. & Wiesner, U. Superconducting Quantum Metamaterials from High Pressure Melt Infiltration of Metals into Block Copolymer Double Gyroid Derived Ceramic Templates. *Adv. Funct. Mater.* **31,** 2100469 (2021).

129. Beaucage, P. A., van Dover, R. B., DiSalvo, F. J., Gruner, S. M. & Wiesner, U. Superconducting Quantum Metamaterials from Convergence of Soft and Hard Condensed Matter Science. *Adv. Mater.* **33,** 2006975 (2021).

130. Yu, F., Thedford, R. P., Hedderick, K. R., Freychet, G., Zhernenkov, M., Estroff, L. A., Nowack, K. C., Gruner, S. M. & Wiesner, U. B. Patternable Mesoporous Thin Film Quantum Materials via Block Copolymer Self-Assembly: An Emergent Technology? *ACS Appl. Mater. Interfaces* **13,** 34732–34741 (2021).

131. Hesse, S. A., Fritz, K. E., Beaucage, P. A., Thedford, R. P., Yu, F., DiSalvo, F. J., Suntivich, J. & Wiesner, U. Materials Combining Asymmetric Pore Structures with Well-Defined Mesoporosity for Energy Storage and Conversion. *ACS Nano* **14,** 16897–16906 (2020).

132. Thouless, D. J., Kohmoto, M., Nightingale, M. P. & den Nijs, M. Quantized Hall Conductance in a Two-Dimensional Periodic Potential. *Phys. Rev. Lett.* **49,** 405–408 (1982).

133. Hasan, M. Z. & Kane, C. L. *Colloquium* : Topological insulators. *Rev. Mod. Phys.* **82,** 3045–3067 (2010).

134. Xiao, D., Chang, M.-C. & Niu, Q. Berry phase effects on electronic properties. *Rev. Mod. Phys.* **82,** 1959–2007 (2010).

135. Haldane, F. D. M. Nobel Lecture: Topological quantum matter. *Rev. Mod. Phys.* **89,** 040502 (2017).

136. Moore, J. E. The birth of topological insulators. *Nature* **464,** 194–198 (2010).

137. Wen, X.-G. Choreographed entanglement dances: Topological states of quantum matter. *Science* **363,** eaal3099 (2019).

138. Klitzing, K. v., Dorda, G. & Pepper, M. New Method for High-Accuracy Determination of the Fine-Structure Constant Based on Quantized Hall Resistance. *Phys. Rev. Lett.* **45,** 494–497 (1980).

139. Halperin, B. I. Quantized Hall conductance, current-carrying edge states, and the existence of extended states in a two-dimensional disordered potential. *Phys. Rev. B* **25,** 2185–2190 (1982).

140. Landau, L. D. in *Collect. Pap. LD Landau* 193–216 (Pergamon, 1965). doi:10.1016/B978-0-08-010586-4.50034-1

141. Haldane, F. D. M. Model for a Quantum Hall Effect without Landau Levels: Condensed-Matter Realization of the 'Parity Anomaly'. *Phys. Rev. Lett.* **61,** 2015–2018 (1988).

142. Kane, C. L. & Mele, E. J. Z2 Topological Order and the Quantum Spin Hall Effect. *Phys. Rev. Lett.* **95,** 146802 (2005).

143. Bernevig, B. A., Hughes, T. L. & Zhang, S.-C. Quantum Spin Hall Effect and Topological Phase Transition in HgTe Quantum Wells. *Science* **314,** 1757–1761 (2006).

144. König, M., Wiedmann, S., Brüne, C., Roth, A., Buhmann, H., Molenkamp, L. W., Qi, X.-L. & Zhang, S.-C. Quantum Spin Hall Insulator State in HgTe Quantum Wells. *Science* **318,** 766–770 (2007).

145. Fu, L., Kane, C. L. & Mele, E. J. Topological Insulators in Three Dimensions. *Phys. Rev. Lett.* **98,** 106803 (2007).

146. Moore, J. E. & Balents, L. Topological invariants of time-reversal-invariant band structures. *Phys. Rev. B* **75,** 121306 (2007).

147. Roy, R. Topological phases and the quantum spin Hall effect in three dimensions. *Phys. Rev. B* **79,** 195322 (2009).

148. Graf, G. M. & Porta, M. Bulk-Edge Correspondence for Two-Dimensional Topological Insulators. *Commun. Math. Phys.* **324,** 851–895 (2013).

149. Raghu, S. & Haldane, F. D. M. Analogs of quantum-Hall-effect edge states in photonic crystals. *Phys. Rev. A* **78,** 033834 (2008).

150. Haldane, F. D. M. & Raghu, S. Possible Realization of Directional Optical Waveguides in Photonic Crystals with Broken Time-Reversal Symmetry. *Phys. Rev. Lett.* **100,** 013904 (2008).

151. Ozawa, T., Price, H. M., Amo, A., Goldman, N., Hafezi, M., Lu, L., Rechtsman, M. C., Schuster, D., Simon, J., Zilberberg, O. & Carusotto, I. Topological photonics. *Rev. Mod. Phys.* **91,** 015006 (2019).

152. Kim, M., Jacob, Z. & Rho, J. Recent advances in 2D, 3D and higher-order topological photonics. *Light Sci. Appl.* **9,** 130 (2020).

153. Yang, Z., Gao, F., Shi, X., Lin, X., Gao, Z., Chong, Y. & Zhang, B. Topological Acoustics. *Phys. Rev. Lett.* **114,** 114301 (2015).

154. Ma, G., Xiao, M. & Chan, C. T. Topological phases in acoustic and mechanical systems. *Nat. Rev. Phys.* **1,** 281–294 (2019).

155. Khanikaev, A. B., Hossein Mousavi, S., Tse, W.-K., Kargarian, M., MacDonald, A. H. & Shvets, G. Photonic topological insulators. *Nat. Mater.* **12,** 233–239 (2013).

156. Rechtsman, M. C., Zeuner, J. M., Plotnik, Y., Lumer, Y., Podolsky, D., Dreisow, F., Nolte, S., Segev, M. & Szameit, A. Photonic Floquet topological insulators. *Nature* **496,** 196–200 (2013).

157. Jörg, C., Letscher, F., Fleischhauer, M. & Freymann, G. von. Dynamic defects in photonic Floquet topological insulators. *New J. Phys.* **19,** 083003 (2017).

158. Galeotti, G., De Marchi, F., Hamzehpoor, E., MacLean, O., Rajeswara Rao, M., Chen, Y., Besteiro, L. V., Dettmann, D., Ferrari, L., Frezza, F., Sheverdyaeva, P. M., Liu, R., Kundu, A. K., Moras, P., Ebrahimi, M., Gallagher, M. C., Rosei, F., Perepichka, D. F. & Contini, G. Synthesis of mesoscale ordered two-dimensional π-conjugated polymers with semiconducting properties. *Nat. Mater.* **19,** 874–880 (2020).

159. Lindner, N. H., Refael, G. & Galitski, V. Floquet topological insulator in semiconductor quantum wells. *Nat. Phys.* **7,** 490–495 (2011).

160. Ming, Y., Chen, P., Ji, W., Wei, B., Lee, C., Lin, T., Hu, W. & Lu, Y. Tailoring the photon spin via light–matter interaction in liquid-crystal-based twisting structures. *Npj Quantum Mater.* **2,** 1–6 (2017).

161. Krappe, U., Stadler, R. & Voigt-Martin, I. Chiral Assembly in Amorphous ABC Triblock Copolymers. Formation of a Helical Morphology in Polystyrene-block-polybutadiene-block-poly(methyl methacrylate) Block Copolymers. *Macromolecules* **28,** 4558–4561 (1995).

162. Wang, H.-F., Yang, K.-C., Hsu, W.-C., Lee, J.-Y., Hsu, J.-T., Grason, G. M., Thomas, E. L., Tsai, J.-C. & Ho, R.-M. Generalizing the effects of chirality on block copolymer assembly. *Proc. Natl. Acad. Sci.* **116,** 4080–4089 (2019).

163. Nielsen, H. B. & Ninomiya, M. The Adler-Bell-Jackiw anomaly and Weyl fermions in a crystal. *Phys. Lett. B* **130,** 389–396 (1983).

164. Armitage, N. P., Mele, E. J. & Vishwanath, A. Weyl and Dirac semimetals in three-dimensional solids. *Rev. Mod. Phys.* **90,** 015001 (2018).

165. Wan, X., Turner, A. M., Vishwanath, A. & Savrasov, S. Y. Topological semimetal and Fermi-arc surface states in the electronic structure of pyrochlore iridates. *Phys. Rev. B* **83,** 205101 (2011).

166. Lu, L., Wang, Z., Ye, D., Ran, L., Fu, L., Joannopoulos, J. D. & Soljačić, M. Experimental observation of Weyl points. *Science* **349,** 622–624 (2015).

167. Fruchart, M., Jeon, S.-Y., Hur, K., Cheianov, V., Wiesner, U. & Vitelli, V. Soft self-assembly of Weyl materials for light and sound. *Proc. Natl. Acad. Sci.* **115,** E3655–E3664 (2018).

168. Epps, T. H., Cochran, E. W., Hardy, C. M., Bailey, T. S., Waletzko, R. S. & Bates, F. S. Network Phases in ABC Triblock Copolymers. *Macromolecules* **37,** 7085–7088 (2004).

169. Yu, F., Zhang, Q., Thedford, R. P., Singer, A., Smilgies, D.-M., Thompson, M. O. & Wiesner, U. B. Block Copolymer Self-Assembly-Directed and Transient Laser Heating-Enabled Nanostructures toward Phononic and Photonic Quantum Materials. *ACS Nano* **14,** 11273–11282 (2020).

170. Berry, M. V. Physics of Nonhermitian Degeneracies. *Czechoslov. J. Phys.* **54,** 1039–1047 (2004).

171. Zhen, B., Hsu, C. W., Igarashi, Y., Lu, L., Kaminer, I., Pick, A., Chua, S.-L., Joannopoulos, J. D. & Soljačić, M. Spawning rings of exceptional points out of Dirac cones. *Nature* **525,** 354–358 (2015).

172. Xu, Y., Wang, S.-T. & Duan, L.-M. Weyl Exceptional Rings in a Three-Dimensional Dissipative Cold Atomic Gas. *Phys. Rev. Lett.* **118,** 045701 (2017).

173. Hodaei, H., Hassan, A. U., Wittek, S., Garcia-Gracia, H., El-Ganainy, R., Christodoulides, D. N. & Khajavikhan, M. Enhanced sensitivity at higher-order exceptional points. *Nature* **548,** 187–191 (2017).

174. Chen, W., Kaya Özdemir, Ş., Zhao, G., Wiersig, J. & Yang, L. Exceptional points enhance sensing in an optical microcavity. *Nature* **548,** 192–196 (2017).

175. Zhong, Q., Ren, J., Khajavikhan, M., Christodoulides, D. N., Özdemir, Ş. K. & El-Ganainy, R. Sensing with Exceptional Surfaces in Order to Combine Sensitivity with Robustness. *Phys. Rev. Lett.* **122,** 153902 (2019).

176. Doppler, J., Mailybaev, A. A., Böhm, J., Kuhl, U., Girschik, A., Libisch, F., Milburn, T. J., Rabl, P., Moiseyev, N. & Rotter, S. Dynamically encircling an exceptional point for asymmetric mode switching. *Nature* **537,** 76–79 (2016).

177. Xu, H., Mason, D., Jiang, L. & Harris, J. G. E. Topological energy transfer in an optomechanical system with exceptional points. *Nature* **537,** 80–83 (2016).

178. Khurgin, J. B., Sebbag, Y., Edrei, E., Zektzer, R., Shastri, K., Levy, U. & Monticone, F. Emulating exceptional-point encirclements using imperfect (leaky) photonic components: asymmetric mode-switching and omni-polarizer action. *Optica* **8,** 563 (2021).

179. Shastri, K. & Monticone, F. Dissipation-induced topological transitions in continuous Weyl materials. *Phys. Rev. Res.* **2,** 033065 (2020).

180. Agarwala, A. & Shenoy, V. B. Topological Insulators in Amorphous Systems. *Phys. Rev. Lett.* **118,** 236402 (2017).

181. Zhou, P., Liu, G.-G., Ren, X., Yang, Y., Xue, H., Bi, L., Deng, L., Chong, Y. & Zhang, B. Photonic amorphous topological insulator. *Light Sci. Appl.* **9,** 133 (2020).

182. Costa, M., Schleder, G. R., Buongiorno Nardelli, M., Lewenkopf, C. & Fazzio, A. Toward Realistic Amorphous Topological Insulators. *Nano Lett.* **19,** 8941–8946 (2019).

183. Wang, Z. F., Liu, Z. & Liu, F. Organic topological insulators in organometallic lattices. *Nat. Commun.* **4,** 1471 (2013).

184. Jain, P., Stroppa, A., Nabok, D., Marino, A., Rubano, A., Paparo, D., Matsubara, M., Nakotte, H., Fiebig, M., Picozzi, S., Choi, E. S., Cheetham, A. K., Draxl, C., Dalal, N. S. & Zapf, V. S. Switchable electric polarization and ferroelectric domains in a metal-organic-framework. *Npj Quantum Mater.* **1,** 16012 (2016).

185. Wei, L., Zhang, X. & Zhao, M. Spin-polarized Dirac cones and topological nontriviality in a metal–organic framework Ni2C24S6H12. *Phys. Chem. Chem. Phys.* **18,** 8059–8064 (2016).

186. Jiang, W., Zhang, S., Wang, Z., Liu, F. & Low, T. Topological Band Engineering of Lieb Lattice in Phthalocyanine-Based Metal–Organic Frameworks. *Nano Lett.* **20,** 1959–1966 (2020).

187. Wang, Y., Liu, Y. & Wang, B. Effects of light on quantum phases and topological properties of two-dimensional Metal-organic frameworks. *Sci. Rep.* **7,** 41644 (2017).

188. Bader, S. D. *Colloquium* : Opportunities in nanomagnetism. *Rev. Mod. Phys.* **78,** 1–15 (2006).

189. Hill, N. A. Why Are There so Few Magnetic Ferroelectrics? *J. Phys. Chem. B* **104,** 6694–6709 (2000).

190. Comes, R., Liu, H., Khokhlov, M., Kasica, R., Lu, J. & Wolf, S. A. Directed Self-Assembly of Epitaxial $CoFe_2O_4$–$BiFeO_3$ Multiferroic Nanocomposites. *Nano Lett.* **12,** 2367–2373 (2012).

191. Ren, S., Briber, R. M. & Wuttig, M. Diblock copolymer based self-assembled nanomagnetoelectric. *Appl. Phys. Lett.* **93,** 173507 (2008).

192. Terzić, I., Meereboer, N. L., Mellema, H. H. & Loos, K. Polymer-based multiferroic nanocomposites *via* directed block copolymer self-assembly. *J. Mater. Chem. C* **7,** 968–976 (2019).

193. Lohrman, J., Liu, Y., Duan, S., Zhao, X., Wuttig, M. & Ren, S. All Conjugated Copolymer Excitonic Multiferroics. *Adv. Mater.* **25,** 783–787 (2013).

194. Xu, J., Berg, A. I., Noheda, B. & Loos, K. Progress and perspective on polymer templating of multifunctional oxide nanostructures. *J. Appl. Phys.* **128,** 190903 (2020).

195. Sreenivasulu, G., Lochbiler, T. A., Panda, M., Srinivasan, G. & Chavez, F. A. Self-assembly of multiferroic core-shell particulate nanocomposites through

DNA-DNA hybridization and magnetic field directed assembly of superstructures. *AIP Adv.* **6,** 045202 (2016).

196. Jain, P., Ramachandran, V., Clark, R. J., Zhou, H. D., Toby, B. H., Dalal, N. S., Kroto, H. W. & Cheetham, A. K. Multiferroic Behavior Associated with an Order−Disorder Hydrogen Bonding Transition in Metal−Organic Frameworks (MOFs) with the Perovskite ABX $_3$ Architecture. *J. Am. Chem. Soc.* **131,** 13625–13627 (2009).
197. Jain, P., Stroppa, A., Nabok, D., Marino, A., Rubano, A., Paparo, D., Matsubara, M., Nakotte, H., Fiebig, M., Picozzi, S., Choi, E. S., Cheetham, A. K., Draxl, C., Dalal, N. S. & Zapf, V. S. Switchable electric polarization and ferroelectric domains in a metal-organic-framework. *Npj Quantum Mater.* **1,** 16012 (2016).
198. Ma, Y. & Sun, Y. Multiferroic and thermal expansion properties of metal-organic frameworks. *J. Appl. Phys.* **127,** 080901 (2020).
199. Cui, H., Wang, Z., Takahashi, K., Okano, Y., Kobayashi, H. & Kobayashi, A. Ferroelectric Porous Molecular Crystal, [Mn $_3$ (HCOO) $_6$](C $_2$ H $_5$ OH), Exhibiting Ferrimagnetic Transition. *J. Am. Chem. Soc.* **128,** 15074–15075 (2006).
200. Nisoli, C., Moessner, R. & Schiffer, P. *Colloquium* : Artificial spin ice: Designing and imaging magnetic frustration. *Rev. Mod. Phys.* **85,** 1473–1490 (2013).
201. Skjærvø, S. H., Marrows, C. H., Stamps, R. L. & Heyderman, L. J. Advances in artificial spin ice. *Nat. Rev. Phys.* **2,** 13–28 (2020).

202. Mistonov, A. A., Grigoryeva, N. A., Chumakova, A. V., Eckerlebe, H., Sapoletova, N. A., Napolskii, K. S., Eliseev, A. A., Menzel, D. & Grigoriev, S. V. Three-dimensional artificial spin ice in nanostructured Co on an inverse opal-like lattice. *Phys. Rev. B* **87,** 220408 (2013).

203. Ortiz-Ambriz, A. & Tierno, P. Engineering of frustration in colloidal artificial ices realized on microfeatured grooved lattices. *Nat. Commun.* **7,** 10575 (2016).

204. Shishkin, I. S., Mistonov, A. A., Dubitskiy, I. S., Grigoryeva, N. A., Menzel, D. & Grigoriev, S. V. Nonlinear geometric scaling of coercivity in a three-dimensional nanoscale analog of spin ice. *Phys. Rev. B* **94,** 064424 (2016).

205. Zwolak, M. & Di Ventra, M. DNA spintronics. *Appl. Phys. Lett.* **81,** 925–927 (2002).

206. Mistonov, A. A., Dubitskiy, I. S., Shishkin, I. S., Grigoryeva, N. A., Heinemann, A., Sapoletova, N. A., Valkovskiy, G. A. & Grigoriev, S. V. Magnetic structure of the inverse opal-like structures: Small angle neutron diffraction and micromagnetic simulations. *J. Magn. Magn. Mater.* **477,** 99–108 (2019).

207. Eagleton, T. S. & Searson, P. C. Electrochemical Synthesis of 3D Ordered Ferromagnetic Nickel Replicas Using Self-Assembled Colloidal Crystal Templates. *Chem. Mater.* **16,** 5027–5032 (2004).

208. Llandro, J., Love, D. M., Kovács, A., Caron, J., Vyas, K. N., Kákay, A., Salikhov, R., Lenz, K., Fassbender, J., Scherer, M. R. J., Cimorra, C., Steiner, U., Barnes, C. H. W., Dunin-Borkowski, R. E., Fukami, S. & Ohno, H. Visualizing Magnetic Structure in 3D Nanoscale Ni–Fe Gyroid Networks. *Nano Lett.* **20,** 3642–3650 (2020).

209. Wolf, S. A. Spintronics: A Spin-Based Electronics Vision for the Future. *Science* **294,** 1488–1495 (2001).

210. Bader, S. D. & Parkin, S. S. P. Spintronics. *Annu. Rev. Condens. Matter Phys.* **1,** 71–88 (2010).

211. Ramin Moayed, M. M., Bielewicz, T., Zöllner, M. S., Herrmann, C. & Klinke, C. Towards colloidal spintronics through Rashba spin-orbit interaction in lead sulphide nanosheets. *Nat. Commun.* **8,** 15721 (2017).

212. Chakravarty, C., Mandal, B. & Sarkar, P. Bis(dithioline)-Based Metal–Organic Frameworks with Superior Electronic and Magnetic Properties: Spin Frustration to Spintronics and Gas Sensing. *J. Phys. Chem. C* **120,** 28307–28319 (2016).

213. Song, X., Wang, X., Li, Y., Zheng, C., Zhang, B., Di, C., Li, F., Jin, C., Mi, W., Chen, L. & Hu, W. 2D Semiconducting Metal–Organic Framework Thin Films for Organic Spin Valves. *Angew. Chem. Int. Ed.* **59,** 1118–1123 (2020).

214. Manuguri, S., Heijden, N. J., Nam, S. J., Narasimhan, B. N., Wei, B., Cabero Z., M. A., Yu, H., Granville, S., McGillivray, D. J., Brothers, P. J., Williams, D. E. & Malmström, J. Polymer Micelle Directed Magnetic Cargo Assemblies Towards Spin-wave Manipulation. *Adv. Mater. Interfaces* **8,** 2100455 (2021).

215. Israelachvili, J. N. *Intermolecular and surface forces*. (Academic press, 2011).

216. Chaikin, P. M. & Lubensky, T. C. *Principles of condensed matter physics*. (Cambridge University Press, 2013).

217. Wan, Y. & Zhao, Dongyuan. On the Controllable Soft-Templating Approach to Mesoporous Silicates. *Chem. Rev.* **107,** 2821–2860 (2007).

218. Thurn-Albrecht, T., Schotter, J., Kastle, G. A., Emley, N., Shibauchi, T., Krusin-Elbaum, L., Guarini, K., Black, C. T., Tuominen, M. T. & Russell, T. P. Ultrahigh-Density Nanowire Arrays Grown in Self-Assembled Diblock Copolymer Templates. *Science* **290,** 2126–2129 (2000).

219. Li, C., Li, Q., Kaneti, Y. V., Hou, D., Yamauchi, Y. & Mai, Y. Self-assembly of block copolymers towards mesoporous materials for energy storage and conversion systems. *Chem. Soc. Rev.* **49,** 4681–4736 (2020).

220. Ryoo, R., Joo, S. H. & Jun, S. Synthesis of Highly Ordered Carbon Molecular Sieves via Template-Mediated Structural Transformation. *J. Phys. Chem. B* **103,** 7743–7746 (1999).

221. Wang, C., Wang, Z. & Zhang, X. Amphiphilic Building Blocks for Self-Assembly: From Amphiphiles to Supra-amphiphiles. *Acc. Chem. Res.* **45,** 608–618 (2012).

222. Aida, T., Meijer, E. W. & Stupp, S. I. Functional Supramolecular Polymers. *Science* **335,** 813–817 (2012).

223. Palmer, L. C. & Stupp, S. I. Molecular Self-Assembly into One-Dimensional Nanostructures. *Acc. Chem. Res.* **41,** 1674–1684 (2008).

224. Chandrasekhar, S. *Liquid Crystals*. (Cambridge University Press, 2010).

225. Gruner, S. M. Stability of lyotropic phases with curved interfaces. *J. Phys. Chem.* **93,** 7562–7570 (1989).

226. Huo, Q., Margolese, D. I. & Stucky, G. D. Surfactant Control of Phases in the Synthesis of Mesoporous Silica-Based Materials. *Chem. Mater.* **8,** 1147–1160 (1996).

227. Coles, H. J. & Pivnenko, M. N. Liquid crystal 'blue phases' with a wide temperature range. *Nature* **436,** 997–1000 (2005).

228. Kikuchi, H., Yokota, M., Hisakado, Y., Yang, H. & Kajiyama, T. Polymer-stabilized liquid crystal blue phases. *Nat. Mater.* **1,** 64–68 (2002).

229. Pieraccini, S., Masiero, S., Ferrarini, A. & Piero Spada, G. Chirality transfer across length-scales in nematic liquid crystals: fundamentals and applications. *Chem Soc Rev* **40,** 258–271 (2011).

230. Lodge, T. & Hiemenz, P. C. *Polymer chemistry*. (CRC Press, 2020).

231. Floudas, G., Vazaiou, B., Schipper, F., Ulrich, R., Wiesner, U., Iatrou, H. & Hadjichristidis, N. Poly(ethylene oxide- *b* -isoprene) Diblock Copolymer Phase Diagram. *Macromolecules* **34,** 2947–2957 (2001).

232. Hajduk, D. A., Harper, P. E., Gruner, S. M., Honeker, C. C., Kim, G., Thomas, E. L. & Fetters, L. J. The Gyroid: A New Equilibrium Morphology in Weakly Segregated Diblock Copolymers. *Macromolecules* **27,** 4063–4075 (1994).

233. Matsen, M. W. & Bates, F. S. Unifying Weak- and Strong-Segregation Block Copolymer Theories. *Macromolecules* **29,** 1091–1098 (1996).

234. Matsushita, Y., Choshi, H., Fujimoto, T. & Nagasawa, M. Preparation and Morphological Properties of a Triblock Copolymer of the ABC Type. *Macromolecules* **13,** 1053–1058 (1980).

235. Stadler, R., Auschra, C., Beckmann, J., Krappe, U., Voight-Martin, I. & Leibler, L. Morphology and Thermodynamics of Symmetric Poly(A-block-B-block-C) Triblock Copolymers. *Macromolecules* **28,** 3080–3097 (1995).

236. Chatterjee, J., Jain, S. & Bates, F. S. Comprehensive Phase Behavior of Poly(isoprene- *b* -styrene- *b* -ethylene oxide) Triblock Copolymers. *Macromolecules* **40,** 2882–2896 (2007).

237. Bates, F. S., Hillmyer, M. A., Lodge, T. P., Bates, C. M., Delaney, K. T. & Fredrickson, G. H. Multiblock Polymers: Panacea or Pandora's Box? *Science* **336,** 434–440 (2012).

238. Hoheisel, T. N., Hur, K. & Wiesner, U. B. Block copolymer-nanoparticle hybrid self-assembly. *Prog. Polym. Sci.* **40,** 3–32 (2015).

239. Warren, S. C., DiSalvo, F. J. & Wiesner, U. Nanoparticle-tuned assembly and disassembly of mesostructured silica hybrids. *Nat. Mater.* **6,** 156–161 (2007).

240. Simon, P. F. W., Ulrich, R., Spiess, H. W. & Wiesner, U. Block Copolymer−Ceramic Hybrid Materials from Organically Modified Ceramic Precursors. *Chem. Mater.* **13,** 3464–3486 (2001).

241. Garcia, B. C., Kamperman, M., Ulrich, R., Jain, A., Gruner, S. M. & Wiesner, U. Morphology Diagram of a Diblock Copolymer−Aluminosilicate Nanoparticle System. *Chem. Mater.* **21,** 5397–5405 (2009).

242. Cowman, C. D., Padgett, E., Tan, K. W., Hovden, R., Gu, Y., Andrejevic, N., Muller, D., Coates, G. W. & Wiesner, U. Multicomponent Nanomaterials with Complex Networked Architectures from Orthogonal Degradation and Binary Metal Backfilling in ABC Triblock Terpolymers. *J. Am. Chem. Soc.* **137,** 6026–6033 (2015).

243. Arora, H., Du, P., Tan, K. W., Hyun, J. K., Grazul, J., Xin, H. L., Muller, D. A., Thompson, M. O. & Wiesner, U. Block Copolymer Self-Assembly–Directed

Single-Crystal Homo- and Heteroepitaxial Nanostructures. *Science* **330,** 214–219 (2010).

244. Li, F., Josephson, D. P. & Stein, A. Colloidal Assembly: The Road from Particles to Colloidal Molecules and Crystals. *Angew. Chem. Int. Ed.* **50,** 360–388 (2011).
245. Xia, Y., Gates, B., Yin, Y. & Lu, Y. Monodispersed Colloidal Spheres: Old Materials with New Applications. *Adv. Mater.* **12,** 693–713 (2000).
246. Bartlett, P. & Campbell, A. I. Three-Dimensional Binary Superlattices of Oppositely Charged Colloids. *Phys. Rev. Lett.* **95,** 128302 (2005).
247. Shevchenko, E. V., Talapin, D. V., Kotov, N. A., O'Brien, S. & Murray, C. B. Structural diversity in binary nanoparticle superlattices. *Nature* **439,** 55–59 (2006).
248. Grzelczak, M., Vermant, J., Furst, E. M. & Liz-Marzán, L. M. Directed Self-Assembly of Nanoparticles. *ACS Nano* **4,** 3591–3605 (2010).
249. Mirkin, C. A., Letsinger, R. L., Mucic, R. C. & Storhoff, J. J. A DNA-based method for rationally assembling nanoparticles into macroscopic materials. *Nature* **382,** 607–609 (1996).
250. Park, S. Y., Lytton-Jean, A. K. R., Lee, B., Weigand, S., Schatz, G. C. & Mirkin, C. A. DNA-programmable nanoparticle crystallization. *Nature* **451,** 553–556 (2008).
251. Boles, M. A., Engel, M. & Talapin, D. V. Self-Assembly of Colloidal Nanocrystals: From Intricate Structures to Functional Materials. *Chem. Rev.* **116,** 11220–11289 (2016).

252. Murray, C. B., Kagan, C. R. & Bawendi, M. G. Synthesis and Characterization of Monodisperse Nanocrystals and Close-Packed Nanocrystal Assemblies. *Annu. Rev. Mater. Sci.* **30,** 545–610 (2000).

253. Glotzer, S. C. & Solomon, M. J. Anisotropy of building blocks and their assembly into complex structures. *Nat. Mater.* **6,** 557–562 (2007).

254. Burda, C., Chen, X., Narayanan, R. & El-Sayed, M. A. Chemistry and Properties of Nanocrystals of Different Shapes. *Chem. Rev.* **105,** 1025–1102 (2005).

255. Sun, Y. Shape-Controlled Synthesis of Gold and Silver Nanoparticles. *Science* **298,** 2176–2179 (2002).

256. Damasceno, P. F., Engel, M. & Glotzer, S. C. Predictive Self-Assembly of Polyhedra into Complex Structures. *Science* **337,** 453–457 (2012).

257. Imhof, A. & Pine, D. J. Ordered macroporous materials by emulsion templating. *Nature* **389,** 948–951 (1997).

258. van Blaaderen, A., Ruel, R. & Wiltzius, P. Template-directed colloidal crystallization. *Nature* **385,** 321–324 (1997).

259. Jiang, P. A Lost-Wax Approach to Monodisperse Colloids and Their Crystals. *Science* **291,** 453–457 (2001).

260. Leunissen, M. E., Christova, C. G., Hynninen, A.-P., Royall, C. P., Campbell, A. I., Imhof, A., Dijkstra, M., van Roij, R. & van Blaaderen, A. Ionic colloidal crystals of oppositely charged particles. *Nature* **437,** 235–240 (2005).

261. Chen, Q., Bae, S. C. & Granick, S. Directed self-assembly of a colloidal kagome lattice. *Nature* **469,** 381–384 (2011).

262. He, M., Gales, J. P., Ducrot, É., Gong, Z., Yi, G.-R., Sacanna, S. & Pine, D. J. Colloidal diamond. *Nature* **585,** 524–529 (2020).

263. Love, J. C., Estroff, L. A., Kriebel, J. K., Nuzzo, R. G. & Whitesides, G. M. Self-Assembled Monolayers of Thiolates on Metals as a Form of Nanotechnology. *Chem. Rev.* **105,** 1103–1170 (2005).

264. Kumar, A., Biebuyck, H. A. & Whitesides, G. M. Patterning Self-Assembled Monolayers: Applications in Materials Science. *Langmuir* **10,** 1498–1511 (1994).

265. Aizenberg, J., Black, A. J. & Whitesides, G. M. Control of crystal nucleation by patterned self-assembled monolayers. *Nature* **398,** 495–498 (1999).

266. Aizenberg, J. Direct Fabrication of Large Micropatterned Single Crystals. *Science* **299,** 1205–1208 (2003).

267. Shekhah, O., Liu, J., Fischer, R. A. & Wöll, Ch. MOF thin films: existing and future applications. *Chem. Soc. Rev.* **40,** 1081 (2011).

268. James, S. L. Metal-organic frameworks. *Chem. Soc. Rev.* **32,** 276 (2003).

269. Diercks, C. S. & Yaghi, O. M. The atom, the molecule, and the covalent organic framework. *Science* **355,** eaal1585 (2017).

270. Seeman, N. C. Nucleic acid junctions and lattices. *J. Theor. Biol.* **99,** 237–247 (1982).

271. Nangreave, J., Han, D., Liu, Y. & Yan, H. DNA origami: a history and current perspective. *Curr. Opin. Chem. Biol.* **14,** 608–615 (2010).

272. Rothemund, P. W. K. Folding DNA to create nanoscale shapes and patterns. *Nature* **440,** 297–302 (2006).

273. Nykypanchuk, D., Maye, M. M., van der Lelie, D. & Gang, O. DNA-guided crystallization of colloidal nanoparticles. *Nature* **451,** 549–552 (2008).

274. Macfarlane, R. J., Lee, B., Jones, M. R., Harris, N., Schatz, G. C. & Mirkin, C. A. Nanoparticle Superlattice Engineering with DNA. *Science* **334,** 204–208 (2011).

275. Douglas, S. M., Marblestone, A. H., Teerapittayanon, S., Vazquez, A., Church, G. M. & Shih, W. M. Rapid prototyping of 3D DNA-origami shapes with caDNAno. *Nucleic Acids Res.* **37,** 5001–5006 (2009).

276. Graser, S., Hirschfeld, P. J., Kopp, T., Gutser, R., Andersen, B. M. & Mannhart, J. How grain boundaries limit supercurrents in high-temperature superconductors. *Nat. Phys.* **6,** 609–614 (2010).

277. Feng, X., Guo, H. & Thomas, E. L. Topological defects in tubular network block copolymers. *Polymer* **168,** 44–52 (2019).

278. Susca, E. M., Beaucage, P. A., Thedford, R. P., Singer, A., Gruner, S. M., Estroff, L. A. & Wiesner, U. Preparation of Macroscopic Block-Copolymer-Based Gyroidal Mesoscale Single Crystals by Solvent Evaporation. *Adv. Mater.* **31,** 1902565 (2019).

279. Novoselov, K. S., Jiang, D., Schedin, F., Booth, T. J., Khotkevich, V. V., Morozov, S. V. & Geim, A. K. Two-dimensional atomic crystals. *Proc. Natl. Acad. Sci.* **102,** 10451–10453 (2005).

280. Reyren, N., Thiel, S., Caviglia, A. D., Kourkoutis, L. F., Hammerl, G., Richter, C., Schneider, C. W., Kopp, T., Ruetschi, A.-S., Jaccard, D., Gabay, M., Muller,

D. A., Triscone, J.-M. & Mannhart, J. Superconducting Interfaces Between Insulating Oxides. *Science* **317,** 1196–1199 (2007).

281. Ruiz, R., Kang, H., Detcheverry, F. A., Dobisz, E., Kercher, D. S., Albrecht, T. R., de Pablo, J. J. & Nealey, P. F. Density Multiplication and Improved Lithography by Directed Block Copolymer Assembly. *Science* **321,** 936–939 (2008).
282. Sai, H., Tan, K. W., Hur, K., Asenath-Smith, E., Hovden, R., Jiang, Y., Riccio, M., Muller, D. A., Elser, V., Estroff, L. A., Gruner, S. M. & Wiesner, U. Hierarchical Porous Polymer Scaffolds from Block Copolymers. *Science* **341,** 530–534 (2013).
283. DeSimone, J. What if 3D printing was 100x faster? *TED Conf.* **March 2015,**
284. Novoselov, K. S. Electric Field Effect in Atomically Thin Carbon Films. *Science* **306,** 666–669 (2004).
285. Butler, S. Z., Hollen, S. M., Cao, L., Cui, Y., Gupta, J. A., Gutiérrez, H. R., Heinz, T. F., Hong, S. S., Huang, J., Ismach, A. F., Johnston-Halperin, E., Kuno, M., Plashnitsa, V. V., Robinson, R. D., Ruoff, R. S., Salahuddin, S., Shan, J., Shi, L., Spencer, M. G., Terrones, M., Windl, W. & Goldberger, J. E. Progress, Challenges, and Opportunities in Two-Dimensional Materials Beyond Graphene. *ACS Nano* **7,** 2898–2926 (2013).
286. Manzeli, S., Ovchinnikov, D., Pasquier, D., Yazyev, O. V. & Kis, A. 2D transition metal dichalcogenides. *Nat. Rev. Mater.* **2,** 17033 (2017).
287. Novoselov, K. S., Mishchenko, A., Carvalho, A. & Castro Neto, A. H. 2D materials and van der Waals heterostructures. *Science* **353,** aac9439 (2016).

288. Chen, X., Fan, X., Li, L., Zhang, N., Niu, Z., Guo, T., Xu, S., Xu, H., Wang, D., Zhang, H., McLeod, A. S., Luo, Z., Lu, Q., Millis, A. J., Basov, D. N., Liu, M. & Zeng, C. Moiré engineering of electronic phenomena in correlated oxides. *Nat. Phys.* **16,** 631–635 (2020).

289. Tran, K., Moody, G., Wu, F., Lu, X., Choi, J., Kim, K., Rai, A., Sanchez, D. A., Quan, J., Singh, A., Embley, J., Zepeda, A., Campbell, M., Autry, T., Taniguchi, T., Watanabe, K., Lu, N., Banerjee, S. K., Silverman, K. L., Kim, S., Tutuc, E., Yang, L., MacDonald, A. H. & Li, X. Evidence for moiré excitons in van der Waals heterostructures. *Nature* **567,** 71–75 (2019).

290. Geim, A. K. & Grigorieva, I. V. Van der Waals heterostructures. *Nature* **499,** 419–425 (2013).

291. Liu, Y., Weiss, N. O., Duan, X., Cheng, H.-C., Huang, Y. & Duan, X. Van der Waals heterostructures and devices. *Nat. Rev. Mater.* **1,** 16042 (2016).

292. Jin, E., Asada, M., Xu, Q., Dalapati, S., Addicoat, M. A., Brady, M. A., Xu, H., Nakamura, T., Heine, T., Chen, Q. & Jiang, D. Two-dimensional sp^2 carbon–conjugated covalent organic frameworks. *Science* **357,** 673–676 (2017).

293. Laibinis, P. E., Whitesides, G. M., Allara, D. L., Tao, Y. T., Parikh, A. N. & Nuzzo, R. G. Comparison of the structures and wetting properties of self-assembled monolayers of n-alkanethiols on the coinage metal surfaces, copper, silver, and gold. *J. Am. Chem. Soc.* **113,** 7152–7167 (1991).

294. Mansky, P. Controlling Polymer-Surface Interactions with Random Copolymer Brushes. *Science* **275,** 1458–1460 (1997).

295. Ohtomo, A., Muller, D. A., Grazul, J. L. & Hwang, H. Y. Artificial charge-modulationin atomic-scale perovskite titanate superlattices. *Nature* **419,** 378–380 (2002).

296. Schlom, D. G., Haeni, J. H., Lettieri, J., Theis, C. D., Tian, W., Jiang, J. C. & Pan, X. Q. Oxide nano-engineering using MBE. *Mater. Sci. Eng. B* **87,** 282–291 (2001).

297. Norton, D. P. Synthesis and properties of epitaxial electronic oxide thin-film materials. *Mater. Sci. Eng. R Rep.* **43,** 139–247 (2004).

298. Ohtomo, A. & Hwang, H. Y. A high-mobility electron gas at the LaAlO3/SrTiO3 heterointerface. *Nature* **427,** 423–426 (2004).

299. Wang, J. Epitaxial BiFeO3 Multiferroic Thin Film Heterostructures. *Science* **299,** 1719–1722 (2003).

300. Mannhart, J. & Schlom, D. G. Oxide Interfaces—An Opportunity for Electronics. *Science* **327,** 1607–1611 (2010).

301. Brinker, C. J., Frye, G. C., Hurd, A. J. & Ashley, C. S. Fundamentals of sol-gel dip coating. *Thin Solid Films* **201,** 97–108 (1991).

302. Huang, E., Pruzinsky, S., Russell, T. P., Mays, J. & Hawker, C. J. Neutrality Conditions for Block Copolymer Systems on Random Copolymer Brush Surfaces. *Macromolecules* **32,** 5299–5303 (1999).

303. Ouk Kim, S., Solak, H. H., Stoykovich, M. P., Ferrier, N. J., de Pablo, J. J. & Nealey, P. F. Epitaxial self-assembly of block copolymers on lithographically defined nanopatterned substrates. *Nature* **424,** 411–414 (2003).

304. Bita, I., Yang, J. K. W., Jung, Y. S., Ross, C. A., Thomas, E. L. & Berggren, K. K. Graphoepitaxy of Self-Assembled Block Copolymers on Two-Dimensional Periodic Patterned Templates. *Science* **321,** 939–943 (2008).

305. Segalman, R. A., Yokoyama, H. & Kramer, E. J. Graphoepitaxy of Spherical Domain Block Copolymer Films. *Adv. Mater.* **13,** 1152–1155 (2001).

306. Rahman, A., Majewski, P. W., Doerk, G., Black, C. T. & Yager, K. G. Non-native three-dimensional block copolymer morphologies. *Nat. Commun.* **7,** 13988 (2016).

307. Majewski, P. W., Rahman, A., Black, C. T. & Yager, K. G. Arbitrary lattice symmetries via block copolymer nanomeshes. *Nat. Commun.* **6,** 7448 (2015).

308. Tavakkoli K. G., A., Gotrik, K. W., Hannon, A. F., Alexander-Katz, A., Ross, C. A. & Berggren, K. K. Templating Three-Dimensional Self-Assembled Structures in Bilayer Block Copolymer Films. *Science* **336,** 1294–1298 (2012).

309. Sinturel, C., Vayer, M., Morris, M. & Hillmyer, M. A. Solvent Vapor Annealing of Block Polymer Thin Films. *Macromolecules* **46,** 5399–5415 (2013).

310. Chavis, M. A., Smilgies, D.-M., Wiesner, U. B. & Ober, C. K. Widely Tunable Morphologies in Block Copolymer Thin Films Through Solvent Vapor Annealing Using Mixtures of Selective Solvents. *Adv. Funct. Mater.* **25,** 3057–3065 (2015).

311. Zhang, Q., Matsuoka, F., Suh, H. S., Beaucage, P. A., Xiong, S., Smilgies, D.-M., Tan, K. W., Werner, J. G., Nealey, P. F. & Wiesner, U. B. Pathways to Mesoporous Resin/Carbon Thin Films with Alternating Gyroid Morphology. *ACS Nano* **12,** 347–358 (2018).

312. *Springer handbook of crystal growth*. (Springer, 2010).

313. Baker, J. L., Widmer-Cooper, A., Toney, M. F., Geissler, P. L. & Alivisatos, A. P. Device-Scale Perpendicular Alignment of Colloidal Nanorods. *Nano Lett.* **10,** 195–201 (2010).

314. Wiesner, U. Lamellar diblock copolymers under large amplitude oscillatory shear flow: Order and dynamics. *Macromol. Chem. Phys.* **198,** 3319–3352 (1997).

315. Keller, A., Pedemonte, E. & Willmouth, F. M. Macro-lattice from Segregated Amorphous Phases of a Three Block Copolymer. *Nature* **225,** 538–539 (1970).

316. Clark, N. A., Hurd, A. J. & Ackerson, B. J. Single colloidal crystals. *Nature* **281,** 57–60 (1979).

317. Okubo, T. Giant Colloidal Single Crystals of Polystyrene and Silica Spheres in Deionized Suspension. *Langmuir* **10,** 1695–1702 (1994).

318. Zakhidov, A. A. Carbon Structures with Three-Dimensional Periodicity at Optical Wavelengths. *Science* **282,** 897–901 (1998).

319. Park, S., Lee, D. H., Xu, J., Kim, B., Hong, S. W., Jeong, U., Xu, T. & Russell, T. P. Macroscopic 10-Terabit-per-Square-Inch Arrays from Block Copolymers with Lateral Order. *Science* **323,** 1030–1033 (2009).

320. Peinemann, K.-V., Abetz, V. & Simon, P. F. W. Asymmetric superstructure formed in a block copolymer via phase separation. *Nat. Mater.* **6,** 992–996 (2007).

321. Tumbleston, J. R., Shirvanyants, D., Ermoshkin, N., Janusziewicz, R., Johnson, A. R., Kelly, D., Chen, K., Pinschmidt, R., Rolland, J. P., Ermoshkin, A.,

Samulski, E. T. & DeSimone, J. M. Continuous liquid interface production of 3D objects. *Science* **347,** 1349–1352 (2015).

322. Walker, D. A., Hedrick, J. L. & Mirkin, C. A. Rapid, large-volume, thermally controlled 3D printing using a mobile liquid interface. *Science* **366,** 360–364 (2019).

323. Li, J., Song, P., Zhao, J., Vaklinova, K., Zhao, X., Li, Z., Qiu, Z., Wang, Z., Lin, L., Zhao, M., Herng, T. S., Zuo, Y., Jonhson, W., Yu, W., Hai, X., Lyu, P., Xu, H., Yang, H., Chen, C., Pennycook, S. J., Ding, J., Teng, J., Castro Neto, A. H., Novoselov, K. S. & Lu, J. Printable two-dimensional superconducting monolayers. *Nat. Mater.* **20,** 181–187 (2021).

324. Henzie, J., Grünwald, M., Widmer-Cooper, A., Geissler, P. L. & Yang, P. Self-assembly of uniform polyhedral silver nanocrystals into densest packings and exotic superlattices. *Nat. Mater.* **11,** 131–137 (2012).

325. Bates, C. M., Maher, M. J., Janes, D. W., Ellison, C. J. & Willson, C. G. Block Copolymer Lithography. *Macromolecules* **47,** 2–12 (2014).

326. Hatton, B., Mishchenko, L., Davis, S., Sandhage, K. H. & Aizenberg, J. Assembly of large-area, highly ordered, crack-free inverse opal films. *Proc. Natl. Acad. Sci.* **107,** 10354–10359 (2010).

327. Vlasov, Y. A., Bo, X.-Z., Sturm, J. C. & Norris, D. J. On-chip natural assembly of silicon photonic bandgap crystals. *Nature* **414,** 289–293 (2001).

328. Minemawari, H., Yamada, T., Matsui, H., Tsutsumi, J., Haas, S., Chiba, R., Kumai, R. & Hasegawa, T. Inkjet printing of single-crystal films. *Nature* **475,** 364–367 (2011).

329. Tosheva, L. & Valtchev, V. P. Nanozeolites: Synthesis, Crystallization Mechanism, and Applications. *Chem. Mater.* **17,** 2494–2513 (2005).

330. Liu, N., Xie, Y., Liu, G., Sohn, S., Raj, A., Han, G., Wu, B., Cha, J. J., Liu, Z. & Schroers, J. General Nanomolding of Ordered Phases. *Phys. Rev. Lett.* **124,** 036102 (2020).

331. Lim, H. S., Lee, J.-H., Walish, J. J. & Thomas, E. L. Dynamic Swelling of Tunable Full-Color Block Copolymer Photonic Gels *via* Counterion Exchange. *ACS Nano* **6,** 8933–8939 (2012).

332. Li, Y., Themistou, E., Zou, J., Das, B. P., Tsianou, M. & Cheng, C. Facile Synthesis and Visualization of Janus Double-Brush Copolymers. *ACS Macro Lett.* **1,** 52–56 (2012).

333. Kim, K., Schulze, M. W., Arora, A., Lewis, R. M., Hillmyer, M. A., Dorfman, K. D. & Bates, F. S. Thermal processing of diblock copolymer melts mimics metallurgy. *Science* **356,** 520–523 (2017).

334. Li, W., Qiu, F. & Shi, A.-C. Emergence and Stability of Helical Superstructures in ABC Triblock Copolymers. *Macromolecules* **45,** 503–509 (2012).

335. Leniart, A. A., Pula, P., Sitkiewicz, A. & Majewski, P. W. Macroscopic Alignment of Block Copolymers on Silicon Substrates by Laser Annealing. *ACS Nano* **14,** 4805–4815 (2020).

336. Meier, E. J., An, F. A., Dauphin, A., Maffei, M., Massignan, P., Hughes, T. L. & Gadway, B. Observation of the topological Anderson insulator in disordered atomic wires. *Science* **362,** 929–933 (2018).

337. Kohle, F. F. E., Hinckley, J. A., Li, S., Dhawan, N., Katt, W. P., Erstling, J. A., Werner-Zwanziger, U., Zwanziger, J., Cerione, R. A. & Wiesner, U. B. Amorphous Quantum Nanomaterials: Amorphous Quantum Nanomaterials (Adv. Mater. 5/2019). *Adv. Mater.* **31,** 1970034 (2019).

338. Kohle, F. F. E., Hinckley, J. A., Li, S., Dhawan, N., Katt, W. P., Erstling, J. A., Werner-Zwanziger, U., Zwanziger, J., Cerione, R. A. & Wiesner, U. B. Amorphous Quantum Nanomaterials. *Adv. Mater.* **31,** 1806993 (2019).

339. Wang, Z. F., Liu, Z. & Liu, F. Organic topological insulators in organometallic lattices. *Nat. Commun.* **4,** 1471 (2013).

340. Wei, L., Zhang, X. & Zhao, M. Spin-polarized Dirac cones and topological nontriviality in a metal–organic framework $Ni_2C_{24}S_6H_{12}$. *Phys. Chem. Chem. Phys.* **18,** 8059–8064 (2016).

341. Jiang, W., Zhang, S., Wang, Z., Liu, F. & Low, T. Topological Band Engineering of Lieb Lattice in Phthalocyanine-Based Metal–Organic Frameworks. *Nano Lett.* **20,** 1959–1966 (2020).

342. The interface is still the device. *Nat. Mater.* **11,** 91–91 (2012).

343. Ge, J.-F., Liu, Z.-L., Liu, C., Gao, C.-L., Qian, D., Xue, Q.-K., Liu, Y. & Jia, J.-F. Superconductivity above 100 K in single-layer FeSe films on doped SrTiO3. *Nat. Mater.* **14,** 285–289 (2015).

344. Phillips, K. R., England, G. T., Sunny, S., Shirman, E., Shirman, T., Vogel, N. & Aizenberg, J. A colloidoscope of colloid-based porous materials and their uses. *Chem. Soc. Rev.* **45,** 281–322 (2016).

345. Slater, A. G. & Cooper, A. I. Function-led design of new porous materials. *Science* **348,** aaa8075 (2015).

346. Bozovic, I. & Ahn, C. A new frontier for superconductivity. *Nat. Phys.* **10,** 892–895 (2014).

347. Interuniversity Microelectronics Centre. Press Release: Imec demonstrates 24nm pitch lines with single exposure EUV lithography on ASML's NXE:3400B scanner. *Imec-Int* (2020).

348. Pak, M., Crotti, D., Yasin, F., Ercken, M., Halder, S., De Simone, D., Vanelderen, P., Souriau, L., Hody, H. & Sankar Kar, G. LCDU optimization of STT-MRAM 50nm pitch MTJ pillars for process window improvement. in *Extreme Ultrav. EUV Lithogr. X* (ed. Goldberg, K. A.) 22 (SPIE, 2019). doi:10.1117/12.2515023

349. Blachut, G., Sirard, S. M., Maher, M. J., Asano, Y., Someya, Y., Lane, A. P., Durand, W. J., Bates, C. M., Dinhobl, A. M., Gronheid, R., Hymes, D., Ellison, C. J. & Willson, C. G. A Hybrid Chemo-/Grapho-Epitaxial Alignment Strategy for Defect Reduction in Sub-10 nm Directed Self-Assembly of Silicon-Containing Block Copolymers. *Chem. Mater.* **28,** 8951–8961 (2016).

350. Tang, C., Lennon, E. M., Fredrickson, G. H., Kramer, E. J. & Hawker, C. J. Evolution of Block Copolymer Lithography to Highly Ordered Square Arrays. *Science* **322,** 429–432 (2008).

351. Gates, B. D., Xu, Q., Stewart, M., Ryan, D., Willson, C. G. & Whitesides, G. M. New Approaches to Nanofabrication: Molding, Printing, and Other Techniques. *Chem. Rev.* **105,** 1171–1196 (2005).

352. Xia, Y. & Whitesides, G. M. Soft Lithography. *Angew Chem Int Ed* **37,** 550–575 (1998).

353. Segalman, R. A. Patterning with block copolymer thin films. *Mater. Sci. Eng. R Rep.* **48,** 191–226 (2005).

354. *Introduction to microlithography: theory, materials, and processing*. (The Society, 1983).

355. Yu, F., Zhang, Q., Thedford, R. P., Singer, A., Smilgies, D.-M., Thompson, M. O. & Wiesner, U. B. Block Copolymer Self-Assembly-Directed and Transient Laser Heating-Enabled Nanostructures toward Phononic and Photonic Quantum Materials. *ACS Nano* **14,** 11273–11282 (2020).

356. Galeotti, G., De Marchi, F., Hamzehpoor, E., MacLean, O., Rajeswara Rao, M., Chen, Y., Besteiro, L. V., Dettmann, D., Ferrari, L., Frezza, F., Sheverdyaeva, P. M., Liu, R., Kundu, A. K., Moras, P., Ebrahimi, M., Gallagher, M. C., Rosei, F., Perepichka, D. F. & Contini, G. Synthesis of mesoscale ordered two-dimensional π-conjugated polymers with semiconducting properties. *Nat. Mater.* **19,** 874–880 (2020).

357. Tan, K. W. & Wiesner, U. Block Copolymer Self-Assembly Directed Hierarchically Structured Materials from Nonequilibrium Transient Laser Heating. *Macromolecules* **52,** 395–409 (2019).

358. Jung, B., Sha, J., Paredes, F., Chandhok, M., Younkin, T. R., Wiesner, U., Ober, C. K. & Thompson, M. O. Kinetic Rates of Thermal Transformations and Diffusion in Polymer Systems Measured during Sub-millisecond Laser-Induced Heating. *ACS Nano* **6,** 5830–5836 (2012).

359. Narayan, J. & Bhaumik, A. Novel phase of carbon, ferromagnetism, and conversion into diamond. *J. Appl. Phys.* **118,** 215303 (2015).

360. Kido, J., Hongawa, K., Okuyama, K. & Nagai, K. White light-emitting organic electroluminescent devices using the poly(*N* -vinylcarbazole) emitter layer doped with three fluorescent dyes. *Appl. Phys. Lett.* **64,** 815–817 (1994).

361. Tarascon, J.-M. & Armand, M. Issues and challenges facing rechargeable lithium batteries. *Nature* **414,** 359–367 (2001).

362. Shin, M. D., Shukla, S., Chung, Y. H., Beiss, V., Chan, S. K., Ortega-Rivera, O. A., Wirth, D. M., Chen, A., Sack, M., Pokorski, J. K. & Steinmetz, N. F. COVID-19 vaccine development and a potential nanomaterial path forward. *Nat. Nanotechnol.* **15,** 646–655 (2020).

363. Allen, T. M. & Cullis, P. R. Liposomal drug delivery systems: From concept to clinical applications. *Adv. Drug Deliv. Rev.* **65,** 36–48 (2013).

CHAPTER 3

PATTERNABLE MESOPOROUS THIN FILM QUANTUM MATERIALS VIA BLOCK COPOLYMER SELF-ASSEMBLY: AND EMERGENT TECHNOLOGY?‡

Abstract

Recent developments in quantum materials hold promise for revolutionizing energy and information technologies. The use of soft matter self-assembly, *e.g.*, by employing block copolymers (BCPs) as structure directing or templating agents, offers facile pathways towards quantum metamaterials with highly tunable mesostructures *via* scalable solution processing. Here, we report the preparation of patternable mesoporous niobium carbonitride-type thin film superconductors through spin-coating of a hybrid solution containing an amphiphilic BCP swollen by niobia sol precursors and subsequent thermal processing in combination with photolithography. Spin-coated as-made BCP-niobia hybrid thin films on silicon substrates after optional photolithographic definition are heated in air to produce a porous oxide, and subsequently converted in a multistep process to carbonitrides *via* treatment up to high temperatures in reactive gases including ammonia.

---

‡Fei Yu*, R. Paxton Thedford*, Konrad R. Hedderick, Guillaume Freychet, Mikhail Zhernenkov, Lara A. Estroff, Katja C. Nowack, Sol M. Gruner, and Ulrich B. Wiesner**.** *ACS Appl. Mater. Interfaces* **13** (29) 34732–34741 (2021)

Grazing incidence small-angle X-ray scattering suggests the presence of ordered mesostructures in as-made BCP-niobia films without further annealing, consistent with a distorted alternating gyroid morphology that is retained upon thermal treatments. Wide-angle X-ray scattering confirms the synthesis of phase-pure niobium carbonitride nanocrystals with rock-salt lattices within the mesoscale networks. Electrical transport measurements of unpatterned thin films show initial exponential rise in resistivity characteristic of thermal activation in granular systems down to 12.8 K, at which point resistivity drops to zero into a superconducting state. Magnetoresistance measurements determine the superconducting upper critical field to be over 16 T, demonstrating material quality on par with niobium carbonitrides obtained from traditional solid-state synthesis methods. We discuss how such cost-effective and scalable solution-based quantum materials fabrication approaches may be integrated into existing microelectronics processing, promising the emergence of a technology with tremendous academic and industrial potential by combining the capabilities of soft matter self-assembly with quantum materials.

Introduction

Nanomaterials derived from block copolymer (BCP) self-assembly are prized for their unique structures and properties, such as highly tunable morphology and periodicity, diverse form factors, large surface area porosity, biocompatibility, *etc*. They have found use in wide-ranging applications in areas including photonics,[1] separation and purification,[2,3] and energy conversion and storage,[4,5] among others. In particular, due to their periodic self-organization on the mesoscale, with lattice constants typically

of order tens of nanometers, use of BCPs as self-assembling lithographic masks or templates in nanofabrication has been a highly researched area for several decades.[6,7] BCPs have been shown as capable of defining 2D and 3D periodic structures in relevant organic and inorganic materials through the process of structure direction using solution-based approaches like solvent evaporation induced self-assembly.[8,9] Numerous materials classes including transition metal oxides and nitrides, non-oxide ceramics, metals, and semiconductors have been architecturally defined on the nanoscale by BCP self-assembly in this way through methods amenable to traditional semiconductor manufacturing.[10–19]

Beyond mature silicon-based technologies, there is accelerating progress of investigations into quantum materials toward novel devices, *e.g.*, for quantum computing applications.[20] In quantum materials, including superconductors, topological insulators, quantum spin liquids or spin ices, quantum-mechanical effects fundamentally alter macroscopic properties.[21] BCPs have begun making inroads into such areas, demonstrating the convergence of soft matter self-assembly science and hard condensed matter physics, *e.g.*, in the form of mesostructured superconductors synthesized through structure direction or templating strategies.[22–24] These studies have shown how BCP nano/mesostructure definition can lead to emergent quantum metamaterials properties *via* modification of fundamental, quantum-level material characteristics. For example, when indium metal, a type-I superconductor, was confined to the minority networks of a BCP self-assembly directed double gyroid, the nanoscale confinement and periodic mesostructure led to pinning of magnetic vortices on the order of the double gyroid lattice size, resulting in macroscopic type-II superconductor

behavior.[23] Furthermore, when superconducting niobium nitride-type materials were structure directed by BCPs into four different mesostructures, without substantial variation of the XRD-measured atomic lattice parameters they displayed a mesostructure-dependent transition temperature (T_c), *i.e.*, a typical fingerprint of metamaterial behavior.[24] Finally, the use of polymer solution based techniques represents a departure from the stringent conditions, *e.g.*, employing high-vacuum, under which quantum materials are typically fabricated.[25] In contrast, facile and cost-effective polymer solution-based routes to quantum materials, such as spin-coating, blading, or 3D printing, promise access to a plethora of form factors not easily achievable *via* techniques like molecular beam epitaxy (MBE) or pulsed laser deposition (PLD).[26] It is the combination of self-assembly based control of nano-/meso-scale structure and order with solution processing, which defines the scientific as well as technological interest in the emergent area of BCP-derived quantum materials.

To date, however, the investigation of BCP-based synthetic routes to such materials has been largely confined to the bulk regime.[19] In order to be integrated into microelectronics processing and demonstrate accessible routes toward real devices, it is desirable to create thin film analogs of such BCP-derived quantum materials. This study reports the fabrication of BCP self-assembly directed mesoporous niobium carbonitride (NbCN)-type superconducting thin film structures on silicon substrates, using a combination of spin-coating, thermal processing, and lithography. Notably, the solution-based approach can lead to material properties on par with niobium carbonitrides obtained from traditional solid-state synthesis methods. We finally discuss how the demonstrated route to patternable, mesoporous superconducting thin films may

become a cost-effective, highly scalable approach that could be fully integrated into existing semiconductor processing technologies toward device fabrication. As such, this work may help open pathways towards soft matter self-assembly based quantum material research with exceptional academic and industrial promise.

Results and discussion

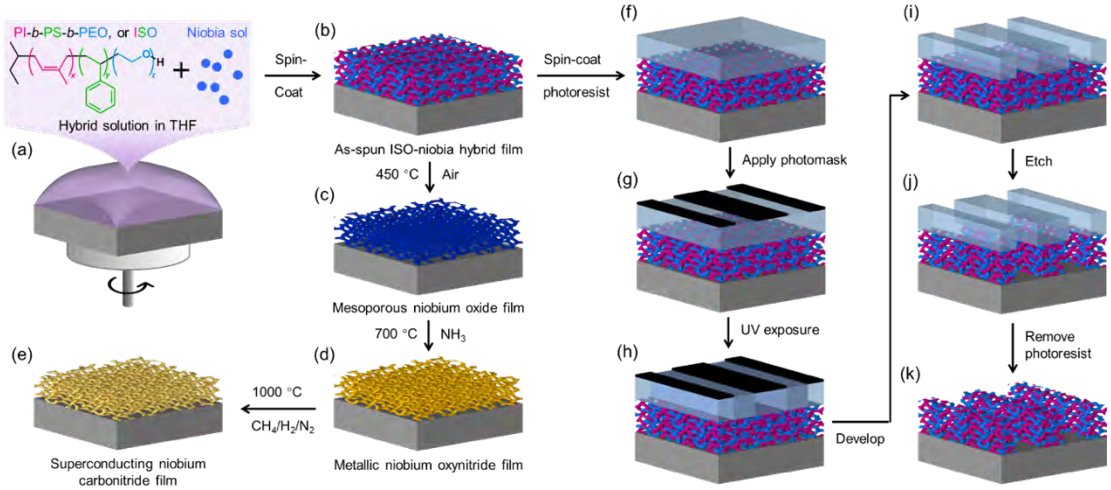

Figure 3.1. *Schematic of solution-based fabrication processes. (a) Triblock terpolymer ISO and precursor niobia sol hybrid solution in THF is spin-coated on a silicon substrate. The sol preferentially mixes with the hydrophilic PEO block: both are depicted in false-coloring as blue. (b) As-spun ISO-niobia hybrid thin film with microphase segregated domains rendered with corresponding colors. The matrix domain of PS block is rendered transparent for illustration only; at this stage the thin film is not porous. (c) Mesoporous niobium oxide thin film after heating in air at 450 °C. (d) Metallic niobium oxynitride thin film after treatment in ammonia (NH_3) at 700 °C. (e) Superconducting niobium carbonitride-type thin film after final treatment in carburizing gas ($CH_4/H_2/N_2$) at 1000 °C. (f) – (k) Photolithography route to prepare patterned thin films that can be further processed along (c) to (e).*

The general solution-based fabrication route toward NbCN-type thin films on silicon substrates is depicted in Figure 3.1, and is based upon past efforts to synthesize similar materials in the bulk (see Experimental Section).[22,24] The structure-directing BCP used in the study is an amphiphilic triblock terpolymer poly(isoprene-*b*-styrene-*b*-ethylene oxide) (PI-*b*-PS-*b*-PEO, referred to as ISO hereafter), synthesized by sequential anionic polymerization according to a method detailed elsewhere.[27] The total number-average molar mass of ISO is 67.7 kg/mol with a polydispersity index of 1.10. The mass fractions of PI, PS, and PEO blocks were determined by ^{1}H nuclear magnetic resonance spectroscopy as 26.0 %, 65.3 %, and 8.7 %, respectively, a composition targeted for achieving the alternating gyroid (G^{A}) morphology.[28] The inorganic niobia sol precursor is prepared in tetrahydrofuran (THF) from the hydrolytic condensation of niobium (V) ethoxide under acidic conditions. Upon mixing the sol solution with a solution of ISO in THF and subsequent spin-coating and solvent evaporation induced self-assembly (Figure 3.1a,b), the niobia sol particles selectively mix with the hydrophilic PEO block of the ISO to form a nanostructured composite thin film.[22]

After spin-coating on a silicon substrate, the ISO-niobia hybrid thin films consist of two interpenetrating minority networks formed by the PI block (Figure 3.1b, magenta) and the PEO block swollen with niobia (Figure 3.1b, blue) embedded in a PS matrix (Figure 3.1b, left transparent). At this stage, as-made composite films are readily patternable through conventional photolithographic means as schematically depicted in Figure 3.1f-k. Using wet or dry etching techniques (Figure 3.5 and Experimental Section) the ISO-niobia thin films can thus be defined into arbitrary areas and shapes,

which are subsequently transformed into superconducting material through further thermal processing. Without any further efforts on post-deposition annealing such as low temperature thermal or solvent vapor annealing (SVA), the hybrid films are treated in air at elevated temperatures up to 450 °C to further condense the niobia and remove the structure directing ISO. Fourier-transform infrared spectroscopy (FTIR) results of as-made and heat-treated samples show the expected disappearance of vibrational bands characteristic of organic components, while thermogravimetric analysis (TGA) documents the associated sample weigh loss (Figure 3.S1). The resulting niobium oxide thin films (Figure 3.1c) show locally ordered mesoporous structures, as evidenced by scanning electron microscopy (SEM, Figure 3.2a). X-ray scattering experiments suggest the morphology of these films is consistent with a deformed G^A structure (*vide infra*; Supplemental Note 3.1 and Figure 3.S2), in which the niobia in the original hybrid film is retained as a single inorganic minority network replicating the PEO plus inorganic domain after the decomposition of polymeric components. To render the thin films electrically conducting, a subsequent nitridation in ammonia (NH_3) is carried out at 700 °C converting the mesoporous oxide into a niobium nitride (NbN, Figure 1d), albeit with some oxygen (and vacancies) likely remaining as discussed in detail in a previous study.[24] The mesostructure appears largely unchanged through this process, with a slight coarsening of the nodes in the network (Figure 3.2b).

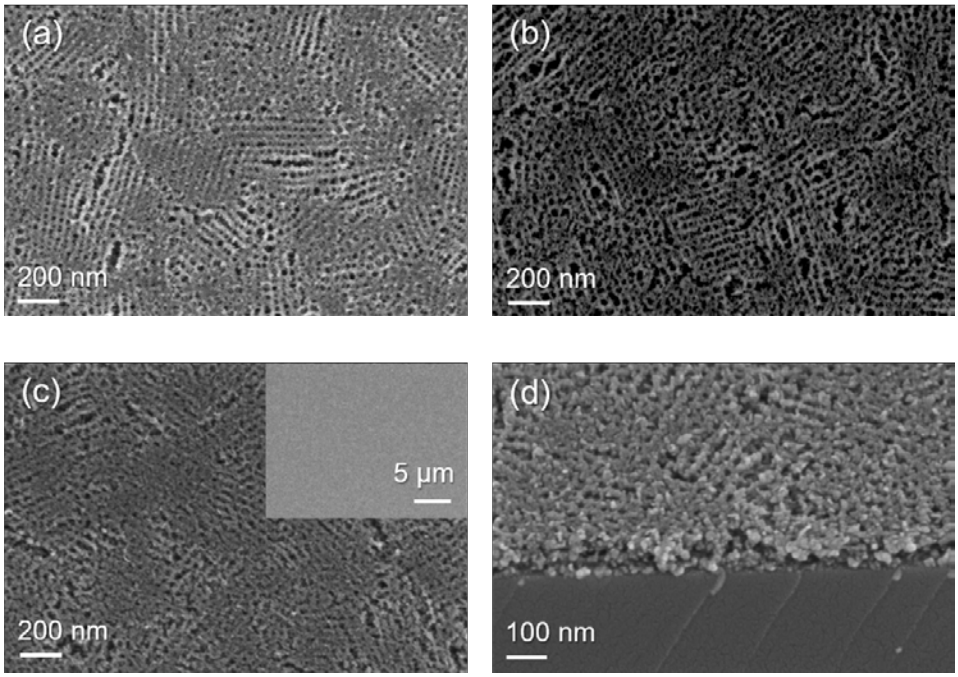

Figure 3.2. *Scanning electron microscopy (SEM) images of thin films at different processing stages and length scales. Plan views of (a) the niobium oxide film; (b) the niobium oxynitride film; (c) the niobium carbonitride film (inset at low magnification demonstrates uniformity across macroscopic length scales). (d) 45-degree cross-sectional view of the niobium carbonitride film displaying the film edge on the cleaved silicon substrate (lower darker part).*

Finally, heating the NbN thin films to 1000 °C in a mixture of methane (CH_4), hydrogen (H_2), and nitrogen (N_2), known as carburizing gas ($CH_4/H_2/N_2$) yields a superconducting niobium carbonitride (NbCN)-type material (Figure 3.1e) without substantial further growth in crystallite size, as demonstrated earlier.[24] The overall mesoporous structure is retained, albeit with additional coalescence of struts discernable in images of the top surface (Figure 3.2c). With the simple spin-coating technique, a uniform thin film with arbitrary lateral dimensions can be fabricated without major

macroscopic defects such as large cracks (see low magnification inset of Figure 3.2c and Figure 3.S3). The thickness of the final niobium carbonitride film is approximately 100 nm (Figure 3.2d); film thickness is expected to be adjustable through varying concentrations of the starting hybrid solution or spinning speeds during spin-coating. Pore sizes as estimated from SEM results are of order 20 nm to 30 nm.

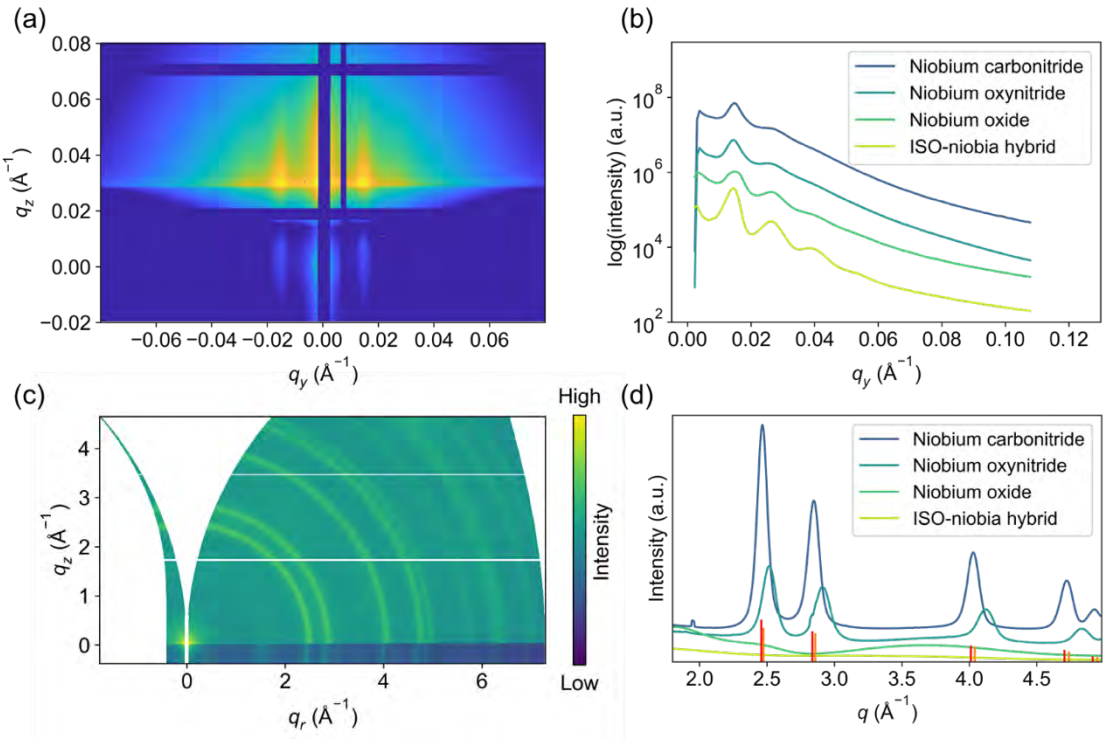

Figure 3.3. *Grazing incidence small-angle X-ray scattering (GISAXS) and wide-angle X-ray scattering (GIWAXS) profiles of thin films at different processing stages. The scattering vector q is defined as 4πsinθ/λ, where 2θ is the scattering angle and λ is the wavelength of X-rays. The subscripts r, y, and z denote the q component within the plane, along the in-plane y direction perpendicular to the X-ray beam, and along the out-of-plane z direction, respectively. (a) 2D GISAXS pattern of carbonitride film after heat treatment to 1000 °C. (b) Line cuts through the Yoneda band*[29] *of GISAXS patterns for different films as a function of processing step, as indicated. (c) 2D GIWAXS pattern of carbonitride film after heat treatment to 1000 °C. (d)*

Azimuthal integration of GIWAXS intensities for different films as a function of processing step, as indicated. Orange and red ticks show expected peak positions and their relative intensities of NbN from the Powder Diffraction File (PDF) #03-065-0436 and of NbC from PDF #03-065-8781, respectively.[30,31]

To obtain structural information about the thin films beyond a local scale probed by electron microscopy, X-ray scattering experiments were performed at the National Synchrotron Light Source II (NSLS-II) Soft Matter Interfaces (SMI) beamline[32] in a grazing incidence geometry. In previous work, an amphiphilic triblock terpolymer with similar block fractions swollen by niobia sol or other additives was shown to self-assemble into the G^A mesophase,[22,28,33] with {110} planes of the G^A parallel to the substrate in the case of thin films.[34] The SEM images in Figure 3.2 display a morphology in which seemingly parallel struts lie at the surface, with a set of thinner struts crossing underneath at 90 ° (see Supplemental Note 3.1). Such observations agree with previous results of G^A thin films with the same orientation, but with possible nascent epitaxial growth into the cylindrical phase.[35] As seen in grazing incidence small-angle X-ray scattering (GISAXS), the primary peak, which would correspond to the (110) plane given a G^A morphology, persists in samples at all stages (Figure 3.3a,b). Detailed analysis of a GISAXS scattering pattern (Supplemental Note 3.1) taken from an as-made ISO-niobia sol composite thin film is consistent with a deformed G^A structure with {110} planes parallel to the substrate, which mainly shrinks in the film normal direction during processing (Figures 3.S2 and 3.S4). This deformation at the unit cell level due to anisotropic forces has been detailed previously in other self-assembling gyroidal

systems.[19,36] It is worth reemphasizing that no efforts were made to improve long-range order of the films *via* post-spin-coating annealing. The degree of mesostructural order as reflected by SEM and GISAXS experiments is the result of the very rapid evaporation of THF during spin-coating and likely represents a structure away from equilibrium. Another notable feature of the GISAXS profiles in Figure 3b is that peak shifting to larger in-plane scattering vector q_y as a result of in-plane shrinkage upon thermal processing is much less pronounced as compared to the bulk.[22] This is likely leading to anisotropic stresses caused by pinning of the films to the supporting substrate during shrinkage. Indeed, a limited amount of network breakage *via* disconnection of neighboring struts is seen in SEM images of thin film top surfaces (Figure 3.2 and Figure 3.S5) upon treatment at elevated temperatures, consistent with this picture.

Overcoming a threshold in atomic crystal quality (*e.g.*, eliminating oxygen or vacancies) is essential for superconductivity in NbCN-type thin films at low temperatures; this is revealed by grazing incidence wide-angle X-ray scattering (GIWAXS, Figure 3.3c,d) results. Scattering peaks in the form of multiple concentric rings appear in the 2D pattern, suggesting small, randomly oriented atomic crystalline domains (Figure 3.3c). This powder-like pattern is expected for nanocrystals forming in a cubic (*i.e.*, isotropic) mesostructured gyroid network as nucleation takes place homogeneously throughout the structure and no preference exists for crystallographic orientation. Consistent with earlier results,[22,24] NbN (or oxynitride) crystallizes first from an amorphous niobium oxide after nitridation at 700 °C in NH_3 (Figure 3.3d). Compared with peak positions expected for cubic rock-salt NbN (lattice parameter 4.39 Å), the phase-pure crystals have a smaller lattice parameter of 4.32 Å, likely due to

remaining oxygen and vacancy defects present in the structure (*i.e*. $NbN_xO_y[]_{1-x-y}$, where [] denotes vacancies).[24] Final treatment in $CH_4/H_2/N_2$ at an even higher temperature of 1000 °C introduces carbon content and increases the lattice size to 4.41 Å, between that of rock-salt NbN and NbC (lattice parameter of 4.43 Å; Figure 3.S6). Along with an increased lattice parameter, coherently scattering domain sizes calculated using the Scherrer equation grew from 4.3 nm in NbN-type films to 5.8 nm in NbCN films. In general, various NbCN films treated under the same conditions were found to have coherent scattering domain sizes ranging from 4.8 nm to 5.8 nm. Consistent with earlier results, the high-temperature processing does not lead to substantial crystal growth, which is responsible for the good structure preservation at the mesoscale across the various processing steps.[24]

For comparison, dense carbonitride thin films were synthesized *via* spin-coating of a pure niobia sol solution (*i.e.*, without ISO) and heat treatment under identical conditions (denoted as the "dense film" hereafter). GIWAXS results show such dense films have a coherent crystallite size on the lower end of the range seen in the porous NbCN films, *i.e.*, 5.2 nm, according to Scherrer analysis. Overall, consistent with observations and discussions in our previous bulk materials study,[22,24] we hypothesize that the mesoporous structures induced by the co-assembly with ISO facilitates the diffusion of reactive gas species to and from the material during high-temperature heat treatments, and promotes solid-state reactions with low tendency for recrystallization, leading to the very slow grain growth observed.[24] This hypothesis is consistent with conventional wisdom, that bulk diffusion significantly contributes to domain growth

only at $T > 0.5\ T_m$, from which for these materials one would not expect bulk crystal growth from temperature alone until about 1150 ˚C.

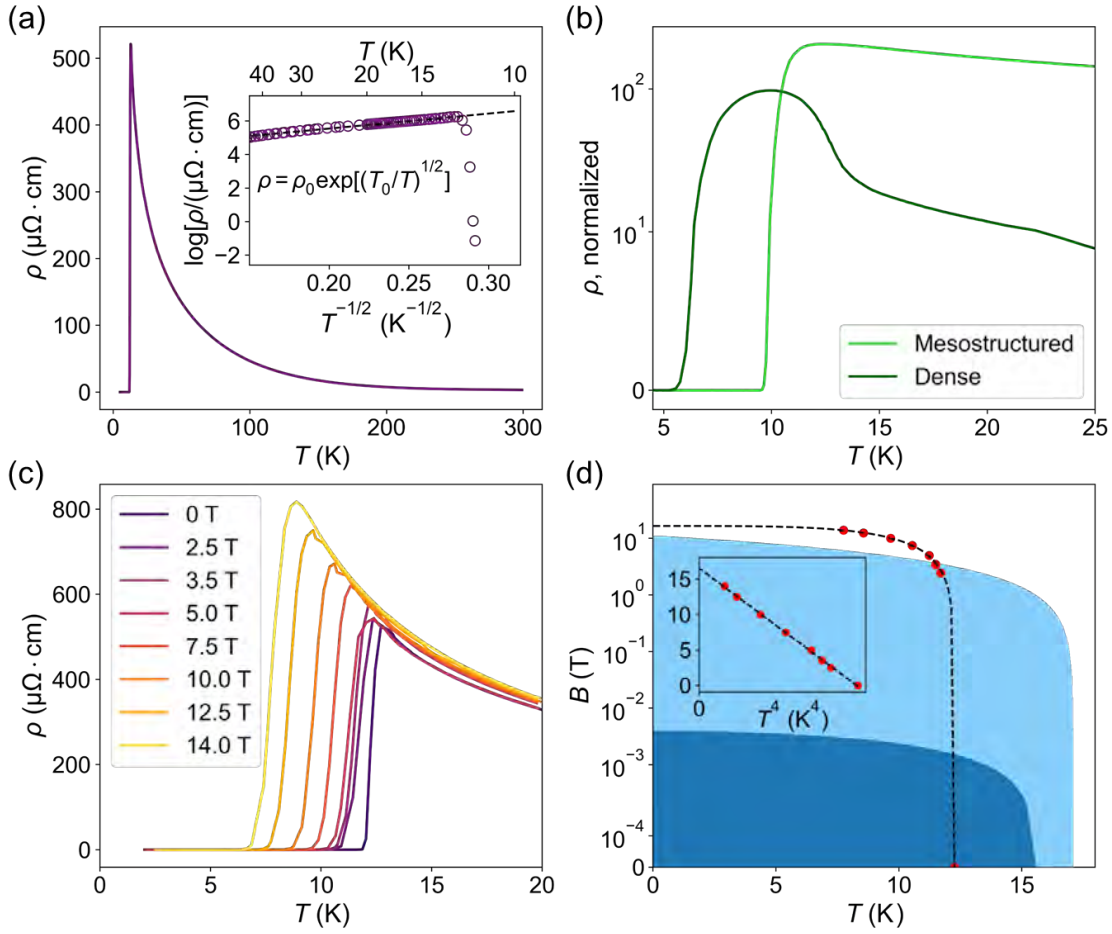

Figure 3.4. *Electrical transport measurements of mesoporous superconducting niobium carbonitride thin films on silicon substrates heat treated in $CH_4/H_2/N_2$ at a temperature of 1000 °C. Measurements were performed using the van der Pauw method. (a) Plot of resistivity (ρ) as a function of temperature (T) at zero field. The inset shows the plot of the logarithm of ρ as a function of $T^{-1/2}$. The linear behavior before the superconducting transition can be fitted with an Arrhenius-like exponential dependence of the form* $\rho = \rho_0 exp\left[\left({}^{T_0}/_{T}\right)^{1/2}\right]$ *with* $\rho_0 = 43$ *μΩ·cm and* $T_0 = 80$ *K. (b) Plot of ρ (normalized with respect to 300 K) as a function of T for*

mesostructured and dense niobium carbonitride thin films. (c) Plot of ρ of the film in (a) as a function of T at varying field strengths. (d) Plot of upper critical field (B_{c2}) as a function of T, together with the depiction of the phase diagram of niobium (carbo)nitride superconductors. The relationship between critical field (B_c) and T is $B_C = B_C(T = 0)\left[1 - \left(T/T_C\right)^{\alpha}\right]$, where T_c is the critical temperature, and α is an empirical fitting parameter. Red points are our experimental B_{c2} values at corresponding T determined as when ρ decreases to half the peak value before the superconducting transition. The data points are fitted with α = 4, shown as the dashed line. The dark blue region represents the behavior of superconducting niobium nitride with a lower critical field (B_{c1}) of 4.0 mT and a T_c of 15.2 K from ref[37], with the boundary fitted with α = 2. The light blue region represents the mixed state of normal and superconducting niobium carbonitride with B_{c2} of 11 T and T_c of 16.7 K from ref[38], with the boundary fitted with α = 1.[39] The inset shows the linear fit of our experimental B_{c2} values when the horizontal axis represents T raised to the power of 4.

Superconductivity in mesoporous NbCN thin films was probed *via* DC transport measurements (Figure 3.4), utilizing a van der Pauw geometry with four chromium/gold metal contacts deposited on the film perimeter *via* thermal evaporation through a shadow mask (see Experimental Section, Figure 3.S3). The resistivity, ρ, of the mesoporous NbCN film (Figure 3.4a) was measured to be 6.91 μΩ·cm at 300 K, comparable to that of the dense film, 5.65 μΩ·cm. During zero-field cooling (ZFC) of the carbonitride, however, a precipitous rise in the resistivity was observed down to the transition temperature (T_c) of 12.8 K with a relatively low value of $\rho_{300\,K}/\rho_{12.8\,K} = 0.0065$. It should be noted that the porosity of the film was not considered for the calculation of resistivity, so the value is likely an overestimation (see Supplemental Note 3.2). At 12.8

K, a sharp decrease to zero resistivity occurred indicating the transition into a superconducting state. This temperature is below the T_c of ~ 17.3 K observed in sputtered NbCN films.[40] The decrease in T_c could be due to differences in the carbon/nitrogen ratio in the mesoporous films as compared to controlled sputter deposition, or to the retention of oxygen or vacancies in the material, as the NbCN synthesized here was converted from a parent oxide rather than grown in an oxygen-free environment. It is also notable that the T_c of the mesoporous sample under ZFC is slightly higher than that of the comparative dense films (Figure 3.4b). This result is further confirmation that the induced porosity and very high surface area in the ISO templated films facilitate material conversions during processing and improve final superconductor quality, possibly through increased reactivity with gaseous species as a result of significantly shortened diffusion distances during annealing enabled by the nanostructure.

The exponential rise in resistivity with decreasing temperature down to T_c is reminiscent of the behavior reported in granular superconducting samples,[41] and has been observed previously in nanocrystalline NbN films.[42–46] In these materials, the finite charging energy associated with individual grains can lead to thermally activated, Arrhenius-like dependence of conductivity on temperature such as is evidenced in Figure 3.4a (inset).[41] An additional contribution to the increased resistivity upon cooling may be increased grain boundary scattering of electrons in the highly granular NbCN thin films.[44] In the case of the mesoporous NbCN thin films of the present work, disorder and granularity in the material arise from both the small crystallite size as well as the nanoscale mesostructural network features. It is notable that these two parameters are

of the same order: the coherent scatting domain size in the NbCN is measured to be 5.8 nm, while the thinnest points of the struts comprising the mesoscale network are ~ 10 nm or less (Figure 3.2, Figure 3.S5). For nanocrystalline NbCN materials structure directed by BCPs, these two parameters are separately tunable through high temperature processing or selection of the BCP templating agent molar mass, respectively. This may become an important future tool for elucidation of the impact of physical confinement on the same order as the average grain size in granular metals and superconductors.

Upon transitioning into the superconducting state at 12.8 K, resistivity is entirely lost. Magnetoresistance measurements of the NbCN thin film (Figure 3.4c) show that a high upper critical field (B_{c2}) is maintained in the mesoporous films, estimated to be over 16 T (Figure 3.4d). This is higher than the B_{c2} of ~ 11 T observed previously in bulk NbCN matieral,[38,39] which further speaks to the relatively high quality materials properties that can be achieved *via* scalable solution based synthesis techniques. Observation of the upper critical field in the mesoporous NbCN along with the superconducting phase behavior of niobium nitride (Figure 3.4d) accentuates this.

It is relevant to point out that nanocrystallinity and mesoscale structuring has been observed to increase the critical field strength in superconductors due to the effect on materials structure at the scale of the coherence length.[23,47,48] However, despite having a slightly larger coherent scattering domain size, the estimated critical field in the mesoporous film is notably higher than that seen in the comparative dense film created *via* a sol-gel route without the use of BCP self-assembly (Figure 3.S7). While materials stoichiometry could be at play, the high lattice constant present in the dense film indicates a low level of oxygen and vacancy content. Thus, the mesostructure itself

may play an important role in critical field enhancement *via* the contribution of surface superconductivity or the increased granularity associated with the interpenetrating strut networks.

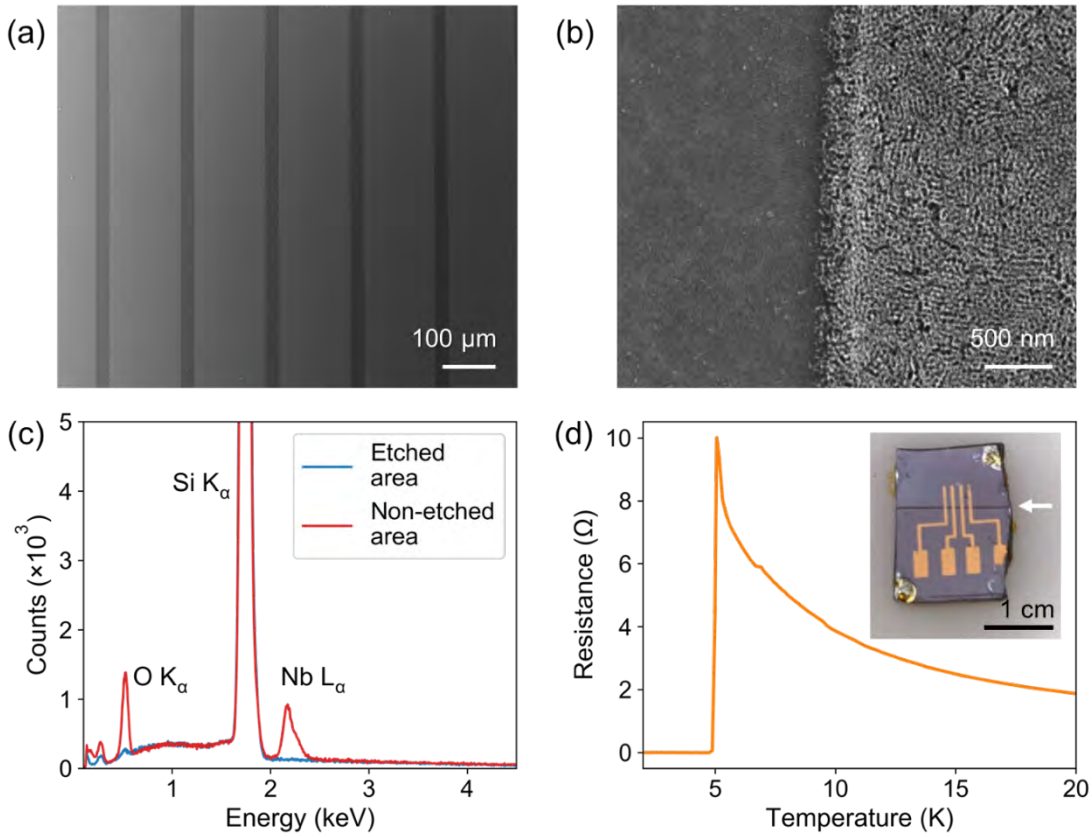

Figure 3.5. *Lithographic patterning of spin-coated thin films on silicon substrates. (a) Plan-view SEM image of niobium carbonitride thin film patterned through photolithography, with 25 um wide strips etched away shown in dark. (b) Higher magnification SEM image of the patterned film showing the edge along with details of the self-assembled mesostructure. (c) Energy-dispersive X-ray spectroscopy (EDS) spectra of areas of plain film (i.e., non-etched area) and etched film after 10-min CF_4 plasma etching. (d) Plot of resistance versus temperature as obtained from an individual patterned 400 μm wide strip thin film area. Inset shows a single lithographically patterned niobium carbonitride strip (400 μm wide) visible to*

the naked eye (white arrow) with four co-linear metal contacts across the strip used for the transport measurements. Note that the niobium carbonitride strip shows up as a darker line against the background in this image captured by an optical microscope, as opposed to the darker area that is etched away in (a), which is captured by SEM.

As a proof-of-concept, we defined microscopic patterns *via* photolithography on spin-coated BCP self-assembly directed thin films to illustrate compatibility of our solution-based synthesis approaches to mesoporous superconducting samples with typical semiconductor nanofabrication processing (Figure 3.1f-k). First, a photoresist is applied on the ISO-niobia hybrid thin films that are pre-treated at 300 °C to minimize swelling or dissolution of the film by photoresist solution, but without complete removal of the ISO template (see Experimental Section). After exposure through a mask and development, 25 μm wide strips of photoresist layers are removed. Pattern transfers are achieved by a combination of wet etching using buffered oxide etchant (BOE, to remove niobia) and dry etching using oxygen plasma (to remove polymeric components). The observed clear and sharp patterns demonstrate the viability for spin-coated ISO-niobia thin films to be incorporated into standard microelectronic processing, with additional self-assembled 3D features at the mesoscale (Figure 3.5a,b).

A separate pattern was transferred from a shadow mask using CF_4 plasma etching. Transfer fidelity is much higher for the ISO-niobia hybrid thin film before any high-temperature heat treatments, whereas the features become smeared when using the mesoporous niobium oxide films (Figures 3.S8 and 3.S9). Porosity in the mesostructured film likely contributes to poor pattern transfer by allowing plasma to

infiltrate void spaces thereby causing undesirable etching of regions of niobium oxide covered/shielded by the mask. This is also likely one of the causes behind the slanted edge seen in Figure 3.5b. Results suggest that the dry etching of thin films with internal nanostructures derived from structure directing agents such as BCPs should proceed before the introduction of porosity in order to maximize directional anisotropy. For our spin-coated films, both CF_4 plasma etching or a combination of wet and dry etching could completely remove the ISO-niobia hybrid materials, as evidenced by the disappearance of the Nb Lα peak in energy-dispersive X-ray spectroscopy (EDS) experiments (Figure 3.5c). Films patterned *via* plasma etching into 400 μm wide strips (Figure 3.5d, inset, white arrow) were found to retain superconductivity at low temperature, but with a transition reduced to 5 K (Figure 3.5d). This shift could be due to chemical inhomogeneity across the surface of mesoporous thin films, which would create multiple percolating superconducting paths of varying composition and transition temperature.

Conclusions

In summary, we reported the preparation of superconducting mesoporous niobium carbonitride-type thin films on silicon substrates derived from BCP self-assembly with niobia precursors using standard polymer solution-based processing in combination with thermal treatments at elevated temperatures under different gas environments. In more detail, the material fabrication route involved spin-coating of ISO terpolymer-niobia sol hybrid solutions and a series of heat treatments in air, ammonia, and carburizing gas at temperatures up to 1000 °C to result in controllable

mesoporosity, nanocrystallinity, and superconducting thin film properties. Specific steps to perfect the BCP self-assembly derived structure after spin-coating, *e.g.*, by means of low temperature thermal or SVA, were not taken but could be added in future protocols. Finally, in proof-of-principle experiments, thin films were shown to be amenable to lithographic patterning through common dry or wet etching techniques, all compatible with regular semiconductor processing. While the relatively high temperatures required to achieve self-assembly directed mesostructure conversion into superconducting materials at first may seem to pose a roadblock to further technology developments, it is perhaps instructive to note that this hurdle may be overcome by the use of transient laser annealing methods.[49] Such methods represent a proven technology currently used in large scale semiconductor manufacturing to eliminate high-temperature furnace treatments. Furthermore, they have previously been demonstrated for the conversion of BCP self-assembly directed hybrid thin films into mesoporous templates as well as for their conformal backfilling with crystalline silicon (cSi) using transient laser annealing processes reaching temperatures above the cSi melting temperature (*i.e.*, over 1400 °C).[14,17,19] We therefore anticipate a clear path towards the development of solution-based approaches to thin film technologies at the intersection between soft matter self-assembly and quantum materials with tremendous academic as well as industrial potential. In particular, the diversity of BCP self-assembly and tunability of structural parameters, *e.g.*, *via* BCP composition and molar mass, provide unprecedented opportunities for the discovery of fundamentally new physics as well as device functionality for potential applications ranging from information technology all the way to energy conversion and storage and sensing.[50]

Experimental Section

Preparation of niobium carbonitride thin films on silicon substrates

Unless otherwise stated, all chemicals were purchased from Millipore-Sigma. Silicon substrates were obtained from Pure Wafer (resistivity 0.01 – 0.02 Ω·cm, doped with boron). Pure gases and gas blends used for thermal film treatments were obtained from Airgas.

The protocol for the sequential anionic polymerization of the triblock terpolymer ISO can be found in prior published work.[27] A combination of proton nuclear magnetic resonance (^{1}H NMR) spectroscopy and gel permeation chromatography (GPC) was used to determine total number-average polymer molar mass (M_n) of 67.7 kg/mol, polydispersity index (PDI) of 1.10, and block weight fractions for PI, PS, and PEO blocks of 26.0 %, 65.3 %, and 8.7 %, respectively.

The preparation of niobia sol and ISO-niobia hybrid solutions is also detailed in a previous publication, and was used with slight modifications.[22] First, 0.50 g ISO was dissolved in 7.00 g anhydrous (99.9%) tetrahydrofuran (THF). In a separate vial for the sol stock solution, 0.96 mL niobium (V) ethoxide (99.999%, Alfa Aesar) was injected to a mixture of 0.56 mL 37 wt% HCl solution and 0.90 mL anhydrous THF under vigorous stirring. After 5 min, another 4.5 mL anhydrous THF was injected to the vial to slow down the hydrolytic condensation. After 2 min of additional stirring, 1.40 g of sol stock solution was added to the ISO solution. The hybrid solution was stirred for 20 h before spin-coating at 2000 rpm for 45 s on a ~ 1×1 cm^2 silicon substrate. For Fourier-transform infrared spectroscopy (FTIR) and thermogravimetric analysis (TGA)

characterizations, the hybrid solution was prepared from 0.050 g ISO mixed with 0.268 mL (for FTIR) or 0.147 mL (for TGA) niobia sol stock solution in 1.0 mL THF. The hybrid solution was poured into a Teflon beaker (inner diameter ~ 1 cm) and heated at 40 °C under a glass dome to evaporate the solvent THF, resulting in a bulk film.

To further condense the niobia sol, the ISO-niobia hybrid thin films were heat treated at 130 °C in air for about 3 h at which stage cross-sectional SEM images showed films to be ~ 650 nm thick. The films were calcined in a tube furnace under static ambient air to remove the templating ISO and to obtain mesoporous niobium oxide films. The heating ramp rate was set at 1 °C/min to 450 °C, with a dwell time of 3 hours at this temperature. Through this process step, the thickness of the niobium oxide films dramatically reduced to ~ 110 nm, again determined from cross-sectional SEM images. The nitridation of the niobium oxide films was performed in a quartz tube furnace using electronic grade ammonia (99.9995% purity) at a flow rate of 8 L/h. The heating protocol used included a ramp rate of 5 °C/min to 700 ˚C, with a 9-hour dwell time at that temperature. For comparative studies between mesostructured and dense thin films, the dwell time in this nitridation step was 3 h. Superconducting niobium carbonitride films were derived by treating the niobium oxynitride films under carburizing gas ($CH_4/H_2/N_2$, 16/4/80 by mole fraction) at a flow rate of 8 L/h, heated at 5 °C/min to 1000 °C with a 3-hour dwell time. The thickness of the final films after this stage was observed to be ~ 100 nm from cross-sectional SEM images, *i.e.*, only slightly reduced from that of the nitride films.

Patterning of niobium carbonitride thin films

Shadow masks were made by cutting fused silica wafers from University Wafer (thickness 180 μm) using a CO_2 laser cutter (VersaLaser VLS3.50). The laser spot size was 25.4 μm operated at 1000 dpi, with 1.5 % power and 2 % speed set in the controlling software. The widths of strips cut out ranged from 25 μm to 800 μm.

To etch the thin films into a strip with defined widths *via* only dry etching, the shadow mask was placed onto the film and CF_4 plasma was applied for 10 min (30 sccm at 40 mTorr, 150 W power) using an Oxford PlasmaLab 80+ etcher.

To pattern thin films using photolithography, ISO-niobia hybrid thin films were first heated at 300 °C for 3 h to further condense the niobia and partially pyrolyze the ISO. After treating films with hexamethyldisilazane primer, S1813 resist was spin-coated on the films at 3000 rpm for 30s (acceleration 10000 rpm/s). The photoresist was then exposed to ultraviolet light (365 nm) for 3 min in vacuum contact mode in an ABM contact aligner. After developing in Microposit MF-321 Developer for 90s, the photoresist layer had a trench depth of ~ 1.6 μm (measured by P7 Profilometer). Thin films were then etched by two cycles of 1 min descum process in the Oxford PlasmaLab 80+ etcher (50 sccm oxygen at 20 mTorr, 50 W power) and a 20-min dip in buffered oxide etchant (BOE, 6:1 concentration). The patterned thin films were finally heat treated using the same protocol as detailed in the previous section in order to convert them into niobium carbonitride.

Characterization

Fourier-transform infrared spectroscopy (FTIR)

FTIR experiment was conducted on Bruker Vertex V80V system in vacuum using the attenuated total reflectance (ATR) configuration. The bulk films of the ISO-niobia hybrid and the niobium oxide after calcination at 450 °C were ground to powder using a mortar and pestle. Spectra were collected using a deuterated triglycine sulfate (DTGS) detector.

Thermogravimetric analysis (TGA)

TGA data was obtained on a TA Instruments Q500 system using bulk films of the ISO-niobia hybrid. A monolithic piece of the ISO-niobia hybrid was heated to 600 ˚C at a rate of 10 °C/min in air while measuring the retained sample mass in order to determine the mass loss.

Scanning electron microscopy (SEM)

SEM images were captured with an in-beam secondary electron (SE) or regular SE detector using a Tescan Mira3 field emission scanning electron microscope (FESEM) operating at 5 kV accelerating voltage or with an inlens EsB detector using a Zeiss GeminiSEM 500 operating at 2 kV accelerating voltage. Samples were coated with gold-palladium prior to imaging (optional).

Grazing incidence X-ray scattering

Grazing incidence X-ray scattering experiments were performed at the National Synchrotron Light Source II (NSLS-II) Soft Matter Interfaces (SMI) beamline with an X-ray energy of 14.0 keV and incident angle of 0.10 °. Grazing incidence small-angle X-ray scattering (GISAXS) patterns were recorded on a Pilatus3 1M pixel array detector

with a sample-to-detector distance (SDD) of 4.97 m. GISAXS data were processed using the MATLAB®-based software GIXSGUI (version 1.7.1)[51] to plot the 2D pattern and produce a line-cut profile through the Yoneda band.[29] Grazing incidence wide-angle X-ray scattering (GIWAXS) patterns were recorded on a Pilatus3 300K-W pixel array detector positioned at 274 mm from the samples. The detector was rotated along a goniometer arc to capture multiple frames with the scattering angle ranging from -3.5 ° to 62 °. Individual GIWAXS frames were stitched and processed using customized python codes at SMI[52] to plot the 2D pattern in reciprocal space and to azimuthally integrate the intensity. Scherrer analysis was performed using JADE software on the (111), (200), (220), and (311) peaks (the four peaks with smallest q shown in Figure 3.3d). A pseudo-Voigt profile was used for peak fitting. The coherently scattering domain sizes τ calculated from the Scherrer equation $\tau = {K\lambda}/{\beta \cos\theta}$ were averaged to obtain the result. The shape factor K was 0.93, while β was the respective peak broadening at half maximum.

Low-temperature transport property measurements

Heat-treated NbCN thin films on silicon substrates were cleaved with a diamond scribe to remove ~ 1 mm from the perimeter of the roughly square samples on every side. This step was taken to prevent inhomogeneous edge material from the spin coating process contributing to transport measurements. Metal contacts of ~ 10 nm of chromium immediately followed by ~ 30 nm of gold were then deposited directly onto the films through a custom cut shadow mask using a Varian bell jar thermal evaporator. The configuration of metal contacts defined in this way are shown in Figure 3.S3 (van der

Pauw configuration for regular films) and in Figure 3.5d (inset, a co-linear configuration for patterned strips).

Transport properties of samples were measured using a Quantum Design Physical Properties Measurement System (PPMS) equipped with a helium reliquifier and 14 T magnet. Samples were mounted onto a standard PPMS resistivity puck using Lakeshore cryogenic varnish, and deposited chromium/gold contacts were wirebonded to metal puck contact pads with aluminum wire using a Westbond model 7400E wedge-wedge ultrasonic/thermosonic wire bonder. In a typical measurement, the external field of the instrument was ramped to the specified field, *e.g.*, 2.5 T, at a rate of 10 mT/s and held at that value. An excitation current of 100 μA was then applied, and the resistance value measured while heating or cooling the sample through the measurement range, *i.e.*, 2 K – 20 K, at a rate of 2 K/min. At each point of the resistivity assessment, the average of 5 measurement was reported as the value of resistance with an observed relative error at least two orders of magnitude lower than the reported value. For van der Pauw configurations, this was repeated for both the vertical and horizontal configurations to obtain the final resistivity value. For patterned films (Figure 3.5), the transport measurement shown in part d was repeated several times without substantial variation between measurements.

Supplementary Information for Chapter 3

Supplemental Note 3.1: Structural analysis of deformed G^A films in Figure 3.2

The view along the [110] direction of the alternating gyroid (G^A, space group $I4_132$, number 214) displays a complicated network with struts at different depth of view. The morphology seen in electron microscopy images can thus change dramatically when the depth of view is altered, especially for the deformed G^A networks.[53] In the context of a G^A lattice, a G^A thin-film structure with {110} planes parallel to the surface (for simplicity, we will assume only the (110) plane, which is the orientation depicted in Figure 3.S4) and shrunk nearly exclusively along the film normal has the *c* axis lying in the plane and parallel to the surface. The *a* and *b* axes point out of the plane at an equal angle with respect to the plane normal, each forming a right angle with the in-plane *c* axis: $\alpha = \beta = 90$ °. The angle γ between *a* and *b* is greater than 90 °, however, as a result of anisotropic shrinkage. Such a deformed G^A model has been successfully used to index the peaks in GISAXS patterns,[34] and a thorough analysis showed the symmetry was reduced to F222 (space group number 22).[19]

Earlier results indeed observed a "cross-bar" morphology of two sets of struts crossing at 90 °, with one set thicker than the other.[53] The thicker-looking struts on top are derived from the initially curved network pathways in G^A overlapping with closely aligned network pathways underneath, creating an impression of greater thickness (Figure 3.S4, also see Figure 2c in ref [35]). The thinner-looking struts are derived from single struts just below the top surface. It is worth noting that the curved network of gyroids arises from a compromise between minimizing interfacial energy between dissimilar blocks and reducing entropic penalty of chain stretching in block copolymers

(BCPs). This is different from what is observed in SEM here in this work, *i.e.*, purely inorganic nanostructures obtained after heat treating ISO-niobia hybrids to decompose and remove organic BCPs. Although the overall mesostructure derived from the curved gyroid network should remain, distortions in local structure and symmetry are expected as the niobium oxide becomes highly condensed and the entropic penalty of chain stretching no longer applies. The graphics in Figure 3.S4 are generated from an idealized level-set calculation[54] that mimics the mesophase derived from the pure BCP system. As such they do not exactly represent the distorted structure of the inorganic materials after thermal treatment, but are useful for general illustration purposes.

It is possible to extract lattice parameters from the SEM image of the mesoporous niobium oxide thin films after 450 °C treatment in air (Figure 3.S5, of which Figure 3.2a is part of) which account for the GISAXS pattern of ISO-niobia hybrid thin film before thermal treatment, where the peaks are the most discernible (Figure 3.S2). The *c* axis points along the thick struts; the average spacing between perpendicularly crossing thin struts represents half the periodicity along the *c* axis. From the SEM image, several areas (Figure 3.S5, blue lines) can be identified to estimate the spacing between thin struts to be approximately 30 nm. Therefore, the value of the *c* parameter should be a little over 60 nm, accounting for the slight in-plane contraction after the film is heated to 450 °C (Figure 3.3b). Similarly, the spacing between the top thick struts is estimated to be approximately 39 nm (Figure 3.S5, gold lines), but this length is a projection of *a* and *b* axes to the film surface as viewed with SEM. Again, this spacing represents half of one period, which is equal to the length of a projection of *a* or *b*, $a\sin(\gamma/2)$ (the two projections are equal as the angle of the *a* and *b* axes to the

film normal are equivalent). Although γ is unknown, this can be approximated from prior results[19,34] and further refined for the current system using analysis of GISAXS data.

Figure 3.S2 shows the GISAXS pattern of an as-made ISO-niobia hybrid thin film before thermal treatment labeled with expected peak positions for a deformed G^A symmetry, as calculated using the GIXSGUI package.[51] The lattice parameters optimized to fit this pattern are as follows: $a = b = 44.5$ nm, $c = 61.0$ nm, $\alpha = \beta = 90$ °, $\gamma = 140$ °. Considering the values estimated from the SEM images for the derived porous oxide, there is good agreement between the expected peak positions and the experimental results, particularly on the primary and secondary peaks on the Yoneda band (q_z = 0.026 Å^{-1}). The azimuthal spreading of intensity indicates orientational variation of the {110} planes, but the radial positions of the expected peaks match with the oval-shaped intensity fluctuations in Figure 3.S2. The length of projection of a or b into the plane $a\sin(\gamma/2) = 41.8$ nm in the hybrid is 7.2 % larger than the spacing of 39 nm between thick struts in the oxide after heat treatment, compared to a 1.7 % change in the orthogonal in-plane direction, *i.e.*, the c direction corresponding to the spacing of thin struts. The resultingly larger change in spacing between neighboring thick struts likely caused greater strain on the thin "cylinders," which is consistent with the phenomenon that most cracks seen in the SEM images occur through the thin cylinders (Figure 3.S5, green ovals) in order to relieve the stress originating from the orthogonal high-shrinkage direction. Lastly, γ is already significantly larger than 90 °, suggesting a large degree of shrinkage of the cubic G^A upon rapid evaporation during spin coating. Anisotropic shrinkage is then exacerbated when the film is treated at higher

temperatures, with film thickness decreasing by over 80 %. Such considerable deformation, likely non-affine, blurs the peaks in X-ray scattering of films at later stages (Figure 3.3), but our analysis here demonstrates that the mesostructural symmetry has its origin in a G^A lattice.

Supplemental Note 3.2: Discussion of resistivity of porous films with internal mesostructures in Figure 3.4

Our current way of calculating the mesoporous film's resistivity is based on a hypothetical dense film that has the full thickness of the mesoporous film, which, strictly speaking, is not an accurate representation. If we were to obtain a more precise resistivity that takes into account the void space, the equation $R = \rho l/A$ can be used, where R, ρ, l, and A are the directly measured resistance, the resistivity calculated for the van der Pauw method, the length of the materials, and the film's cross sectional area, respectively. The non-standard mesoporous films with internal structures prepared from BCP self-assembly pose additional challenges for determining the exact value of ρ as A varies at different positions in the network structure. Nonetheless, an approximation of the upper and lower bounds of resistivity can be calculated from the maximum and minimum areal coverage of the cross section of conducting material. Figure 5 in ref [51] depicts the areal fraction of the matrix domain for double gyroids along different zone axes. For our deformed alternating gyroid networks, if we assume the cross section is perpendicular to the (110) plane that is parallel to the film surface, then the variation of the area that is covered by niobium compounds should be half the difference between unity and the red curve in the aforementioned figure, since the single gyroid network

remaining in our films is one of the two interpenetrating double gyroid minority network domains. This means the areal coverage by conducting material responsible for measured electrical conduction ranges from 12 % to 21 %. By using $R = \rho l/A$, we estimate the resistivity may be 12 % (minimum) to 21 % (maximum) of our reported results that are calculated assuming the film has the full thickness.

These estimated boundary cases have to be considered with caution, however. First, the alternating gyroid network structure in our samples is not the perfect structure depicted in Figure 3.S4 or Figure 5 in ref [51], therefore the areal fraction associated with a particular plane is not as well defined. Second, the actual areal coverage depends on the volume fraction of the niobium type material in the film, and can be different from Figure 5 in ref [51]. While we think the volume fraction in our case should be close, the thin film geometry precludes accurate measurements of porosity by gas sorption, which therefore remains an estimate. Lastly, network connectivity is related to the quality of periodic order, and influences electrical conductivity, as can be imagined in series/parallel circuits. All these factors may lead to variations in behavior, which is not accounted for in our simple approximations.

Supplemental Figures

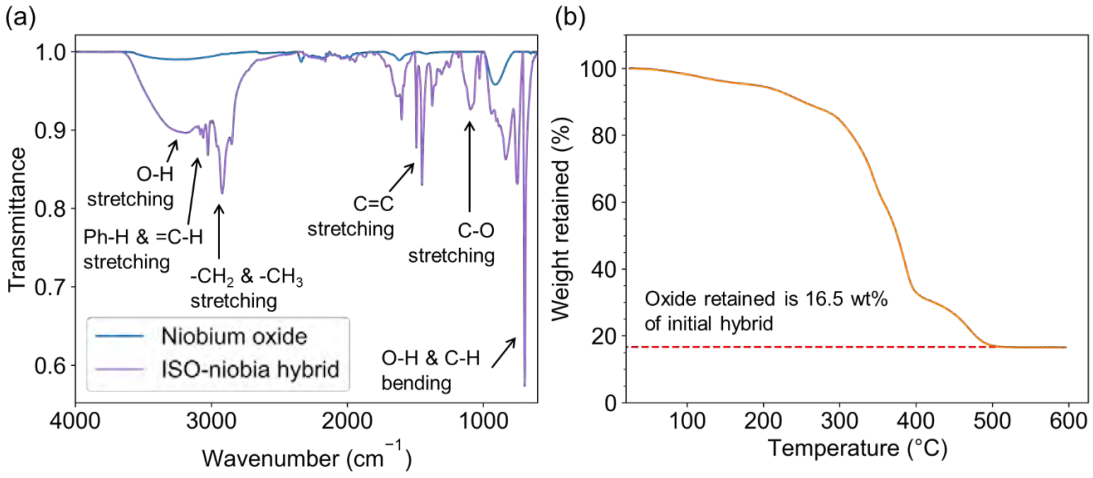

Figure 3.S1. *(a) Fourier-transform infrared spectroscopy (FTIR) spectra of ISO-niobia hybrid and mesoporous niobium oxide after calcination at 450 °C. (b) Thermogravimetric analysis (TGA) curve of ISO-niobia hybrid up to 600 °C in air.*

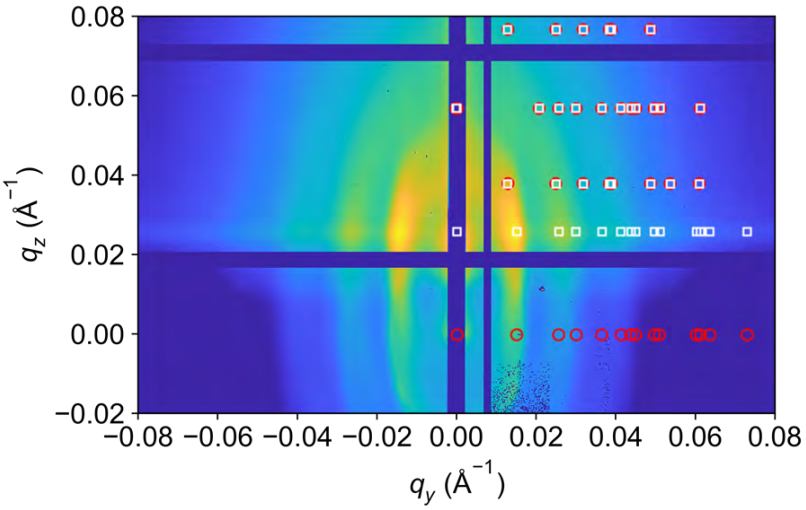

Figure 3.S2. *GISAXS pattern of the ISO-niobia hybrid thin film indexed with expected peak positions based on G^A symmetry ($I4_132$) with $a = b = 44.5$ nm, $c = 61.0$ nm, $\alpha = \beta = 90$ °, $\gamma = 140$ °. The peaks are only shown on the right half for clearer comparison with the left, and the expected positions are symmetrical with respect to $q_y = 0$. White squares and red circles represent peak positions through reflection and transmission channels, respectively.*

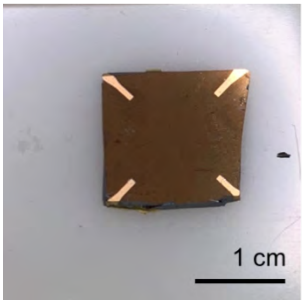

Figure 3.S3. *Photo of a superconducting niobium carbonitride film with chromium/gold metal contacts deposited on the four corners in a van der Pauw geometry*[55] *for typical transport property measurements.*

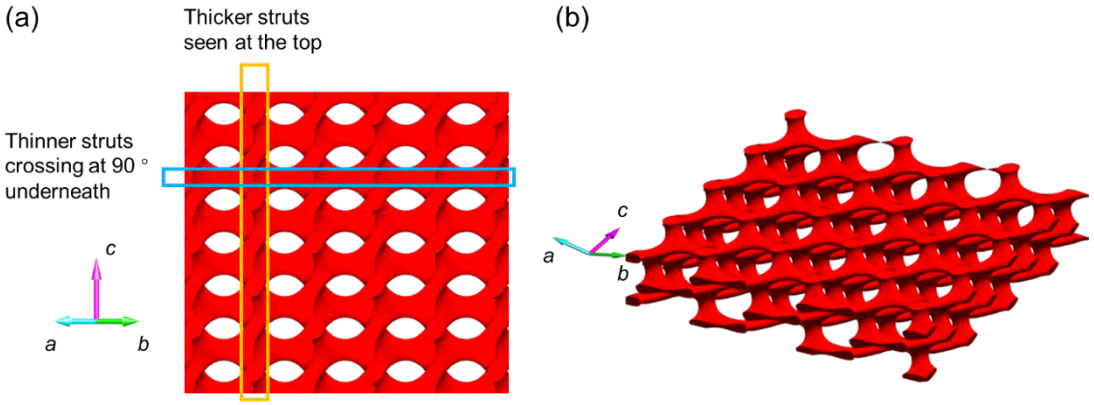

Figure 3.S4. *Illustration of alternating gyroid (G^A) structures generated from level-set calculations, with directions of lattice vectors a, b, and c indicated. (a) Plan view along [110] direction with (110) plane parallel to the surface. The struts within the gold rectangle appear as a cylinder in SEM, while those within the blue rectangle form the thinner cylinder crossing at 90 ° underneath. (b) A tilted view of the same structure.*

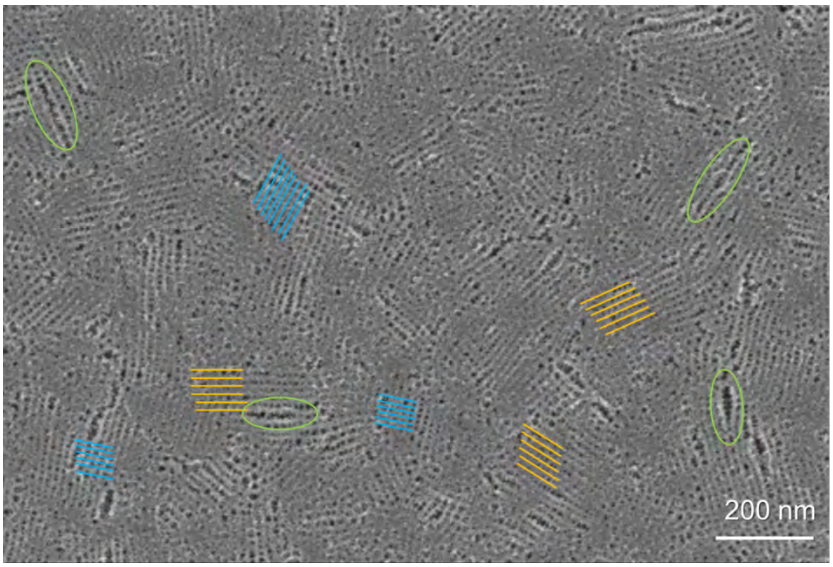

Figure 3.S5. *Plan-view SEM image of the mesoporous niobium oxide film. Gold and blue lines show the positions of thick and thin struts in selected areas, respectively. Green ovals show select areas with small cracks.*

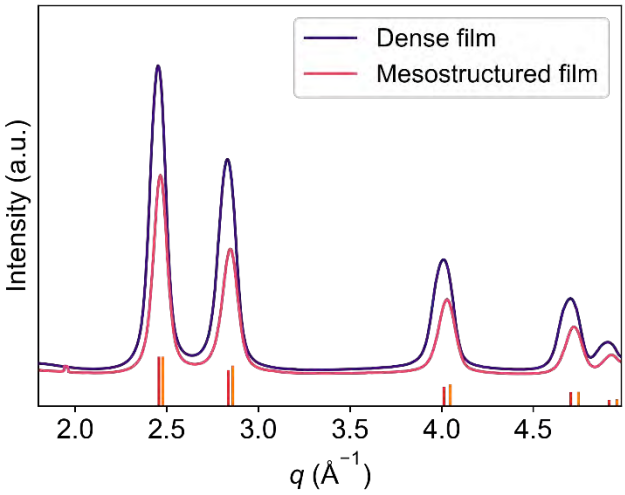

Figure 3.S6. *Azimuthal integration of GIWAXS intensities for the ISO-templated mesostructured niobium carbonitride film and dense film derived from pure niobia sol. Red and orange ticks show expected peak positions and their relative intensities for NbC (PDF #03-065-8781) and NbN (PDF #03-065-0436), respectively.*

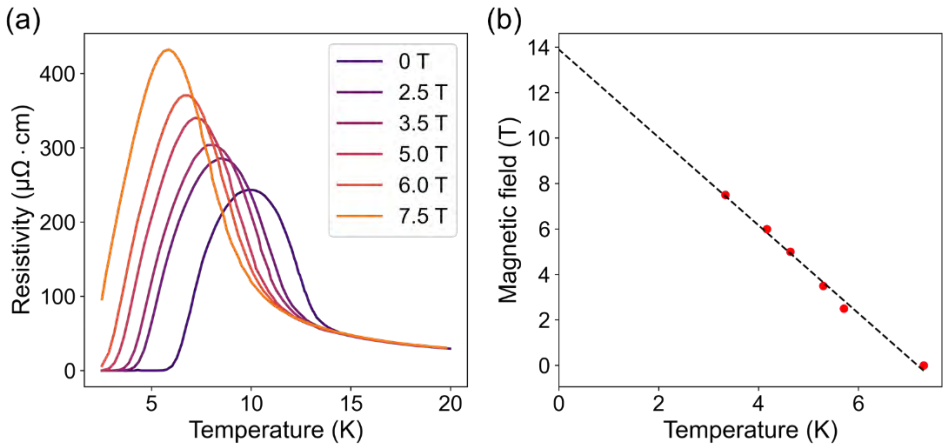

Figure 3.S7. *(a) Magnetoresistance measurements on the dense film at varying fields. (b) Plot of upper critical field (B_{c2}) versus temperature, where temperatures are determined at the points where the resistivity decreases to half the maximum value before the superconducting transition. The dashed line is a linear fit of the data points as described in the main text.*

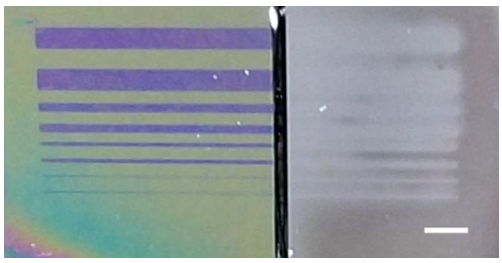

Figure 3.S8. *Photos of etched ISO-niobia hybrid thin film (left) and niobium oxide thin film (right) with patterns transferred from shadow masks. Scale bar represents 1 mm.*

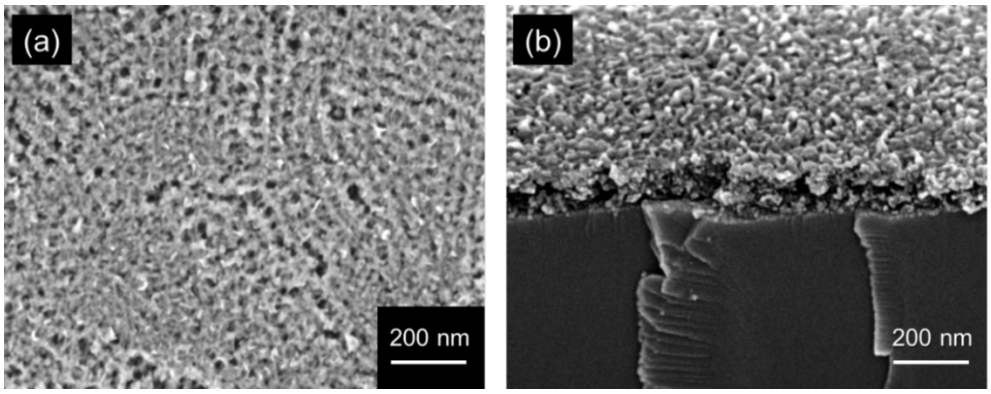

Figure 3.S9. *(a) Plane-view and (b) 45-degree cross-sectional SEM images of superconducting niobium carbonitride patterned through CF_4 plasma etching with a shadow mask.*

REFERENCES

1. Urbas, A., Sharp, R., Fink, Y., Thomas, E. L., Xenidou, M. & Fetters, L. J. Tunable Block Copolymer/Homopolymer Photonic Crystals. *Adv Funct Mater* **12,** 812–814 (2000).
2. Peinemann, K.-V., Abetz, V. & Simon, P. F. W. Asymmetric superstructure formed in a block copolymer via phase separation. *Nat. Mater.* **6,** 992–996 (2007).
3. Dorin, R. M., Phillip, W. A., Sai, H., Werner, J., Elimelech, M. & Wiesner, U. Designing block copolymer architectures for targeted membrane performance. *Polymer* **55,** 347–353 (2014).
4. Werner, J. G., Rodríguez-Calero, G. G., Abruña, H. D. & Wiesner, U. Block copolymer derived 3-D interpenetrating multifunctional gyroidal nanohybrids for electrical energy storage. *Energy Env. Sci* **11,** 1261–1270 (2018).
5. Li, C., Li, Q., Kaneti, Y. V., Hou, D., Yamauchi, Y. & Mai, Y. Self-assembly of block copolymers towards mesoporous materials for energy storage and conversion systems. *Chem. Soc. Rev.* **49,** 4681–4736 (2020).
6. Park, M., Harrison, C., Chaikin, P. M., Register, R. A. & Adamson, D. H. Block Copolymer Lithography: Periodic Arrays of ~10^11 Holes in 1 Square Centimeter. *Science* **276,** 1401–1404 (1997).
7. Bates, C. M., Maher, M. J., Janes, D. W., Ellison, C. J. & Willson, C. G. Block Copolymer Lithography. *Macromolecules* **47,** 2–12 (2014).
8. Orilall, M. C. & Wiesner, U. Block copolymer based composition and morphology control in nanostructured hybrid materials for energy conversion and storage: solar cells, batteries, and fuel cells. *Chem Soc Rev* **40,** 520–535 (2011).

9. Hoheisel, T. N., Hur, K. & Wiesner, U. B. Block copolymer-nanoparticle hybrid self-assembly. *Prog. Polym. Sci.* **40,** 3–32 (2015).
10. Kamperman, M., Garcia, C. B. W., Du, P., Ow, H. & Wiesner, U. Ordered Mesoporous Ceramics Stable up to 1500 °C from Diblock Copolymer Mesophases. *J. Am. Chem. Soc.* **126,** 14708–14709 (2004).
11. Malenfant, P. R. L., Wan, J., Taylor, S. T. & Manoharan, M. Self-assembly of an organic–inorganic block copolymer for nano-ordered ceramics. *Nat. Nanotechnol.* **2,** 43–46 (2007).
12. Warren, S. C., Messina, L. C., Slaughter, L. S., Kamperman, M., Zhou, Q., Gruner, S. M., DiSalvo, F. J. & Wiesner, U. Ordered Mesoporous Materials from Metal Nanoparticle-Block Copolymer Self-Assembly. *Science* **320,** 1748–1752 (2008).
13. Lee, J., Orilall, M. C., Warren, S. C., Kamperman, M., DiSalvo, F. J. & Wiesner, U. Direct access to thermally stable and highly crystalline mesoporous transition-metal oxides with uniform pores. *Nat Mater* **7,** 222–228 (2008).
14. Arora, H., Du, P., Tan, K. W., Hyun, J. K., Grazul, J., Xin, H. L., Muller, D. A., Thompson, M. O. & Wiesner, U. Block Copolymer Self-Assembly–Directed Single-Crystal Homo- and Heteroepitaxial Nanostructures. *Science* **330,** 214–219 (2010).
15. Kim, E., Vaynzof, Y., Sepe, A., Guldin, S., Scherer, M., Cunha, P., Roth, S. V. & Steiner, U. Gyroid-Structured 3D ZnO Networks Made by Atomic Layer Deposition. *Adv. Funct. Mater.* **24,** 863–872 (2014).

16. Robbins, S. W., Sai, H., DiSalvo, F. J., Gruner, S. M. & Wiesner, U. Monolithic Gyroidal Mesoporous Mixed Titanium–Niobium Nitrides. *ACS Nano* **8,** 8217–8223 (2014).

17. Tan, K. W., Jung, B., Werner, J. G., Rhoades, E. R., Thompson, M. O. & Wiesner, U. Transient laser heating induced hierarchical porous structures from block copolymer-directed self-assembly. *Science* **349,** 54–58 (2015).

18. Lim, H., Kani, K., Henzie, J., Nagaura, T., Nugraha, A. S., Iqbal, M., Ok, Y. S., Hossain, Md. S. A., Bando, Y., Wu, K. C. W., Kim, H.-J., Rowan, A. E., Na, J. & Yamauchi, Y. A universal approach for the synthesis of mesoporous gold, palladium and platinum films for applications in electrocatalysis. *Nat. Protoc.* **15,** 2980–3008 (2020).

19. Yu, F., Zhang, Q., Thedford, R. P., Singer, A., Smilgies, D.-M., Thompson, M. O. & Wiesner, U. B. Block Copolymer Self-Assembly-Directed and Transient Laser Heating-Enabled Nanostructures toward Phononic and Photonic Quantum Materials. *ACS Nano* **14,** 11273–11282 (2020).

20. Basov, D. N., Averitt, R. D. & Hsieh, D. Towards properties on demand in quantum materials. *Nat. Mater.* **16,** 1077–1088 (2017).

21. Keimer, B. & Moore, J. E. The physics of quantum materials. *Nat. Phys.* **13,** 1045–1055 (2017).

22. Robbins, S. W., Beaucage, P. A., Sai, H., Tan, K. W., Werner, J. G., Sethna, J. P., DiSalvo, F. J., Gruner, S. M., Van Dover, R. B. & Wiesner, U. Block copolymer self-assembly–directed synthesis of mesoporous gyroidal superconductors. *Sci. Adv.* **2,** e1501119 (2016).

23. Thedford, R. P., Beaucage, P. A., Susca, E. M., Chao, C. A., Nowack, K. C., Van Dover, R. B., Gruner, S. M. & Wiesner, U. Superconducting Quantum Metamaterials from High Pressure Melt Infiltration of Metals into Block Copolymer Double Gyroid Derived Ceramic Templates. *Adv. Funct. Mater.* **31,** 2100469 (2021).
24. Beaucage, P. A., Van Dover, R. B., DiSalvo, F. J., Gruner, S. M. & Wiesner, U. B. Superconducting Quantum Metamaterials from Convergence of Soft and Hard Condensed Matter Science. *Adv. Mater.* **in press,** (2021).
25. Samarth, N. Quantum materials discovery from a synthesis perspective. *Nat. Mater.* **16,** 1068–1076 (2017).
26. Diao, Y., Shaw, L., Bao, Z. & Mannsfeld, S. C. B. Morphology control strategies for solution-processed organic semiconductor thin films. *Energy Env. Sci* **7,** 2145–2159 (2014).
27. Bailey, T. S., Pham, H. D. & Bates, F. S. Morphological Behavior Bridging the Symmetric AB and ABC States in the Poly(styrene- *b* -isoprene- *b* -ethylene oxide) Triblock Copolymer System. *Macromolecules* **34,** 6994–7008 (2001).
28. Werner, J. G., Hoheisel, T. N. & Wiesner, U. Synthesis and Characterization of Gyroidal Mesoporous Carbons and Carbon Monoliths with Tunable Ultralarge Pore Size. *ACS Nano* **8,** 731–743 (2014).
29. Yoneda, Y. Anomalous Surface Reflection of X Rays. *Phys. Rev.* **131,** 2010–2013 (1963).
30. Lengauer, W. & Ettmayer, P. Preparation and Properties of Compact Cubic δ-NbN1-x. *Monatsh Chem* **117,** 275–286 (1986).

31. Rudy, E., Benesovsky, F. & Sedlatschek, K. Untersuchungen im System Niob-Molybdän-Kohlenstoff. *Monatsh Chem* **92,** 841–855 (1961).
32. Zhernenkov, M., Canestrari, N., Chubar, O. & DiMasi, E. Soft matter interfaces beamline at NSLS-II: geometrical ray-tracing vs. wavefront propagation simulations. in (eds. Sanchez del Rio, M. & Chubar, O.) 92090G (2014). doi:10.1117/12.2060889
33. Li, Z., Hur, K., Sai, H., Higuchi, T., Takahara, A., Jinnai, H., Gruner, S. M. & Wiesner, U. Linking experiment and theory for three-dimensional networked binary metal nanoparticle-triblock terpolymer superstructures. *Nat Commun* **5,** 3247 (2014).
34. Zhang, Q., Matsuoka, F., Suh, H. S., Beaucage, P. A., Xiong, S., Smilgies, D.-M., Tan, K. W., Werner, J. G., Nealey, P. F. & Wiesner, U. B. Pathways to Mesoporous Resin/Carbon Thin Films with Alternating Gyroid Morphology. *ACS Nano* **12,** 347–358 (2018).
35. Guliyeva, A., Vayer, M., Warmont, F., Takano, A., Matsushita, Y. & Sinturel, C. Transition Pathway between Gyroid and Cylindrical Morphology in Linear Triblock Terpolymer Thin Films. *Macromolecules* **52,** 6641–6648 (2019).
36. Feng, X., Burke, C. J., Zhuo, M., Guo, H., Yang, K., Reddy, A., Prasad, I., Ho, R.-M., Avgeropoulos, A., Grason, G. M. & Thomas, E. L. Seeing mesoatomic distortions in soft-matter crystals of a double-gyroid block copolymer. *Nature* **575,** 175–179 (2019).
37. Mathur, M. P., Deis, D. W. & Gavaler, J. R. Lower Critical Field Measurements in NbN Bulk and Thin Films. *J. Appl. Phys.* **43,** 3158–3161 (1972).

38. Raine, M. J. & Hampshire, D. P. Characterization of the Low Temperature Superconductor Niobium Carbonitride. *IEEE Trans. Appl. Supercond.* **21,** 3138–3141 (2011).

39. Note that the value of Bc2 of 11 T reported in ref 35 is extrapolated using data taken from multiple types of measurements of ac-susceptibility, magnetic hysteresis, and heat capacity, in addition to resistivity that is the property probed in this work.

40. Gavaler, J. R., Janocko, M. A. & Jones, C. K. Superconducting Properties of Niobium Carbonitride Thin Films. *Appl. Phys. Lett.* **19,** 305–307 (1971).

41. Beloborodov, I. S., Lopatin, A. V., Vinokur, V. M. & Efetov, K. B. Granular electronic systems. *Rev. Mod. Phys.* **79,** 469–518 (2007).

42. Nigro, A., Nobile, G., Rubino, M. G. & Vaglio, R. Electrical resistivity of polycrystalline niobium nitride films. *Phys Rev B* **37,** 3970–3972 (1988).

43. Tyan, J.-H. & Lue, J. T. Grain boundary scattering in the normal state resistivity of superconducting NbN thin films. *J Appl Phys* **75,** 325–331 (1994).

44. Senapati, K., Pandey, N. K., Nagar, R. & Budhani, R. C. Normal-state transport and vortex dynamics in thin films of two structural polymorphs of superconducting NbN. *Phys. Rev. B* **74,** 104514 (2006).

45. Sanjinés, R., Benkahoul, M., Sandu, C. S., Schmid, P. E. & Lévy, F. Electronic states and physical properties of hexagonal β-Nb 2N and δ′-NbN nitrides. *Thin Solid Films* **494,** 190–195 (2006).

46. Kang, L., Jin, B. B., Liu, X. Y., Jia, X. Q., Chen, J., Ji, Z. M., Xu, W. W., Wu, P. H., Mi, S. B., Pimenov, A., Wu, Y. J. & Wang, B. G. Suppression of

superconductivity in epitaxial NbN ultrathin films. *J Appl Phys* **109,** 033908 (2011).

47. Bose, S. & Ayyub, P. A review of finite size effects in quasi-zero dimensional superconductors. *Rep. Prog. Phys.* **77,** 116503 (2014).
48. Taylor, D. M. J., Al-Jawad, M. & Hampshire, D. P. A new paradigm for fabricating bulk high-field superconductors. *Supercond. Sci. Technol.* **21,** 125006 (2008).
49. Tan, K. W. & Wiesner, U. Block Copolymer Self-Assembly Directed Hierarchically Structured Materials from Nonequilibrium Transient Laser Heating. *Macromolecules* **52,** 395–409 (2019).
50. Broholm, C., Fisher, I., Moore, J., Murnane, M., Moreo, A., Tranquada, J., Basov, D., Freericks, J., Aronson, M., MacDonald, A., Fradkin, E., Yacoby, A., Samarth, N., Stemmer, S., Horton, L., Horwitz, J., Davenport, J., Graf, M., Krause, J., Pechan, M., Perry, K., Rhyne, J., Schwartz, A., Thiyagarajan, T., Yarris, L. & Runkles, K. *Basic Research Needs Workshop on Quantum Materials for Energy Relevant Technology*. 1616509 (2016). doi:10.2172/1616509
51. Jiang, Z. GIXSGUI: a MATLAB toolbox for grazing-incidence X-ray scattering data visualization and reduction, and indexing of buried three-dimensional periodic nanostructured films. *J Appl Crystallogr* **48,** 917–926 (2015).
52. Pandolfi, R. J., Allan, D. B., Arenholz, E., Barroso-Luque, L., Campbell, S. I., Caswell, T. A., Blair, A., De Carlo, F., Fackler, S., Fournier, A. P., Freychet, G., Fukuto, M., Gürsoy, D., Jiang, Z., Krishnan, H., Kumar, D., Kline, R. J., Li, R., Liman, C., Marchesini, S., Mehta, A., N'Diaye, A. T., Parkinson, D. Y., Parks, H.,

Pellouchoud, L. A., Perciano, T., Ren, F., Sahoo, S., Strzalka, J., Sunday, D., Tassone, C. J., Ushizima, D., Venkatakrishnan, S., Yager, K. G., Zwart, P., Sethian, J. A. & Hexemer, A. *Xi-cam* : a versatile interface for data visualization and analysis. *J. Synchrotron Radiat.* **25,** 1261–1270 (2018).

53. Guliyeva, A., Vayer, M., Warmont, F., Takano, A., Matsushita, Y. & Sinturel, C. Transition Pathway between Gyroid and Cylindrical Morphology in Linear Triblock Terpolymer Thin Films. *Macromolecules* **52,** 6641–6648 (2019).
54. Wohlgemuth, M., Yufa, N., Hoffman, J. & Thomas, E. L. Triply Periodic Bicontinuous Cubic Microdomain Morphologies by Symmetries. *Macromolecules* **34,** 6083–6089 (2001).
55. Webster, J. G. & Eren, H. *Measurement, instrumentation, and sensors handbook: electromagnetic, optical, radiation, chemical, and biomedical measurement*. (CRC press, 2017). at <https://webapps.unitn.it/Biblioteca/it/Web/LibriElettroniciDettaglio/125813>

CHAPTER 4

TUNABLE PLURONIC SELF-ASSEMBLY BASED QUANTUM MATERIALS: MESOPOROUS SUPERCONDUCTORS MADE EASY[⊥]

We report the synthesis of ordered mesoporous niobium carbonitride superconductors from self-assembly of Pluronic-family block copolymers with a niobium(V) ethoxide-based sol in ethanol. Resulting mesoscale hexagonal cylinder-forming nanocomposites are first converted to atomically amorphous, mesoporous niobium oxide monoliths via calcination in air to 400 ˚C. A sequence of heat treatments of porous oxides in reactive gases to at least 750 ˚C and as high as 850 ˚C then produces phase-pure niobium carbonitride superconductors while maintaining mesoscale order. Architectural parameters such as mesopore diameter and wall thickness are tunable via selection of templating agents and pore expanders. This broadly accessible Pluronics-based method enables mesostructure-property correlation studies in the emerging field of quantum metamaterials, and paves the way for studies into the confinement of guest species in tailorable mesoporous superconductors.

[⊥]R. Paxton Thedford*, Corson A. Chao*, Fei Yu, William R. Tait, Dana Chapman, Peter A. Beaucage, Guillaume Freychet, Mikhail Zhernenkov, Sarah A. Hesse, Christopher J. Tassone, Katja C. Nowack, Sol M. Gruner, and Ulrich Wiesner. (*In preparation)* 2022

Introduction

Block copolymers (BCPs) have been investigated for structure direction of ordered mesoporous materials (OMMs) in applications ranging from catalysis to energy storage to drug delivery,[1,2] and recently into quantum materials synthesis.[3–7] First observations in the emerging field of BCP-derived superconducting quantum metamaterials suggest that mesostructure fundamentally alters quantum-level characteristics thereby controlling macroscopic property profiles.[6,7] Furthermore, polymer solution-based synthetic approaches to quantum materials avoid stringent experimental conditions as are found in e.g., high vacuum growth techniques; this allows for direct lithographic patterning,[8] and may open up access to hitherto unavailable sample form factors. Soft matter enabled quantum materials thus hold substantial academic and technological promise; one could envision a trajectory similar to organic semiconductors.[9,10]

To date BCP structure direction of superconductors has been achieved using relatively high-molar mass custom-made triblock terpolymers, e.g., in the form of poly(isoprene-*b*-styrene-*b*-ethylene oxide) (ISO).[5,6] For a broad range of mesoporous metal oxides, the commercially available Pluronics family of poly(ethylene oxide-*b*-propylene oxide-*b*-ethylene oxide) (PEO-PPO-PEO) ABA triblock copolymers[11–15] has allowed for highly precise structural tunability,[11,16–19] and control over host-guest interactions within OMMs.[20–23] It remains challenging, however, to create highly crystalline non-oxides with Pluronic copolymers in the absence of carbonaceous additives or chemical functionalization due to the small pore wall thickness of resulting inorganic materials.[24–26] For example in 2017 Wei *et al.*[1] remarked that "…*[ordered*

mesoporous] metal carbides, nitrides and sulfides can hardly be achieved by the commercial Pluronic templates." In the same year we reported synthetic routes from Pluronic-directed oxides to transition metal nitrides using ammonia (NH_3),[27] but the resulting materials were not of high enough quality to reach the superconducting state.

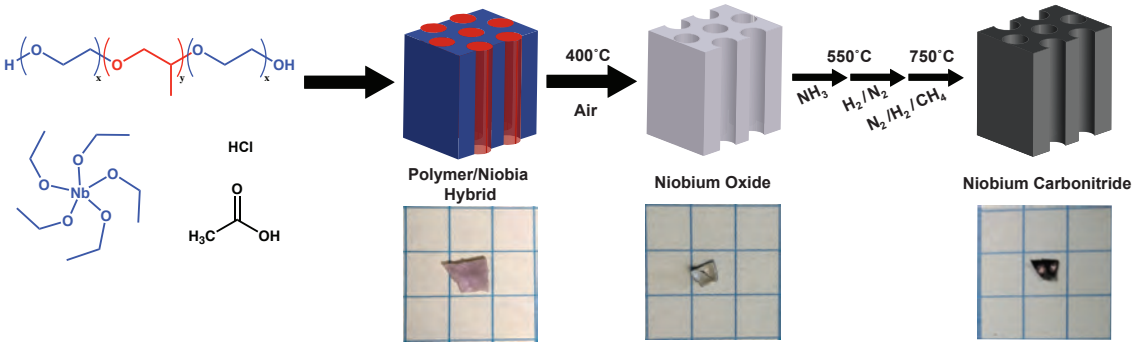

Figure 4.1: *Synthesis route to a mesoporous superconducting CUS-86 NbCN via co-assembly of Pluronic F127 with a niobium(V) ethoxide-derived sol (top row). Photographs of materials on quarter-inch grid paper (bottom row).*

Here we report the successful synthesis of mesoporous superconductors with hexagonal order (referred herein as CUS-86, followed by the maximum processing temperature) using BASF Pluronic BCPs and a specific multistep heating protocol involving multiple gas mixtures in addition to ammonia, motivated by recent studies with larger molar mass ISO BCPs (Figure 4.1).[6] For example, a mesostructured Pluronic F127-niobia composite is first prepared via evaporation of an acetic and hydrochloric acid catalyzed niobium(V) ethoxide sol-gel/polymer solution in ethanol.[27] The as-made material is calcined in air at 400˚C to remove organic components and produce

amorphous niobium oxide monoliths. Conversion to the final superconducting carbonitride is then achieved in multiple steps: the oxide is first heated at 5˚C per minute to 550˚C in a tube furnace under flowing ammonia for 3 hours; remaining at that temperature, the tube is then purged with dilute forming gas (H_2/N_2) for 30 minutes. Finally, the resulting nitride is directly heated at 20˚C per minute to at least 750˚C for 90 minutes and then allowed to passively cool, all under carburizing gas ($CH_4/H_2/N_2$; see Supplementary Information for details).

Results and Discussion

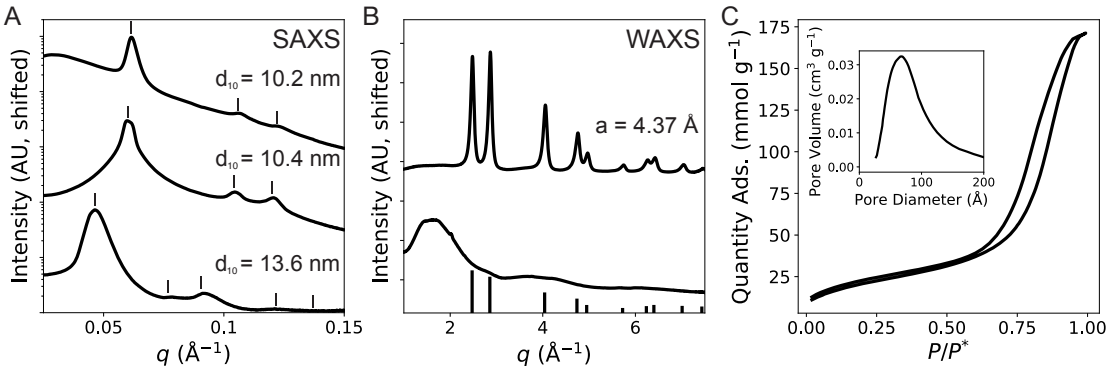

Figure 4.2: *SAXS/WAXS and N_2 sorption characterization results for Pluronic F127-derived CUS-86-750˚C at various processing stages. (A) SAXS profiles of the as-made polymer-niobia hybrid (bottom), oxide (middle), and CUS-86-750˚C NbCN (top). (B) WAXS profiles of the oxide (bottom) and CUS-86-750˚C (top). Black ticks along the bottom denote expected peak positions and intensities for NbN (PDF #03-065-0436).*[28,29] *(C) N_2 sorption isotherm for CUS-86-750˚C. Inset: BJH-derived pore size distribution.*[30]

Synchrotron small-angle and wide-angle X-ray scattering (SAXS/WAXS)[31] patterns of materials at different synthesis stages are displayed in Figure 4.2. Observed

SAXS peak positions are consistent with hexagonal lattices with d_{10} spacings of 13.6 nm, 10.4 nm, and 10.2 nm for hybrid, oxide, and carbonitride (NbCN), respectively (Figure 4.2A, Figure 4.S1). Shrinkage of the hexagonal structure from the hybrid to oxide during calcination agrees with previous studies.[15] Further changes in lattice characteristics upon transitioning from oxide to carbonitride are minimal. In Figure 4.2B, the oxide appears atomically amorphous, consistent with previous observations.[15,27] Processing of this parent mesoporous oxide up to 750˚C (vide infra) produces crystalline NbCN consistent with a rock-salt structure (space group $Fm3m$) of lattice constant 4.37 Å. This is lower than reported values for high temperature synthesis of NbN (4.39 Å)[28] or NbC (4.47 Å)[32] due to the retention of oxygen and vacancies,[5,27] the latter of which niobium nitrides may be particularly prone to contain.[33] The upper bound for coherent scattering domain size of the atomic NbCN lattice is calculated via Debye-Scherrer analysis to be 4.4 nm. This crystallite size is consistent with the minimal grain growth and reactive re-precipitation model reported previously,[6] and smaller than the pore wall thickness (vide infra).

The nitrogen isotherm shown in Figure 4.2C of F127-derived CUS-86-750˚C carbonitride supports the existence of regular open mesopores, showing type IV(a) behavior with H1 hysteresis[34] with a surface area of 79 m^2 g^{-1}.[35] The pore size distribution obtained via BJH analysis is shown in the inset of Figure 4.2C.[30] The average mesopore diameter of 6.6 nm was determined using the adsorbed gas volume at the end of capillary condensation and the BET-derived surface area.[36] Scanning and transmission electron microscopy (SEM/TEM) images of CUS-86-750˚C (Figure 4.3) corroborate the conclusions from SAXS and nitrogen sorption that the carbonitride

maintains a high degree of hexagonal order with accessible mesopores. SEM determined final thickness of CUS-86 monoliths was of order 130 μm (Figure 4.S2).

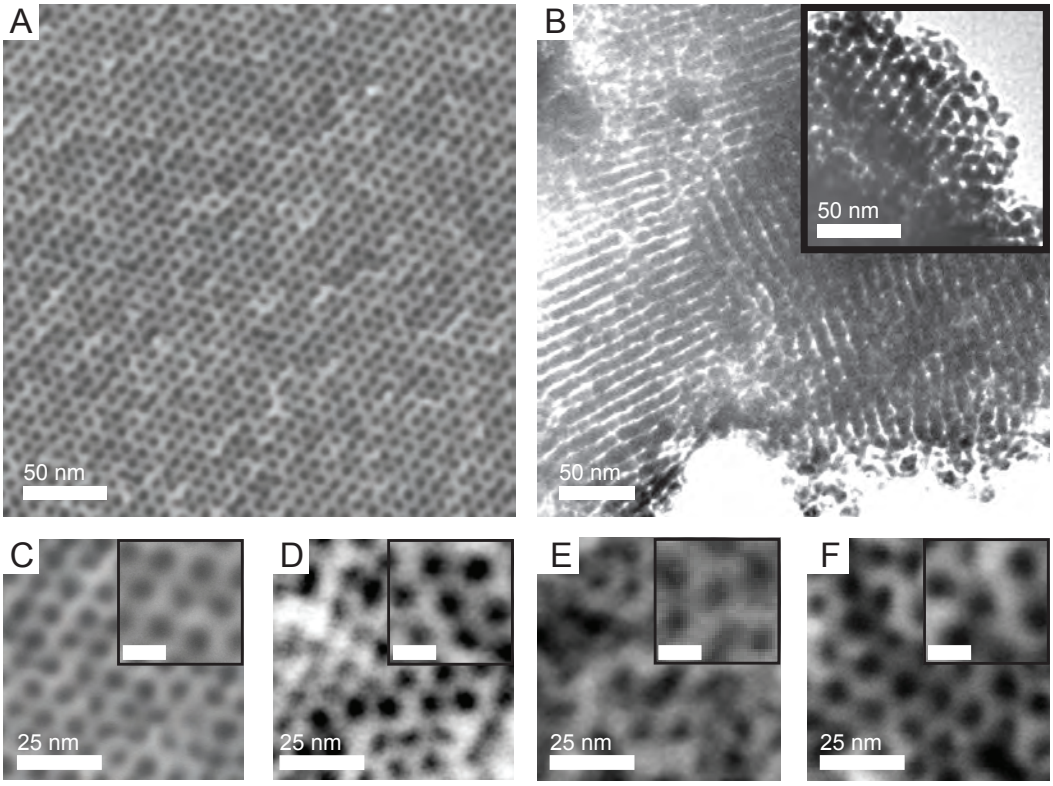

Figure 4.3: *Electron microscopy characterization of CUS-86-750˚C synthesized with various Pluronic templating agents and pore expanders. (A,B) SEM (A) and TEM (B) micrographs of Pluronic F127-derived mesoporous NbCN (Table 1, first entry). As shown in (B), the hexagonal mesophase is typically polycrystalline. (C-F) Higher magnification SEM images of (C) Pluronic F127-derived CUS-86-750˚C; (D) CUS-86-750˚C synthesized using F127 with PPG as a pore expander (Table 1, second entry); (C) CUS-86-750˚C synthesized using Pluronic F108 (Table 1, third entry); (F) CUS-86-750˚C synthesized using Pluronic F108 and TiPB as a pore expander (Table 1, fourth entry). Insets in C-F show slightly magnified SEM images; scale bars in each correspond to 10 nm. In all SEM images, focus is on cylinders approximately parallel to the beam direction.*

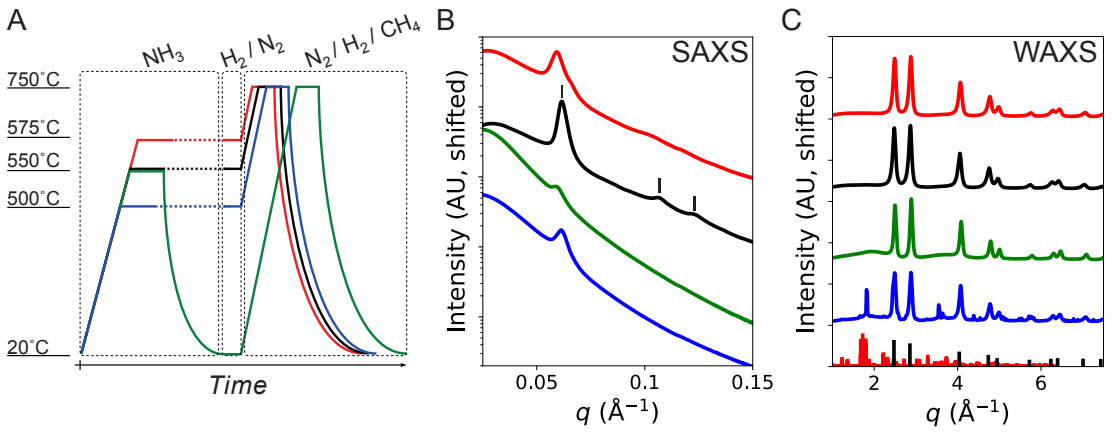

Figure 4.4: *The effect of thermal processing on final carbonitride structure. (A) Color coded schematic of thermal processing protocols, with dashed lines denoting temporal jumps forward. (B,C) SAXS (B) and WAXS (C) traces for the final carbonitride materials, assigned by color to the respective heating protocols as shown in (A). Black and red tick marks along the bottom correspond to the expected peak positions and intensities for NbN (PDF #03-065-0426)*[28,29] *and h-*Nb_2O_5,[37] *respectively.*

Successful conversion of mesoporous oxides into phase-pure NbCN with retained hexagonal order required careful optimization. Figure 4.4 shows SAXS and WAXS results for four carbonitrides produced from the same F127-derived parent oxide using different processing protocols (Figure 4.4A). Heating an oxide at 20˚C per minute to 500 ˚C in ammonia for 3 hours (see ESI for details) results in incomplete nitridation, and upon further treatment in carburizing gas at 750˚C a crystalline oxide phase is formed in addition to a NbCN phase (Figure 4.4C, blue trace). This disrupts the mesostructure, resulting in the disappearance of higher order SAXS peaks and decrease in primary peak intensity (Figure 4.4B, blue trace). On the path to CUS-86-750˚C,

treatment of the oxide instead to 550˚C in ammonia more fully converts the material, and upon carburization a phase-pure NbCN forms (Figure 4.4C, black trace) with a coherent scattering domain size of the atomic lattice of 4.4 nm (vide supra). Carburization must take place immediately following nitridation to successfully produce CUS-86. Cooling of the nitride to room temperature instead, and then re-heating during carburization results in a longer total processing time under the different gases. This increases the coherent scattering domain size to 6.2 nm (Figure 4.4C, green trace) and leads to a near total loss of mesostructure as suggested from SAXS (Figure 4.4B, green trace). Further, the final unit cell parameter of the carbonitride in the cooling/re-heating case is 4.34 Å, slightly lower than that of CUS-86-750˚C (4.37 Å). This points to the material stoichiometry (of the form $NbC_xN_yO_z[]_{1-x-y-z}$, where [] denotes vacancies) as more nitrogen rich in the case of the cooled nitride (green traces), which dwelt longer in an ammonia atmosphere during cooling, as compared to CUS-86-750˚C (black traces).[32] This is corroborated by nitridation occurring at a slightly higher temperature of 575˚C followed directly by carburizing treatment (Figure 4.4, red traces) also resulting in a final carbonitride with a slightly lower unit cell parameter of 4.36 Å (Figure 4.4C, red trace). Nitridation at 575˚C leads to a larger coherent domain size of 4.9 nm, however, and degradation of the hexagonal order (Figure 4.4B, red trace). These results together suggest that grain growth and mesostructure disruption occur primarily during nitridation, but that there exists a stoichiometric threshold which must be reached to prevent co-crystallization of niobium oxide during carburization.

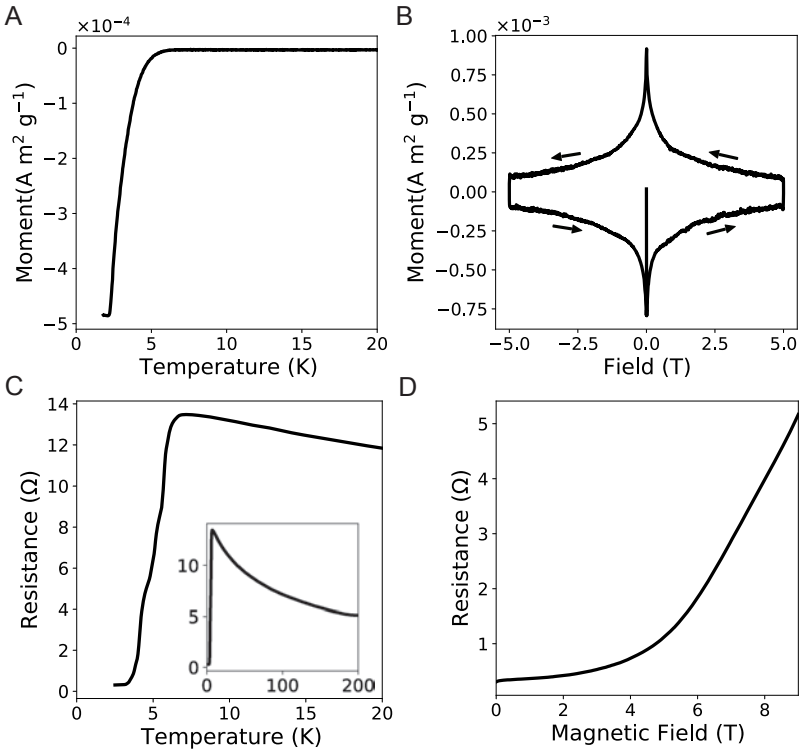

Figure 4.5: *Characterization of Pluronic F127-derived CUS-86-750˚C by Vibrating Sample Magnetometry (VSM) and DC transport. (A) VSM magnetic moment in a 10 mT external field from 2 to 20 K. (B) VSM magnetization loop up to ± 5 T performed at 2 K. Arrows denote field scanning direction. (C) DC 4-point resistance from 2 to 20 K with no external applied field. Inset, resistance measurement from 2 to 200 K. (D) Magnetoresistance measurement conducted at 2 K.*

At low temperatures F127-derived CUS-86-750˚C transitions into a superconducting state (Figure 4.5), displaying a Meissner state below a $T_c \approx 6$ K (Figure 4.5A).[38] This behavior was consistent between multiple separate sample batches and after prolonged storage in air (Figure 4.S3). CUS-86-750˚C exhibits a clear Type-II hysteresis typical of NbN and NbCN superconductors (Figure 4.5B).[5,39,40] As CUS-86-

750˚C is cooled from 200 K towards the superconducting transition, a precipitous rise in resistance occurs (Figure 4.5C, inset); this behavior is indicative of a thermally activated mechanism of transport in the nanocrystalline, granular material (see also Figure 4.S4),[41,42] and agrees with previous studies on mesoporous thin film NbCN.[8] A sharp drop in resistance begins close to the T_c ≈6 K seen in VSM. During this drop several slope changes are evident (e.g., at 5 K), indicating multiple transitions and pointing to non-uniformities within the sample (Figure 4.5C). Magnetoresistance measurements at 2 K of CUS-86-750˚C show a broad recovery to the normal state resistance with a distinct slope change around 5 T (Figure 5D), an approximate measure of the low temperature critical field. It has been well established that critical parameters such as upper critical field or transition temperature in NbCN are a function of material composition[39,43–46]; critical temperature and field strength in CUS-86-750˚C is lower than in traditionally synthesized NbCN ($T_c \approx 17.3$ K, $B_{c2} \approx 11$ T)[39]. Along with the multiple transitions in Figure 5C, this speaks to a high content of vacancies and oxygen as well as chemical inhomogeneity. Along with fluctuations[47] or difficulties in contacting the sample (see Experimental section, Figure S5), this might also explain the residual resistance observed below T_c.

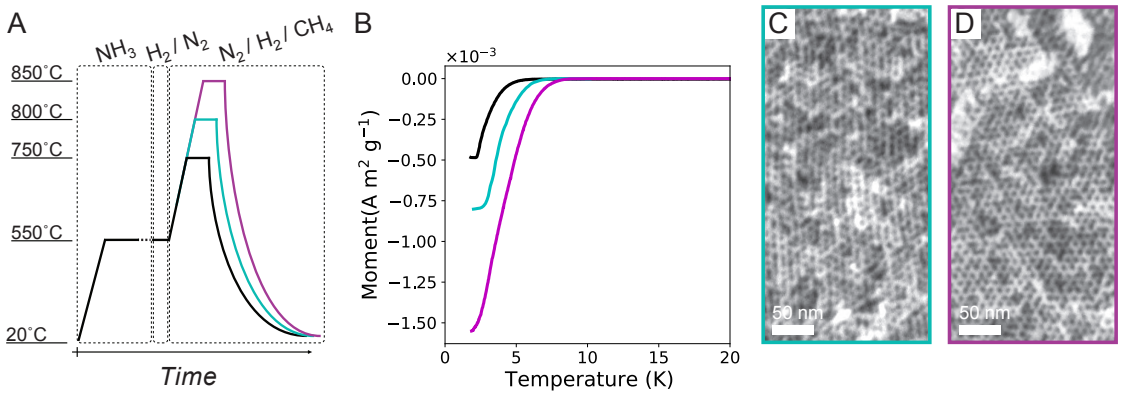

Figure 4.6: *The effect of increased carburization temperature on CUS-86. (A) Color-coded thermal processing schematic of carbonitrides produced from the same parent oxide. (B) VSM magnetic moment from 2 to 20 K under a 10 mT external field for CUS-86 materials synthesized according to A. (C&D) SEM micrographs of CUS-86 as synthesized according to A.*

While earlier in this report we focus on establishing the minimum thermal processing conditions to preserve mesostructure and achieve superconductivity, carburization temperature may be increased beyond 750˚C. In Figure 4.6A, black traces show the method for producing CUS-86-750˚C as characterized in Figure 4.2 and Figure 4.4, heating to 750˚C in carburizing gas. In cyan and magenta are shown procedures in which, after nitridation at 550˚C in ammonia, material is heated to 800 or 850 ˚C, respectively, in carburizing gas. This systematically increases the temperature at which CUS-86 transitions into the Meissner state, up to ≈8 K for CUS-86-850˚C, as well as the maximum magnetization at 2K (Figure 4.6B). The improvement in superconductor properties demonstrates that higher processing temperatures improve NbCN crystal quality, but as shown in Figure 4.6C and D the hexagonal mesostructure is unaffected. This provides further evidence for previous work which found that no significant grain

growth occurs in mesoporous NbCNs below 1100˚C.[6] As a additional note, further experiments find that hexagonally mesoporous superconductors are obtainable without the use of an intermediate forming gas step (Figure 4.S6, orange).

Finally, to demonstrate mesostructure tunability in CUS-86 carbonitrides, we employed Pluronic F108 as well as F127 and pore expanders poly(propylene glycol) monobutyl ether (PPG, $M_n \approx 1{,}000$ g mol^{-1}), or triisopropylbenzene (TiPB). Characterization results (Figure 4.2A, Figure 4.3D-F, Figure 4.S7-8) are summarized in Table 4.1.

Pluronic template	Formula	Additive	Mass ratio Pluronic: Additive	d_{100} (nm)	pore size‡ (nm)	surface area‡ (m^2/g)	Wall thickness (nm)	Onset T_c** (K)
F127	$EO_{99}PO_{65}EO_{99}$	-	-	10.2*	6.7	79	5.1§	6
		PPG	4 : 1	10.8†	7.7	64	4.8¶	7
F108	$EO_{133}PO_{49}EO_{133}$	-	-	10.9†	5.3	76	7.3¶	6.5
		TiPB	4 : 1	11.3†	7.8	49	5.2¶	6

Table 4.1: *Characteristics of Pluronic family block copolymer derived CUS-86-750˚C materials.*

* *Determined by SAXS.*

† *Determined by SEM.*

‡ *Determined by nitrogen sorption.*[36]

§ *Derived from SAXS & nitrogen sorption*

¶ *Derived from SEM & nitrogen sorption.*

** *Determined by VSM.*

Conclusion

In summary, we report a successful protocol for the synthesis of the mesoporous superconductor CUS-86 using commercially available, low molar mass Pluronic triblock copolymers. Carefully optimized thermal processing of BCP templated niobium oxides overcomes a longstanding challenge in the field of Pluronics derived OMMs to produce crystalline NbCN while retaining hexagonal mesostructure up to processing temperatures of 850˚C. The achieved crystal quality is such that CUS-86 becomes superconducting below a T_c of up to ≈8 K and B_{c2} of ≈5 T. Mesophase lattice parameter, mesopore diameter, surface area, and wall thickness can be varied through choice of Pluronic BCP and pore expander. The demonstrated ability to finely shim through structural parameters enables detailed mesostructure-property correlation studies in the emerging field of quantum metamaterials. We also expect this report will be of broad interest to the mesoporous materials community for the study of organic or inorganic guest species confined in this previously inaccessible superconducting nitride class of Pluronics-derived OMMs.

Supplementary Information for Chapter 4

Materials and Methods

Niobium(V) ethoxide (99.999% metals basis) was obtained from Alfa Aesar (Ward Hill, MA, USA). Pluronic F127, Pluronic F108, poly(propylene glycol) monobutyl ether (PPO) (average M_n~1,000 g/mole), triisopropylbenzene (TiPB) (95%), and ethanol (anhydrous) were obtained from Sigma-Aldrich (St. Louis, MO, USA). Acetic acid (glacial) and hydrochloric acid (37%) were obtained from Fisher Scientific (Hampton, NH, USA). Ammonia (electronic grade, 99.9995%), forming gas (4% hydrogen, balance nitrogen, certified standard), carburizing gas (4% hydrogen, 16% methane, balance nitrogen, certified standard) and nitrogen (ultra-high purity, 99.999%) were purchased from Airgas (Radnor, PA, USA). All materials were used as received.

Unless otherwise stated, in a typical synthesis procedure 0.40 g of Pluronic F127, 0.285 mL of acetic acid, and 0.236 mL of hydrochloric acid were added to 7.5 mL of ethanol in a 20 mL glass scintillation vial with a Teflon lined cap. For trials using F108 Pluronics, 0.4 g of F108 polymer was used instead of F127. For trials in which pore expanders were used, 0.100 g of TiPB or PPO was then added. For the trials corresponding to SAXS images shown in Figure 4.S1A & C, 0.265 mL of hydrochloric acid was used instead. Solutions were stirred until all components fully dissolved, for a time greater than 3 hours but not exceeding 5 hours. 0.625 mL of niobium (V) ethoxide was then added to the solutions dropwise under vigorous stirring, at which point the solutions were seen to adopt a pale yellow color. Solutions were then stirred for a period of time greater than 11 hours but not exceeding 12 hours, under stirring conditions which produced a regular vortex within the vials. At the end of this time, solutions were

immediately poured into 4 cm diameter teflon beakers and placed atop a glass evaporation dish on a hotplate set to 40˚C. A hemispherical glass dome was then placed over the teflon beakers to form a loose seal against the bottom glass dish. Solutions were then allowed to evaporate unperturbed until visually appearing to be completely dry, a process which took place over 2-3 days. Upon drying, a solid films were observed at the bottom of the teflon beaker. In a variety of cases the appearance of these film ranged from a transparent, glass-candy-like orange-yellow to a completely opaque eggshell colored film. Dried films were heated to 130˚C, either atop the hotplate on which evaporation was performed or separately in an oven at ambient pressure, for a period of 6-10 hours. After cooling, films could easily be removed from teflon beakers for subsequent thermal processing. At this stage the as-made polymer/inorganic composite films were measured with a micrometer screw gauge to be ≈200 μm in thickness. After thermal processing was complete, this resulted in a final CUS-86 monolith thickness of order 130 μm (Figure 4.S2). It is expected that this thickness should be easily tunable by varying of the evaporation dish size or by using processing methods such as spray, dip, or spin-coating.

All further thermal processing took place in a Lindberg (Riverside, MI, USA) model 55035 tube furnace using a 1” quartz tube and a custom-built gas manifold with electronically actuated valves for automatic gas switching. As-made polymer-niobia hybrid monoliths were placed into a quartz crucible and set in the tube furnace centered directly over the thermocouple, and the tube was left open to air. Calcination then proceeded by heating the as-made composite in ambient air at a rate of 1˚C per minute to 400 ˚C, at which temperature the samples dwelt for 3 hours. The system was then

allowed to cool to room temperature statically, at an average rate of approximately 25˚C per minute. During the conversion to the oxide, hybrid monoliths appeared to shrink irregularly and crack on occasion, but often retained their overall macroscopic shape and monolithic form as shown in Figure 4.1. Visually white oxides were then heated under controlled gas atmospheres, with a gas flow rate of 10 L/min in all cases. To produce the superconducting CUS-86-750˚C as shown in Figures 4.2, 4.3A-C, 4.4 (black traces), 4.5, 4.6, 4.S1-5, and 4.S6-8 (black traces) the following protocol was followed. Oxide monoliths were first heated under flowing ammonia at a rate of 5 ˚C per minute to 550 ˚C and held at this temperature for 3 hours. The gas atmosphere was then switched to flowing forming gas while the tube temperature was maintained at 550 ˚C for 30 minutes. After this point the gas was switched to carburizing gas and the tube was heated at a rate of 20 ˚C per minute to 750 ˚C and held at this temperature for 90 minutes. The tube was then allowed to statically cool under flowing carburizing gas, at an observed average rate of 25 ˚C per minute. Upon cooling below 100 ˚C, the gas atmosphere was then switched to flowing nitrogen for a period of two hours in order to disperse any remaining methane in the system. Final carbonitride samples appeared visually black and slightly reflective.

In various protocols as depicted in Figure 4.4A and Figure 4.6A, modifications were made to this thermal treatment protocol. For the materials depicted by the blue and red traces in Figure 4.4, the oxide was initially heated to 500 ˚C or 575 ˚C, respectively, under flowing ammonia; all other parts of the protocol remained the same. For the material depicted by the green traces in Figure 4.4, the sample was allowed to cool statically to room temperature after the nitridation step, after which the tube was purged

with forming gas while at room temperature for 30 minutes, before proceeding through the carburizing step as previously described. The data shown in the orange trace of Figure 4.S6 was obtained for materials made without the use of an intermediate forming gas step; carburizing gas was instead used to purge the tube for 30 minutes at 550 ˚C after ammonia treatment before heating to 750 ˚C in carburizing gas. In Figure 4.6, materials shown in cyan or magenta were heated after a forming gas purge step to 800 or 850 ˚C, respectively, instead of 750 ˚C during the treatment under carburizing gas. All other ramp rates and dwell times remained unchanged.

Nitrogen sorption measurements were conducted on a Micromeritics (Norcross, GA, USA) ASAP 2020 Accelerated Surface Area and Porosimetry System. Powdered CUS-86 samples were degassed for 24 hours at 120 ˚C prior to measurement. Pore size distributions shown in the inset of Figure 4.2C, and in Figure 4.S7 were calculated via the Barrett-Joyner-Halenda[30] method. Average mesopore diameter was calculated by dividing the volume of nitrogen adsorbed at the end of capillary condensation by the total BET area measured.[36]

Small- and wide-angle X-ray scattering (SAXS/WAXS) data were obtained at the National Synchrotron Light Source (NSLS-II) Soft Matter Interfaces (SMI) beamline in a transmission geometry using an incident X-ray energy of 16.1 keV and beam size of 20 μm by 200 μm. Monolithic sample flakes were oriented with the flat faces roughly perpendicular to the incident beam, such that the volume illuminated passed through the entire thickness of the ≈ 130 μm thick pieces (Figure 4.S2). SAXS patterns were obtained with a Dectris (Baden-Daettwil, CH) Pilatus3 1M pixel array detector at a sample-to-detector distance of 5 m. It was observed that hexagonal

mesophase texture and orientation as probed by SAXS varied greatly between batches of CUS-86 prepared under the same conditions (Figure 4.S1). WAXS patterns were obtained with a Pilatus3 300 K-W detector at a distance of 274 mm, which was rotated about a goniometer arc to record multiple images spanning scattering angles from -3.5˚ to 62˚. Individual WAXS frames were stitched (see Figure 4.S4), and the composite WAXS images as well as SAXS images were processed and integrated into intensity vs. q profiles using customized python codes at SMI.[48] Primary peak position and expected reflections for SAXS traces were determined using customized additions for the Nika package in Igor Pro.[49] Scherrer analysis to determine coherent scattering domain size was performed with JADE software using the first five apparent peaks in the WAXS traces, a shape factor of 0.93, and a pseudo-Voigt profile.

Additional SAXS and WAXS data not shown in this report were collected at the Stanford Synchrotron Radiation Lightsource (SSRL). Small-angle X-ray scattering (SAXS) was performed at the SSRL beamline 1-5. The beamline was configured to use 12 keV (1.033 Å) X-rays with a slit defined beam size of 300 by 300 μm. A Rayonix SX165 CCD area detector was used to collect the data in a transmission geometry. The nominal distance of the detector was 2859 mm downstream of the sample as determined by a silver behenate reference. Wide-angle X-ray scattering (WAXS) was performed at the SSRL beamline 11-3. The X-ray beam energy was 12.7 keV (0.976 Å) with a slit defined beam size of 150 by 150 μm. The data was collected with a 2D Rayonix MX225 CCD area detector in transmission geometry. The sample to detector distance was either 146 mm or 246 mm downstream of the sample as determined by a lanthanum hexaboride standard.

CUS-86 materials were prepared for SEM by affixing to aluminum sample stubs using double sided conductive carbon adhesive tape (Electron Microscopy Services), and then broken such that a freshly cleaved surface could be imaged. SEM images were captured with a Zeiss (Oberkochen, DE) Gemini series inlens energy selective backscattered (EsB) electron detector using a Zeiss GeminiSEM 500 operating at 2 kV accelerating voltage. Coating with gold−palladium prior to imaging is optional. Materials were prepared for TEM by first hand grinding to a powder with a mortar and pestle, followed by sonication in ethanol and deposition on a copper TEM grid (Electron Microscopy Sciences; Hatfield, PA, USA). Transmission electron micrographs were obtained using an FEI (Hillsboro, OR, USA) F20 TEM/STEM operating at 200 kV.

VSM data were obtained on a Quantum Design (San Diego, CA, USA) Dynacool Physical Property Measurement System (PPMS) equipped with the VSM add-on, a cryostat capable of temperatures from 1.8-400K, and a 9T superconducting magnet. The mass of CUS-86 samples were measured using a Cahn 28 automatic electrobalance, and then the monolithic flakes were mounted onto quartz rods using Lakeshore cryogenic varnish. Quartz sample mounts were then press fit into brass holders such that CUS-86 monoliths were oriented perpendicular to the external magnetic field. Samples were cooled to 2K under zero external field, and then a magnetic field of 10 mT was applied to locate sample position within the VSM pickup coils. Once centered in the coils, sample temperature was ramped to 20K at a rate of 1 K per minute while measuring the magnetic moment with an averaging time of 1 second per data point. For field dependent magnetization measurements, the samples were

cooled to 2K under zero field, and the external field ramped to 5 T, then to -5 T, and back to 0 T at a rate of 5 mT per second. Sample magnetic moment was measured during this field scan with an averaging time of 1 second per measurement. In all measurements, the magnetic moment was normalized to sample mass and at each data point relative error was observed to be at least one order of magnitude less than the reported value.

Four-point resistance measurements were conducted on a Quantum Design PPMS equipped with a 9 T magnet and an EverCool II helium reliquefier. CUS-86-750˚C monoliths were mounted using Stycast 2850FT epoxy onto silicon carrier chips pre-patterned with four gold contact pads. 503 silver conductive paint (Electron Microscopy Sciences) was used to make four colinear contacts on the CUS-86-750˚C monolith to the gold contact pads (Figure 4.S5). During this process of mounting samples and contacting with silver paint, it was observed that samples fractured easily, and that multiple attempts of fabricating silver paint traces had to be made before resulting in a sample with four working contacts. This speaks to the non-trivial process of forming good electrical contacts with the uneven, porous surface of CUS-86 monoliths.

The silicon carrier chip contacting a CUS-86-750˚C monolith was mounted onto a Quantum Design resistivity sample puck using cryogenic varnish and a Westbond model 7400E wedge−wedge ultrasonic/thermosonic wire bonder. Resistance values were measured using an excitation current of 100 μA while cooling to 2K at a rate of 2 K per minute. For magnetoresistance measurements, the sample temperature was held at 2K and the resistance similarly measured while ramping the external field to 9 T at a

rate of 10 mT per second. At each data point the average of 5 measurements was taken to be the reported resistance value, with a relative error at least three orders of magnitude less than the reported value in every case. After the process of cooling and reheating the sample, it was found that several silver paint contacts were disrupted and became electrically isolated.

Supplemental Figures

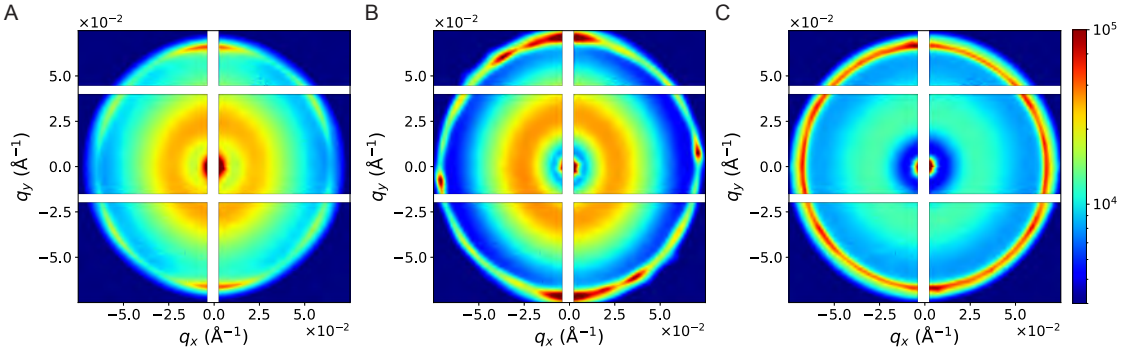

Figure 4.S1*: 2D SAXS diffraction images of three separate batches of CUS-86-750˚C made with F127 Pluronics under various conditions (see methods). (A) Pattern of a primarily single domain in the illuminated 20 µm by 200 µm x-ray beam. Pattern is indicative of a hexagonally packed cylinder mesophase with a d_{10} = 10.7 nm, in which the long axis of the cylinders is oriented roughly parallel to the incident beam but with a globally preferred tilt about an axis perpendicular to the beam.*[50] *(B) 2D SAXS image which was azimuthally integrated to produce the top trace of Figure 4.2A and black trace of Figure 4.4B. The pattern appears to show 3 separate domains of the form described in (A), but with varying orientations and a d_{10} = 10.2 nm. (C) Azimuthally symmetric pattern indicative of randomly oriented hexagonal domains with a d_{10} = 10.6 nm. Right: log scale intensity color map for A-C.*

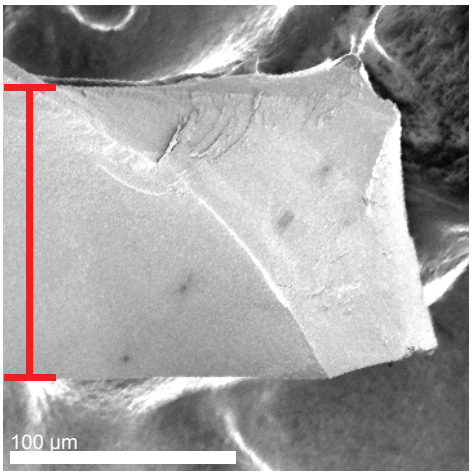

Figure 4.S2*: Representative low magnification cross-section SEM micrograph of the right most edge of a CUS-86-750˚C NbCN monolith, showing a thickness on the order of 130 µm. Red inset visual aide demonstrates the cross-sectional thickness of 130 µm on the horizontally oriented sample.*

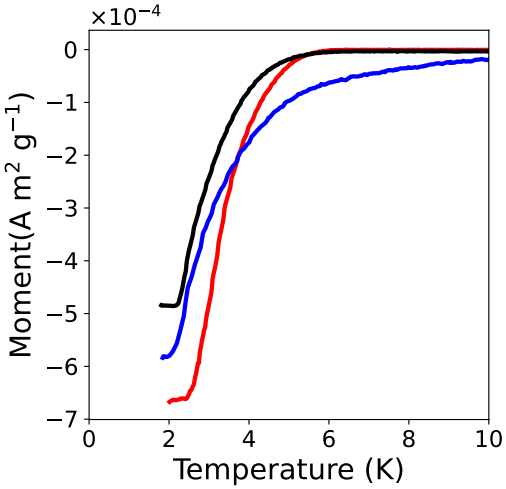

Figure 4.S3: *VSM magnetic moment in an external magnetic field of 10 mT from 2-20 K for three separate batches of CUS-86-750˚C made with Pluronic F127 (Table 1, first entry) according to the 550 ˚C in ammonia, 750 ˚C in carburizing gas protocol described in the methods: batch measured ~3 weeks after synthesis (black trace, identical to Figure 4.5A), a batch measured ~4 weeks after synthesis and synchrotron X-ray measurement (blue trace), and a batch measured ~3 months after synthesis (red trace).*

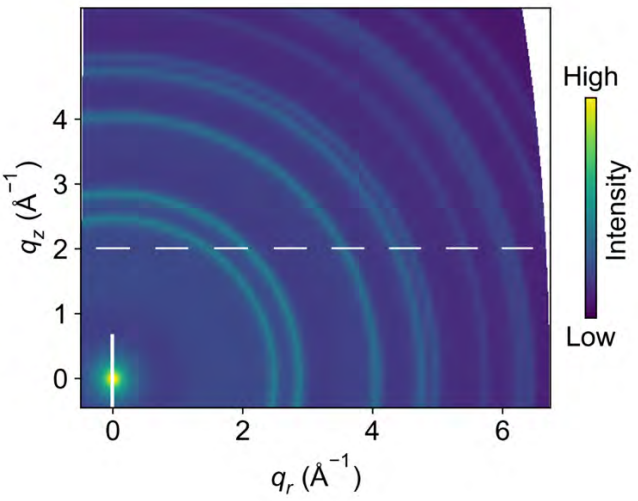

Figure 4.S4: *Composite 2D WAXS image of F127-derived CUS-86-750˚C (see Methods). The azimuthal integration of this dataset is depicted in Figure 4.2B (top trace) and Figure 4.4C (black trace). The broad and azimuthally isotropic diffraction peaks are indicative of a polycrystalline sample with a relatively small coherent scattering domain size.*

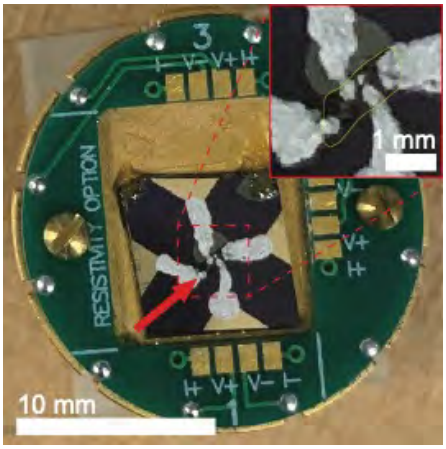

Figure 4.S5: *Photograph of CUS-86-750˚C contacted with silver paint and mounted onto PPMS resistivity puck prior to DC transport measurements. Red inset arrow points approximately at the bottom left point of the contacted sample and along the direction of its orientation. Top right inset shows an enlarged region, with a yellow line approximately outlining the CUS-86-750˚C sample.*

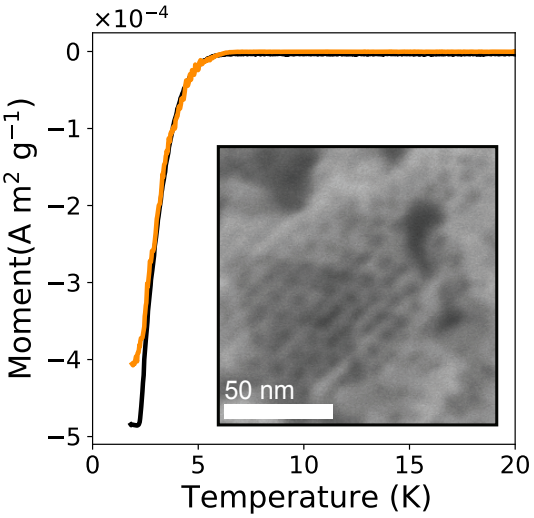

Figure 4.S6*: Characterization of F127-derived CUS-86-750˚C carbonitride synthesized using standard conditions (see black trace in Figure 4.4A) but without the use of forming gas (see Methods). VSM magnetic moment from 2 to 20 K for CUS-86-750˚C made without forming gas (orange trace) and for comparison CUS-86-750˚C made with a forming gas purge (black, seen also in Figure 4.5A). Inset: SEM micrograph of CUS-86-750˚C made without the use of forming gas, displaying retention of hexagonally ordered mesopores.*

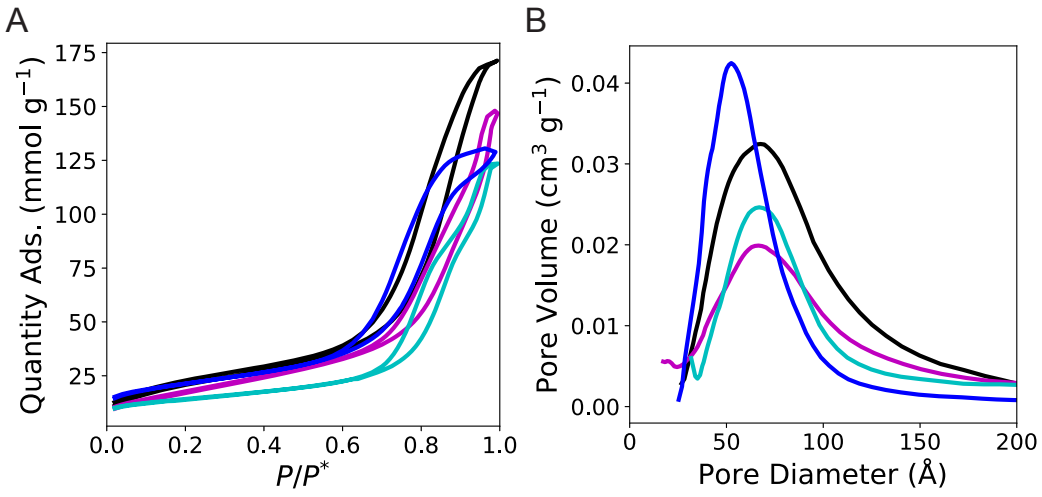

Figure 4.S7: *Nitrogen sorption isotherms (A) and BJH derived pore size distributions (B) for CUS-86-750˚C materials: F127 material without pore expanders (red), F127 with PPG (magenta), F108 material without pore expanders (blue), and F108 with TiPB (cyan).*

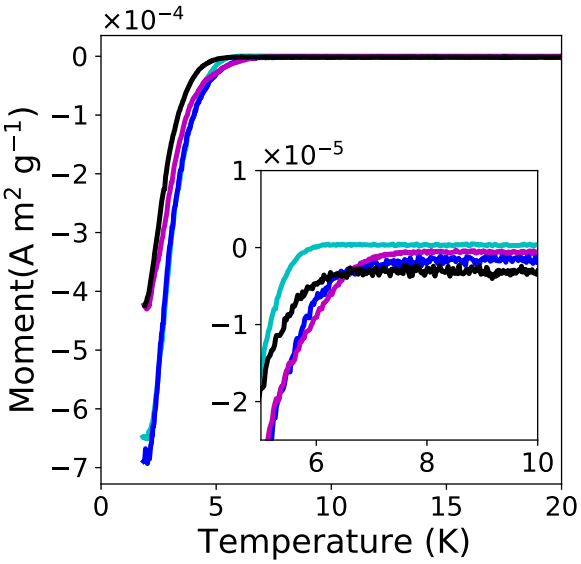

Figure 4.S8*: VSM magnetic moment of CUS-86-750˚C made with varying pluronics and additives: F127 without pore expanders, identical to the black traces shown in Figures 4.5A and 4.S7B (black trace, Table 1 first entry), F127 with PPG (magenta trace, Table 1 second entry), F108 without pore expanders (blue trace, Table 1 third entry), and F108 with TiPB (cyan trace, Table 1 fourth entry). All measurements were conducting in an external field of 10 mT, while heating the sample environment from 2 K to 20 K. Inset at a scale to emphasize transition onset.*

REFERENCES

1. Wei, J., Sun, Z., Luo, W., Li, Y., Elzatahry, A. A., Al-Enizi, A. M., Deng, Y. & Zhao, D. New Insight into the Synthesis of Large-Pore Ordered Mesoporous Materials. *J. Am. Chem. Soc.* **139,** 1706–1713 (2017).
2. Orilall, M. C. & Wiesner, U. Block copolymer based composition and morphology control in nanostructured hybrid materials for energy conversion and storage: solar cells, batteries, and fuel cells. *Chem. Soc. Rev.* **40,** 520–535 (2011).
3. Yu, F., Zhang, Q., Thedford, R. P., Singer, A., Smilgies, D.-M., Thompson, M. O. & Wiesner, U. B. Block Copolymer Self-Assembly-Directed and Transient Laser Heating-Enabled Nanostructures toward Phononic and Photonic Quantum Materials. *ACS Nano* **14,** 11273–11282 (2020).
4. Fruchart, M., Jeon, S.-Y., Hur, K., Cheianov, V., Wiesner, U. & Vitelli, V. Soft self-assembly of Weyl materials for light and sound. *Proc Natl Acad Sci USA* **115,** E3655–E3664 (2018).
5. Robbins, S. W., Beaucage, P. A., Sai, H., Tan, K. W., Werner, J. G., Sethna, J. P., DiSalvo, F. J., Gruner, S. M., Van Dover, R. B. & Wiesner, U. Block copolymer self-assembly–directed synthesis of mesoporous gyroidal superconductors. *Science Advances* **2,** e1501119 (2016).
6. Beaucage, P. A., van Dover, R. B., DiSalvo, F. J., Gruner, S. M. & Wiesner, U. Superconducting Quantum Metamaterials from Convergence of Soft and Hard Condensed Matter Science. *Adv. Mater.* **33,** 2006975 (2021).

7. Thedford, R. P., Beaucage, P. A., Susca, E. M., Chao, C. A., Nowack, K. C., Van Dover, R. B., Gruner, S. M. & Wiesner, U. Superconducting Quantum Metamaterials from High Pressure Melt Infiltration of Metals into Block Copolymer Double Gyroid Derived Ceramic Templates. *Adv. Funct. Mater.* **31,** 2100469 (2021).
8. Yu, F., Thedford, R. P., Hedderick, K. R., Freychet, G., Zhernenkov, M., Estroff, L. A., Nowack, K. C., Gruner, S. M. & Wiesner, U. B. Patternable Mesoporous Thin Film Quantum Materials via Block Copolymer Self-Assembly: An Emergent Technology? *ACS Appl. Mater. Interfaces* **13,** 34732–34741 (2021).
9. Diao, Y., Shaw, L., Bao, Z. & Mannsfeld, S. C. B. Morphology control strategies for solution-processed organic semiconductor thin films. *Energy Environ. Sci.* **7,** 2145–2159 (2014).
10. Sirringhaus, H. 25th Anniversary Article: Organic Field-Effect Transistors: The Path Beyond Amorphous Silicon. *Adv. Mater.* **26,** 1319–1335 (2014).
11. Zhao, D. Triblock Copolymer Syntheses of Mesoporous Silica with Periodic 50 to 300 Angstrom Pores. *Science* **279,** 548–552 (1998).
12. Zhao, D., Huo, Q., Feng, J., Chmelka, B. F. & Stucky, G. D. Nonionic Triblock and Star Diblock Copolymer and Oligomeric Surfactant Syntheses of Highly Ordered, Hydrothermally Stable, Mesoporous Silica Structures. *J. Am. Chem. Soc.* **120,** 6024–6036 (1998).
13. Gu, D. & Schüth, F. Synthesis of non-siliceous mesoporous oxides. *Chem. Soc. Rev.* **43,** 313–344 (2014).

14. Meynen, V., Cool, P. & Vansant, E. F. Verified syntheses of mesoporous materials. *Microporous and Mesoporous Materials* **125,** 170–223 (2009).
15. Fan, J., Boettcher, S. W. & Stucky, G. D. Nanoparticle Assembly of Ordered Multicomponent Mesostructured Metal Oxides via a Versatile Sol−Gel Process. *Chem. Mater.* **18,** 6391–6396 (2006).
16. Cao, L., Man, T. & Kruk, M. Synthesis of Ultra-Large-Pore SBA-15 Silica with Two-Dimensional Hexagonal Structure Using Triisopropylbenzene As Micelle Expander. *Chem. Mater.* **21,** 1144–1153 (2009).
17. Seah, G. L., Wang, L., Tan, L. F., Tipjanrawee, C., Sasangka, W. A., Usadi, A. K., McConnachie, J. M. & Tan, K. W. Ordered Mesoporous Alumina with Tunable Morphologies and Pore Sizes for CO_2 Capture and Dye Separation. *ACS Appl. Mater. Interfaces* **13,** 36117–36129 (2021).
18. Dunphy, D. R., Sheth, P. H., Garcia, F. L. & Brinker, C. J. Enlarged Pore Size in Mesoporous Silica Films Templated by Pluronic F127: Use of Poloxamer Mixtures and Increased Template/SiO_2 Ratios in Materials Synthesized by Evaporation-Induced Self-Assembly. *Chem. Mater.* **27,** 75–84 (2015).
19. Kruk, M. Access to Ultralarge-Pore Ordered Mesoporous Materials through Selection of Surfactant/Swelling-Agent Micellar Templates. *Acc. Chem. Res.* **45,** 1678–1687 (2012).
20. Huber, P. Soft matter in hard confinement: phase transition thermodynamics, structure, texture, diffusion and flow in nanoporous media. *J. Phys.: Condens. Matter* **27,** 103102 (2015).

21. Morris, R. E. & Wheatley, P. S. Gas Storage in Nanoporous Materials. *Angew. Chem. Int. Ed.* **47,** 4966–4981 (2008).

22. Davis, M. E. Ordered porous materials for emerging applications. *Nature* **417,** 813–821 (2002).

23. Argyo, C., Weiss, V., Bräuchle, C. & Bein, T. Multifunctional Mesoporous Silica Nanoparticles as a Universal Platform for Drug Delivery. *Chem. Mater.* **26,** 435–451 (2014).

24. Ramasamy, E., Jo, C., Anthonysamy, A., Jeong, I., Kim, J. K. & Lee, J. Soft-Template Simple Synthesis of Ordered Mesoporous Titanium Nitride-Carbon Nanocomposite for High Performance Dye-Sensitized Solar Cell Counter Electrodes. *Chem. Mater.* **24,** 1575–1582 (2012).

25. Stefik, M., Sai, H., Sauer, K., Gruner, S. M., DiSalvo, F. J. & Wiesner, U. Three-Component Porous−Carbon−Titania Nanocomposites through Self-Assembly of ABCBA Block Terpolymers with Titania Sols. *Macromolecules* **42,** 6682–6687 (2009).

26. Li, Y., Horia, R., Tan, W. X., Larbaram, N., Sasangka, W. A., Manalastas, W., Madhavi, S. & Tan, K. W. Mesoporous Titanium Oxynitride Monoliths from Block Copolymer-Directed Self-Assembly of Metal–Urea Additives. *Langmuir* **36,** 10803–10810 (2020).

27. Beaucage, P. A., Susca, E. M., Gruner, S. M. & Wiesner, U. B. Discovering Synthesis Routes to Hexagonally Ordered Mesoporous Niobium Nitrides Using Poloxamer/Pluronics Block Copolymers. *Chem. Mater.* **29,** 8973–8977 (2017).

28. Lengauer, W. & Ettmayer, P. Preparation and properties of compact cubic ?-NbN1?x. *Monatsh Chem* **117,** 275–286 (1986).

29. Groom, C. R., Bruno, I. J., Lightfoot, M. P. & Ward, S. C. The Cambridge Structural Database. *Acta Crystallogr B Struct Sci Cryst Eng Mater* **72,** 171–179 (2016).

30. Joyner, L. G., Barrett, E. P. & Skold, R. The Determination of Pore Volume and Area Distributions in Porous Substances. II. Comparison between Nitrogen Isotherm and Mercury Porosimeter Methods. *J. Am. Chem. Soc.* **73,** 3155–3158 (1951).

31. Zhernenkov, M., Canestrari, N., Chubar, O. & DiMasi, E. Soft matter interfaces beamline at NSLS-II: geometrical ray-tracing vs. wavefront propagation simulations. in (eds. Sanchez del Rio, M. & Chubar, O.) 92090G (2014). doi:10.1117/12.2060889

32. Pessall, N., Gold, R. E. & Johansen, H. A. A study of superconductivity in interstitial compounds. *Journal of Physics and Chemistry of Solids* **29,** 19–38 (1968).

33. Miura, A., Takei, T., Kumada, N., Wada, S., Magome, E., Moriyoshi, C. & Kuroiwa, Y. Bonding Preference of Carbon, Nitrogen, and Oxygen in Niobium-Based Rock-Salt Structures. *Inorg. Chem.* **52,** 9699–9701 (2013).

34. Thommes, M., Kaneko, K., Neimark, A. V., Olivier, J. P., Rodriguez-Reinoso, F., Rouquerol, J. & Sing, K. S. W. Physisorption of gases, with special reference to the evaluation of surface area and pore size distribution (IUPAC Technical Report). *Pure and Applied Chemistry* **87,** 1051–1069 (2015).

35. Brunauer, S., Emmett, P. H. & Teller, E. Adsorption of Gases in Multimolecular Layers. *J. Am. Chem. Soc.* **60,** 309–319 (1938).

36. Schoeffel, M., Brodie–Linder, N., Audonnet, F. & Alba–Simionesco, C. Wall thickness determination of hydrophobically functionalized MCM-41 materials. *J. Mater. Chem.* **22,** 557–567 (2012).

37. Kato, K. Structure refinement of *H* -Nb_2O_5. *Acta Crystallogr B Struct Sci* **32,** 764–767 (1976).

38. Tinkham, M. *Introduction to superconductivity*. (Dover Publ, 2015).

39. Raine, M. J. & Hampshire, D. P. Characterization of the Low Temperature Superconductor Niobium Carbonitride. *IEEE Trans. Appl. Supercond.* **21,** 3138–3141 (2011).

40. Mathur, M. P., Deis, D. W. & Gavaler, J. R. Lower Critical Field Measurements in NbN Bulk and Thin Films. *Journal of Applied Physics* **43,** 3158–3161 (1972).

41. Beloborodov, I. S., Lopatin, A. V., Vinokur, V. M. & Efetov, K. B. Granular electronic systems. *Rev. Mod. Phys.* **79,** 469–518 (2007).

42. Nigro, A., Nobile, G., Rubino, M. G. & Vaglio, R. Electrical resistivity of polycrystalline niobium nitride films. *Phys. Rev. B* **37,** 3970–3972 (1988).

43. Matthias, B. T. Transition Temperatures of Superconductors. *Phys. Rev.* **92,** 874–876 (1953).

44. Troitskiy, V. N., Domashnev, I. A., Kurkin, E. N., Grebtsova, O. M., Berestenko, V. I., Balikhin, I. L. & Gurov, S. V. Synthesis and Characteristics of Ultra-Fine Superconducting Powders in the Nb–N, Nb–N–C, Nb–Ti–N–C systems. *Journal of Nanoparticle Research* **5,** 521–528 (2003).

45. Williams, M. W., Ralls, K. M. & Pickus, M. R. Superconductivity of cubic niobium carbo-nitrides. *Journal of Physics and Chemistry of Solids* **28,** 333–341 (1967).

46. Ohmer, M. C. & Frederick, W. G. D. Some superconducting properties of multifilamentary niobium carbonitride. *Journal of Applied Physics* **45,** 1382–1384 (1974).

47. Lehtinen, J. S., Sajavaara, T., Arutyunov, K. Yu., Presnjakov, M. Yu. & Vasiliev, A. L. Evidence of quantum phase slip effect in titanium nanowires. *Phys. Rev. B* **85,** 094508 (2012).

48. Pandolfi, R. J., Allan, D. B., Arenholz, E., Barroso-Luque, L., Campbell, S. I., Caswell, T. A., Blair, A., De Carlo, F., Fackler, S., Fournier, A. P., Freychet, G., Fukuto, M., Gürsoy, D., Jiang, Z., Krishnan, H., Kumar, D., Kline, R. J., Li, R., Liman, C., Marchesini, S., Mehta, A., N'Diaye, A. T., Parkinson, D. Y., Parks, H., Pellouchoud, L. A., Perciano, T., Ren, F., Sahoo, S., Strzalka, J., Sunday, D., Tassone, C. J., Ushizima, D., Venkatakrishnan, S., Yager, K. G., Zwart, P., Sethian, J. A. & Hexemer, A. *Xi-cam* : a versatile interface for data visualization and analysis. *J Synchrotron Rad* **25,** 1261–1270 (2018).

49. Ilavsky, J. Nika: software for two-dimensional data reduction. *J Appl Crystallogr* **45,** 324–328 (2012).

50. Gruner, S. M., Rothschild, K. J. & Clark, N. A. X-ray diffraction and electron microscope study of phase separation in rod outer segment photoreceptor membrane multilayers. *Biophysical Journal* **39,** 241–251 (1982).

CHAPTER 5

SUPERCONDUCTING QUANTUM METAMATERIALS FROM HIGH PRESSURE MELT INFILTRATION OF METALS INTO BLOCK COPOLYMER DOUBLE GYROID DERIVED CERAMIC TEMPLATES[δ]

Abstract

Mesoscale order can lead to emergent properties including phononic bandgaps or topologically protected states. Block-copolymers offer a route to mesoscale periodic architectures, but their use as structure directing agents for metallic materials has not been fully realized. We demonstrate a versatile approach to mesostructured metals via bulk block-copolymer self-assembly derived ceramic templates. Molten indium is infiltrated into mesoporous, double gyroidal silicon nitride templates under high pressure to yield bulk, three-dimensionally (3D) periodic nanocomposites as free-standing monoliths which exhibit emergent quantum-scale phenomena. Vortices are artificially introduced when double gyroidal indium metal behaves as a type II superconductor, with evidence of strong pinning centers arrayed on the order of the double gyroid lattice size. Sample behavior is reproducible over months, showing high stability. High pressure infiltration of bulk block-copolymer self-assembly based ceramic templates is an enabling tool for studying high-quality metals with previously inaccessible architectures, and paves the way for the emerging field of block-copolymer derived quantum metamaterials.

[δ] R. Paxton Thedford[*], Peter A. Beaucage[*], Ethan M. Susca, Corson A. Chao, Katja C. Nowack, Robert B. Van Dover, Sol M. Gruner, and Ulrich Wiesner. *Adv. Funct. Mater.* **31** 2100469(1-9) (2021).

Introduction

Synthesis of quantum materials is currently focused at the atomic scale, but many interesting phenomena could lurk in structures defined by their order on the scale of tens to hundreds of nanometers.[1] It is known that mesoscale features can impart desirable attributes in superconductors for instance, such as improvement in critical temperature or current.[2–5] Extensive work has been performed on the effect of two dimensional confinement or ordering in the thin film regime, demonstrating for example the thickness dependence of transition temperature and tunable flux pinning in thin film periodic arrays.[6–10] In contrast, there have been far fewer investigations of *three* dimensionally (3D) ordered superconductors, and of the existing studies in this vein all but a handful focus on isolated nano-objects or nano-wires.[11–13] The use of block-copolymer (BCP) self-assembly in the bulk gives access to numerous 3D co-continuous network morphologies (including chiral networks), and may impart the ability to control structure across characteristic lengths in superconductors (i.e., London penetration depth, Ginzburg-Landau correlation length).[14–16] This is in stark contrast to conventional inorganic atomic lattices and is due to the dependence of BCP self-assembly directed lattice parameters on molar mass, which can be precisely tailored over a wide range by polymer synthesis.

Furthermore, numerous studies suggest or showcase emergent properties when mesoscale 3D network morphologies typical of bulk BCP self-assembly are imparted to a metallic material: topologically protected Weyl points, novel behavior in superconductors, and complete photonic bandgaps in the visible spectrum provide a few examples.[17–19] The experimental realization of these metamaterials has been limited,

however, by a lack of accessible synthesis routes for high-quality metallic materials from bulk BCP self-assembled structures. High fidelity transfer of self-assembled architectures into metals has been considered a grand challenge in BCP structure–directed materials for the past decade. While strides have been made towards mesostructured metals via the incorporation of metallic nanoparticles in a specific BCP domain[20], most approaches focus on backfilling a BCP self-assembly directed porous structure with metal by electro- or electroless deposition.[11,21–23] Such methods typically only achieve complete and uniform backfilling in thin films through careful control of synthetic parameters, and lack generalizability.

In this work we demonstrate a robust, versatile route to mesostructured metal superconductors using high pressure melt infiltration of liquid indium metal into bulk BCP self-assembly–derived mesoporous double gyroid ceramic templates. The combination of an exclusively physical process of infiltration with an extremely resilient ceramic template is expected to be broadly transferrable to many materials. As such, this method represents a fundamental and broad advance in the synthesis of high-quality bulk mesostructured metals from BCP structure directed porous templates, and is an enabling step for the full realization and fundamental understanding of self-assembly derived metamaterials.

To date the only existing route to a mesostructured superconductor with bulk block copolymer self-assembly derived 3D periodic network structure, which allows facile tuning of *both* morphology *and* lattice parameters, is via bulk BCP-inorganic hybrid self-assembly into a single (alternating) gyroid (only one of the two gyroid minority networks is constituted by the superconducting material).[19] This method

requires multiple processing steps, however, to convert mesostructured niobia into niobium nitride and other refractory ceramics. Such an approach inherently convolutes material chemistry and mesostructure formation due to the sensitivity of high-temperature solid-state reactions to surface area or chemistry and the wide array of possible substituents. Thus, the direct comparison of various morphologies or lattice parameters may not be easily possible. Similarly challenging is the comparison of such materials to their corresponding bulk equivalents, making it difficult to parse the effects of mesostructure and chemistry on the final superconductor properties.

Results and Discussion

Materials Synthesis and Structural Characterization

A platform based upon pure metals solves these issues, yielding compositionally simple and stable materials for the direct investigation of the effects of mesostructure on superconductivity. To that end, in this work we use high pressure infiltration of molten indium into a porous silicon oxynitride (SiON) ceramic to create novel bulk nanocomposites with double gyroid morphology (Figure 5.1a). In a method previously reported,[24] a poly(isoprene-*b*-styrene-*b*-dimethylamino-ethylmethacrylate) (PI-*b*-PS-*b*-PDMAEMA, or simply ISA) triblock terpolymer with overall molar mass of 79 kDa, polydispersity of 1.09 and with I, S, and A block volume fractions of about 20 %, 30 %, and 50 %, respectively, is used to structure direct poly(methyl vinyl silazane) (PMVS) into a hybrid material with double gyroid structure via evaporation induced self-assembly (EISA). The nanostructured bulk ISA/PMVS composite monolith is then converted via thermal processing into a mesoporous SiON ceramic (Figure 5.2), which

serves as a mechanically strong and chemically resistant template for the infiltration of molten metal. After EISA, the hybrid BCP/polysilazane composite monolith (Figure 5.2a, solid trace) exhibits the first seven reflections uniquely characteristic of a double gyroid with a d_{100} of 125 nm. This structure is retained after pyrolysis in ammonia to 1000 ˚C despite isotropically shrinking to a d_{100} spacing of 73 nm (Figure 5.1a, dashed trace) in the SiON material. In nitrogen sorption/desorption measurements the resulting ceramics show a type IV-H_1 hysteresis (Figure 5.2b) as expected for well-ordered mesoporous materials and consistent with earlier studies.[24] The Brunauer-Emmett-Teller (BET) derived surface area of a representative sample is 21 m^2/g, with a narrow Barrett-Joyner-Halenda (BJH) pore size distribution centered around 18 nm (Figure 5.2b, inset).[25] After infiltration of the two interpenetrating minority network void spaces of the mesoporous ceramic with molten indium (green volume in Figure 5.1b), the domain spacing is unchanged while higher order reflections appear to decrease in intensity (Figure 5.2a, dotted trace). The absence of these higher order peaks is likely due to measurement differences: SAXS data for the ISA/PMVS and ceramic monoliths were obtained at synchrotron sources, while SAXS data for the indium infiltrated sample was obtained using a rotating anode lab source. Retention of the peaks characteristic of the double gyroid space group in the top trace, the absence of any additional or forbidden reflections as a result *e.g.* of lattice distortions, and scanning

electron microscopy (SEM) analysis shown in Figure 5.3 however all suggest that the mesostructure is largely undisturbed by the metal infiltration.

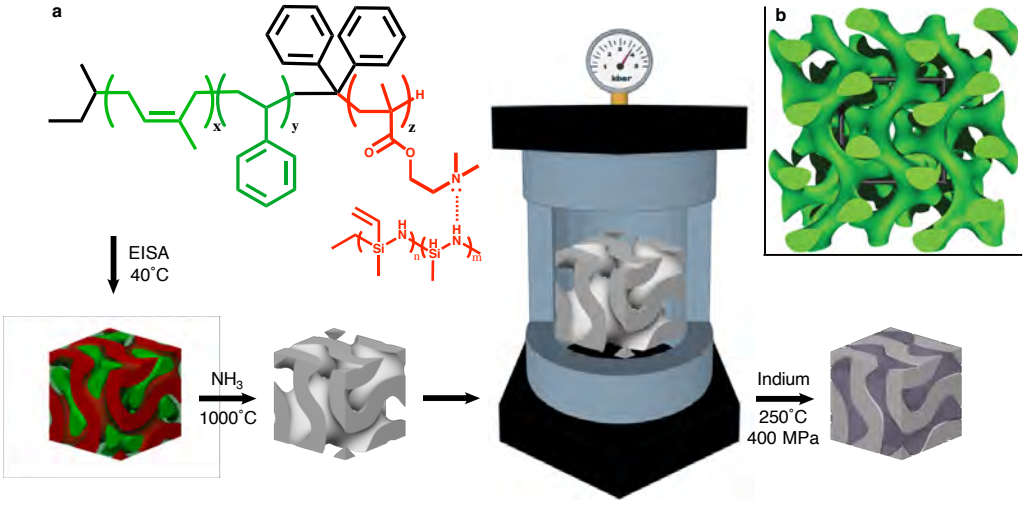

Figure 5.1*: Schematic of the route to a periodically structured indium metal/SiON composite with double gyroid morphology. a) A mixture of ISA terpolymer and PMVS undergoes EISA at 40 ˚C to yield a double gyroid structured hybrid, which is then fired at 1000 ˚C in ammonia to yield a mesoporous ceramic template. The resulting SiON matrix is placed in a custom reactor with indium metal and heated to 250 ˚C under 400 MPa of pressure, yielding a metal infiltrated gyroidal ceramic. b) Rendering of the two interpenetrating minority networks of the double gyroid structure, that after high pressure processing are backfilled with indium metal. The cubic unit cell is shown in black.*

Infiltration of the free-standing, monolithic SiON template is accomplished by heating the ceramic and metal together under vacuum above the melting point of indium before applying a large isostatic pressure of up to 400 MPa of helium. The pressure required for infiltration of the porous material is approximated by the Young-Laplace

equation (supplemental information). It was observed that no infiltration of indium occurred using pressures up to 7 MPa, likely a result of the high surface energy of the liquid metal and its large contact angle with the SiON (supplemental information). After isostatic pressure is used to force the liquid metal into the network channels of the template, the system is cooled and depressurized, trapping solidified indium in the pores of the monolith. In the resulting gyroidal In/SiON composite, indium fills the voided double minority network phase within a SiON majority double gyroid matrix. X-ray diffraction (XRD) traces for indium metal used in the infiltration and indium metal/ceramic composite after infiltration are shown in Figure 5.S1.

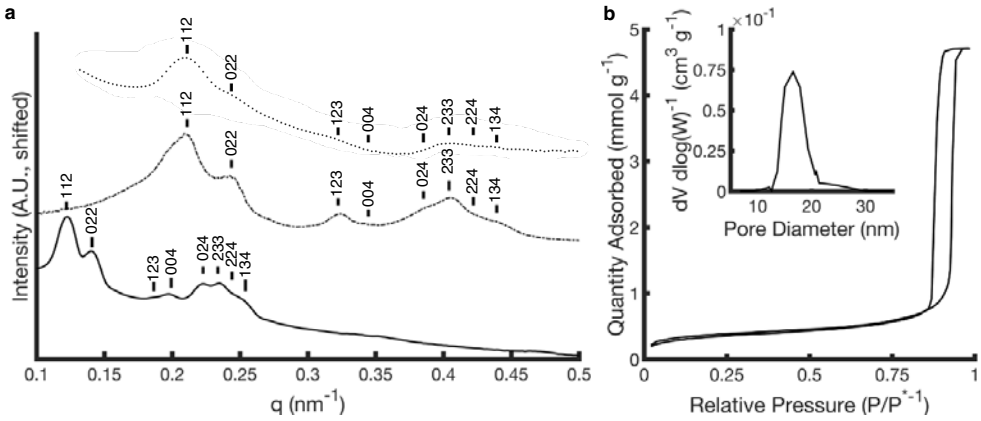

Figure 5.2*: Schematic of the route to a periodically structured indium metal/SiON composite with double gyroid morphology. a) Representative SAXS traces of the ISA/PMVS hybrid (bottom, solid line; d_{100} = 125 nm), pyrolyzed SiON ceramic (middle, dashed line; d_{100} = 73 nm), and indium infiltrated ceramic (top, dotted line; d_{100} = 73 nm). Ticks above each pattern together with Miller indices show the first eight expected reflections for the Ia3d space group (#230) consistent with the double gyroid structure. Curves are vertically displaced for clarity. b) Nitrogen adsorption and desorption isotherms for the double gyroidal SiON template via N_2*

physisorption. Inset: pore size distribution calculated via the Barrett-Joyner-Halena (BJH) method for the mesoporous ceramic.[25]

The extent of indium infiltration is visualized via energy dispersive x-ray spectroscopy (EDX; Figure 5.3). The homogenous distribution across the sample (Figure 5.3a) suggested by the elemental map (Figure 5.3b) is corroborated by the characteristic x-ray emission for indium and silicon across the width of the monolith shown in Figure 5.3c. Aside from residual bulk indium depicted at the left surface of the monolith (later removed by chemical etching and polishing prior to magnetic measurements), the distribution of indium (from the backfilled network) as compared to silicon (from the ceramic matrix) is relatively constant throughout the composite. These results suggest homogeneous backfilling throughout the more than 50 micron thick freestanding sample, demonstrating that high pressure melt infiltration of BCP based mesoporous templates is a viable approach to bulk mesostructured metals.

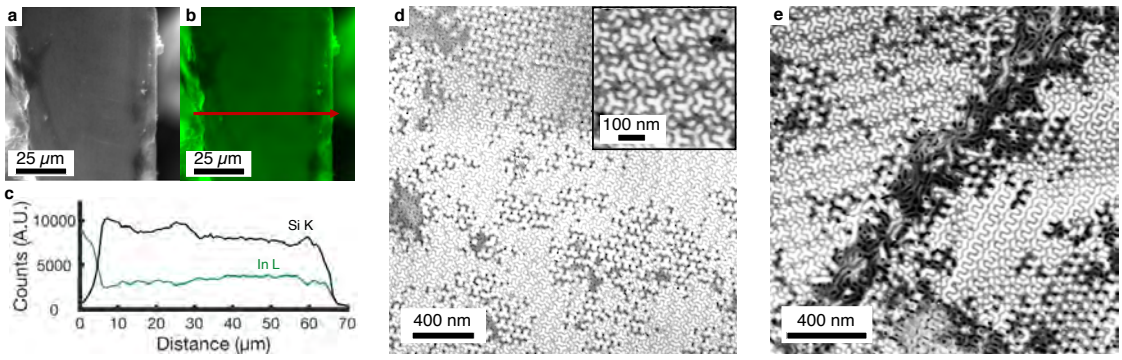

Figure 5.3: *EDX and SEM characterization of an indium infiltrated mesoporous double gyroidal SiON. a) SEM micrograph of an In/SiON composite cross section at low magnification. b) EDX elemental map of the image depicted in a; areas with detectable indium are shaded in*

green. c) EDX photon counts in x-ray fluorescence energy ranges characteristic of indium (green) and silicon (black) across the red line shown in b. d) Back-scattered electron (BSE) micrograph of a polished In/SiON composite at a magnification that allows visualization of the double gyroidal structure. A higher magnification image of a separate area is shown in the inset (top right). e) BSE micrograph of the polished composite showing a grain boundary between two mesoscale double gyroid domains (In regions appear bright, while SiON regions appear dark).

Backscattered electron micrographs make use of the high atomic weight (high Z) contrast present between the SiON matrix and indium network phases to highlight the mesoscale structure: bright areas of the images in Figure 5.3d correspond to the high Z indium while darker areas correspond to the lower Z ceramic. While these two images corroborate successful overall backfilling with indium (*vide supra*), the micrograph in Figure 5.3e highlights that areas with incomplete filling of the template remain. These are often associated with the boundaries of two mesoscopic double gyroid grains at different orientations (shown here along the bottom left to upper right diagonal). It appears that along the grain boundary, indium fills only a small fraction of the SiON template void fraction. From EDX analysis showing macroscopically homogenous indium infiltration and SEM micrographs of individual grains, we hypothesize that this is due to mesostructural heterogeneity as opposed to inconsistency in backfilling. During infiltration, indium metal fills the continuous networked porous volume, leaving empty the isolated and inaccessible voids at, e.g., grain boundaries. This is supported by recent large volume electron microscopy reconstructions of BCP double gyroids

showing the presence of network breaking defects that would impede backfilling of the voided channels.[26]

Gyroidal In/SiON Nanocomposites in the Superconducting State

Superconducting properties of the indium/SiON composite, as revealed by vibrating sample magnetometry (VSM) and four-point DC transport measurements, are depicted in Figure 5.4. For comparison, pure indium was cut from the same batch used for the infiltration and flattened into a 100 μm foil, on the same order of thickness as the 63 μm thick composite monolith. Comparison of the behavior (Figure 5.4a) of mesostructured indium (green) to its bulk equivalent (red) reveals substantial differences, including distinctly different behavior around the transition temperature (T_c). Pure indium exhibits a narrow transition at ≈ 3.4 K, consistent with literature reports. The polished mesoscopic sample, in contrast, exhibits a much broader transition. Superconducting behavior is observed at a high temperature 'onset' of 3.7 K, while the transition midpoint is depressed to ca. 3.1 K.

The increase in the T_c onset is compelling evidence that the mesoscale structure of the indium is dictating electronic behavior, agreeing with predictions and measurements in indium nanoparticles or thin films.[27] This effect may be explained as a result of lower frequency surface phonon modes, which reduce the average phonon frequency in a confined system, so called "phonon-softening".[28] The simultaneous broadening of the transition is also likely a consequence of the mesoscale confinement of indium in the two void networks of the SiON template. Residual strain from the high pressure infiltration is likely contributing, but cannot fully explain the behavior

observed; indium metal under 200 MPa of pressure experiences a decrease in T_c of less than 0.1 K.[29] Similar phenomena have been observed in isolated superconducting wires, where the broadening of resistive transitions can be attributed the generation of quantum phase slips.[30,31] Furthermore, in isolated nanoparticle systems, reduction in particle size below ≈ 20 nm leads to the so-called quantum size effect (QSE) from the discretization of electronic bands.[32] The QSE opposes phonon softening in superconductors, lowering the T_c compared to the bulk value. The counterbalancing nature of these effects in mesoscopic superconductors presents an interesting opportunity for interconnected architectures such as the double gyroid: the networked structure could take advantage of the T_c boosting effects of phonon softening while avoiding T_c depression from quantum confinement. At the same time, the exquisite control afforded by BCP self-assembly may allow for topological engineering of the QSE for additional improvement of T_c through exploitation of effects such as the coherent shell effect.[5]

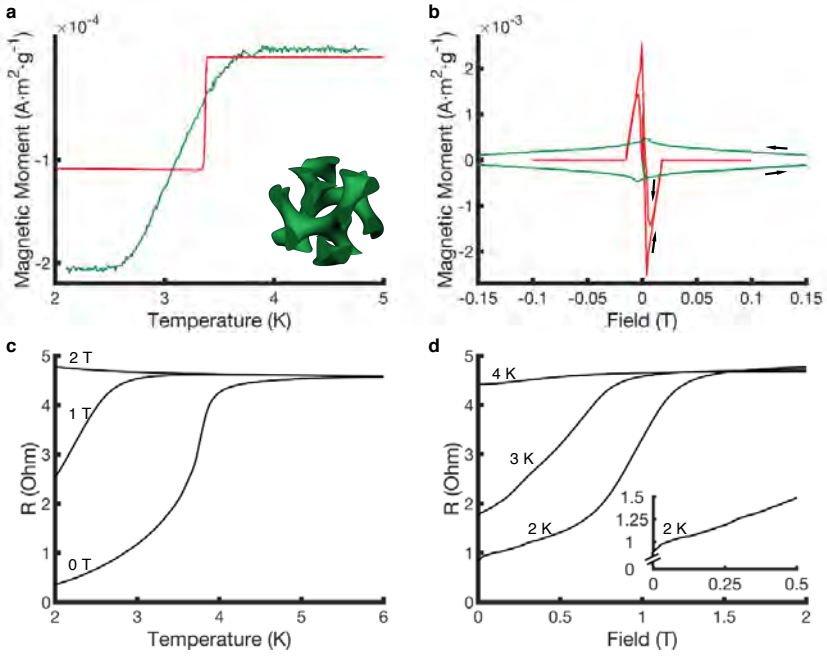

***Figure 5.4**: VSM characterization of double gyroidal indium/SiON nanocomposite (green traces) and bulk indium (red traces) shown in parts a and b. a) Magnetic moment measurements over temperatures near the critical temperature of indium. All measurements carried out in an external field of 8 mT. Inset (bottom right): Rendering of interpenetrating indium metal minority networks in the SiON composite; the ceramic matrix is not shown to reveal minority network connectivity. b) Magnetic moment measurements from 0 to 0.75 T, with arrows depicting field scanning direction for both samples. Transport behavior of the indium/SiON nanocomposite as measured by four-point probe technique. c) resistance measurements over a range of temperatures close to the superconducting transition temperature at different applied fields: 0 T, 1T, and 2 T. d) resistance measurements over a range of external field strengths at different sample temperatures: 2 K, 3 K, and 4 K. Inset: resistance measurements at 2 K at low field strengths.*

The magnetization behavior of the In/SiON composite also differs substantially from that of the pure metal (Figure 5.4b). The 100 μm thick pure indium foil (red trace) behaves as a characteristic type-I superconductor, with an initial linear decrease in magnetic moment up to 3.8 mT. Near ≈ 3.8 mT the pure indium appears to transition into an intermediate state, increasing in susceptibility until fully entering a normal state above the critical field of $\mu_o H_c \approx 23$ mT. This behavior is consistent with reports of superconductivity in indium films.[33,34] The magnetization curve of the pure indium foil exhibits some hysteresis upon scanning the field in the field lowering direction due to demagnetization, similar to the "topological" hysteresis seen in the intermediate type I state of lead foils of similar thickness.[35] In sharp contrast, the indium confined to the 63 μm thick double gyroidal composite monolith (green trace) exhibits emergent behavior

characteristic of hard type II superconductors. The slope of the magnetization in the initial linear regime at low fields gives a magnetic susceptibility of ≈ –0.8, assuming an average density of ≈ 5 g cm^{-3} for the SiON/In composite. While this does not account for demagnetization in the irregular platelet-like sample, this entails that some flux penetration occurs even below H_{c1}. Upon raising the external field significant hysteresis is observed, with the lower critical field (H_{c1}) depressed below the bulk to $\mu_o H_c$ = 2.5 mT, while the upper critical field (at which magnetization completely disappears) increases to ≈ 0.63 T **(**Figure 5.S2). This upper critical field matches the characteristic field for overlapping vortices on a triangular lattice of 62 nm, comparable to the double gyroid unit cell size of 73 nm. Further, the irreversibility of the magnetization curve implies the introduction of strong pinning centers in the In/SiON composite. It is notable that this emergent magnetization behavior of double gyroidal indium is reproducible even after several months of storage under ambient conditions (Figure 5.S3) suggesting high sample stability. While point defects (such as chemical impurities or vacancies) can serve as pinning sites,[36] the chemically inert melt infiltration and absence of such strong pinning centers in the bulk sample suggests that the origin of the pinning is likely the mesostructure. This is corroborated by work performed on inverse opal templated metals, where evidence suggests vortex pinning commensurate with the opal lattice size.[37,38] However, in contrast to the inverse opal type structures, which consist of large nodes connected by an order of magnitude smaller in diameter 'weak links', the gyroid structures present in this work consist of networked struts of relatively homogeneous diameter throughout. This distinction is important for consideration of the origin of flux

pinning as well other properties which arise due to confinement, as explored in the next section.

Transport behavior of the confined indium metal roughly matches the behavior observed in the magnetization measurements. A distinct transition to a superconducting state at ≈ 3.5 K in zero external field is displayed in Figure 5.4c, with similar broadening observed. Just above the onset temperature of 3.7 K exhibited in the magnetization measurements, a distinct slope change is seen with deviations from the normal resistance up to 6 K. This excess conductivity in the normal state just above the critical temperature is often observed in systems with reduced dimensionality, where fluctuations are expected to have a much greater relative effect.[39] In Figure 5.4d, distinct transitions appear at field strengths matching the critical fields as seen in Figures 5.4b and 5.S2. At the observed lower critical field of ≈ 2.5 mT, a change in slope can be noticed for the sample measured at 2K. Starting at ≈ 0.63 T, another transition can be seen matching the upper critical field. Here too it is observed that the transition is relatively broad, with deviations from the normal state resistance occurring up to much higher fields than in the magnetization measurements. This could be indicative of longer lived surface superconductivity in the double gyroidal material,[40] which would contribute much less to the bulk magnetization.

Important to this consideration is the presence of the dielectric SiON ceramic matrix forming an interface with the indium throughout the composite. It is known that at the interface of metal and insulator, superconductivity can nucleate at surfaces parallel to the external field up to a critical field H_{c3} higher than the upper critical field H_{c2} by almost a factor of two.[41,42] This would correspond to surface nucleation up to an

external field of ≈ 1.3 T in the case of the In/SiON, which roughly matches the slope change above 1 T seen in Figure 5.4d. The 3D networked double gyroidal indium studied here has a very large relative surface area. Therefore non-negligible contributions of surface superconductivity from indium/SiON interfaces oriented parallel to the external field to the transport can be expected. The presence of the ceramic SiON matrix/separator (as opposed to e.g. air) in the composite could be important for surface plasmons confined to the dielectric/metal interface or Josephson coupling of neighboring superconductor wire networks, though it should be noted that the ≈20 nm thickness of the SiON interlayer in this work likely precludes significant tunneling current.[43–45] However, as previously mentioned, a particular strength of BCP self-assembly is the ability to tune the lattice parameter of mesoscopic architectures while maintaining material symmetry. Theoretically this could enable decreasing the SiON dielectric matrix thickness below a threshold to achieve high tunneling currents and Josephson coupling between the distinct, interpenetrating left- and right-handed chiral networks of the double gyroid.

The residual resistance observed in Figure 5.4d and e could also be a result of inhomogeneity in the double gyroidal indium network itself. As shown in Figure 5.3e, mesoscale grain boundaries in the mesoscale polycrystalline double gyroidal template can prevent complete filling of the void space. At such boundaries, only a few isolated indium pathways connect more completely filled double gyroid grains. These ≈ 18nm diameter isolated wires could account for the incomplete flux exclusion observed below H_{c1}, and may be prone to thermally activated phase slips below the critical temperature. This has been observed to yield a finite resistance in type I superconductor nanowires.[31]

The Effect of Mesostructure on Superconducting Properties

The overall shift from type-I to type-II behavior is consistent with the observed change in the underlying material properties and length scales. The Ginzburg-Landau-Abrikosov-Gor'kov (GLAG) theory of superconductors classifies superconductor type in terms of the energy of the superconductor-normal interface, which in turn is determined by the Cooper pair coherence length, ξ_0, and London penetration depth, λ_L. The ratio between these two characteristic lengths, termed the Ginzburg-Landau (GL) parameter, κ, defines the point at which a material switches from type I to type II behavior as $1/\sqrt{2}$. This parameter is highly dependent on the mean free electron path, which can be substantially reduced in granular or "dirty"superconductors.[42] The reduction in mean free electron path has been observed to result in type I to type II transitions in many metals in thin film and nanoscale geometries, including inverse opal lattices.[12,37,46] In indium thin films, however, the transition from type I intermediate structures to vortex formation at high field strength does not occur until films become thinner than 80 nm.[46] In the case of the 63 μm thick composite In/SiON double gyroid reported here, it is therefore the mesoscale periodic structure of the indium metal which is likely dictating the material properties. This can be further demonstrated by an estimation of the effective characteristic lengths in the double gyroidal indium via equation (5.1).

$$H_{c2} = \frac{\phi_0}{2\pi\mu_0\xi^2} \tag{5.1}$$

In this relationship, derived by GLAG theory, H_{c2} corresponds to the upper critical field at 0 K, ξ to the effective coherence length at 0 K, and ϕ_0 to the magnetic flux quantum. Observation of the upper critical field of the double gyroidal indium at varying temperature (Figure 5.S2) and a fit to the GL relation $H_{c2}(T) = H_{c2}(0) \cdot \left(1 - \left({}^{T}/_{T_c}\right)^2\right)$ (Figure 5.S5) gives the values for $H_{c2}(0)$, ξ , and T_c shown in Table 1. The effective London penetration depth can then be estimated from the effective coherence length using the dirty limit expressions $\xi = 0.865\left(\xi_0 l_{eff}\right)^{1/2}$, and $\lambda = 0.66\lambda_L\left(\xi_0/l_{eff}\right)^{1/2}$ where ξ_0 and λ_L are taken as the bulk values of indium and *l* is the effective electron mean free path.[42] While simplistic, this treatment matches the critical temperature as detected in Figure 4 and the observed lower critical fields reasonably well (Figure 5.S4b).

	T_c (K)	$\mu_0 H_0$(T)	ξ(nm)	λ_L (nm)	κ
Bulk	3.37†	2.8 x 10^{-2}†	360*	65*	0.18
Double Gyroid	3.67	0.83	20	670	33.5

Table 5.1*: Critical values and characteristic lengths for bulk indium metal as compared to parameters calculated for the mesostructured indium in the double gyroidal metal/ceramic composite.*

† Critical temperature and field for bulk indium previously reported.[47]

** Characteristic lengths for bulk indium previously reported.*[48]

From Table 5.1 it is apparent that the GL parameter, κ, and thus the superconductor type, changes drastically in the mesostructured indium relative to the bulk. Notably, the estimated coherence length in the double gyroidal metal network, ξ = 20 nm, is on the same order as the BJH derived pore size, 18 nm (Figure 5.2), and the average ballistic path within the confines of a model strut network, 23 nm (supplemental information, Figure 5.S5). Though an approximation, this is further evidence that the mesoscopic architecture is determining the electron mean free path. For comparison, the mean free electron path in bulk indium metal at room temperature has been measured as 8.65 nm.[49] If it is assumed that few impurities are introduced into the indium during the pressure infiltration, the mean free path should be at least an order of magnitude higher at temperatures <4 K. In the double gyroidal indium however, the implied mean free path is found to be 1.5 nm; within the confined strut network of the ceramic template the maximum possible line-of-sight path can range from a few nanometers in the surface normal direction to several hundreds of nanometers along certain crystallographic directions (Figure 5.S5). In theory this may lead to other metamaterials behavior such as angle dependent magnetization or vortex pinning and magnetic lock-in/flux-trapping from particular alignment of the external field with respect to the orientation of a single crystal double gyroid metal network.[50] Changing the mesoscale domain size of the template while maintaining the double gyroid morphology, or vice versa, could lead to other interesting phenomena. Through the use of bulk BCP self-assembly for the creation of networked mesoporous architectures, the platform described here uniquely combines all of these capabilities.

Conclusions

These proof-of-principle measurements of double gyroidal indium superconductors show substantial promise for high pressure metal infiltration of BCP derived ceramic templates as a facile, stable, and tunable platform for the investigation of complex 3D mesoscale geometries in metals. In this work, gyroid structured indium has been shown to be a quantum metamaterial: the induced mesoscopic architecture substantially changes superconducting properties through a modification of fundamental, quantum level characteristics, *i.e.* the superconducting coherence length. The backfilling of double gyroidal ceramic templates with other metals such as aluminum, silver, or gold is predicted to yield materials with novel photonic and electronic properties.[17,18,23,51] Beyond pure metals, polymers,[52] metallic glasses,[53] and a few ordered crystalline materials have proven amenable to pressure driven nanomoulding.[54] Finally, more extensive investigation into this emerging class of materials may be possible by expanding the high-pressure infiltration technique into single-crystal gyroidal templates, which have only recently become available.[50] Thus, the use of high-pressure infiltration together with bulk BCP self-assembly–derived ceramic templates presents a wide array of potential projects bridging the disparate fields of soft matter and quantum materials.

Experimental Section

Materials

Unless otherwise stated, all chemicals were obtained from Sigma Aldrich and used as received. Polysilazane, trade name Durazane 1800, was donated by Greg

McCraw of EMD Performance Material - Branchburg, New Jersey. Double gyroidal SiON ceramic templates were prepared using a previously-described method.[24] In brief, 0.698 g of a poly(isoprene-b-styrene-b-dimethylamino ethylmethacrylate) "ISA" triblock terpolymer with overall molar mass 79 kDa (polydispersity of 1.09 with I, S, and A blocks having a volume fraction of 19.6 %, 30.7 %, and 49.7 %, respectively) was mixed with 0.386 g of a commercial poly(methyl vinyl silazane) (PMVS) "Durazane 1800" and 20.425 g toluene. After mixing, the solution was allowed to evaporate in a double-diffusion cell at 40 °C over a span of two weeks to yield a free-standing, double gyroid structured hybrid monolith with a thickness of ≈ 100 μm. This hybrid monolith was etched under CF_4 plasma for 40 minutes on each side to remove any surface abnormalities. Small portions were then cut from the etched sample and heated to 1000 °C at a rate of 5 °C min^{-1} under ammonia gas at a flow rate of 15 L min^{-1} to produce freestanding double gyroidal monoliths. Indium wire (99.999% purity) was purchased from the Indium Corporation and cut into 1 cm sections. These sections were cleaned prior to use by rinsing in aqueous hydrochloric acid with a mass fraction of 10 % followed by isopropanol. The sections were stored under isopropanol until use to inhibit oxide growth.

Small Angle X-Ray Scattering

SAXS data for the hybrid ISA/PMVS monolith (Figure 5.1c solid trace) was obtained at the Soft Matter Interfaces beamline (12-ID) of the National Synchrotron Light Source II (NSLS II). Data for the pyrolyzed porous double gyroidal ceramic template (Figure 5.1c, dashed trace) was obtained at the G1 station at the Cornell High

Energy Synchrotron Source (CHESS). Data for the composite indium backfilled ceramic (Figure 5.1c, dotted trace) was acquired on a custom-built small angle x-ray scattering beamline. The home-built SAXS apparatus utilized a copper rotating anode x-ray generator and a phosphor-coupled charge-coupled detector. This setup is described in detail elsewhere.[55] SAXS images taken at NSLS II were collected on a Pilatus 1M detector using a monochromatic x-ray beam with an energy of 16.10 keV and sample to detector distance of 8.3 m. SAXS images obtained at CHESS were collected with an energy of 9.84 keV and sample to detector distance of 2.2 m with an Eiger 1M pixel array detector. Two dimensional scattering images were integrated azimuthally using the Nika software package.[56]

Nitrogen Physisorption

N_2 sorption measurements were performed on a Micromeritics ASAP 2020 Accelerated Surface Area and Porosimetry System. Powdered SiON ceramic was first degassed at 120 °C for 12 hours before sorption measurement at -196 °C. Pore size distribution was calculated via the Barrett-Joyner-Halenda method.

High Pressure Infiltration

Sample infiltration was performed in a custom-built high pressure / high temperature cell, using a high pressure manifold described previously with some modifications.[57] The cell consisted of a set of stainless steel fittings rated for 413 MPa (High Pressure Equipment Co. -Erie, Pennsylvania) wrapped in a fiberglass-jacketed heat tape with a K type thermocouple embedded in the fitting thread using thermal

grease. Samples to be infiltrated were placed in ca. 3 cm long, 4 mm diameter glass tubes with one end sealed in order to contain the molten In and avoid contamination of the stainless steel cell walls. An activated carbon filter was placed between the cell and the manifold system to prevent indium vapor contamination of other parts of the apparatus. The temperature just beyond this carbon filter was actively monitored to check for any potential annealing behavior in the manifold itself. The manifold was connected to a portable turbomolecular pump (Edwards Inc. - Burgess Hill, United Kingdom), and routinely reached the pump base pressure of 10^{-5} Pa during pump-out. In a typical infiltration procedure, a SiON template was placed in the bottom of a glass tube. One or two 1 cm pieces of cleaned indium wire were then quickly placed in the tube and the tube inserted into the reactor. The reactor was connected to the pressure manifold and placed under vacuum, typically within 2 min of removal of the indium wire from storage in isopropanol. The sample was allowed to degas at 60 °C until the pump reached its base pressure, typically 8 to 12 hours. The cell was then heated at 10 °C min^{-1} to 250 °C and held at this temperature under vacuum. It is important to heat the metal above its melting temperature with the SiON template under vacuum so that the molten metal completely encapsulates the porous monolith. This ensures that when isostatic pressure via He gas is applied to the system, the pressure differential from the exterior of the melt to the interior pore volume is maximized, which is the driving force for infiltration. After 2 hours the valve to the vacuum system was closed and the manifold backfilled with helium gas. The high-pressure pump was then switched on until the manifold pressure reached about 400 MPa of helium, though it should be noted that successful infiltration was seen to take place using pressures of only 200 MPa. This

pressure was held for one hour, after which the heating was switched off and the cell allowed to cool to 60 °C. After depressurization the infiltrated composite monolith could then be retrieved by breaking the glass tube and carefully heating the indium slug until molten with a fine tipped soldering iron.

Scanning Electron Microscopy

Infiltrated monoliths were freeze fractured using liquid nitrogen, and the fractured cross section used for EDX characterization. Other pieces of the infiltrated monoliths were polished with diamond lapping films and used for backscattered electron imaging. Scanning electron micrographs and EDX measurements were taken using a Zeiss Gemini 500 microscope. Backscattered electron images were taken at an accelerating voltage of 1 keV, and EDX measurements taken at an accelerating voltage of 12 keV. For elemental mapping and cross section line scan data, EDX measurements were taken across the entirety of the image shown in Figure 5.3b with a pixel size of 100 by 100 nm. AZtec software from Oxford Instruments was used for the data analysis.

Vibrating Sample Magnetometry

VSM data were taken using the Quantum Design VSM add-on for the Physical Property Measurement System (PPMS), equipped with a cryostat capable of accessing temperatures from 1.8 K to 400 K, a 9 T superconducting magnet, and an EverCool II Helium Reliquefier. Polished mesoporous Indium/SiON composites were briefly etched in 10% HCl to remove any bulk indium clinging to the surface. The polished and etched monolith was mounted using Lakeshore cryogenic varnish on a quartz brace, which was

then press-fit into a brass half-tube sample holder with the polished sample surface normal to the magnetic field. For bulk comparison measurements, a small piece of indium wire from the same source was cut with a razor, pressed with a digital micrometer screw gauge to 100 μm thickness, and mounted similarly with the foil perpendicular to the magnetic field. In both cases, the sample was cooled to 2.0 K under zero applied field, then a small field of 2 mT was applied to locate the sample by scanning the VSM transport through its range. For moment vs. temperature measurements, the field was then ramped quickly to 8 mT and the sample warmed to 5 K at a rate of 0.25 K min^{-1}. For moment vs field measurements, the sample was located using the above procedure, then warmed to 5 K and zero-field-cooled to 2 K to erase any magnetic history. The field was then ramped at 5 mT s^{-1} to 0.75 T, then back to -0.75 T and then finally to 0 T For all measurements, magnetic moment is normalized to the mass of indium metal present.

Four-point probe transport measurements

Data was obtained using the Quantum Design PPMS as described above. Etched and freshly polished indium/SiON composites (different than those used for VSM measurements) were mounted onto silicon carrier chips using small amounts of Lakeshore cryogenic varnish. (100) silicon carrier chips with a 100 nm thermal oxide layer were patterned with four gold contact pads, and 503 silver paint obtained from Electron Microscopy Sciences was used to make four co-linear contacts with the In/SiON composite and leads to the gold contact pads. The carrier chip containing the sample was then mounted to the PPMS via wirebonding. In all measurements, a 100 μA

bias current was applied between the outermost contacts for resistance measurement. For resistance vs temperature measurements, the sample was cooled to 2K under zero field, and the external field was quickly ramped to the respective value. The sample temperature was then ramped to 6 K at a rate of 0.2 K min^{-1}. For resistance vs field measurements, the sample was cooled to the respective temperature under zero field. The field was then ramped to 2 T at a rate of 5 mT s^{-1}. For all measurements the average of 10 measurements is reported, and the relative error at each point was measured as 3 orders of magnitude or lower than the reported resistance value.

Supplementary Information for Chapter 5

Supplementary Figures

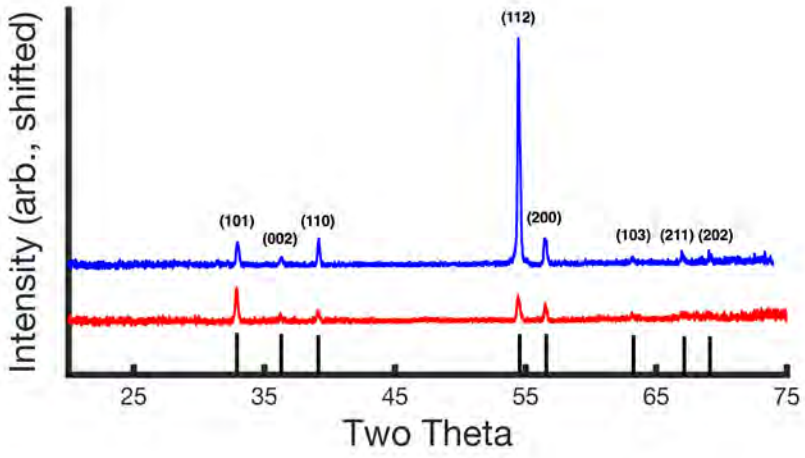

Figure 5.S1*: X-ray diffraction (XRD) traces for indium metal (red trace) used in the infiltration and indium metal/ceramic composite (blue trace) after infiltration. Bottom tick marks show expected peak indices and positions (black) for pure indium metal. It should be noted that in the case of both the bulk and mesostructured indium metal a high degree of sample texturing was seen, resulting in the large differences in relative peak intensities.*

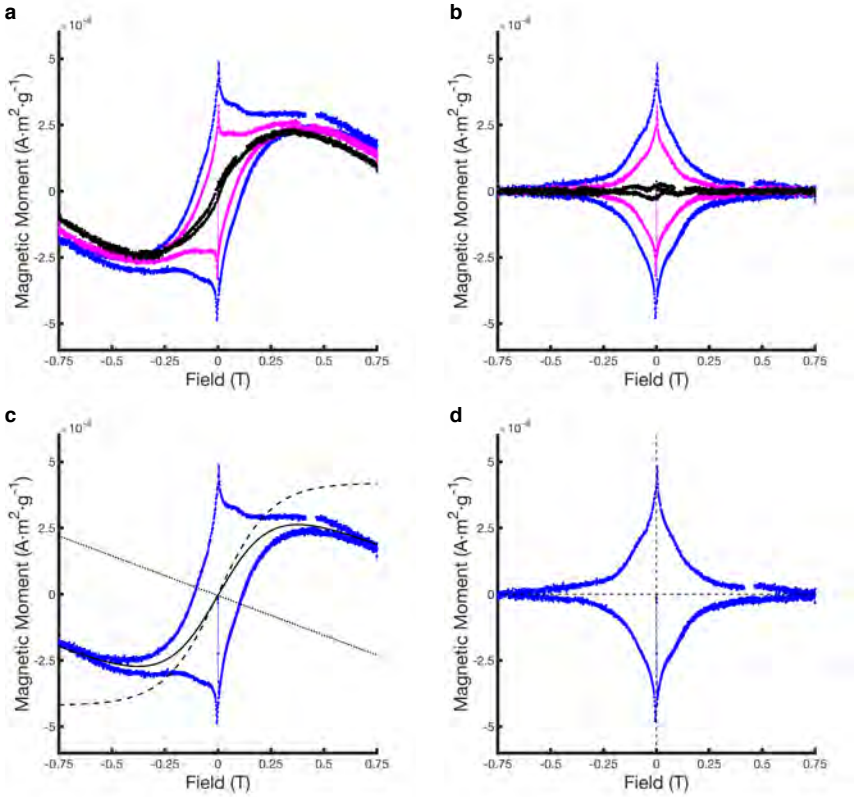

Figure 5.S2: *Background subtraction of full magnetization loops of double gyroidal indium/SiON composites to isolate hysteretic component. a) Raw field dependent magnetization of mesostructured indium at 2 K (blue trace), 2.5 K (magenta trace), and 4 K (black trace) showing significant non-hysteretic background signal above the double gyroidal indium* T_c *of ≈ 3.67 K. b) Background subtracted data at 2, 2.5, and 4 K obtained via subtraction of the 4 K trace multiplied by a temperature dependent fitting parameter. This prefactor was selected to minimize the summed square value of non-hysteretic magnetic signal at very high fields (±1 T), and was seen to vary linearly with temperature. c) Unsubtracted magnetization loop at 2 K (blue trace) and representative components of background signal: paramagnetic signal (dashed black trace), diamagnetic signal (dotted black trace), and combined background signal (solid black trace). d) Background subtracted magnetization loop at 2 K, dotted lines added for visual guidance.*

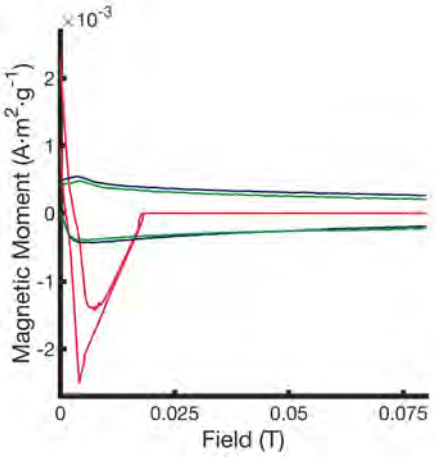

Figure 5.S3: *Magnetization measurements at low field for a 100 μm bulk indium foil (red), a double gyroidal indium sample measured less than 48 hours after infiltration (blue), and the same double gyroidal indium sample measured after nine months of storage at room temperature in open air (green). All measurements were performed at 2K after cooling under zero field. The green trace represents a subset of the data as shown in the main text figure 5.4b. The very nearly overlapping traces from the 'new' as compared to 'old' material demonstrates a very high degree of stability and lack of sensitivity to oxidation.*

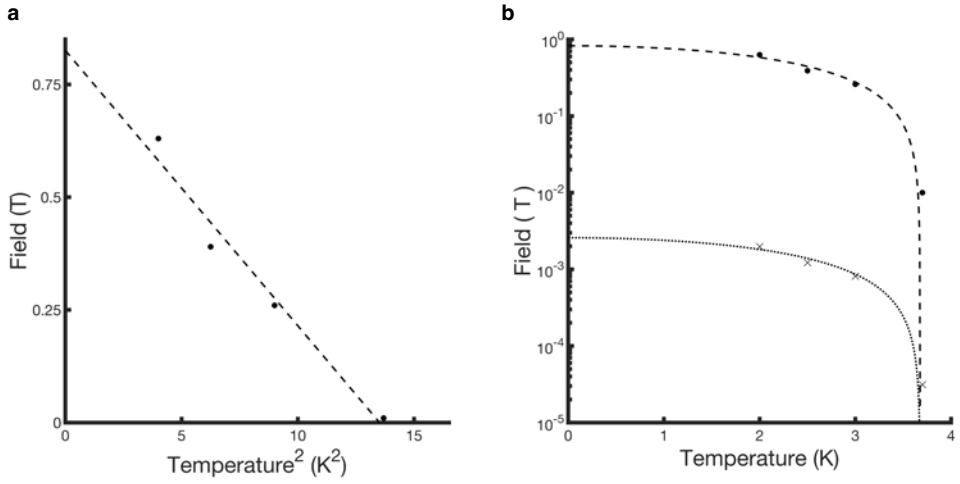

Figure 5.S4: *Observed critical fields for double gyroidal indium during field dependent magnetization at varying temperature as shown in Figure 5.S2. a) Linear fit of the upper critical field with respect to the square of the temperature, used to determine $H_{c2}(0)$ and T_c. Black circles denote observed upper critical field at respective temperature, taken to be the point at which hysteresis disappeared in the raw data (Figure 5.S2a) and the sample magnetic moment in both the forward and reverse field scanning direction matched within an instrumental margin of error. b) Superconducting phase diagram for double gyroidal indium showing critical field with respect to temperature. Observed upper critical field again denoted by black circles, lower critical field estimated using the calculated effective κ shown as black crosses. Lines are of the form* $H_{c2}(T) = H_{c2}(0) \cdot \left(1 - \left({}^{T}/_{T_c}\right)^2\right)$ *for guidance;* $\mu_0 H_{c1}(0)$ *estimated as 0.82 T using the relation* $H_{c1} = H_{c2}/2\kappa^2 \ln(\kappa)$.

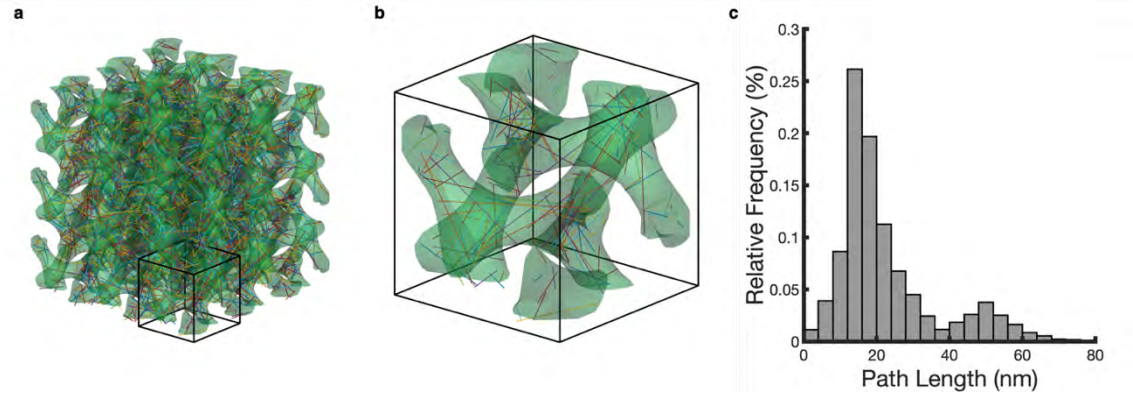

Figure 5.S5: *Visualization of confinement within the network struts of a core shell double gyroid structure. a) A model volume used for Monte Carlo sampling of ballistic paths, spanning three Ia3d unit cells in the x, y, and z dimensions. The volume shaded in green represents both the left- and right-handed strut networks at a combined volume fraction of 0.288 of the unit cell volume. Lines drawn within this green volume denote randomly sampled straight paths, drawn in multiple colors for effect. Black outlines denote the boundaries of one cubic unit cell. b) A larger depiction of a single Ia3d unit cell, with the strut network volume shaded green and sampled paths drawn in as lines. Black borders again denote the edges of the unit cell. c) A histogram showing the distribution of 4,446 randomly sampled paths within the volume shown in b, with an average path length of 23 nm.*

Supplementary Note 5.1: Approximation of Pressures Required for Metal Infiltration of Mesoporous Templates

Equation (5.2), the Young-Laplace equation, gives the capillary pressure, ΔP, induced by a liquid of surface tension γ with a contact angle of θ on a solid with pores of diameter d. This rlation has been shown to be valid down to the nanoscale.[58] The surface tension of liquid indium has previously been reported as 573 mN/m, and the contact angle of liquid indium on silicon oxynitride can be approximated as 125˚ from

studies on materials with very similar composition and surface energies.[59,60] The pore diameter of the SiON template used in this case was measured to be an average of 18 nm.

$$\Delta P = \frac{4\gamma \cos\theta}{d} \tag{5.2}$$

From Equation (5.2), pressures upwards of 70 MPa are required to overcome capillary pressure for infiltration in the double gyroidal ceramic template shown in this work. Extrapolation of this relation for indium metal across common length scales of bulk block-copolymer self-assembly derived structures shows that the range of pressures is easily accessible using commercially available high-pressure systems: from 26 MPa for 50 nm diameter pores to 260 MPa for 5 nm pores.

Supplementary Note 5.2: Modelling of Ballistic Paths within a Double Gyroid Strut Network

The double gyroid structure can be approximated by a level set function of the form shown in Equation (5.3), where x, y, and z are spatial coordinates, a is the unit cell length or the d_{100}, and t is a constant which determines the volume fractions of the spaces divided by the level surface.[61] The surfaces at $0 < |t| \leq 1.413$ define two interpenetrating volumes which correspond to the left and right handed networks of the gyroid structure, separated by a matrix phase of finite thickness for $0 < |t|$.

$$F(x,y,z) = \sin\left(\frac{2\pi x}{a}\right)\cos\left(\frac{2\pi y}{a}\right) + \sin\left(\frac{2\pi y}{a}\right)\cos\left(\frac{2\pi z}{a}\right) + \sin\left(\frac{2\pi z}{a}\right)\cos\left(\frac{2\pi x}{a}\right) = \pm 2 \tag{5.3}$$

For the core-shell double gyroid structured ISA/PMVS composite films used in this work, the volume fraction of the hydrophilic matrix phase (A-block and PMVS) can be calculated as 71.2 % by volume assuming a density of 1.18 g cm^{-3} for the PDMAEMA block of the ISA terpolymer and 1.00 g cm3 for the PMVS.[24] If the composite structure is assumed to isotopically shrink during thermal processing without a significant change in the volume fraction occupied by the A+PMVS phase to that occupied by the SiON ceramic, the void fraction in the porous ceramic would be equal to that of the combined isoprene (core) and styrene (shell) in the parent film, 28.8 % by volume. If the two void networks are assumed to be completely filled by indium metal upon infiltration, the volume occupied by the indium strut networks can be approximated by the level set function in Equation (5.3) with t = 1.09. Through Monte Carlo sampling of 'starting' coordinates as well as ballistic path directions within this volume, the average ballistic path length can then be modeled.

In order to perform this modelling, the level set function is first evaluated with unit cell length a equal to the d_{100} of the ceramic and indium/SiON composite as determined by SAXS, 73 nm (Figure 5.2). This evaluation is done on a three-dimensional mesh of points equally spaced at 3.65 nm and spanning three unit cells in the x, y, and z dimensions, with linear interpolation performed between these 'vertex' points to define 'face' which altogether comprise the level surface (Figure 5.S5a, green shaded structure). After defining this surface, 4,446 points are randomly selected within the 'interior' of the networks such that $t = F(x, y, z) < \pm 1.09$. For every point selected in this way, a random direction is defined. The distance from the point to the closest

intersection of the level surface is then measured within 0.25 nm, traveling in a straight line along the 'forward' direction randomly chosen as well as 'backwards' in the inverse direction. The total path length is then recorded as the sum of both the 'forward' and 'backward' path length (Figure 5.S5a and b, multicolored lines). The relative frequency of path lengths is displayed in the histogram in Figure 5.S5c, with a bin size of 4 nm. The mean path length of all those samples was found to be 23 nm.

Supplemental experimental methods

X-ray Diffraction (XRD): XRD data was collected on a Bruker D8 General Area Detector Diffraction System with a 1.6 kW Cu-Kα source and beam size of 0.5 mm. 2D diffraction images were collected at 15° intervals with a 5 minute exposure time at each angle. 2D images were stitched together and integrated into one-dimensional traces using Bruker Diffract Suite Software.

Vibrating Sample Magnetometry: Data was obtained using the VSM add-on for the Quantum Design PPMS DynaCool System. Double gyroidal SiON/In samples other than those measured in Figure 5.3 were similarly etched, polished, and mounted with varnish onto quartz braces. After cooling to 2K under zero field, samples were located by scanning the VSM through its range in an external field of 2 mT. Samples were then warmed to 10 K and cooled again to 2K under zero field. Sample temperature was then set at the temperature as shown in Figure 5.S1, and the external field was scanned across all four quadrants from 0 T, to 1 T, to 0 T, to -1 T, then back to 0 T. Field strength was swept at a rate of 5 T s^{-1}, and the magnetic moment value was taken to be the average

of 10 measurements at intervals of 25 mT. Magnetic moment measurements in all cases are normalized to the mass of indium metal present.

REFERENCES

1. Broholm, C., Fisher, I., Moore, J., Murnane, M., Moreo, A., Tranquada, J., Basov, D., Freericks, J., Aronson, M., MacDonald, A., Fradkin, E., Yacoby, A., Samarth, N., Stemmer, S., Horton, L., Horwitz, J., Davenport, J., Graf, M., Krause, J., Pechan, M., Perry, K., Rhyne, J., Schwartz, A., Thiyagarajan, T., Yarris, L. & Runkles, K. *Basic Research Needs Workshop on Quantum Materials for Energy Relevant Technology*. 1616509 (2016). doi:10.2172/1616509
2. Feighan, J. P. F., Kursumovic, A. & MacManus-Driscoll, J. L. Materials design for artificial pinning centres in superconductor PLD coated conductors. *Supercond. Sci. Technol.* **30,** 123001 (2017).
3. Ishida, S., Iyo, A., Ogino, H., Eisaki, H., Takeshita, N., Kawashima, K., Yanagisawa, K., Kobayashi, Y., Kimoto, K., Abe, H., Imai, M., Shimoyama, J. & Eisterer, M. Unique defect structure and advantageous vortex pinning properties in superconducting CaKFe4As4. *Npj Quantum Mater.* **4,** 27 (2019).
4. Haugan, T., Barnes, P. N., Wheeler, R., Meisenkothen, F. & Sumption, M. Addition of nanoparticle dispersions to enhance flux pinning of the YBa2Cu3O7-x superconductor. *Nature* **430,** 867–870 (2004).
5. Bose, S., García-García, A. M., Ugeda, M. M., Urbina, J. D., Michaelis, C. H., Brihuega, I. & Kern, K. Observation of shell effects in superconducting nanoparticles of Sn. *Nat. Mater.* **9,** 550–554 (2010).

6. Menghini, M., Wijngaarden, R. J., Silhanek, A. V., Raedts, S. & Moshchalkov, V. V. Dendritic flux penetration in Pb films with a periodic array of antidots. *Phys. Rev. B* **71,** 104506 (2005).
7. Yan, R., Khalsa, G., Schaefer, B. T., Jarjour, A., Rouvimov, S., Nowack, K. C., Xing, H. G. & Jena, D. Thickness dependence of superconductivity in ultrathin NbS_2. *Appl. Phys. Express* **12,** 023008 (2019).
8. Savinov, V., Tsiatmas, A., Buckingham, A. R., Fedotov, V. A., de Groot, P. A. J. & Zheludev, N. I. Flux Exclusion Superconducting Quantum Metamaterial: Towards Quantum-level Switching. *Sci. Rep.* **2,** 450 (2012).
9. Geim, A. K., Grigorieva, I. V., Dubonos, S. V., Lok, J. G. S., Maan, J. C., Filippov, A. E., Peeters, F. M. & Deo, P. S. Mesoscopic superconductors as `artificial atoms' made from Cooper pairs. *Phys. B Condens. Matter* **249–251,** 445–452 (1998).
10. Gomez, A., Gonzalez, E. M. & Vicent, J. L. Superconducting vortex dynamics on arrays with bicrystal-like structures: matching and rectifier effects. *Supercond. Sci. Technol.* **25,** 124006 (2012).
11. He, M., Wong, C. H., Tse, P. L., Zheng, Y., Zhang, H., Lam, F. L. Y., Sheng, P., Hu, X. & Lortz, R. "Giant" Enhancement of the Upper Critical Field and Fluctuations above the Bulk T_c in Superconducting Ultrathin Lead Nanowire Arrays. *ACS Nano* **7,** 4187–4193 (2013).
12. Bose, S. & Ayyub, P. A review of finite size effects in quasi-zero dimensional superconductors. *Rep. Prog. Phys.* **77,** 116503 (2014).

13. Lozano, D. P., Couet, S., Petermann, C., Hamoir, G., Jochum, J. K., Picot, T., Menéndez, E., Houben, K., Joly, V., Antohe, V. A., Hu, M. Y., Leu, B. M., Alatas, A., Said, A. H., Roelants, S., Partoens, B., Milošević, M. V., Peeters, F. M., Piraux, L., Van de Vondel, J., Vantomme, A., Temst, K. & Van Bael, M. J. Experimental observation of electron-phonon coupling enhancement in Sn nanowires caused by phonon confinement effects. *Phys. Rev. B* **99,** 064512 (2019).
14. Bates, F. S., Hillmyer, M. A., Lodge, T. P., Bates, C. M., Delaney, K. T. & Fredrickson, G. H. Multiblock Polymers: Panacea or Pandora's Box? *Science* **336,** 434–440 (2012).
15. Meuler, A. J., Hillmyer, M. A. & Bates, F. S. Ordered Network Mesostructures in Block Polymer Materials. *Macromolecules* **42,** 7221–7250 (2009).
16. Bardeen, J., Cooper, L. N. & Schrieffer, J. R. Theory of Superconductivity. *Phys. Rev.* **108,** 1175–1204 (1957).
17. Hur, K., Hennig, R. G. & Wiesner, U. Exploring Periodic Bicontinuous Cubic Network Structures with Complete Phononic Bandgaps. *J. Phys. Chem. C* **121,** 22347–22352 (2017).
18. Fruchart, M., Jeon, S.-Y., Hur, K., Cheianov, V., Wiesner, U. & Vitelli, V. Soft self-assembly of Weyl materials for light and sound. *Proc. Natl. Acad. Sci.* **115,** E3655–E3664 (2018).
19. Robbins, S. W., Beaucage, P. A., Sai, H., Tan, K. W., Werner, J. G., Sethna, J. P., DiSalvo, F. J., Gruner, S. M., Van Dover, R. B. & Wiesner, U. Block copolymer

self-assembly–directed synthesis of mesoporous gyroidal superconductors. *Sci. Adv.* **2,** e1501119 (2016).

20. Warren, S. C., Messina, L. C., Slaughter, L. S., Kamperman, M., Zhou, Q., Gruner, S. M., DiSalvo, F. J. & Wiesner, U. Ordered Mesoporous Materials from Metal Nanoparticle-Block Copolymer Self-Assembly. *Science* **320,** 1748–1752 (2008).
21. Hsueh, H.-Y., Huang, Y.-C., Ho, R.-M., Lai, C.-H., Makida, T. & Hasegawa, H. Nanoporous Gyroid Nickel from Block Copolymer Templates via Electroless Plating. *Adv. Mater.* **23,** 3041–3046 (2011).
22. Cowman, C. D., Padgett, E., Tan, K. W., Hovden, R., Gu, Y., Andrejevic, N., Muller, D., Coates, G. W. & Wiesner, U. Multicomponent Nanomaterials with Complex Networked Architectures from Orthogonal Degradation and Binary Metal Backfilling in ABC Triblock Terpolymers. *J. Am. Chem. Soc.* **137,** 6026–6033 (2015).
23. Vignolini, S., Yufa, N. A., Cunha, P. S., Guldin, S., Rushkin, I., Stefik, M., Hur, K., Wiesner, U., Baumberg, J. J. & Steiner, U. A 3D Optical Metamaterial Made by Self-Assembly. *Adv. Mater.* **24,** OP23–OP27 (2012).
24. Susca, E. M., Beaucage, P. A., Hanson, M. A., Werner-Zwanziger, U., Zwanziger, J. W., Estroff, L. A. & Wiesner, U. Self-Assembled Gyroidal Mesoporous Polymer-Derived High Temperature Ceramic Monoliths. *Chem. Mater.* **28,** 2131–2137 (2016).

25. Barrett, E. P., Joyner, L. G. & Halenda, P. P. The Determination of Pore Volume and Area Distributions in Porous Substances. I. Computations from Nitrogen Isotherms. *J. Am. Chem. Soc.* **73,** 373–380 (1951).

26. Feng, X., Burke, C. J., Zhuo, M., Guo, H., Yang, K., Reddy, A., Prasad, I., Ho, R.-M., Avgeropoulos, A., Grason, G. M. & Thomas, E. L. Seeing mesoatomic distortions in soft-matter crystals of a double-gyroid block copolymer. *Nature* **575,** 175–179 (2019).

27. Leavens, C. R. & Fenton, E. W. Superconductivity of small particles. *Phys. Rev. B* **24,** 5086–5092 (1981).

28. McMillan, W. L. Transition Temperature of Strong-Coupled Superconductors. *Phys. Rev.* **167,** 331–344 (1968).

29. Jennings, L. D. & Swenson, C. A. Effects of Pressure on the Superconducting Transition Temperatures of Sn, In, Ta, Tl, and Hg. *Phys. Rev.* **112,** 31–43 (1958).

30. Sharifi, F., Herzog, A. V. & Dynes, R. C. Crossover from two to one dimension in *in situ* grown wires of Pb. *Phys. Rev. Lett.* **71,** 428–431 (1993).

31. Lehtinen, J. S., Sajavaara, T., Arutyunov, K. Yu., Presnjakov, M. Yu. & Vasiliev, A. L. Evidence of quantum phase slip effect in titanium nanowires. *Phys. Rev. B* **85,** 094508 (2012).

32. Bose, S., Galande, C., Chockalingam, S. P., Banerjee, R., Raychaudhuri, P. & Ayyub, P. Competing effects of surface phonon softening and quantum size effects on the superconducting properties of nanostructured Pb. *J. Phys. Condens. Matter* **21,** 205702 (2009).

33. Dolan, G. J. Direct observations of the magnetic structure in thin films of Pb, Sn, and In. *J. Low Temp. Phys.* **15,** 111–132 (1974).

34. Harper, F. E. & Tinkham, M. The Mixed State in Superconducting Thin Films. *Phys. Rev.* **172,** 441–450 (1968).

35. Prozorov, R., Giannetta, R. W., Polyanskii, A. A. & Perkins, G. K. Topological hysteresis in the intermediate state of type-I superconductors. *Phys. Rev. B* **72,** 212508 (2005).

36. Blatter, G., Feigel'man, M. V., Geshkenbein, V. B., Larkin, A. I. & Vinokur, V. M. Vortices in high-temperature superconductors. *Rev. Mod. Phys.* **66,** 1125–1388 (1994).

37. Aliev, A. E., Lee, S. B., Zakhidov, A. A. & Baughman, R. H. Superconductivity in Pb inverse opal. *Phys. C Supercond.* **453,** 15–23 (2007).

38. Bykov, A. A., Gokhfeld, D. M., Savitskaya, N. E., Terentjev, K. Y., Popkov, S. I., Mistonov, A. A., Grigoryeva, N. A., Zakhidov, A. & Grigoriev, S. V. Flux pinning mechanisms and a vortex phase diagram of tin-based inverse opals. *Supercond. Sci. Technol.* **32,** 115004 (2019).

39. Skocpol, W. J. & Tinkham, M. Fluctuations near superconducting phase transitions. *Rep. Prog. Phys.* **38,** 1049–1097 (1975).

40. Strongin, M., Paskin, A., Schweitzer, D. G., Kammerer, O. F. & Craig, P. P. Surface Superconductivity in Type I and Type II Superconductors. *Phys. Rev. Lett.* **12,** 442–444 (1964).

41. Saint-James, D. & Gennes, P. G. Onset of superconductivity in decreasing fields. *Phys. Lett.* **7,** 306–308 (1963).

42. Tinkham, M. *Introduction to superconductivity*. (Dover Publ, 2015).

43. Laplace, Y. & Cavalleri, A. Josephson plasmonics in layered superconductors. *Adv. Phys. X* **1,** 387–411 (2016).

44. Economou, E. N. Surface Plasmons in Thin Films. *Phys. Rev.* **182,** 539–554 (1969).

45. Lu, Q., Bollinger, A. T., He, X., Sundling, R., Bozovic, I. & Gozar, A. Surface Josephson plasma waves in a high-temperature superconductor. *Npj Quantum Mater.* **5,** 69 (2020).

46. Dolan, G. J. Critical thicknesses for the transition from intermediate- to mixed-state behavior in superconducting thin films of Pb, Sn, and In. *J. Low Temp. Phys.* **15,** 133–160 (1974).

47. Eisenstein, J. Superconducting Elements. *Rev. Mod. Phys.* **26,** 277–291 (1954).

48. Donnelly, R. J. in *Phys. Vade Mecum* (American Institute of Physics).

49. Gall, D. Electron mean free path in elemental metals. *J. Appl. Phys.* **119,** 085101 (2016).

50. Susca, E. M., Beaucage, P. A., Thedford, R. P., Singer, A., Gruner, S. M., Estroff, L. A. & Wiesner, U. Preparation of Macroscopic Block-Copolymer-Based Gyroidal Mesoscale Single Crystals by Solvent Evaporation. *Adv. Mater.* **31,** 1902565 (2019).

51. Feng, X., Guo, H. & Thomas, E. L. Topological defects in tubular network block copolymers. *Polymer* **168,** 44–52 (2019).

52. Costner, E. A., Lin, M. W., Jen, W.-L. & Willson, C. G. Nanoimprint Lithography Materials Development for Semiconductor Device Fabrication. *Annu. Rev. Mater. Res.* **39,** 155–180 (2009).

53. Kumar, G., Tang, H. X. & Schroers, J. Nanomoulding with amorphous metals. *Nature* **457,** 868–872 (2009).

54. Liu, N., Xie, Y., Liu, G., Sohn, S., Raj, A., Han, G., Wu, B., Cha, J. J., Liu, Z. & Schroers, J. General Nanomolding of Ordered Phases. *Phys. Rev. Lett.* **124,** 036102 (2020).

55. Finnefrock, A. C., Ulrich, R., Toombes, G. E. S., Gruner, S. M. & Wiesner, U. The Plumber's Nightmare: [1] A New Morphology in Block Copolymer−Ceramic Nanocomposites and Mesoporous Aluminosilicates. *J. Am. Chem. Soc.* **125,** 13084–13093 (2003).

56. Ilavsky, J. Nika: software for two-dimensional data reduction. *J. Appl. Crystallogr.* **45,** 324–328 (2012).

57. Kim, C. U., Kapfer, R. & Gruner, S. M. High-pressure cooling of protein crystals without cryoprotectants. *Acta Crystallogr. D Biol. Crystallogr.* **61,** 881–890 (2005).

58. Liu, H. & Cao, G. Effectiveness of the Young-Laplace equation at nanoscale. *Sci. Rep.* **6,** 23936 (2016).

59. Harding, F. L. & Rossington, D. R. Wetting of Ceramic Oxides by Molten Metals Under Ultrahigh Vacuum. *J. Am. Ceram. Soc.* **53,** 87–90 (1970).

60. Klein, R., Desmaison-Brut, M., Ginet, P., Bellosi, A. & Desmaison, J. Wettability of silicon nitride ceramic composites by silver, copper and silver copper titanium alloys. *J. Eur. Ceram. Soc.* **25,** 1757–1763 (2005).

61. Dolan, J. A., Wilts, B. D., Vignolini, S., Baumberg, J. J., Steiner, U. & Wilkinson, T. D. Optical Properties of Gyroid Structured Materials: From Photonic Crystals to Metamaterials. *Adv. Opt. Mater.* **3,** 12–32 (2015).

CHAPTER 6

CONCLUSION

In this dissertation several methods were presented for the synthesis of mesoscale ordered superconducting materials using block copolymers (BCPs) as structure directing agents: mesostructured NbCN thin films targeted toward device integration, bulk hexagonally mesoporous NbCN materials derived from commercially available Pluronics BCPs, and indium/SiON ceramic composites with cubic gyroidal structure from high pressure infiltration. Each chapter described new structures, properties or processing capabilities, made possible through the use of solution processible self-assembling soft matter components, which are difficult or inaccessible via traditional superconductor synthesis techniques usually involving ultrahigh vacuum.

After an introduction chapter summarizing the challenges addressed in this thesis, the second chapter provided an overview of the emerging field of soft matter enabled quantum materials. Examples were given of superconductors, topological materials, and magnetic materials synthesized using self-assembling soft matter components, and the properties or new capabilities arising in each case were discussed. A few perspective vignettes were then given, speculating on how the field of soft matter may impact future studies and syntheses of quantum materials by enabling new technology or revealing new phenomena.

The third chapter described a route to patternable mesoporous thin film NbCN superconductors by making use of a self-assembling triblock terpolymer to structure

direct a niobium ethoxide based sol in a spin coating process. Multiple discrete processing steps in ammonia and carburizing gas up to 1000 ˚C produced phase pure rock-salt NbCN with a lattice parameter of 4.41 Å and a mesostructure consistent with a distorted cubic alternating gyroid of unit cell dimension of approximately 50 nm. The final film had transport properties consistent with a highly granular superconductor with a critical temperature of 12.8 K and upper critical field over 16 T. Critical temperature and critical field were much improved in the porous gyroidal NbCN thin films as compared to a similarly processed dense film. This suggested that the high surface area and porosity aided in the conversion of the parent oxide or nitride at high temperatures in reactive gas environments. The critical field of 16 T was also higher than that of bulk NbCN materials synthesized by traditional techniques, which suggested that the mesostructure plays a role in enhancing the critical field. As made polymer-niobia composite thin films were patternable by standard photolithographic methods, which showcased the amenability of this solution-based soft matter self-assembly directed superconductor fabrication approach to planar processing.

In the fourth chapter, crystalline and hexagonally mesoporous NbCN superconductors (CUS-86) were synthesized using commercially available block copolymers of the Pluronics family. Through careful thermal processing employing multiple reactive gas annealing steps, Pluronics templated amorphous parent oxides were converted into phase pure rock salt NbCN materials with a lattice constant of 4.37 Å, coherent scattering domain size of 4.4 nm, and retained hexagonal structure. Use of varying Pluronics templating agents or pore swelling hydrophobic small molecules and homopolymers tuned the final material pore size between 5.3 and 7.8 nm. Using

magnetization and transport measurements, CUS-86 materials were characterized as highly granular type II superconductors with a critical temperature of up to ≈ 8 K and upper critical field of ≈ 5 T.

In the fifth chapter, using high pressure infiltration of molten indium into BCP derived ceramic templates, indium metal superconductors were created with cubic double gyroidal network structure. The double gyroid structure of the parent mesoporous ceramic was retained through the infiltration process, as was the unit cell size of 73 nm. Homogenous infiltration throughout the interior of 60 micron thick monoliths was demonstrated, with the exception of some unfilled voids seen at mesoscopic grain boundaries of the gyroid structure. In comparison with bulk indium metal, the mesostructured gyroidal indium had a broadened and enhanced superconducting transition temperature, with an onset of 3.7 K. This behavior could be rationalized by the contribution of increased surface area to stronger phonon coupling. Furthermore, the gyroidal indium behaved as a type II superconductor, with evidence of magnetic hysteresis and an upper critical field of 0.63 T due to the introduction of hard vortex pinning centers. This was conjectured to be an effect of the change in coherence length due to the BCP induced metal nanoconfinement, calculated to be 20 nm in the gyroidal indium as compared to 360 nm in bulk indium metal. This value of coherence length was notably on the order of the gyroid strut size. This suggested that the BCP induced mesostructure substantially changed fundamental quantum level materials properties which in turn dictated macroscopic superconductor behavior.

Looking toward future efforts in the area of BCP derived mesostructured superconductors, one can envision several directions for research which capitalize on

and extend the work presented in this thesis. The preceding chapters represent the foundational synthetic practices and tools necessary to establish scalable solution-based processing methods, create real devices, and investigate the fundamental effects of BCP mesostructure on superconductivity. The work which follows may use these tools to reach further from the field of soft matter into that of quantum materials to achieve greater sophistication in fabrication, analysis, and fundamental understanding.

In the area of thin films, the work presented in chapter three now enables the creation of test devices and architectures which are easily integrated into highly developed planar fabrication and analysis methods. In the work described in chapter three this allowed for much more precise transport measurements than has been possible for past studies of bulk materials, and resulted in the important new insight that BCP templated NbCN materials are highly granular superconductors. Further design of test architectures, made possible through lithographic means such as those demonstrated, and interrogation of transport properties should provide additional insights and enable targeting of device applications. It is expected that the characterization of mesoporous NbCN thin films as Josephson junction arrays will be of particular interest, as this may have relevance in quantum sensing and quantum computing applications.

From the work using Pluronics, it is anticipated that future investigations will be inspired by the wealth of existing studies using this class of commercial BCPs, and their derived mesoporous materials, to discover new processing methods and capabilities for BCP-derived superconductors. As one example, Pluronics BCPs have previously been used for the development of inks in 3D printing of polymeric, inorganic, and composite materials. With the work described in chapter four presenting a viable route to convert

Pluronics based printed parts into mesoporous superconductors, there is now a clear pathway for the development of 3D printable superconductors with both controlled mesoporosity and macroscopic shapes. In another example more targeted towards fundamental science, ordered mesoporous NbCN superconductors made using Pluronics might now be studied as hosts for molecular guest species, as has been demonstrated in numerous mesoporous materials derived from this class of ABA diblock copolymers. Having established routes to a new superconducting class of Pluronics derived nitrides, one may expect that studies of host-guest interactions below the superconducting transition of the mesoporous host may find new phenomena resulting from the interaction of magnetic vortices or surface plasmons with such guest molecules.

Lastly, one may expect that the method developed in chapter five will become crucial for elucidating the specific effects of 3D mesoscale architectures on superconductor behavior. The chemical simplicity of this mesostructured superconductor formation platform based on pure metal differentiates it from work in other chapters using NbN or NbCN, allowing for the decoupling of materials mesostructure formation and chemistry. Furthermore, the described high-pressure infiltration method is compatible with recently developed routes to ceramic templates which are macroscopic single crystals of the double gyroid. This will allow for the synthesis of single crystal gyroid indium superconductors with known crystal orientation relative to external coordinate systems. In turn, this will enable the investigation of phenomena associated with the mesoscale gyroid lattice without the confounding effects of grain boundaries and polycrystallinity. In particular, it is

expected that magnetic small-angle neutron scattering performed on such indium infiltrated gyroidal single crystals will become a critical tool to elucidate the effects of mesoscopic structural lattices, e.g., on the structure and dynamics of the expected magnetic flux lattices in the mixed state of the investigated superconductors.

Further questions could be inspired by the work presented in this thesis, the investigation into which will require the development of new materials and methods in addition to extending those accomplished here. Some of these questions are targeted toward 'known' areas, where there can be some reasonable suspicion that fertile intellectual ground awaits; others may be venturing into more unknown waters. In the former category, it is apparent that materials properties are dictated by structure across multiple length scales: atomic crystallinity and granularity, mesoscopic symmetry and grain size/structure, and macroscopic shape or form factor. Our ability to reliably control materials structure at these length scales during synthesis will thus directly enable new structure-property studies and greatly aid in the understanding of soft matter derived quantum materials.

Increased control over atomic grain size and texture of BCP templated crystalline materials would aid many important investigations, including those into BCP derived mesostructured superconductors. As an example, the gyroidal indium presented in chapter 5 was found to be polycrystalline at the atomic level. However, through modification of infiltration procedure or use of annealing methods, it may be possible to obtain single crystal indium domains of macroscopic dimension (i.e., on the order of the monolithic gyroidal ceramic template in size). This would allow for more sophisticated magnetic and electronic measurements of superconducting gyroidal

indium in which an external field or current is applied along a specific axis relative to the indium crystal lattice. Further, if such annealing could be done in conjunction with the use of single crystal gyroidal ceramic templates discussed earlier, the result would be a "single crystal of a single crystal." Such simultaneous control of both atomic and mesoscopic order over macroscopic lengths would achieve a long-sought goal of BCP templating, and for the first time allow one to fully decouple the effects of atomic and mesoscopic structure on BCP derived superconducting materials.

Along this line, another area which might be further explored itself is that of BCP ordering over macroscopic dimensions towards bulk, mesoscale single crystals. Here two questions are posed: can we determine how such single crystal structures are formed, and can we control this process to tailor the alignment, size, and/or shape of BCP derived mesoscale single crystals? Previous work found that, through a particular method involving solvent recirculation in an evaporating film, large (centimeter sized) single crystals of the double gyroid structure could be obtained. It was considered that the action of the orthogonal forces of solvent evaporative flux and fluid flow from recirculation contributed to the growth and alignment of these gyroidal single crystals. Further investigation into the mechanism by which these mesoscale single crystals are formed could bear valuable fruit: contributing to the fundamental understanding of self-assembly and alignment processes in BCPs, especially with cubic structures, and increasing the level of control which is possible in the synthesis of mesoscale bulk single crystals.

This investigation could proceed by a few different methods. In the first, tracer particles might be used in the initial BCP solution as a tool for envisioning fluid flow.

Fluorescently or otherwise labelled particles, which may or may not energetically prefer to reside in one BCP domain, of a known size and transport characteristics would be added to the initial solution. During the evaporation/recirculation process the effect of fluid flow on the distribution of these tracer particles would then allow for a rough determination of spatially and temporally dependent fluid flow profiles in the system over the course of evaporation. Such information could then be used in conjunction with simulations to determine critical values of evaporation rate, fluid velocity, recirculation rate, temperature, etc. which are required for the achievement of large single crystal regions.

Resulting insights could then be fed into another experimental thrust aimed at more rigorous control over single crystal growth. In initial work, recirculation of solvent in an evaporating BCP solution was affected through the placement of a concave glass watch glass over a Teflon evaporation dish. This rudimentary process serendipitously resulted in record-sized single crystals of the gyroid structure, but left much to be desired in the way of adjustable process parameters. Replicating this environment in a more controllable experimental apparatus could allow one to "turn more knobs," adjusting parameters such as the evaporation rate (e.g., through control over vapor phase solvent concentration), solvent recirculation rate, or temperature. Using insight gained from tracer particle experiments and simulations, macroscopic single crystals of BCP structures might then be produced under known conditions. This control could then be leveraged into a better fundamental understanding of single crystal growth, and extended to create single crystals of larger dimensions or in alternative shapes and geometries. Such an achievement would have important implications not only to the

work in BCP derived superconductors (*vide supra)*, but to the entire field of BCP and soft matter self-assembly which has continually sought methods for controlling and improving long range order in self-assembled materials.

One such area in which much progress has been made improving long range order of BCP structures is in thin films. However, the capabilities developed for the ordering of BCP films or polymer/organic hybrids has not been fully realized in the synthesis of BCP derived superconductor films. In the mesoporous NbCN thin films described in chapter 3 it was shown that the rapid evaporation of solvent during the spin coating process, without any additional annealing, led to poor long-range order of the self-assembled structure and deformation of the thermodynamically preferred cubic morphology. While in some cases this deformation can lead to fortuitous symmetry breaking, the application of post-processing might be used to improve order and recover cubic gyroidal symmetry in final superconducting films. At this point the exact effects this achievement would bring is not entirely clear, but previous work has shown that mesoscale connectivity and symmetry can have implications for superconducting properties and other electronic, photonic, or phononic phenomena.

Beyond further structural control of established materials such as the SiON/indium composites and NbCN presented in this thesis, expansion into other types of materials could lead to much interesting new phenomena. Though limited to relatively low temperatures by the experimental apparatus, the high pressure melt infiltration method described in chapter 5 could be generalized to many other metals or alloys. This could lead to the achievement of bulk monoliths of gyroidally structured metals such as silver, aluminum, or gold, which have previously been considered of

interest for emergent photonic or plasmonic effects. Further, the BCP derived mesoporous template used for the infiltration need not be an amorphous SiON ceramic, but likely could be any one of the many silicates, metal oxides, metal nitrides, metals, etc. which have been successfully mesostructured using BCP self-assembly. Combining this freedom of materials choice in the mesoporous template and the infiltrated metal, one could envision a wealth of possible composites of dielectric, metallic, semiconducting, and superconducting materials. There is good reason to believe that emergent effects could be achieved through judicious materials choice in a mesostructured nanocomposite, as there are many documented effects of proximity and interfaces in superconductors and beyond. With the manyfold increase in surface or interfacial area as compared to, e.g., epitaxially grown thin films, BCP derived quantum materials might even display such emergent effects in an enhanced or altered way.

Lastly, on the subject of expanding into new types of materials, it should be noted that while this thesis focused entirely on superconducting quantum materials, there is defined interested in using BCP self-assembly in the synthesis of other types of quantum matter. As described in chapter 2, there are a multitude of opportunities for soft matter to have impact in topological and magnetic materials. While progress has been made, the establishment of a BCP derived quantum material (e.g., a mesostructured topological insulator or spin ice, etc.) has yet to be achieved in either area. However, combining the methods developed in this thesis with new materials synthesis routes may provide a few viable paths. As one example: if a ferromagnetic material such as cobalt-iron oxide can be structured directed by BCPs into a mesoporous template, then backfilled with a ferroelectric polymer such as PVDF using high pressure melt

infiltration, the resulting material should behave as a multiferroic. With the additional complexity of mesoscopic structure and interpenetration in the composite, novel properties not seen in bulk or thin film analogs might well be found. Similar schemes can be developed based upon work described in other chapters of this thesis: pluronics based routes to topological insulators in which processing is informed by the work achieving high quality NbCN, thin film magnetic materials with artificially defined spin textures synthesized and processed into test architectures such as was done with NbCN thin films, and further.

Thus, it is apparent that many open questions and unexplored paths remain for the emerging field of BCP derived superconductors and other quantum materials. The work presented in this thesis has answered a few questions, but even more so has highlighted the areas into which further investigation might be usefully directed. Using the tools provided in previous chapters, and informed by the (recently accelerated) progress in quantum materials science, future work into soft matter enabled quantum materials can now begin to fulfil the promise of discovering new properties, emergent phenomena, and increased processing capabilities.